Multi-cracking of Reinforced Concrete Structures : Image Correlation Analysis and Modelling

Nuraziz Handika

Université Fédérale
Toulouse Midi-Pyrénées

THÈSE

En vue de l'obtention du

DOCTORAT DE L'UNIVERSITÉ DE TOULOUSE

Délivré par :

Institut National des Sciences Appliquées de Toulouse (INSA de Toulouse)

Présentée et soutenue par :
Nuraziz HANDIKA
Le mercredi 1 février 2017
Titre :

Multi-fissuration des structures en béton armé :
Analyse par corrélation d'images et modélisation

Jury :

Alain MILLARD, Directeur de recherche, CEA Saclay	Rapporteur
Farid BENBOUDJEMA, Professeur, ENS Cachan, Université Paris-Saclay	Rapporteur
Luc DAVENNE, Professeur, IUT de Ville d'Avray	Examinateur
Alain SELLIER, Professeur, Université Toulouse III Paul Sabatier	Directeur de thèse
Géraldine CASAUX-GINESTET, Maître de Conférences, INSA de Toulouse	Co-Directrice

---

École doctorale et discipline ou spécialité :
ED Mécanique, Energétique, Génie Civil et Procédé (MEGEP) : Génie civil

Unité de recherche :
Laboratoire Matériaux et Durabilité des Constructions (LMDC)
135, Avenue de Rangueil 31077 Toulouse Cedex 04, France

Directeur/trice(s) de Thèse :
Alain SELLIER
Géraldine CASAUX-GINESTET

AUTHOR: Nuraziz HANDIKA **Year**: 2017

DIRECTOR OF THESIS: Prof. Alain Sellier and Dr. Géraldine Casaux-Ginestet

TITLE: Multi-cracking of Reinforced Concrete Structures: Image Correlation Analysis and Modelling

ABSTRACT

The modelling of cracking of reinforced concrete using the finite element method requires taking into account, in addition to the concrete damage, three phenomena: the specificity of the steel-concrete bond, the self-stress due to shrinkage, and the probabilistic scale effect due to the heterogeneity of concrete. This research is based on an experimental campaign to obtain the behaviour of the bond and the characteristics of the cracks on structural elements. The technique of digital image correlation was used to observe the spacing and opening of the cracks.

The steel-concrete bond is considered in modelling using elastoplastic interface elements based on the experimental results of the pull-out tests. The effects of shrinkage are taken into account via a poro-mechanical framework. Finally, the probabilistic scale effect is integrated into the modelling via a random field method and then a weakest link one. Modelling is applied to the reinforced concrete structural element studied in the laboratory, which makes it possible to quantify the relative importance on cracking of the steel-concrete bond, the stresses induced by shrinkage, and the tensile strength heterogeneity of the material.

Keywords: Crack modelling, FEM, Digital Image Correlation, Steel-concrete bond, Shrinkage, Probabilistic scale effect.

This page is intentionally left blank

AUTEUR : Nuraziz HANDIKA **Année**: 2017

DIRECTEUR DE THESE : Prof. Alain Sellier and Dr. Géraldine Casaux-Ginestet

TITRE : Multi-fissuration des structures en béton armé : Analyse par corrélation d'images et modélisation

RESUME

La modélisation de la fissuration du béton armé à l'aide de la méthode des éléments finis nécessite de prendre en compte, outre l'endommagement du béton, trois phénomènes : la spécificité de la liaison acier-béton, l'autocontrainte due au retrait, et l'effet d'échelle probabiliste dû à l'hétérogénéité du béton. Cette recherche s'appuie sur une campagne expérimentale pour obtenir le comportement de la liaison et les caractéristiques des fissures sur des éléments de structures. La technique de corrélation d'images numériques a été utilisée pour observer l'espacement et l'ouverture des fissures.

La liaison acier-béton est considérée dans la modélisation à l'aide d'éléments d'interface élasto-plastiques basés sur les résultats expérimentaux des tests de pull-out. Les effets du retrait sont pris en compte via un cadre poro-mécanique. Enfin, l'effet d'échelle probabiliste est intégré dans la modélisation via une méthode de champs aléatoires, puis de maillon faible. La modélisation est appliquée à l'élément de structure en béton armé étudié en laboratoire ce qui permet de quantifier l'importance relative de la liaison acier-béton, des contraintes induites par le retrait empêché, et de l'hétérogénéité du matériau.

Mots-clés : Modélisation des fissures, MEF, Corrélation d'images, Liaison acier-béton, Retrait, Effet d'échelle probabiliste.

This page is intentionally left blank

RESUME

Le béton armé (BA) est l'un des matériaux de construction les plus couramment utilisés dans le monde depuis son développement au cours du 20ème siècle. Dans la plupart des cas, la question de la durabilité des structures en béton armé devient la principale préoccupation parce qu'elle est nécessaire pour garantir le fonctionnement du bâtiment. La durabilité est assez souvent liée à la fissuration de ces structures. Dans certaines circonstances, une fois que des fissures se sont produites, les infiltrations de l'extérieur et les fuites de l'intérieur sont inévitables. Ces problèmes peuvent entraîner une dégradation du béton et nuire davantage à la fonction du bâtiment. Par conséquent, la maîtrise de la fissuration sur les structures en béton armé est primordiale.

La norme européenne Eurocode 2 (Eurocode 2, 2005) limite l'ouverture des fissures pour les éléments des structures en fonction de leur classe d'exposition. Cette norme fournit aussi une méthode pour calculer l'ouverture de fissure maximale dans les éléments structuraux. Le Projet National Ceos.fr (CEOS.fr, 2015) a proposé de nouvelles formulations pour le calcul des ouvertures de fissure, ainsi que pour leur espacement, en enrichissant le Code Modèle (MC 2010, 2013) qui met en évidence les insuffisances de l'Eurocode 2. La formulation proposée a recommandé de tenir en compte de trois paramètres importants pour le calcul sur les éléments structuraux : la meilleure prise en compte de la contrainte de cisaillement de la liaison acier-béton, la contrainte de retrait induisant la contrainte initiale dans le béton et l'effet d'échelle probabiliste pour déterminer la valeur de la résistance à la traction du béton. Par conséquent, la modélisation de la fissuration du béton armé pour les structures de grandes dimensions et complexes s'appuie sur la méthode des éléments finis, outre l'endommagement du béton, la prise en compte de ces trois phénomènes doit être clarifiée.

Cette thèse a pour objectif général de quantifier le rôle de chacun des trois paramètres mentionnés précédemment et leurs combinaisons pour trouver les méthodes de modélisation les plus efficaces pour le calcul des ouvertures de fissures. Cette recherche est basée sur des campagnes expérimentales pour obtenir le comportement local de la liaison acier-béton et les caractéristiques des fissures sur les éléments structuraux en utilisant un système de corrélation d'images numériques (CIN). Pour atteindre cet objectif, la première partie du travail concerne les essais de caractérisation pour le béton, pour la barre d'acier et pour la liaison acier-béton. Dans la deuxième partie du travail qui concerne les simulations numériques, les modèles sont choisis et appliqués sur des éléments de structure. Ensuite, plusieurs améliorations des simulations numériques relatives à chacun des trois paramètres mentionnés ci-dessus sont testées.

Cette thèse est organisée en trois chapitres: Le **chapitre 1** propose une revue bibliographique qui commence par l'étude de la fissuration des structures en béton armé du point de vue de la norme européenne. Ensuite, plusieurs travaux expérimentaux et de modélisations numériques des

fissures dans le béton armé, ainsi qu'une technique plus récente pour mesurer les ouvertures de fissures sont présentés.

Basés sur les recommandations de PN Ceos.fr, les trois principaux paramètres mentionnés précédemment doivent être clarifiés. Concernant la liaison acier-béton, la zone de transition peut être modélisée en discrétisant une zone d'interface avec un comportement mécanique propre. Un modèle analytique d'Eligehausen (Ciampi et al., 1981; Eligehausen et al., 1983), ou des résultats de l'essai d'arrachement de type pull-out, peuvent être appliqués comme loi élasto-plastique avec écrouissage isotrope. L'application du critère de Von Mises dans cette zone semble judicieux puisque dans le béton avec enrobage épais, comme dans le cas du test de pull-out, la force de liaison est indépendante du confinement actif (Torre-Casanova et al., 2013). L'utilisation de ce modèle dans le contexte des éléments finis en utilisant l'élément solide avec quelques millimètres d'épaisseur autour des barres d'acier permet de modéliser de façon réaliste la zone dégradée observée.

Concernant au phénomène du retrait, la présence d'une barre d'acier provoque une retenue durant le retrait du béton. Cette condition induit une contrainte initiale qui peut affecter la première force de fissuration. Ici, on s'intéresse à cet effet du retrait sur le comportement mécanique. Cette condition peut être modélisée dans un contexte de poro-mécanique. L'une des méthodes est la formulation de Van-Genuchten qui se traduit par un état de pré-endommagement à la fin du retrait. Cet état explique la réduction initiale de rigidité observée expérimentalement sur des éléments en béton armé.

Vis-à-vis des effets d'échelle probabilistes, des études récentes ont montré l'effet de la taille structurelle des éléments sur les valeurs de résistance mécanique observée localement dans l'élément. L'effet sur le comportement global, sur l'ouverture maximale des fissures et sur leur espacement est très important. Plusieurs méthodes numériques peuvent être utilisées afin de prendre en compte ce phénomène. La méthode de la bande tournante (*Turning Band Method*, TBM) peut être utilisée pour déterminer un champ de résistance en traction aléatoire dans les éléments (Michou et al., 2015) ou un champ de module d'Young aléatoire (Matallah et al., 2010) du béton. Une autre méthode développée au laboratoire LMDC, WL² (*Weakest Link and Localization*) (Sellier and Millard, 2014) peut être une alternative pour prendre en compte l'effet d'échelle de manière déterministe.

Ce chapitre nous amène aux trois aspects importants qui doivent être développés pour une modélisation numérique plus précise des structures en béton armé: la modélisation de la liaison acier-béton, l'influence du retrait et l'hétérogénéité à l'origine de l'effet d'échelle. Ces aspects ont dû être clarifiés dans le contexte de la modélisation de la fissuration des structures.

Le **chapitre 2** est dédié exclusivement à l'importance de la zone de transition entre l'armature et l'élément en béton, appelée zone d'interface. Tout d'abord, ce chapitre présente des essais caractéristiques des matériaux pour le béton, pour la barre en acier et pour la zone d'interface acier-béton. Les essais d'arrachement de type pull-out ont été effectués pour obtenir le comportement de la barre d'acier et du béton environnant. Ensuite, les tests de traction, observés

par un système de corrélation d'images numériques, ont été effectués pour identifier le comportement de fissuration sur deux éprouvettes prismatiques en béton armé. Un acier à Haute Adhérence de diamètre 12 mm est coulé dans un volume de béton avec 40 cm de longueur d'ancrage.

En ce qui concerne les simulations numériques, une loi élasto-plastique avec un critère de Von Mises est utilisée dans un élément volumétrique représentant la zone d'interface avec glissement plastique. Suite aux observations expérimentales, une épaisseur de 3 mm est choisie pour discrétiser cette zone. Ensuite, une simulation a été réalisée pour le test de traction sur l'élément prismatique. La comparaison avec les résultats expérimentaux a montré l'importance du comportement de l'interface avec glissement plastique qui a donné de meilleurs résultats quant à l'ouverture des fissures, au comportement global force - déplacement relatif et à l'indépendance vis-à-vis de la taille du maillage. Néanmoins, ce modèle nécessite certaines améliorations, en particulier pour la localisation des premières fissures et l'ouverture des fissures, menant au chapitre 3.

Dans le **chapitre 3**, le modèle de la liaison acier-béton présenté dans le chapitre 2 est appliqué sur une poutre en béton armé. Il est démontré que, malgré l'utilisation de la zone d'interface entre la barre d'acier et le béton, la modélisation numérique de la poutre béton armé nécessite encore la prise en compte d'autres aspects pour obtenir des résultats numériques plus réalistes à l'échelle à la fois locale et globale.

Un essai de flexion quatre points a été effectué sur des poutres rectangulaires en béton armé. L'observation des fissures a été effectuée avec le système de corrélation d'images numériques. Ensuite, le modèle de la zone d'interface choisi (voir chapitre 2) a été appliqué à cet élément de structure. Toutes les barres en acier ont été modélisées en prenant en compte une couche d'éléments pour la zone d'interface.

Dans la première démarche de modélisation, la nécessité d'appliquer dans la zone d'interface un comportement de glissement plastique a été confirmée. Cependant, une plus grande raideur initiale et une surestimation de la force de la première propagation de fissure ont été obtenues. Dans la deuxième démarche, l'effet du retrait sur le comportement mécanique a été pris en compte pour obtenir un état de contrainte initial réaliste dans le béton. Afin de reproduire ces effets du retrait, le degré de saturation est varié. En effet, le degré de saturation est directement lié à la pression capillaire par les équations de Van-Genuchten dans le contexte de poro-mécanique. Les résultats mettent en évidence que la perte de raideur initiale, ainsi que l'apparition des fissures près des aciers transversaux peuvent s'expliquer par le retrait. Pourtant, cela n'a pas été suffisant pour modéliser la propagation de fissure et pour avoir le comportement global après la première fissuration.

Dans les deux prochaines démarches de modélisation, le caractère aléatoire des propriétés du béton a été pris en compte avec la contrainte de retrait et avec la zone d'interface. Les méthodes de la bande tournante (*Turning Band Method*, TBM) et de la *Weakest Link et localisation* (WL^2) ont été respectivement testées dans la troisième et quatrième démarche de modélisation. Avec la

méthode TBM, trois champs aléatoires ont été générés. Ces champs ont conduit à différents faciès de fissuration et de variation de l'ouverture des fissures qui étaient plus réalistes que dans la modélisation précédente (la deuxième démarche). Cependant, il a fallu plusieurs échantillonnages aléatoires pour avoir un comportement représentatif d'une structure réelle. Cette application a aussi montré que la méthode TBM doit toujours être utilisé avec le volume total de béton pour avoir la zone la plus faible la plus réaliste pour chaque échantillonnage.

La méthode de WL^2 évite d'avoir recours à plusieurs échantillonnages aléatoires. Cette méthode permet de prendre en compte le maillon le plus faible, même avec un modèle simplifié pour lequel le volume total a été remplacé par un quart de volume et des conditions de symétrie. La méthode a abouti à une meilleure concordance de la relation force-déplacement expérimentalement que dans les cas de la méthode TBM. Malgré une version simplifiée de WL^2 en utilisant le volume constant sur tout la poutre, ce modèle a été capable de reproduire les faciès de fissuration les plus probables, comme le montre la fonction de densité de probabilité obtenue pour l'ouverture de fissure la plus proche de celle expérimentale.

Ainsi, cette étude montre l'importance de trois aspects essentiels dans la modélisation des fissures : la zone d'interface entre le béton et la barre d'acier qui peut être montrée dans les résultats des essais de pull-out, le retrait du béton qui contrôle principalement la rigidité initiale et le pré-endommagement de béton, les propriétés aléatoires qui doivent être prises en compte pour avoir une évolution réaliste des forces de première fissuration, de l'espacement et des ouvertures des fissures.

Mots-clés: Modélisation des fissures, MEF, Corrélation d'images, Liaison acier-béton, Retrait, Effet d'échelle probabiliste.

ACKNOWLEDGEMENT

This present work is the result of a collaboration that may be achieved through the commitment and support of many people. I would like to warmly thank my thesis director Alain Sellier (Professor at Université Paul Sabatier Toulouse), for his human and scientific qualities, his daily availability and his enthusiasm during my many unexpected short meeting in his office. My sincere gratitude is presented to Géraldine Casaux-Ginestet (Assistant professor at INSA Toulouse) for her supports, her advices and to integrate me into the teaching team of INSA. My deepest appreciation is expressed for their directions and patience during my doctorate in LMDC.

This research was mainly developed at the LMDC laboratory, INSA Toulouse, l'Université Fédérale Toulouse Midi-Pyrénnés, in which I have benefited from a pleasant environment, surrounded by helpful staffs. I would like to thank Gilles Escadeillas, the former Director of LMDC, and Alain Sellier, the current Director, for the opportunities to use Digital Image Correlation (DIC) system and also for the training.

I take this opportunity to express my thankfulness to Mr. Luc Davenne, it has been my honour to have you as the president of Jury. I would also like to thank my rapporteurs, Farid Benboudjema, Professor in ENS Cachan and Alain Millard, Research Director at the CEA in Saclay, for the interest in my works, your detailed reading and your pertinent criticisms that have provided advices and suggestions.

The financial support provided by the co-financing between Indonesian Government, precisely the Directorate General of Resources for Research, Technology & Higher Education Ministry of Research, Technology and Higher Education Republic of Indonesia; and the *Bourse du Gouvernement Français*, by the Campus France which was allocated during the whole period of my study, is gratefully acknowledged.

I would like to express my gratitude to all the professors and lecturers I have worked with, especially in Béton Armé courses, Sébastien Mercadier and Nathalie Domède. I thank Prof. Anaclet Turatsinze for giving me some advice in experimental works. I sincerely thank Prof. Frédéric Duprat, Prof. Jean-Paul Balayssac, Laurie Lacarrière, and Thierry Vidal for the opportunity to participate in the visit day of FIB (*Fédération Internationale Béton*) in summer 2016. The fruitful discussion with the member of FIB has provided me a great motivation.

I would like to convey my gratefulness to Nary for introducing me to perform concrete casting in laboratory, for all advices, methods, standards, regulations etc. I thank all technicians, especially in mechanical testing group. Carole for her helps for strain gauges, LVDT measurements and acquisition system. Moreover, in working on DIC, together with Guillaume,

regulation of the equipment and making the speckle pattern. Also, I thank Bernard, Frédéric, Yann, Sylvain and René for any helps in laboratory.

During my stay at the LMDC, I worked with numerous people who contributed to this work. I met friends with well-tempered characters. My office colleagues: Raphaëlle, Rémy, Khadim, Jin, Célimène, Rudy, Emmanuel, Aurélie, Alexandre, Zeye, Souad, Guy, Pablo and Julie. A very special mention to my friends "the LMDC Cast3M team", Saïd, Thomas, Hugo and Ponleu, we had a lot of interesting discussions. There are also Billy, Mathilde, Sophie, Asad, Gaël, Sylvain, Pierre, Yvan, Célestine, Kahina, Maha, Quan, Nam, Isabelle, Moustapha, Ilgar, and all other doctorate students in LMDC.

I express my gratitude to the professors and lecturers in Civil Engineering Department Universitas Indonesia for all of their supports. Prof. Katili, Bu Elly, Bu Essy, Pak Madsuri, Pak Heru, Bu Cece dan Pak Widjojo. My fellas, Bastian and Sandy, also Cipta, thank you for the friendship and insight that you have brought to me. I thank my friends from Indonesian Student Associations in Toulouse, Mas Yoga, Kang Dede and others that cannot be mentioned one by one. Very special thanks to my friends Mba Mungky, Ibu Sylvi, Ami, Alex, Dennis, Hafiz, Irene, Iwan, Habieb, Amin, Raisa, Syarif, Indri, Bu Yunah, Bu Ninik, Mba Lenny, Pak Ferdy and Mas Haris for organizing my defense buffet and their presence in my defense. Mba Nanda, Aulia, Nadya, Sofwan dan Kang Dadan, thank you for the grammar correction.

Finally, my sincere gratitude goes to my family in Indonesia, in particular to my parents, Mama and Papa, my brother Agam, my sister, Chacha for their love, infinite and unconditional support in the most difficult moments. I thank my parents for sharing their commitment to work and the perseverance when the tasks and responsibility may seem overwhelming.

As thanks are a more or less perilous exercise, I would also like to thank all the uncited people who might feel pained not to be mentioned. Let them find in these lines the expression of my deep consideration. It would not be easier without your presence by my side.

Terima kasih.

Ing Ngarso Sung Tulodho Ing Madya Mangun Karso Tut Wuri Handayani

Proverb by Ki Hadjar Dewantara (in Javanese language), 1889-1959

"(For those) in front should set an example, (for those) in the middle should raise the spirit, and (for those) behind should give encouragement"

This page is intentionally left blank

Table of Contents

List of Figures

List of Tables

This page is intentionally left blank

General Introduction

Reinforced Concrete (RC) is the most widely used construction building material worldwide. In almost cases, durability issue of RC structures becomes the main concern as it can guarantee the building's function. Durability is closely related to the cracking behaviour in RC structures. Under some circumstances, once cracks occurred in RC structures, infiltration from the exterior is unavoidable; leakage from the interior is inevitable either. These problems could lead to degradation of material strength and further could impair building's function. Therefore, quantifying the cracks on reinforced concrete structures is mandatory.

European building codes Eurocode 2 (Eurocode 2, 2005) limits the crack opening for structural elements based on their exposure classes and provides the design crack's formulation, Recently, PN Ceos.fr (CEOS.fr, 2015) proposed the formulation of crack width and spacing enriching the Model Code 2010 (MC 2010, 2013) which shows the insufficiency of Eurocode 2. The proposed formulation recommended three important parameters for the calculation of structural elements, such as a better consideration of the steel-concrete bond stress, the shrinkage strain inducing initial stress and also the probabilistic scale effect in determining the value of concrete tensile strength. Therefore, in the cracking modelling of large and complex reinforced concrete structures using the finite element method, the consideration of these phenomena in addition to the concrete damage needs to be clarified.

This doctorate thesis has objective general to quantify the role of each of the three parameters (mentioned previously) and their combinations to find the most effective crack modelling methods. This research is based on experimental campaigns to obtain the local behaviour of the bond and the characteristics of the cracks on structural elements using Digital Image Correlation system. To achieve this objective, the work starts with characterisation tests for the concrete, the steel bar and the steel-concrete bond. The models are fitted and applied to structural elements. Then, several improvements relative to each of the three points aforementioned are tested. This working method is presented schematically in Figure i.

This thesis is organised into three chapters: **Chapter 1** gathers some literature reviews that starts with the cracking on Reinforced Concrete (RC) structures from standard building code point of view. Then, several experimental works and numerical modelling of crack on RC are presented along with the latest technique to measure the cracks. This chapter leads us to the three important aspects which need to be proven for accurate RC numerical modelling: the steel-concrete bond stress, the induced stress on concrete due to shrinkage and the heterogeneities of concrete characteristics.

In **Chapter 2**, the importance of the transition zone between rebar and concrete element is

studied exclusively. It consists firstly to identify an interfacial behaviour law from experimental results. An elastoplastic law with a Von Mises criterion is used to consider steel-concrete sliding in a volumetric element representing the interfacial zone. Secondly, this elasto-plastic law is used on a simple RC prismatic element. Comparison to the experimental results shows the necessity of this interface model with plastic sliding degradation. Nevertheless, more improvements are still needed especially to assess the first crack opening.

In **Chapter 3**, the steel-concrete bond model clarified in Chapter 2 is applied on an RC beam. It is shown that despite using interfacial transition zone between steel bar and concrete, numerical modelling on RC beam still requires other aspects to obtain better results in term of crack opening and global behaviour. Therefore, pre-damage due to shrinkage in poro-mechanics framework and random mechanical properties are envisioned for RC modelling. To this purpose, the modelling considers first these phenomena independently and then their combinations are progressively examined.

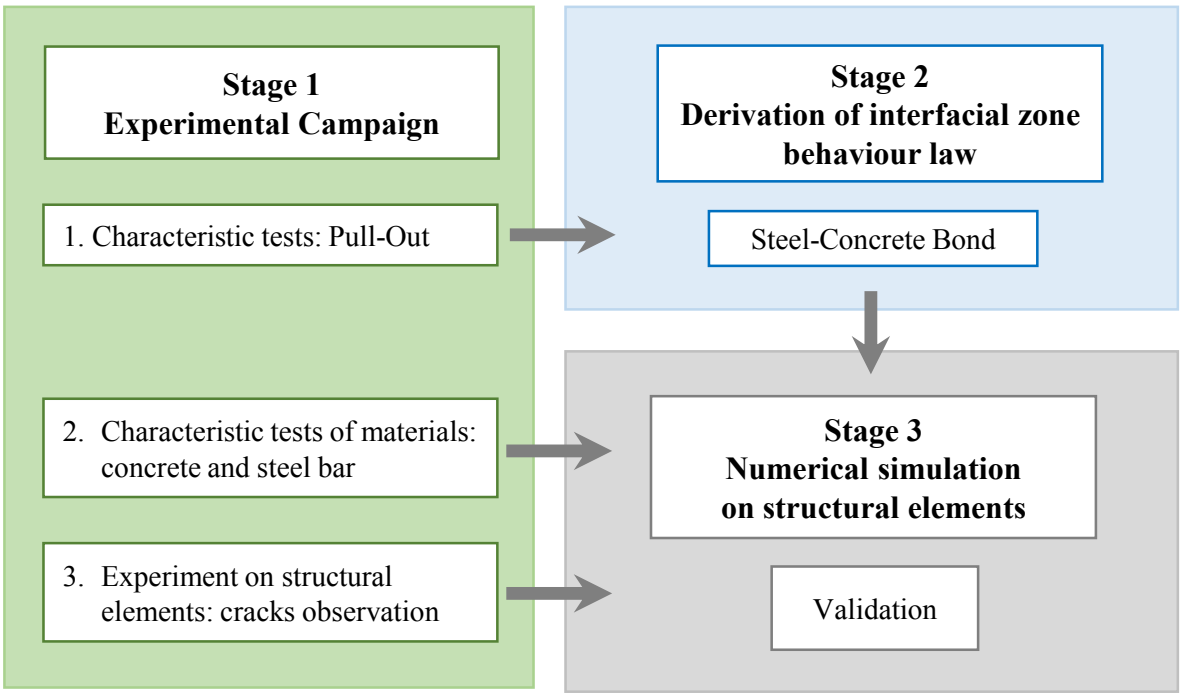

Figure i. Schema of working methods on crack modelling.

Chapter 1

State of the art

This literature review starts with the cracking on Reinforced Concrete (RC) structures from standard building code point of view. After that, several experimental works and numerical modelling of crack on RC are presented. This chapter leads us to the three important aspects which stay to be clarified for accuracy in RC numerical modelling: the steel-concrete bond stress, the induced stress on concrete due to shrinkage and the heterogeneities of concrete characteristics.

This page is intentionally left blank

1. 1. Crack on RC structures

1. 1. 1. Control of crack width and crack spacing in design codes

Cracks can occur in a Reinforced Concrete (RC) structure when it is subjected to bending, shear, torsion or tension loading. They may also arise from other phenomena, for example, shrinkage. Some problems such as a leakage from the inside of the structure, an intrusion from the exterior or corrosion in the steel bar may occur because of the cracks. Thus, the crack opening has to be limited in order to maintain the proper functioning or the durability of the structure.

In the actual condition, the crack width in an RC structure can vary between wide limits and cannot be estimated precisely. The limiting requirements of cracks are available in Eurocode 2 (Eurocode 2, 2005). Up to this acceptable limit of crack, the functioning of structures is not considered impaired. The maximum acceptable value of crack width ($w_{\max}$) is 300 µm for all exposure classes under the action of *quasi-permanent* combination of loads. The lower recommended crack width limit may be used for a special condition, such as in a case of water-retaining structures and even in absence of durability problem, a maximal opening of 400 µm is required to preserve safety aspect of the structure.

During the design process, the engineers have to control the maximum crack width of structures which is defined as a characteristic crack with a probability level "*k*" to be exceeded (Mosley et al., 2007). Currently and for basic element (beam, column, etc.), the design crack width according to Eurocode 2 (Eurocode 2, 2005), w_k, is calculated based on the maximum crack spacing ($S_{r,\max}$) as expressed in Equation 1.1.

$$w_k = s_{r,\max}\left(\varepsilon_{sm} - \varepsilon_{cm}\right) \tag{1. 1}$$

Where:

w_k	=	The design crack width
$s_{r,\max}$	=	The maximum crack spacing
ε_{sm}	=	The mean strain in the reinforcement under the relevant combination of loads
ε_{cm}	=	The mean strain in the concrete between cracks

The expression $\varepsilon_{sm} - \varepsilon_{cm}$ is given by the following formulae.

$$\varepsilon_{sm} - \varepsilon_{cm} = \frac{\sigma_s - k_t \dfrac{f_{ct,eff}}{\rho_{p,eff}}\left(1 + \alpha_e\ \rho_{p,eff}\right)}{E_s} \geq 0{,}6\,\frac{\sigma_s}{E_s} \tag{1. 2}$$

Where:

σ_s	=	The stress in the tension reinforcement calculated in the cracked concrete section
k_t	=	The factor dependent on the duration of the loading. $k_t = 0{,}6$ for a short-term loading

and $k_t = 0{,}4$ for a long-term loading

E_s = The design value of a modulus of elasticity of reinforcing steel

$f_{ct,eff}$ = The mean value of the tensile strength of the concrete effective at the time when the first cracks occur

$\rho_{p,eff}$ = The effective reinforcement ratio. For non-pre-stressed beam:

$\rho_{p,eff} = A_s / A_{c,eff}$

A_s = The area of reinforcing steel

$A_{c,eff}$ = The effective area of concrete in tension surrounding the reinforcement with

$h_{c,eff} = \min\left(2{,}5(h-d);(h-x)/3;h/2\right)$

α_e = The ratio E_s / E_{cm}

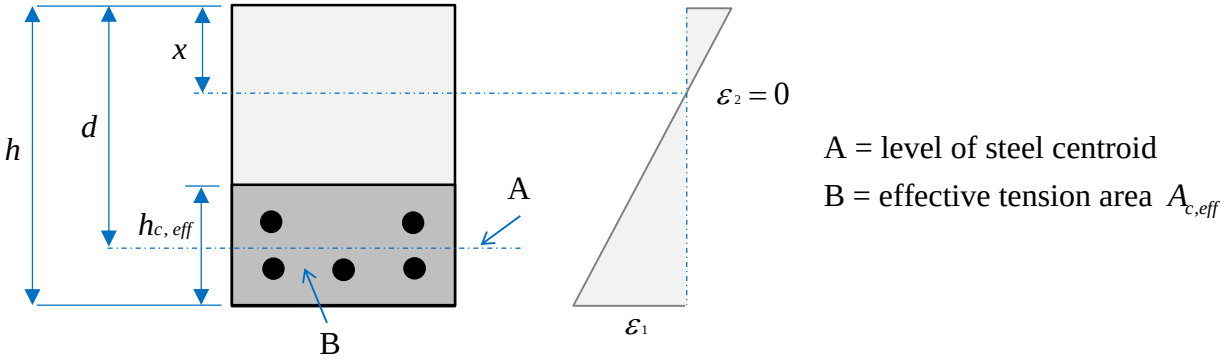

Figure 1. 1. Effective tension area for a beam case (Eurocode 2, 2005).

Furthermore, the crack spacing can be calculated by using the following expression.

$$s_{r,\max} = k_3 c + k_1 k_2 k_4 \phi / \rho_{p,eff} \quad (1.3)$$

Where:

c = The cover concrete to the longitudinal reinforcement

k_1 = The coefficient which considers the bond properties. $k_1 = 0{,}8$ for ribbed bar and $k_1 = 1{,}6$ for non-ribbed bar

k_2 = The distribution of strain coefficient. $k_2 = 0{,}5$ for bending and $k_2 = 1{,}0$ for pure tension

k_3 = For cover concrete $c \le 25$ mm, $k_3 = 3{,}4$. Otherwise $k_3 = 3{,}4(25/c)^{2/3}$

k_4 = 0,425

ϕ = The bar diameter

According to Equations (1.1), (1.2) and (1.3), Eurocode 2 suggests the crack width and spacing calculation by taking into account the type of the bar (ribbed or non-ribbed), the concrete's mechanical properties (E_{cm}, f_{ct}) and the steel bar's mechanical properties (diameter, E_S). The type of loading application on the structure is taken into account by the distribution of strain coefficient (k_2).

Beside Eurocode 2, there are some recommendations to calculate the crack width and the maximum crack spacing based on The French National Project called PN Ceos.fr (CEOS.fr, 2015). These expressions contain some enrichments of the proposed equations in the Model Code 2010 (MC 2010, 2013) from the experimental research project.

$$w_d = 2\, l_{s,\max} \left(\varepsilon_{sm} - \varepsilon_{cm} - \varepsilon_{cs}\right) \tag{1. 4}$$

Where : $l_{s,\max} = c + \frac{1}{4}\frac{f_{ctm}}{\tau_{bms}}\frac{\phi}{\rho_{s,ef}}$

$$\tau_{bms} = 1{,}8\, f_{ctm}$$

$$\varepsilon_{sm} - \varepsilon_{cm} - \varepsilon_{cs} = \frac{\sigma_s - \beta.\sigma_{sr}}{E_s} + \eta_r.\varepsilon_{sh}$$

Where:

$l_{s,\max}$	=	The length over which slip between concrete and steel occurs
ε_{sm}	=	The average steel strain over the length $l_{s,\max}$
ε_{cm}	=	The average concrete strain over the length $l_{s,\max}$
ε_{cs}	=	The strain of the concrete due to (free) shrinkage
f_{ctm}	=	The mean value of the tensile strength of the concrete
τ_{bms}	=	The bond stress
ε_{sh}	=	The relative strain due to shrinkage
η_r	=	The coefficient reflecting the contribution due to shrinkage

In Equations (1.4), to determine the crack width, it is suggested to consider the bond stress (τ_{bms}), the shrinkage strain (ε_{sh}) and also the scale effect (to obtain the precise value of f_{ctm}). So, from an analytical point of view, PN Ceos.fr has already recommended three parameters for the calculation of structural elements on RC structure. It would be necessary for the calculation of large or complex structures to take into account numerically in a FEM context, the steel-concrete bond stress, the shrinkage strain that induced initial stress in the concrete and the probabilistic scale effect. Before going to the FEM, let's have a look to the experimental investigations about these phenomena.

1. 1. 2. Experimental results overview

In the laboratory, there have been a lot of works dedicated for studying the crack on RC structures. Along with the works, there are some developments on the methods that are used to measure the crack propagation and the reinforcement's strain where the cracks open. In this section, the experimental crack observations and the existing method of experiments are presented.

A. Experimental crack observation

In order to investigate the crack opening, there are mainly two types of experiments. The first

one is tensile tests on RC prismatic element in which one steel bar reinforcement was cast inside a concrete volume and the crack propagation can be seen on the concrete surface. The second one is flexural tests on beams. It could be a three-point or a four point flexural test either with or without the presence of the notch on the mid-span of the beam. In this section, some crack observation experiments are presented.

1. Crack on tensile test

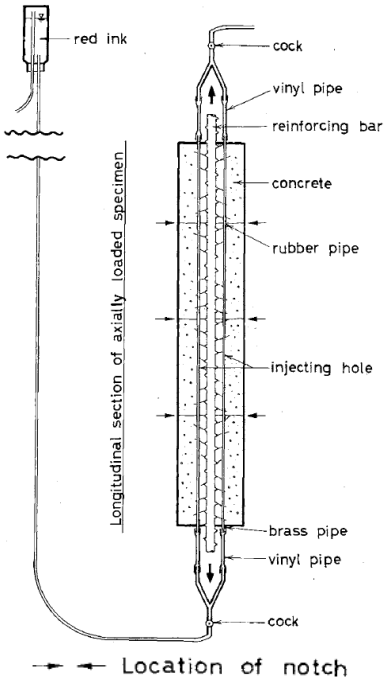

(a) Test configuration with the ink.

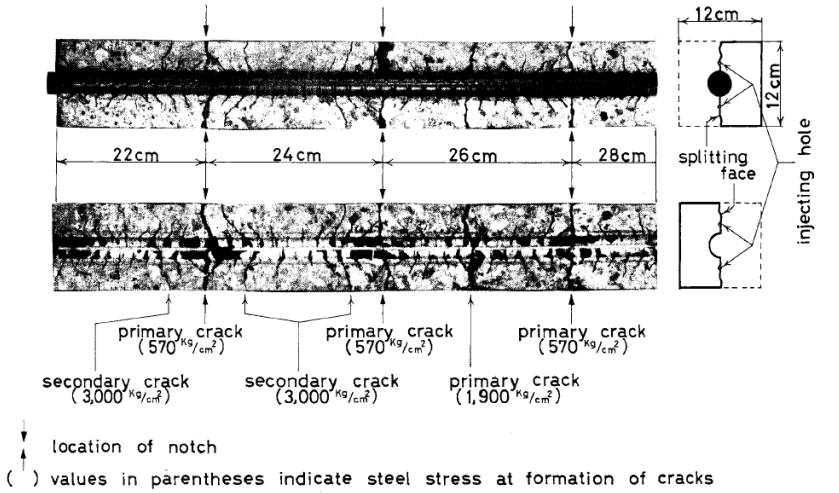

(b) The longitudinal splitting face with a 32 mm of bar diameter.

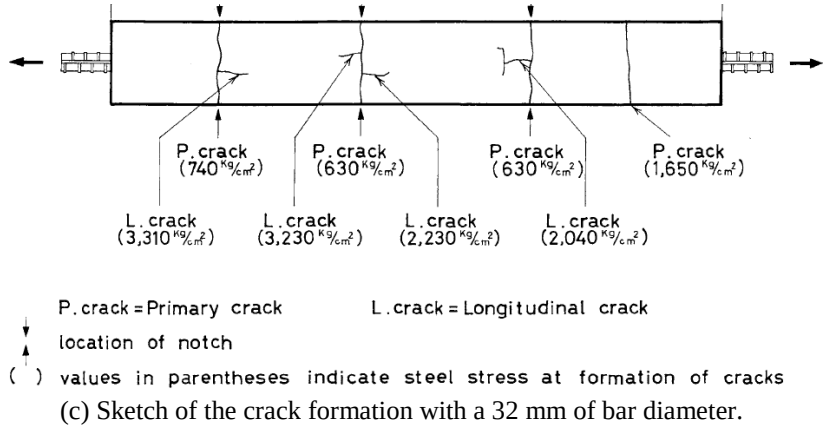

(c) Sketch of the crack formation with a 32 mm of bar diameter.

Figure 1. 2. Tensile test of Goto. (Goto, 1971).

Cracks observation on a tensile test using a single deformed reinforcing bar encased concentrically in a concrete prism was performed by Goto (Goto, 1971). The configurations of the specimens are 10 x 10 x 100 cm^3 for a deformed bar with 19 mm diameter and 12 x 12 x 100 cm^3 for a deformed bar with 32 mm diameter. Four shallow notches were made to generate the primary cracks. The cracks were dyed by injecting ink into the specimens (see Figure 1.2 (a)). After finishing the test, the specimens were split into two part and the dyed cracks were investigated to see the damage occurred around the steel bar.

In this study, four types of cracks were classified: the primary crack, the secondary crack, the internal crack and the longitudinal crack. The *primary crack* was a radial crack that propagated

to the concrete surface (notched) with approximately 60° of inclination. The *internal crack* was the cracks appeared in between two ribs which could propagate to the concrete surface for further loading application forming the *secondary crack*. The action of the ribs to the concrete abutment created a radial deformation around the steel bar that provoked the *longitudinal cracks* initiation at the face of the primary crack.

Another study of a tensile test was performed by Michou (Michou et al., 2015). Three tensile tests on prismatic elements with 10 cm x 10 cm of cross section and 100 cm of anchorage length were carried out. The steel bar that was used had the diameter of 12 mm (see Figure 1.3 (a)). The tensile tests were performed under imposed displacement loading up to the yield strength of the steel bar. The multiple transverse cracks were localised during the loading. Without notch on the concrete surface, we can see the variation of crack number from three specimens as shown in Figure 1.3 (b). For a quantitative point of view, the evolution of the maximum crack opening for each specimen is presented in Figure 1.3 (c). The first crack propagations for three specimens occurred when force reached 20 kN with approximately 200 µm of crack width for each specimen. Moreover, the sum of the crack opening (see Figure 1.3 (d)) presented a good similarity of the three specimens. This representation allows observing the multiple propagations of cracks.

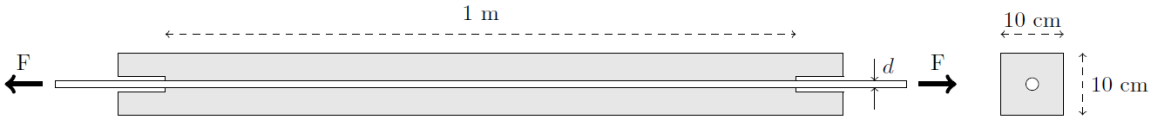

(a) The configuration of the Tie beam specimen.

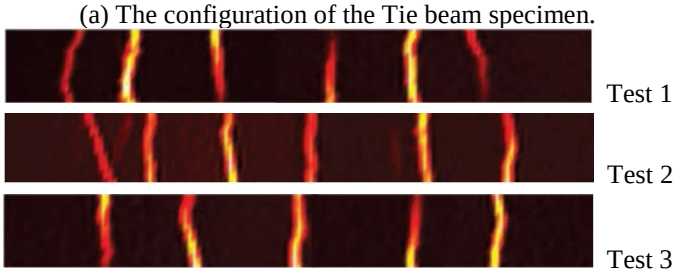

(b) The cracking pattern of the three specimens at the yielding point of the steel bar.

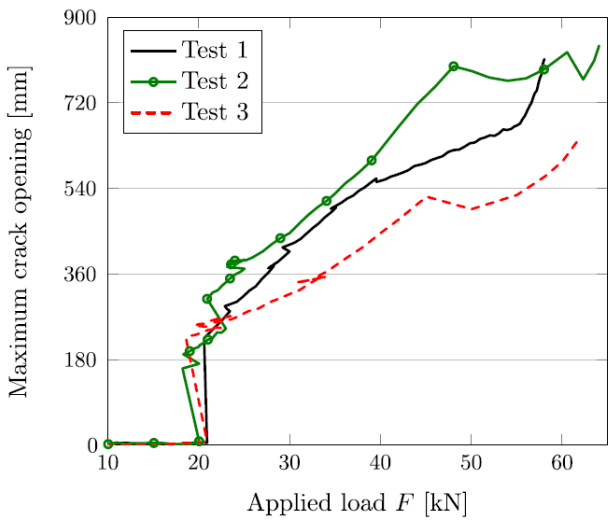

(c). The maximum crack opening

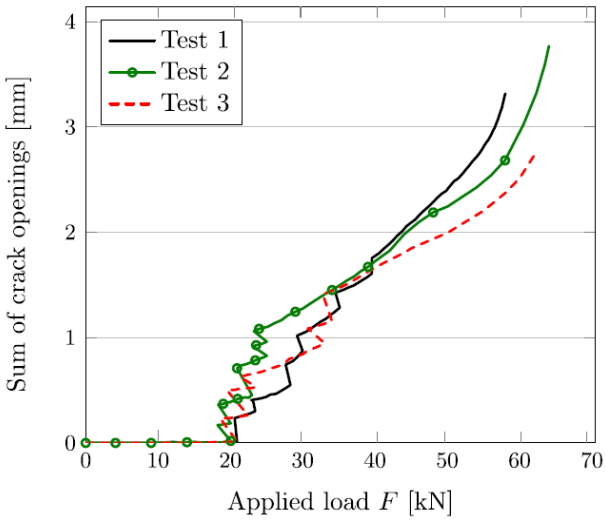

(d) The sum of crack opening

Figure 1. 3. Tensile test results from (Michou et al., 2015).

The two tests presented previously used a one-meter length of test specimen which led to multiple cracks. Another tensile test on prisms (dimension 9 cm x 9 cm x 76 cm) with the objective to study the coupling between the cracking and the transfer of fluid through the crack opening was performed by (Desmettre, 2011). This test employed a good system of testing (bearing plates and grip tubes system on the two ends of the test piece) to distribute the stress along the specimens so in a relatively short tensile specimen (76 cm), the multi cracks occurred.

2. Crack on flexion tests

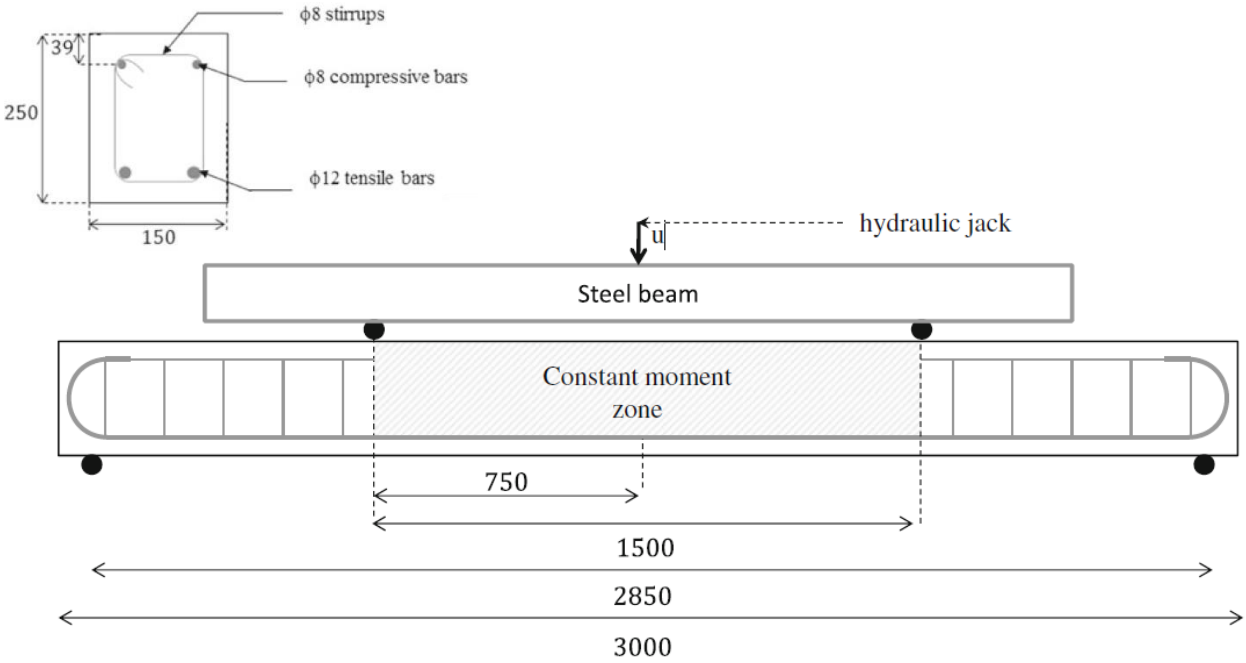

(a) Detail of the specimens and configuration of the experimental campaign.

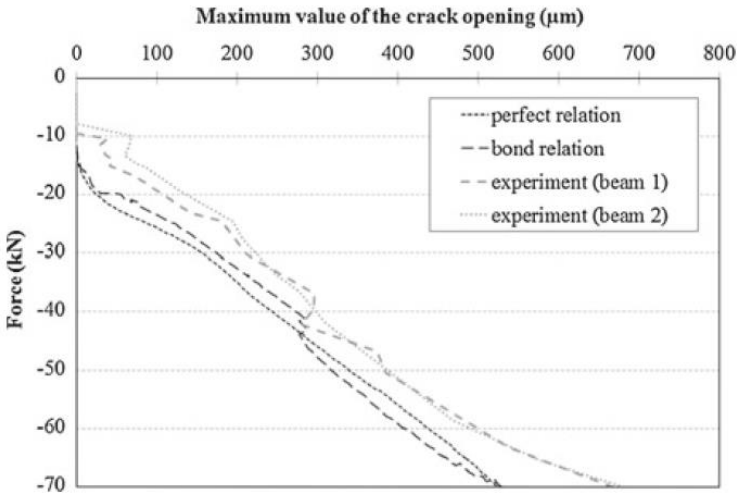

(b) The maximum value of the crack opening on the bottom line of the beam along the constant moment zone.

Figure 1. 4. Crack observation on RC beam with a rectangular section (Jason et al., 2013).

A study of four-point flexural tests on RC beam with a rectangular section was performed by (Jason et al., 2013). Two identical specimens were observed especially on 1,5 metre of their constant moment zone (see Figure 1.4). Bending cracks propagated from the bottom part in a

vertical direction reaching the neutral axis of the beam. The crack width was measured on the bottom part of the beam along the constant moment zone, or the zone under tension stress. The quantification of the crack width shows different value of the maximum crack opening for each beam.

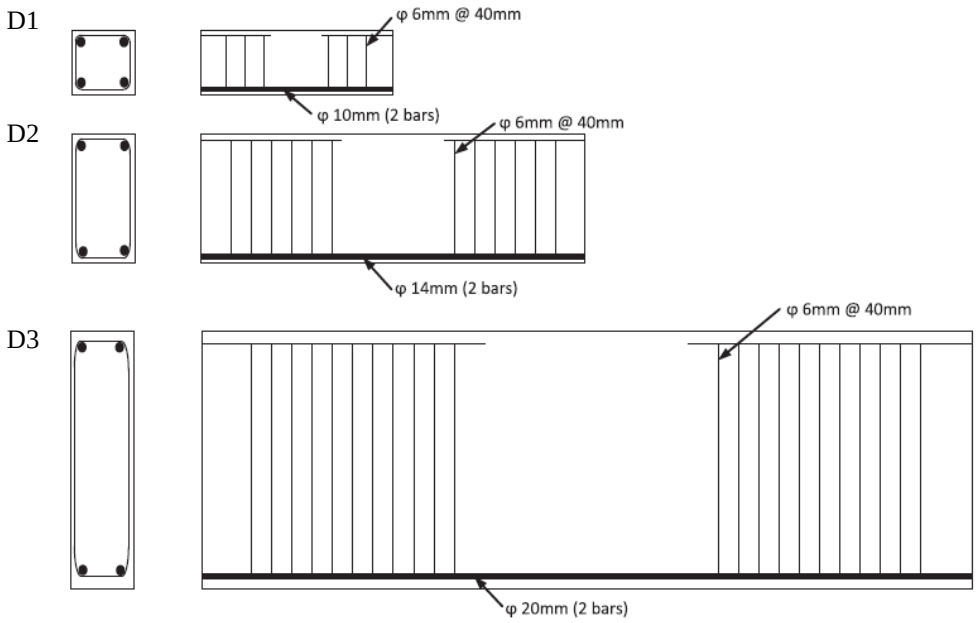

(a) The detail of geometry and reinforcements D1, D2 and D3 successively

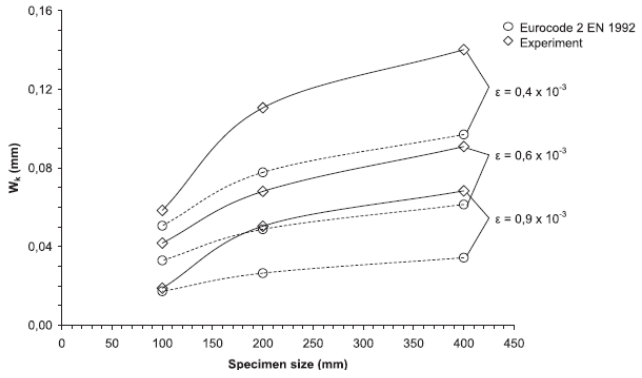

(b). The size effect on the experimental and the calculated crack opening

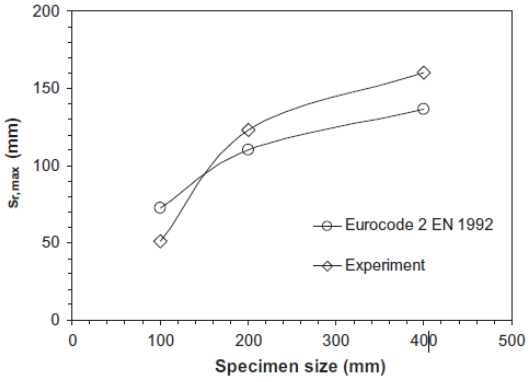

(c). The experimental and the calculated value of the maximum spacing at 300 MPa of steel stress.

Figure 1. 5. The detail of geometry of reinforcements and the experimental results. (Alam et al., 2015)

Three-point flexural tests on RC beam with a rectangular section and three different dimensions were performed by (Alam et al., 2015), see the configuration in Figure 1.5(a). This work has the interest to point out the deficiency of Eurocode 2 to predict the crack width and the maximum crack spacing on beams of different size. The effect of the structural size can be seen on the measured crack width (see Figure 1.5(b)). The calculated crack width using Eurocode 2 were underestimated for all the three sizes. The larger the size of the specimen, the larger the difference (error) between the calculated and the measured crack width was obtained. Moreover, Eurocode 2 also underestimates the crack spacing of the specimen with larger sizes (D2 and D3),

as shown in Figure 1.5(c). This study shows that analytical relationships supplied by Eurocode 2 are accurate only for beams with geometric configurations close to the ones used to establish them. This remark was also confirmed during CEOS.fr (CEOS.fr, 2015) project where the crack width's prediction capability has been tested and do not match systematically with experimental results. These studies comparing standards and experimental conclude that the stress states and the concrete properties around rebar's are certainly miss estimated by the empirical relationships and should be assessed more precisely using FEM if a structure differ significantly from the ones used to establish the standards.

B. Method of experiments

To have a better understanding of cracking, several tools to measure the cracks and the reinforcement strains are clarified. A classical tool such as the crack-measuring-microscope allows measuring the crack width on the surface of the structure. The user has to make a direct contact to the specimen to measure the opening which is sometimes inconvenient. Another tool called Crack Opening Displacement (COD) gauge can be used to measure the crack tip opening (Alam, 2011; Hameed, 2010) for notched beams. Meanwhile, for larger structures where crack positions are in principle unknown, Digital Image Correlation is preferable. Besides, it is also interesting to inspect the strain of the steel reinforcement; measuring using electric gauges suffer from the problem of their position relatively to the random position of the cracks; so recently, optical fibres methods were clarified to measure the strain profile along the steel bar and deduce the bond stress by derivation. Below, the latest measurement tools to observe the crack and the reinforcement strain in the cracked zones in the laboratory are explained.

1. Digital Image Correlation system

The Digital Image Correlation (DIC) was originally developed by (Sutton et al., 1983) to study the evolution of the displacement field of a specimen subjected to a mechanical loading. This technique has been established experimentally to measure the crack opening, the crack spacing and the cracking pattern in mechanics of solids and concrete materials domain (Alam, 2011; Alam et al., 2015; CEOS.fr, 2015; Choi and Shah, 1997; Corr et al., 2007; Jason et al., 2013; Michou et al., 2015).

The DIC system is often referred as a contactless measurement method that acquires images in digital format and performs the analysis to extract the measurement, movement, etc. This system allows measuring the available fields of set points on a surface (Alam, 2011). As a contactless system, the observation of the behaviour beyond the failure point of a material is possible. The latest DIC system uses a 3D images correlation with a *stereovision* technique. The *stereovision* technique uses two rigidly linked cameras that enable us to measure the displacement field from at least two pairs of corresponding images at different times of deformation of the object (Orteu, 2002). This technique allows the correction in its depth which means a slight movement forward or backward of the specimen during the test can be corrected.

To use DIC, a speckle pattern (in black and white colours) is applied on the observation

surface. This speckle can be made by a spray paint forming a random pattern (kilonewton Sarl, 2010). During the loading application, this attached speckle follows the deformation or the displacement of specimen. The digital cameras capture successively this condition throughout the test (see Figure 1.6). The stored digital image is represented as a simple scalar value, in a grey level unit, and is denoted as $f(x)$. The x argument is discretized into elementary pixels, in 2D along with a regular square grid (Roux et al., 2009). If we consider $f(x)$ as the initial state (image at time t as a reference condition) and $g(x)$ as the image at time t+1, they are related by an in-plane displacement field $u(x)$ following the expression in Equation 1.5. This equation is frequently referred as *brightness conservation* (Roux et al., 2009).

$$g(x) = f(x + u(x)) \tag{1. 5}$$

Regularisation of equation 1.5 is necessary to restrain the variability of $u(x)$, since its determination is very difficult. The displacement $u(x)$ is restricted in a specific given functional space as follow:

$$u(x) = \sum_n \omega_n \psi_n(x) \tag{1. 6}$$

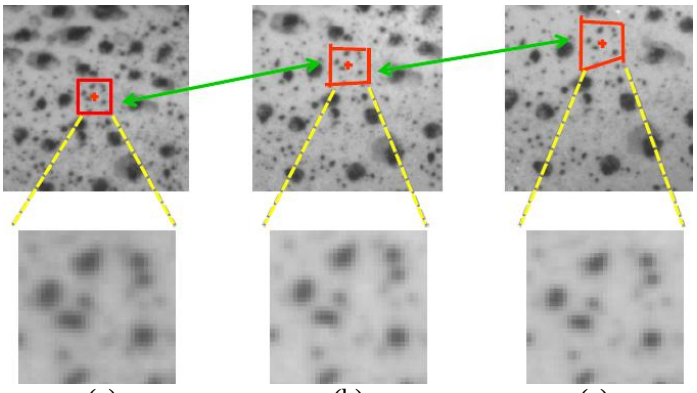

(a) (b) (c)

Figure 1. 6. Images following the speckle pattern on the specimen.
(a) At instant t1. (b) At instant t2 (deformed). (c) At instant t3 (deformed).
Courtesy of (kilonewton Sarl, 2010; Solutions, 2012, p.)

An iterative procedure of correlation is necessary to estimate $u(x)$ by minimising a function Φ in the space ω_n of the correlation area. There are some correlations criteria that can be used, the two of them are:

- SSD (*Sum of Squared Differences*)

  This criterion can be used in low-contrast conditions.

$$\Phi^2(\omega_n) = \int [g(x) - f(x + u(x))]^2 \, dx \tag{1. 7}$$

- ZSSD (*Zero-normalized sum of squared differences*)

  This criterion takes into account both a scale factor and an offset of grayscale. It is recommended in a case of significant changes in brightness.

$$\Phi^2(\omega_n) = \int \left[\left(g(x) - \bar{g} \right) - \left(f\left(x + u(x)\right) - \bar{f} \right) \right]^2 dx \qquad (1.\ 8)$$

Where:

$\bar{f}$ = The average grey levels over the domain of correlation in the references images

$\bar{g}$ = The average grey levels over the domain of correlation in the deformed state images

An estimator called correlation-based similarity criteria (SSD or ZSSD) is used in DIC system to find the possible similarities in the different neighbouring points. So, this advanced technology uses an estimator (statistic) on the speckle pattern in such way to deduce $u(x)$. From this procedure, we can obtain displacement field that can be used for further analysis. Furthermore, with some refinement and colour gradation, the crack pattern can be reproduced visually.

Crack measurement using DIC system

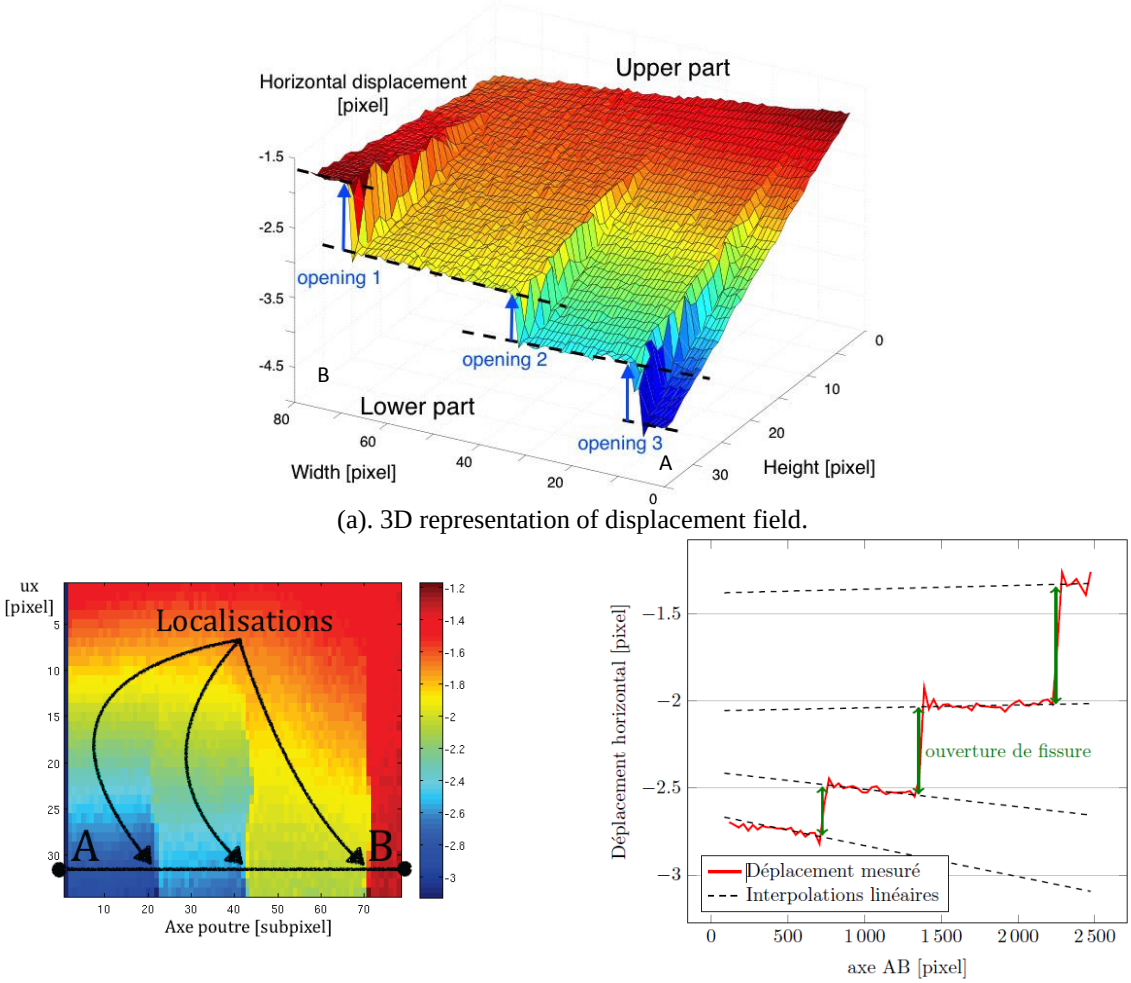

(a). 3D representation of displacement field.

(b). 2D representation of displacement field.

(c). Multiple linear regression to obtain crack width.

Figure 1. 7. The extraction of crack width from displacement field measured by DIC (Michou, 2015).

In a work using DIC by (Michou, 2015), pre-stressed beams were subjected to a four-point bending load. The extraction of the crack opening was obtained from the displacement field. In Figure 1.7 (a) and (b), representations of a displacement field are shown in 3D and 2D successively. The crack width is measured at the level of the passive reinforcement on the bottom part of the beam. So, along with the line AB (Figure 1.7 (b)), a displacement field is extracted and results in a stair-shaped curve as presented in Figure 1.7 (c). The jumping value in horizontal displacement indicates the crack opening. Then, multiple linear interpolations are used to obtain the crack opening. Evidently, the accuracy of the crack measurement depends on several parameters, such as the quality of the photography, the lighting (brightness and contrast) and the speckle pattern.

2. Fibre optic

The DIC system observes a surface of the specimen subjected to mechanical loading. In fact, the crack propagation on the surface is related to the reinforcement strain in the cracked zones. A measuring device called fibre optic is available to measure linear deformation field in the steel bar reinforcement. From this strain, the stress distribution along the bar can be deduced. This technique was used on the steel bars in (Michou, 2015; Tixier, 2013) to supply the parameter identification on the steel-concrete bond behaviour. Figure 1.8 (b) shows the strain along a bar at three different stages of loading for a pull out test. The fact that the strain profile in pull-out test is quasi linear whatever the applied force demonstrates that for a given applied force the bond stress is quasi-constant along the bar, that allows to compute the local bond stress directly from the applied force. This observation will lead us to consider the pull out test response as representative of the local behaviour of steel concrete bond. Meanwhile, Figure 1.8 (c) shows the strain along a bar for a tensile test on tie beam. The strain profile of the bar captures the location of the transverse cracks. In the cracked zones the reinforcement strain is higher since the bearing resistance of concrete reaches zero.

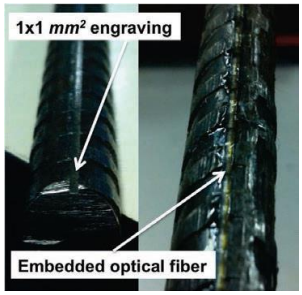

(a). Fibre optic instrumentation.

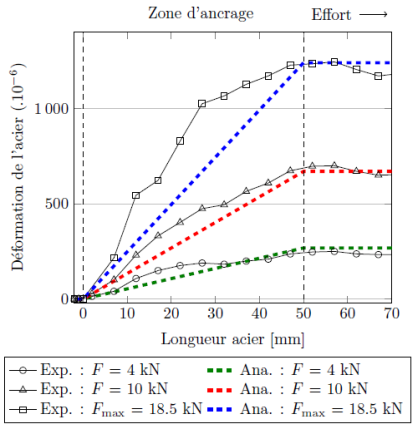

(b). Measured deformation along the bar for a pull-out test.

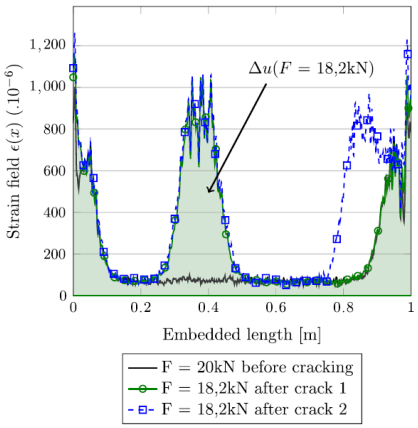

(c). Measured deformation along the bar for a tensile test on tie beam.

Figure 1. 8. Fibre optic instrumentation (Michou, 2015).

1. 2. Behaviour of Steel-Concrete Bond

The transfer of forces between reinforcement and concrete is assured by the *interface zone*. By definition, the interface zone is an area of concrete which surrounds the steel bar. Chemical and physical adhesion between two materials in this zone governs the force transmission from the steel bar to the concrete and inversely. Moreover, the presence of ribs and the collision to concrete reveals a particular distribution of aggregates around the steel bar. The aggregates distribution at this level is rather like mortar due to the absence of the coarse aggregates (*wall effect* (De Larrard, 2009)). Therefore, this interface zone is less rigid than the plain concrete and has a particular behaviour.

Numerous researches have been performed experimentally to understand the intrinsic mechanism of this specific steel-concrete bond behaviour. Then, numerically, several models to take into account the interface zone on RC structures have been proposed. In this second sub-chapter, the discussion is divided into three parts. In the first part, some experimental are presented to show the tests observing the behaviour of this zone from a mechanical point of view. Then, the second part is focused on the mechanism and the influential parameters from experimental works. In the last part, several existing proposed models are described.

1. 2. 1. Experimental tests for parameter identifications

A. Pull-out test

According to (fib, 2000), to study the steel-concrete bond, the relevant experimental works are typically performed on short or long specimens. The short specimen tests are basically done to obtain a uniform distribution of the bond stress along a short single bar ($l \leq 5\phi$) so the local bond-slip behaviour and the maximal strength are obtained, this fact was recently confirmed by (Michou, 2015) as mentioned before. One example is the pull-out tests performed by Eligehausen (Eligehausen et al., 1983). This type of test is suggested as a local bond-slip characteristic test according to RILEM (RILEM, 1970).

One of the complete studies on the steel-concrete bond that has been used as reference was the experimental campaign by (Eligehausen et al., 1983). This experiment performed 125 pull-out tests that included studies in some parameters such as the loading history (cyclic or monotone), the confinement effect, the steel bar diameter, the loading rate and the concrete compressive strength. Only in a small surface (five times the bar diameter) reinforcement was in contact with the concrete as presented in Figure 1.9. Based on these experimental results, the authors established an analytical model for a stress-slip relationship (presented in Section 1.2.3).

B. Tensile test

Beside pull-out test, a tensile test on a single deformed reinforcing bar encased concentrically in a concrete prism is usually performed too. Once the specimen is subjected to a tensile load and the normal stress in the concrete reaches the concrete tensile strength, a macro crack appears. This test is intended to study the specific characteristic of concrete cracks with the presence of a

steel bar (including the number of cracks, the crack width and spacing) and it allows observing the interface degradation for the final cracking pattern.

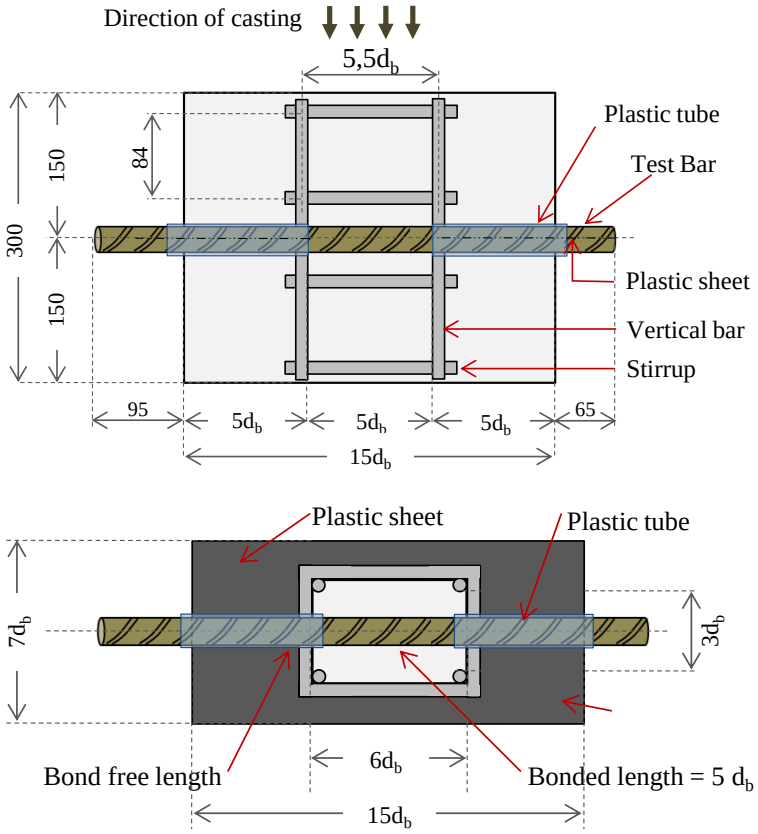

(a) Detail of pull-out test specimen.

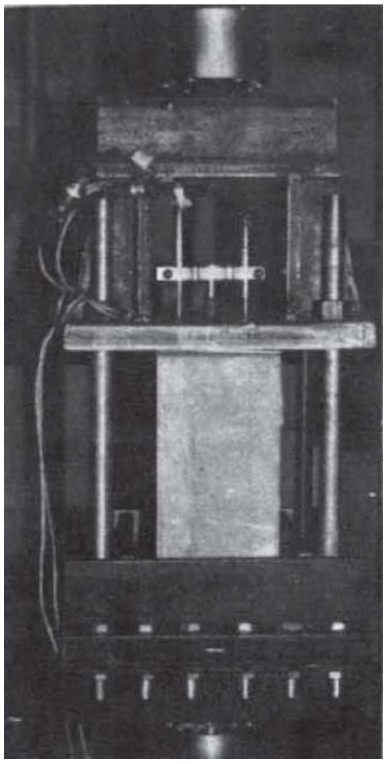

(b) Testing Machine

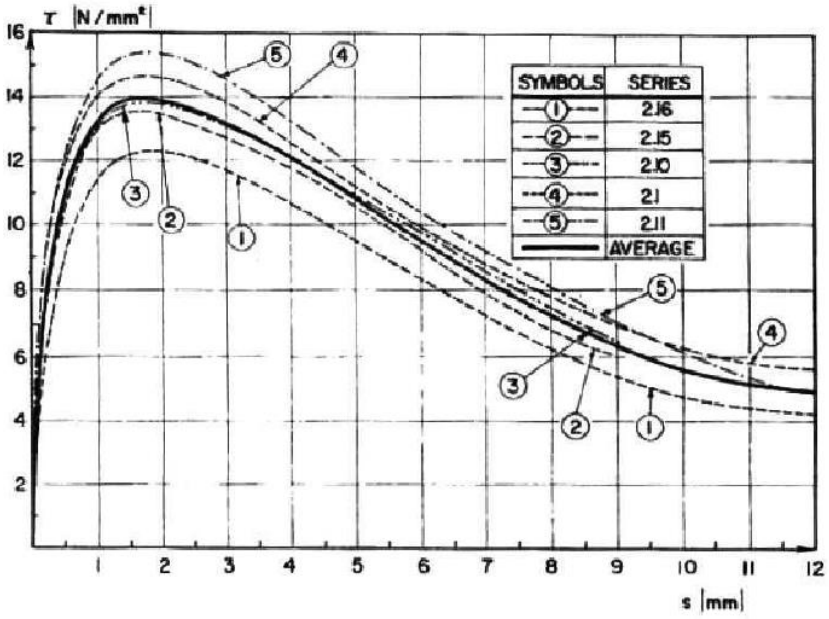

(c) Experimental results in the stress-slip relationship.

Figure 1. 9. Pull-out experimental test. (As illustrated in (Eligehausen et al., 1983))

Tensile test by Goto (Goto, 1971) presented in Section 1.1.2 was intended to perform this

study. The mechanical interaction between the ribs of the bar on the abutments of the concrete is the domain mechanism of the bond behaviour. Tensile test by (Michou, 2015) employed the fibre optic system to study the stress distribution as previously presented in Part 1.1.2 B. This is interesting to see the coherence of crack opening on the concrete surface and the deformation field along the anchorage length.

In addition, there have been a lot of pull-out tests and tensile tests to study the bond behaviour (Clement, 1987; Farra, 1995; Gambarova and Rosati, 1996; Hameed, 2010). Most of the tests served the parameter identifications of the bond behaviour (fib, 2000). A lot of parameters are considered, such as the concrete properties (compressive strength), the confinement effect, the form of the specimen (cylindrical (Kolani, 2012) or prismatic), the steel bar properties (ribbed or non-ribbed bar), the loading application (monotone or cyclic), etc. depending on the objective of the study. The steel-concrete bond study on non-conventional steel bar (bar with a square section) was performed by (Phan, 2012). The important contribution from these experiments is the observed degradation mechanism on the steel-concrete bond that will be explained in the following section.

1. 2. 2. Degradation mechanism of the steel-concrete bond

In fact, the suggested configuration of the pull-out test specimen by RILEM (RILEM, 1970) is intended to obtain a sliding failure, a failure that is allowable to occur on the steel-concrete bond. This failure results in a pulled out of the bar from the concrete volume. This plastic sliding failure is used to develop the local behaviour of the steel-concrete bond model (Dominguez Ramirez, 2005).

From the experimental works on pull-out, the degradation mechanism has been observed. Based on (ACI 408R-03, 2003; Eligehausen et al., 1983; fib, 2000; Goto, 1971; Lutz and Gergely, 1967), there are three main transfer mechanisms of forces on steel-concrete bond:

- The chemical adhesion of two different materials
- The frictional forces based on the roughness of the steel-concrete collision, the transverse forces and the relative slip of concrete and steel bar.
- The anchorage mechanisms or bearing mechanism of ribs against concrete structures.

The degradation mechanism under monotonic loading is illustrated in Figure 1.10 based on the work of (Dominguez Ramirez, 2005). The transfer mechanism and gradual deterioration were from various experimental research works (Eligehausen et al., 1983; Gambarova and Rosati, 1996; Goto, 1971). A more specific explanation can also be found in (fib, 2000).

In the initial state, the steel-concrete bond is identified as a *perfect liaison*. Once uniaxial traction of the bar is applied, a small bearing resistance from chemical adhesion takes places. When it is no longer able to resist, a very small movement of the steel relative to the concrete, called *slip*, occurs and the concrete strength replaces the role to bear the acting forces. At this stage, conical-tapered-micro-cracks propagate at the edge of the ribs against the concrete (point

A in Figure 1.10 (d)). Further loading application implies gradual compaction that prompts crushing on the concrete facing the ribs. As consequence, a larger slip and an enlargement of crack width occur. This phase is noted as the first degradation phase of the bond (point B in Figure 1.10 (d)).

The second phase of degradation starts exactly just before the peak point of ultimate strength (point C in Figure 1.10 (d)). Some collisions of cracks appear and of course more enlargement of cracks. Then, the steel-concrete bond passes to its softening phase or a declining of its resistance phase (point D in Figure 1.10 (d)). Friction between crushed concrete and concrete happens because slip larger than 1 mm occurs. At the end (point E in Figure 1.10 (d)), the rib slides to the position of the next rib and it is confirming the complete deterioration of the liaison.

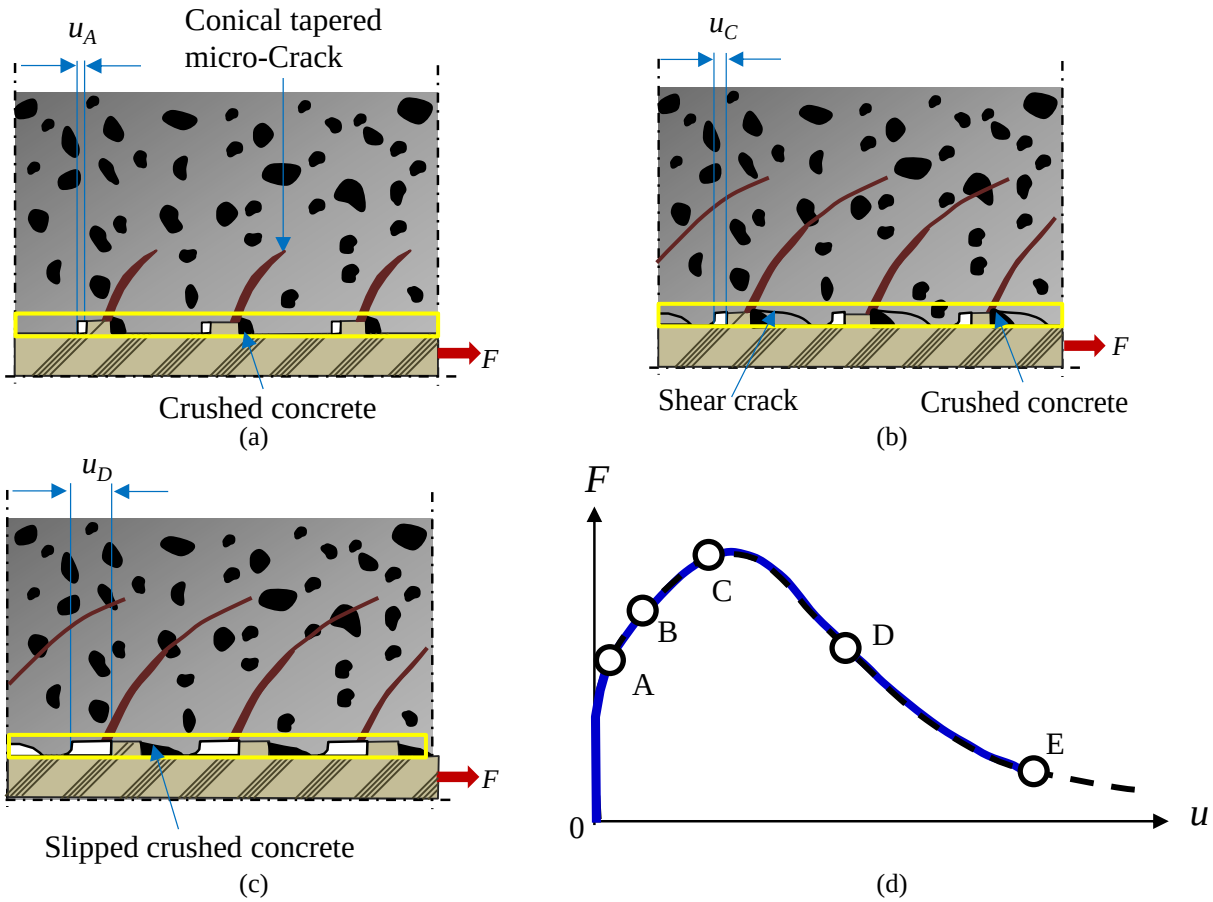

Figure 1. 10. Mechanism of deterioration of steel-concrete bond. (As illustrated in (Dominguez Ramirez, 2005))

1. 2. 3. Steel-Concrete Bond Modelling

Although the complete mechanisms act on a local scale as presented in Figure 1.10, the bond stress is considered in a comprehensive way and constant over a length of Δx (see Figure 1.11). It is calculated based on the variation of the internal forces of the reinforcement. In Figure 1.11 (a), the complete stress acting around steel bar under tension test is presented. This relation (Equation 1.9) calculates the average bond stress of the steel-concrete collision along Δx

according to the simplified scheme in Figure 1.11. (b).

The degradation mechanism and the obtained measured value from experiments are very important for the numerical modelling. Several analytical models have been proposed from the obtained results. In the following, the empirical-analytical model is explained followed by the proposed numerical modelling. The analytical model is usually employed as an evolution law in the numerical modelling.

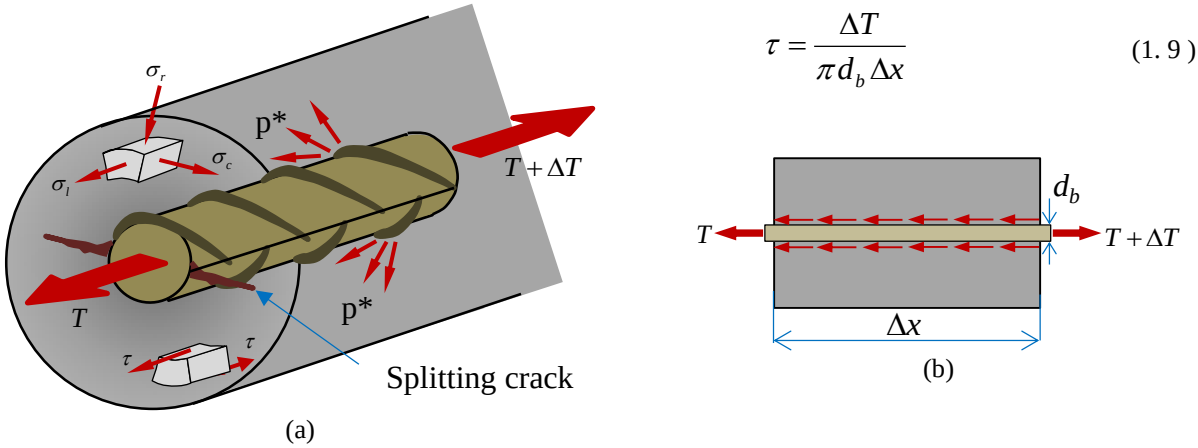

Figure 1. 11. Bond stress in the interfacial zone.
(a) Detailed configuration (Illustration is remade according to (Gambarova and Rosati, 1996). (b). Simplification of bond stress scheme according to (Wight and MacGregor, 2011).

A. Semi-empirical model

Based on the experimental works of (Eligehausen et al., 1983), the Evolution law model was proposed (Ciampi et al., 1981). This model has been used to represent bond behaviour. Enriched model from Eligehausen's can be found in (MC 2010, 2013) with some coefficient to consider physical condition of steel reinforcement bar and its configuration embedded in concrete (see Table 1.1 the proposed value for pull-out test).

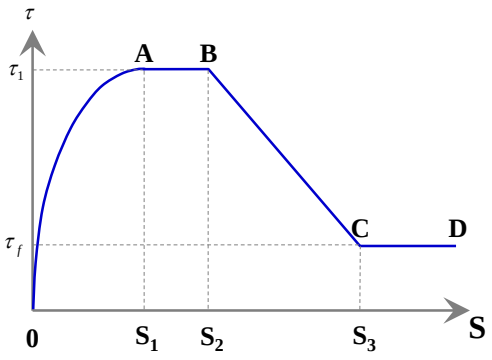

Interval	Bond Stress
$0 \le s \le s_1$	$\tau = \tau_{max}\left(s/s_1\right)^{\alpha}$
$s_1 \le s \le s_2$	$\tau = \tau_{max}$
$s_2 \le s \le s_3$	$\tau = \tau_{max} - \left[\left(\tau_{max} - \tau_f\right)\frac{(s-s_2)}{(s_3-s_2)}\right]$
$s > s_3$	$\tau = \tau_f$

Figure 1. 12. Eligehausen's analytical model of the steel-concrete bond.
As illustrated in (Eligehausen et al., 1983)

Table 1. 1. Parameters defining bond stress according to (MC 2010, 2013).

	Good bond condition	**All other condition**	
$\tau_{\max}$	$2{,}5\sqrt{f_{cm}}$	$1{,}25\sqrt{f_{cm}}$	f_{cm} = concrete compressive stress
s_1	1,0 mm	1,8 mm	
s_2	2,0 mm	3,6 mm	
s_3	c_{clear}	c_{clear}	c_{clear} = the clear distance between ribs
α	0,4	0,4	
τ_f	$0{,}4\tau_{\max}$	$0{,}4\tau_{\max}$	

B. Numerical modelling

There are several ways to model numerically the steel-concrete bond. Some classifications of the interface model exist, such as a classification based on the scale of the modelling, the geometrical representation of the interface zone, the mechanical behaviour of the interface itself, or based on the geometrical representation of the steel bar. In this section, the first and the second classification are discussed.

Three scales were adopted to categorise bond models (Cox and Herrmann, 1998). The first scale classification is called *rib-scale*. Explicit discretization of the ribs (the thickness, the larger and the angle of inclination) is considered. The fact that, the dimension of the rib is smaller than concrete, this scale modelling is very challenging in coupling to concrete damage model. This type of model works well for the early response of bond (before the large slip and concrete crushing). The second one is called *member-scale*. This model is very useful for application in larger and complicated structures. Typically, the reinforcing bar is modelled one-dimensionally and bond behaviour is usually only focused on the shear stress and slip relationship. The third one is called *bar-scale* model which is the best compromise model because of its practical application. A term called *interface* is often idealised to represent the homogenization of mechanical interaction of the ribs and the surrounding concrete.

Based on the geometrical of the interface, there are two ways to model this transition zone: *an interface with a thickness* (volumetric element of the interface) and *an interface model without thickness* (double nodes element of the interface).

For *the interface model with thickness*, the volumetric element of the interface was used by (Hameed, 2010; Kolani, 2012; Michou, 2015; Sellier et al., 2013a) as illustrated in Figure 1.13. The steel bar was meshed using bar element with two nodes. The bar is surrounded by a solid element representing steel-concrete bond interfacial zone. A Von Mises or a Drucker-Prager law can be chosen as the criterion. The bond strength is not dependent of the active confinement for the case with a thick concrete cover (Torre-Casanova et al., 2013) which supported the use of Von Mises criterion. The evolution law may use the analytical model of Eligehausen's as presented in Figure 1.12 (Ciampi et al., 1981; Eligehausen et al., 1983), or the behaviour

deduced from pull-out tests as in (Hameed, 2010; Kolani, 2012). The most recent works by (Michou et al., 2015) considered the ribs on the reinforcing bar explicitly to take into account the heterogeneities properties of the steel-concrete interface.

This three-dimensional approach offers three advantages: it limits the number of parameters to be identified; the robustness of the model is ensured by the absence of surface penetration problems; the computing time remains with reasonable use of continuous models for concrete and interface. The hardening law used in this model can be from pull-out experimental works. So, this type of model is sufficiently well-known in governing the steel-concrete bond behaviour.

There are two types of *interface model without thickness* (the double nodes), such as the surface element of interface and the lineic element. This type of interface model connects the steel and the surrounding concrete by a steel-stress vector with a stiffness matrix or kinematical relations. Using the Eligehausen's evolution law, a surface element called joint was implemented in Cast3M (CEA, 2012). In the work by (Millard and Vivier, 2006), specific joint elements are used to model the degradation of the steel-concrete bond due to corrosion. Respecting the geometry of the bar, the interface element surrounded the steel bar and a Coulomb type elasto-plastic model was employed.

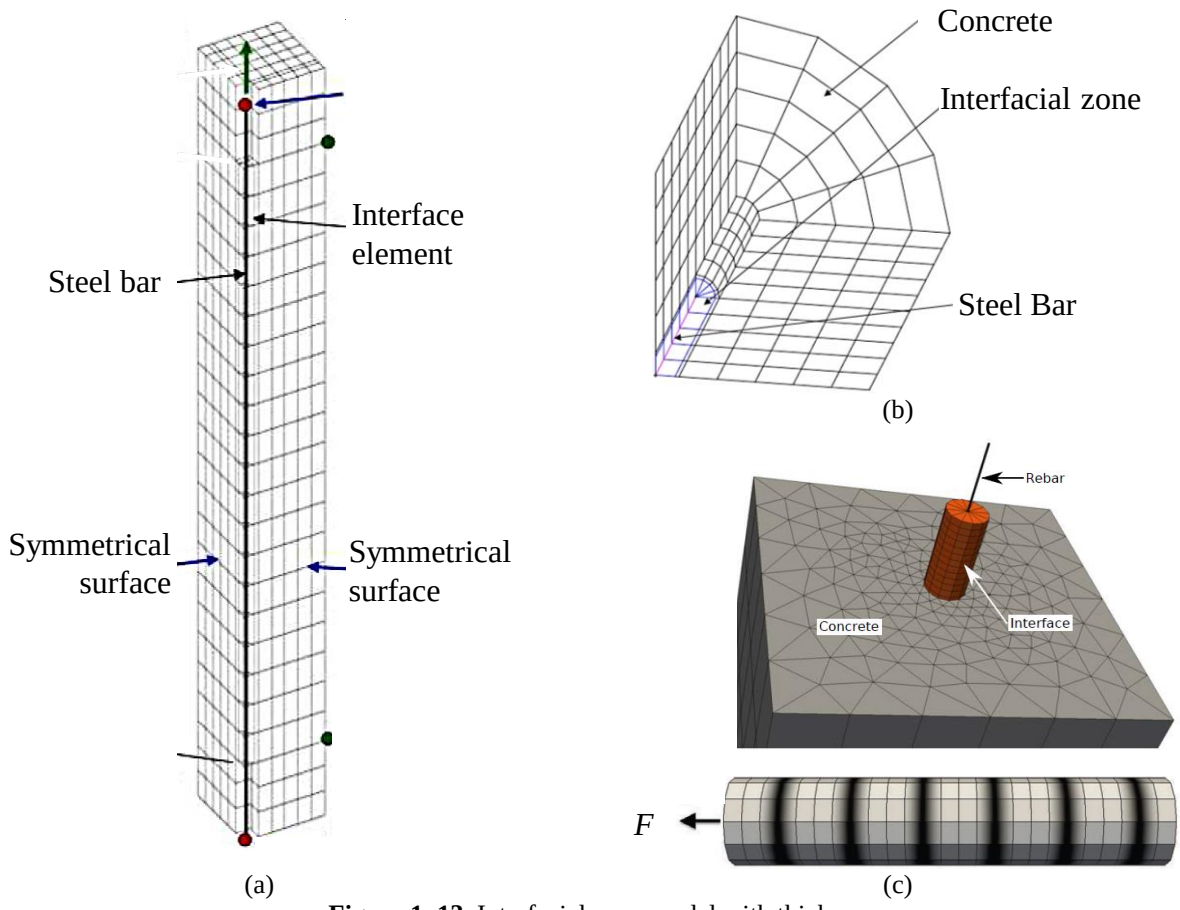

Figure 1. 13. Interfacial zone model with thickness.
(a). Works performed by (Hameed, 2010) and (b) (Kolani, 2012). (c). Consideration of heterogeneities the in the steel-concrete interfacial zone (Michou, 2015).

The lineic element model was proposed by (C Mang et al., 2015) from the initial work by (Casanova et al., 2012) and it is already implemented in Cast3M finite element code (CEA, 2012). This element has a zero thickness four-node element (each has three DOF) that is able to associate steel truss element (1D) and an associated superimposed segment perfectly bonded to the surrounding concrete (3D). In this works, this element uses the bond slip-law from (Torre-Casanova et al., 2013) that is enriched for cyclic loading based on the previous experimental works (Casanova et al., 2012). In the application on tie-beam, it shows its capability to reproduce the stress transfer steel-concrete and also crack opening. In a condition with a sufficiently finer mesh size of concrete surrounding the bar, the stress concentration induced by the bar into the concrete can lead to almost a total deterioration of concrete around the bars. A later development of this method suggested a distribution of the bar force to four nodes, for example using a static condensation method aiming to delocalise the bar force in a sufficient large zone of concrete to avoid concrete damage (Llau, 2016).

1. 3. Crack modelling on concrete material

It is well-known that when concrete is under tension stress, cracks propagate perpendicularly to the main tensile stress. The degradation in the concrete material occurs progressively. It is started on the diffuse micro-cracking in the matrix of cement paste. When concrete tensile strength is overstepped, the coalescence of several micro cracks induces macro-cracks. This macro crack represents a localisation of crack as a discontinuity of the material. As this study aims to model the cracks, we are concentrating on the behaviour of quasi-fragile material under tensile loading.

In the FEM context, the crack modelling is based on the continuous domain (continuum mechanics). Some different types of crack modelling exist based on the method how to define and how to model the crack, such as smear crack (usually used in damage model with either non-local or local version), cohesive element model and XFEM. In the smear crack model, the total strain which consists of the elastic strain of the solid material and the strain due to cracking (Rashid, 1968; Rots and Blaauwendraad, 1989) is modelled by diffusive degradation of the finite elements. In the work of (Rossi and Wu, 1992), crack is defined in a surface way by the intermediate cohesive element (joint element) on the border of the finite elements. In the XFEM modelling (Moës et al., 1999), the degree of freedom is enriched that allows representing crack evolution explicitly and the joint element is placed on the cracked area following the opening. For this thesis, the damage model is chosen to model the concrete material.

1. 3. 1. Behaviour law of concrete

A. Damage Model

The Damage theory based on continuum mechanics was firstly introduced in 1958 by Kachanov (Kachanov, 1958) to study the rupture provoked by creep. This idea was considered in France in 1971 by Lemaitre (Lemaitre, 1971) on the basis of the thermodynamics irreversible

process. This theory consists of the description of the phenomena from the initial state (non-damaged) to the initiation of a crack. It denotes the more or less progressive deterioration of a material due to the appearance of damage. This theory is used mainly for the modelling of geomaterial characterised by strain softening.

In this model, the cracked material is considered as a continuous medium and homogeneous. The damage is quantified as:

$$D = \frac{S_D}{S} \tag{1. 10}$$

Where S_D is the damaged area and S is the apparent area as presented in Figure 1.14. The effective area is defined as $\tilde{S} = S - S_D$. So, if $D = 1$, the material is completely deteriorated and if $D = 0$, the material is undamaged. The damage theory is characterised by a strain-equivalent principle as illustrated in Figure 1.15. An application of force on a surface S produces an apparent stress σ and leads to a damaged state. The strain-equivalent principle defines an equivalent condition of the same material where an effective stress $\tilde{\sigma}$ works on the effective area $\tilde{S}$ (in which D equals to zero).

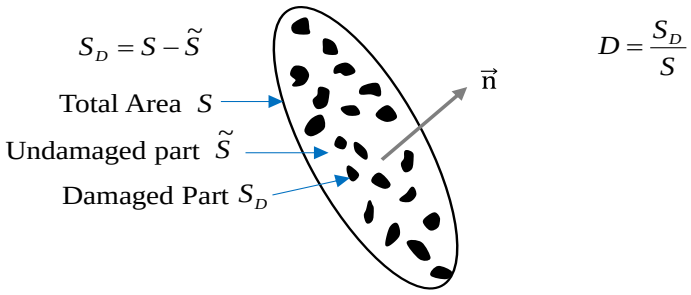

Figure 1. 14. A representative area of a damaged solid.
(Illustration is remade according to (Lemaitre et al., 2009))

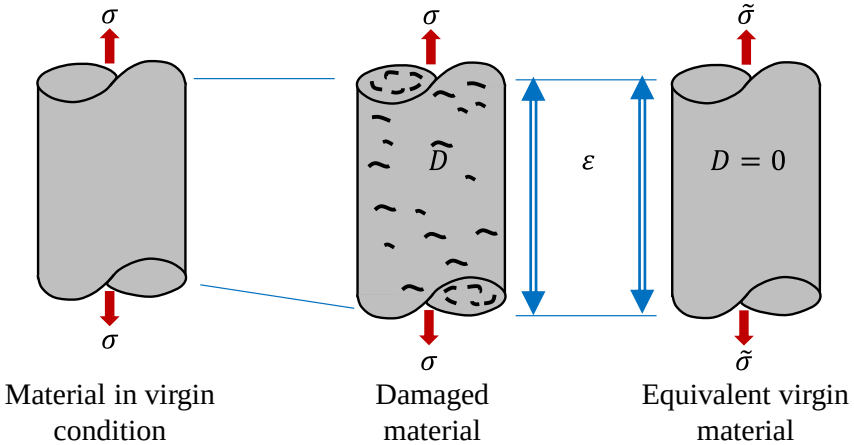

Figure 1. 15. Effective stress and strain-equivalence principle.
(Illustration is remade according to (Lemaitre et al., 2009))

So, the effective stress is expressed as:

$$\tilde{\sigma} = \frac{\sigma}{1-D} \tag{1. 11}$$

The elastic modulus of the damaged material is expressed as $E = (1-D)E_0$.

The damage of a material can be taken into account through the description of the variation in the elastic characteristics of the material. The stiffness of the material is thus directly related to the variable of damage.

B. Model of Mazars

Damage model for quasi-brittle material has been developed since many years ago. Mazars (Mazars, 1986) developed an **isotropic elastic damage model** for concrete that became a reference for numerous damage modelling thereafter. Mazars resorted to the isotropic damage theory to describe the loss of the concrete tensile stiffness. A scalar damage *D* variable was introduced in this model which is in the interval [0,1]. This model associates the damage to the local extension by the variable $\hat{\varepsilon}$ expressed as:

$$\hat{\varepsilon} = \sqrt{\sum_{i=!}^{3} \langle \varepsilon_i \rangle_+^2} \tag{1. 12}$$

The ε_i is the principal component of the strain tensor defined as:

$$\langle \varepsilon_i \rangle_+ = \varepsilon_i \quad \text{if } \varepsilon_i \geq 0 \tag{1. 13}$$
$$\langle \varepsilon_i \rangle_+ = 0 \quad \text{if } \varepsilon_i < 0$$

The material is modelled as elastic isotrope in the initial state and it stays elastic isotrope in the damage state. The loss of the stiffness is written as:

$$\sigma = (1-D)\Lambda : \varepsilon \tag{1. 14}$$

With Λ is the fourth order tensor of elasticity. And the damage is written as the combination of a tensile damage D_t and a compression damage D_c.

$$D = \alpha_t D_t + \alpha_c D_c \tag{1. 15}$$

The coefficients α_t and α_c are linked to the tensile and compressive stress successively. The unsymmetrical tensile and compression behaviour is defined by the damage threshold and the evolution of the damage.

The advantage of isotropic damage is its simplicity of implementation. The damage variable *D,* which is a scalar, in this case, facilitates the numerical implementation. In the condition of monotonic loading, this model is good to model the crack opening with a tensile stress that is in normal position to the plane of the crack.

In a condition with more complex loading, the damage on concrete becomes more complex. This condition needs, for example, a definition of damage in tensor form. The anisotropic model proposed by (Dahlblom and Ottosen, 1990; Desmorat et al., 2007; Sellier et al., 2013) was

introduced to allow simulation of large structures with complex loading condition.

The crack modelling in this work is assessed by the concrete model developed in LMDC laboratory (Sellier et al., 2013b).

C. Model of LMDC

The LMDC concrete model is an orthotropic damage model (Sellier et al., 2013b). Under the tensile condition, this model uses the Rankine criterion in the three orthogonal tensile principal stresses. Also, Hillerborg regularisation is used to control the fracture energy dissipation (Hillerborg et al., 1976), so the independence of the cracking energy toward mesh is verified. This model is also able to consider non-radial loading path by adopting the rotating crack method used by (Sellier and Bary, 2002; Theiner and Hofstetter, 2009). The behaviour under tension is presented in Figure 1.16.

The behaviour law of the cracked material is expressed:

$$\sigma = (1 - D_t) S_0 \, \varepsilon \tag{1. 16}$$

With D_t represents tensile damage and S_0 represents the undamaged stiffness matrix.

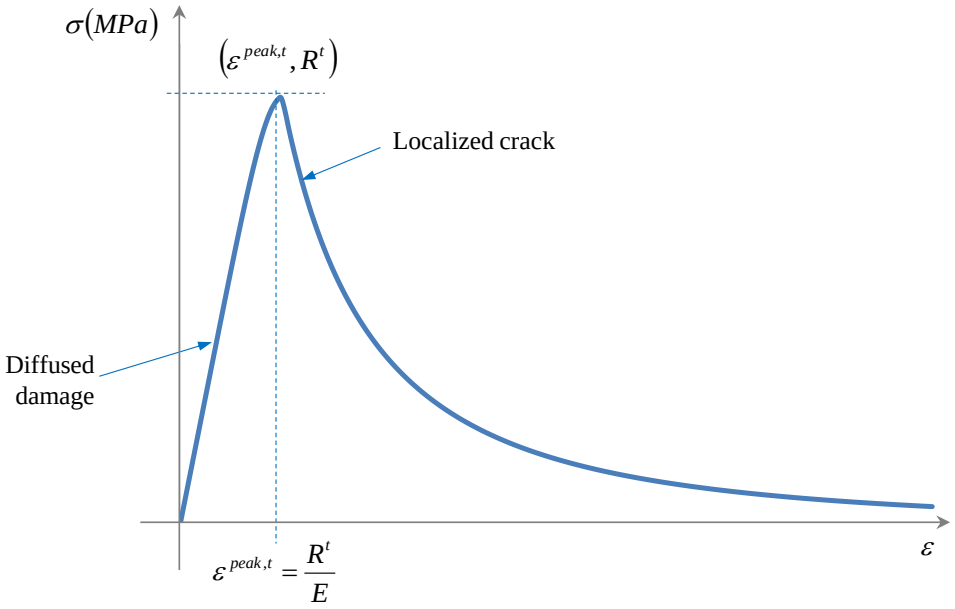

Figure 1. 16. Behaviour law under tension loading: test on one CUB8 element. From LMDC Model (Sellier et al., 2013a, 2013b)

At the pre-peak condition, homogenization theory is applied. The diffused damage at pre-peak condition expressed as micro-crack density (d_I^t ranging from 0 to 1), is given by the following formulae. This pre-peak damage can be induced by shrinkage as explained in the next part.

$$d_I^t = 1 - \exp\left(-\frac{1}{m^t} \left(\frac{\tilde{\sigma}_I^R}{\sigma_u^t} \right)^{m^t} \right) \tag{1. 17}$$

Where:

$\tilde{\sigma}_I^R$ = Rankine stress tensor in principal direction

m^t and σ_u^t = Parameter of the model to be chosen so that the curve pass through the point $\left(\varepsilon^{peak,t}, R^t\right)$

$\left(\varepsilon^{peak,t}, R^t\right)$ = Strain at peak and tensile strength of concrete

As schematically shown in Figure 1.17, once the peak of the tensile stress is reached, the diffused tensile micro-cracks in the previous step will group together forming a localisation of a macro-crack. In Figure 1.16, the propagation of macro-crack is punctuated by $\varepsilon^{peak,t}$ as the start of the softening phase.

Adopting Hillerborg's method (Hillerborg et al., 1976) energy dissipation takes place in the weakest or in the most loaded element that is proportional to element's size. This dissipation must be equal to the fracture energy per unit area (G_f^t) and is formulated as expressed by the following equation. The fracture energy per unit area (G_f^t) is an area under the curve of tensile stress and deformation of concrete. In this post-peak phase, the parameters of damage law are adjusted automatically to the size of the mesh element in its principal direction.

$$G_f^t = \left(\frac{\left(R^t\right)^2}{2E} + \int_{\varepsilon^{pic,t}}^{\varepsilon_I^t} E\left(1-d_I^t\right)\varepsilon_I \, d\varepsilon_I \right) \ell_I \qquad (1.\ 18)$$

Where:

ε_I^t = Strain of rupture in principal direction depending on the size of FE

ℓ_I = Size of finite element in principal direction of tension

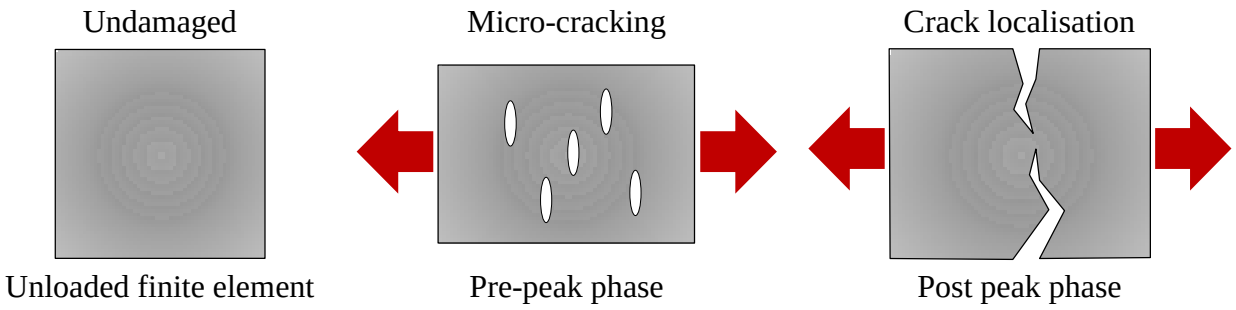

Figure 1. 17. Evolution of the crack opening phase from undamaged, micro-crack to localised crack. (Sellier et al., 2013a, 2013b)

The crack width can be obtained using the following expression. When crack localized, the micro-crack density equals to 1 ($d_I^t \to 1$) and the crack width is the product of the deformation times the size of the element ($w_I = \varepsilon_I \ell_I$). Equation 1.19 allows accessing the crack opening since the track initiation, which uses the crack density over the damage at the peak of the tensile condition.

$$w_I = \langle \tilde{\sigma}_I \rangle_+ \frac{\ell_I}{E} \left\langle \frac{d_I^t - d^{pic,t}}{1 - d^{pic,t}} \right\rangle_+ \quad (1.19)$$

Where:

d_I^t = Crack density in the principal direction

w_I = Crack width in the principal direction

$d^{pic,t}$ = Damage at the peak point of tension

Under this condition, only the positive effective stress ($\tilde{\sigma}_I$) as well as the damage greater than the peak value can open the crack.

1. 3. 2. Shrinkage's effect

Shrinkage is usually defined as a contraction in the fresh concrete or in the hardened concrete following the loss of water without mechanical loading application (Mensi et al., 1988). In the case of reinforced concrete, the presence of steel bar creates a restraint to concrete shrinkage. The concrete that tends to shrink is encountered by the presence of the steel bar. The effect of restraint to shrinkage can cause a decreasing of stiffness (Gilbert, 2001).

There are three types of shrinkage, such as autogenous shrinkage, drying shrinkage and thermal shrinkage. At the early age, *Autogenous shrinkage* is the consequence of a hydration reaction which occurs in the absence of water source. This condition leads to a tension stress in the global volume of concrete that can produce micro-cracking on the concrete (Aïtcin and Mindess, 2013). *Drying shrinkage* is related to the differential gradient between the cover and the core concrete in a function of the depth (CEOS.fr, 2015; Gilbert, 2001; Makani, 2011). Deformation due to drying shrinkage on the concrete surface can affect premature cracks (Chamseddine, 1996). *Thermal shrinkage* is usually defined as a deformation due to the changing condition from high temperature during hydration reaction to the cooling phase. This condition has a large effect in massif structures only.

The induced stress on concrete and the restraining action from the steel bar during the hardening phase due to shrinkage are possible to create damage before the mechanical loading application. That's why shrinkage must be considered in the RC modelling. Several models have been proposed to model shrinkage. In this study, the delayed strain is modelled using the model proposed by (Sellier et al., 2013a, 2013b).

The delayed strain of solid skeleton is coupled to a plastic strain model that ensures the stress field compatibility with the strength criteria. This model was established in the poro-mechanics in which, the total stress is related to the effective stress and the interstitial stress (Sellier and Buffo-Lacarrière, 2009). It was developed basically from the experimental works of Acker (Acker, 2003). The stress in interstitial or pore pressure is considered through poro-mechanics

framework as described in the idealised unidirectional rheological scheme below (see Figure 1.18). From this scheme, if water pressure (P_w) changes, the solid skeleton will be affected.

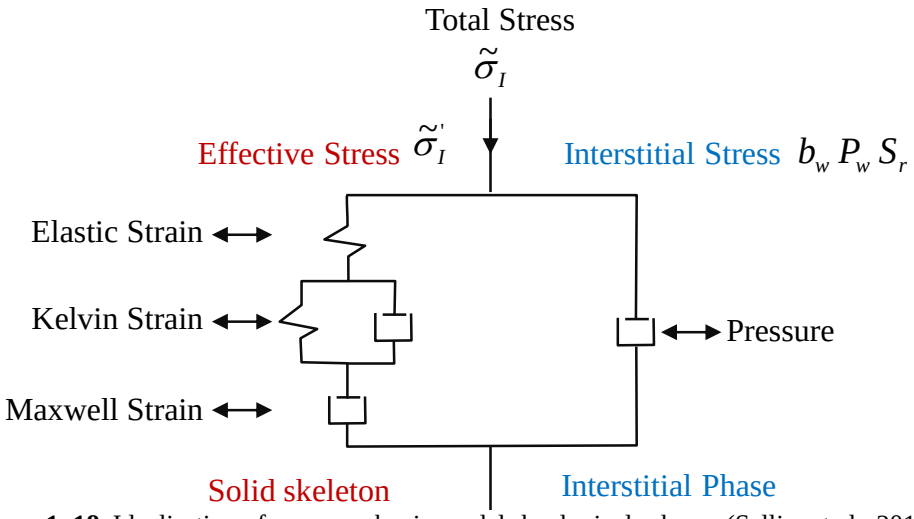

Figure 1. 18. Idealisation of poro-mechanic model rheological scheme (Sellier et al., 2016).

In this model, pressure can be in the form of gas or water, for our case, it is simplified as water pressure inside the pore. This idea presents the condition of induced stress on concrete after water content in the concrete is changed. So, the degree of saturation is obviously changed that consequently will modify the pressure. It is always convenient to resort to the capillary pressure theory in the context of poro-mechanics. Among the numerous poro-mechanic models, Van-Genuchten's model (Van-Genuchten, 1980) can be used. In this model, Van Genuchten introduced a water capillary pressure model as follow:

$$P_w = M_{sh}\left(1 - S_r^{\left(-\frac{1}{m_{vg}}\right)}\right)^{(1-m_{vg})} \qquad (1.\ 20)$$

Where:

P_w	=	Water pressure in pore
S_r	=	Water saturation rate
M_{sh}	=	Van Genuchten Modulus
m_{vg}	=	Van Genuchten exponent

Due to its coupling mechanism in the model, this condition will induce an effective stress in the solid skeleton (concrete) as expressed in Equation 1.21. In other words, shrinkage is modelled by giving a *pre-stress*, so concrete is already under tension if strain is constrained. Note that in Equation 1.21, term involving σ_{dc} considers the drying creep which is assumed created by a modification of Biot coefficient b_w (Sellier et al., 2016).

$$\frac{\partial \tilde{\sigma}_I}{\partial t} = \frac{\partial \tilde{\sigma}_I'}{\partial t} + \frac{\partial (b_w P_w)}{\partial t}\left(1 - \frac{|\sigma_I|}{\sigma_{dc}}\right) \quad (1.\ 21)$$

Where:

P_w = Water pressure in pore

S_r = Water saturation rate

In a work conducted by (Michou et al., 2015), the delayed strain was taken into account in the tension test modelling. The first crack localisation is obtained closer to the experiments than the case where the delayed strain was disregarded. Although it was able to catch the first crack localisation, the results did not fit for the initial stiffness of structures.

1. 3. 3. Probabilistic scale effect

A study of experimental works measuring the concrete tensile strength (R_t) using a lot of specimens with different volumes was performed by (Rossi et al., 1994). The results show that R_t for the first crack initiation in the case of large structures subjected to tension is weaker than the average R_t measured on the direct tension specimen. This reduction shows the concrete's random properties and it is the consequence of the *probabilistic scale effect* phenomenon (Rossi et al., 1994). CEOS.fr (CEOS.fr, 2015) defines the term of *scale effect* as a modification of concrete tensile strength in a large size element of structure in comparison to the average measured value of the concrete tensile strength in the laboratory.

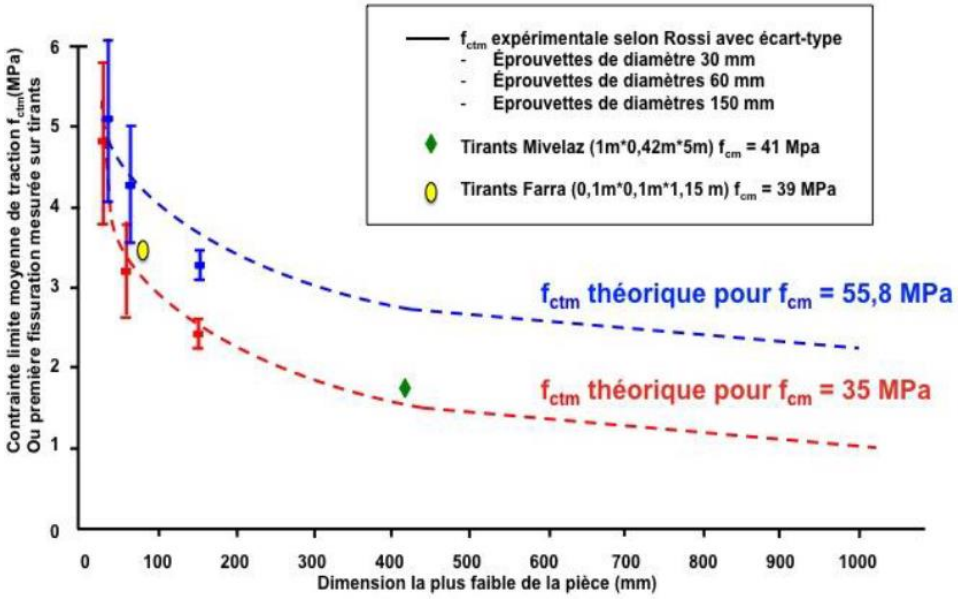

Figure 1. 19. The evolution of the concrete tensile strength (R_t) in a function of specimen's size. As presented in (CEOS.fr, 2015).

In Figure 1.19, the experimental results from Rossi (Rossi et al., 1994) are traced with the

obtained standard deviation. The first crack initiation for the tensile test of Mivelaz (Mivelaz, 1996) and Farra (Farra, 1995) for large size are also plot. The reduction of standard deviation occurs with the increase in volume.

According to Figure 1.19, the larger the dimension of the structure, the higher the reduction of concrete tensile strength (R_t) occurs for the first cracks. As R_t is important to initiate the cracks, the probabilistic scale effect should be taken into account in RC crack modelling. Otherwise, the first crack initiation occurs lately and the crack opening in the further loading can be underestimated. So, the scale effect is closely related to the first cracking propagation. Basically, there are two methods to consider concrete random properties, such as random field and Weibull's theory which are discussed here. Moreover, a new development from Weibull method called *Weakest Link and Localization* (WL^2) theory is also presented (Sellier and Millard, 2014).

A. Random Field

The first way to take into account the scale effect is random field which is considered as statistical methods. *Random field* is a method that is usually used to capture spatial variability of the input variables. Experimental works serve this statistical input data (mean, variance and covariance). So, by using this method, we generate, for example, a variation of R_t in the volume of concrete, a mechanical characteristic random field. Some parts are weaker while some others are stronger. Normally, in case of homogeneous applied stress, the first crack propagation will start from the lowest R_t (the weakest zone). Several methods to generate *random field* appropriately exist and they result in spatial functions (Van der Have, 2015). One of them is called *Turning Band Method*.

Turning band method (TBM) was proposed by Matheron (Matheron, 1973) and is considered in (Mantoglou and Wilson, 1982) and (Fenton, 1990). Two- or three-dimensional spatially correlated random variable can be generated from a series of 1D process. This method starts by defining a number of lines with a random direction in the considered domain. The realisation of isotropic Gaussian random fields is generated from the sum of line process. The sum of the orthogonal projections of the one-dimensional process divided by the square root of the number of lines determines the grid points of the random field mesh (Fenton, 1990; Mantoglou and Wilson, 1982; Matallah et al., 2010; Van der Have, 2015). This relationship is described in Equation 1.22 below.

$$Z(\vec{x}_n) = \frac{1}{\sqrt{L}} \sum_{k=1}^{L} Z_k\left(\xi_{n,k}\right) \tag{1. 22}$$

Where:

$\vec{x}_n$	=	Field points ($n = 1,..., N$)
N	=	Number of field points
$Z_k\left(\xi_{n,k}\right)$	=	Orthogonal projection of $\vec{x}_n$ onto line k

For each line, there is one-dimensional covariance $C_1(\vec{h})$ that is derived from the three-dimensional covariance $C_z(\vec{h})$following the relationship:

$$C_1(\vec{h}) = \frac{d}{dh}\left[hC_z(\vec{h})\right] \tag{1. 23}$$

In which, the vector $\vec{h}$ is a vector that relates two field points.

This method is implemented in Cast3M (CEA, 2012) as an operator called ALEA. An isotropic exponential form of three-dimensional covariance is shown below (CEA, 2012; Matallah et al., 2010):

$$C_{ij} = \mathrm{SD}^2 \exp\left(-\sqrt{\left(\frac{d_1^2}{l_1^2} + \frac{d_2^2}{l_2^2} + \frac{d_3^2}{l_3^2}\right)}\right) \tag{1. 24}$$

Where:

SD	=	standard deviation
d_1, d_2 et d_3	=	coordinates of the P_i and P_j (two points in mesh field)
l_1, l_2 et l_3	=	correlation lengths in three direction

Application of random field to assess crack openings in RC structures was performed by some researchers. The generation of a spatially correlated concrete Young's Modulus using TBM was conducted by (Matallah et al., 2010) on a tensile test of RC tie-beam structures. The tests on RC tie beam by (Michou et al., 2015) generated a random field of concrete tensile strength. Both random field generations were conducted in accordance with the experimental tests on concrete. The force and displacement relationship of these results can be seen in Figure 1.20.

The results show the different responses on the cracking behaviour. In the force-displacement curve, apparently, the random field does not influence the elastic behaviour of concrete for both cases that can be seen the exact same initial stiffness before the initialization of first crack(s). Then, after the first cracks propagated, the continuing behaviour is different but similar in tendencies for each numerical simulation.

The number of cracks itself can also be obtained different one from the others (Michou et al., 2015). The position of the cracks obviously depends on the generated random field properties on concrete. In fact, the less the number of cracks, the larger the maximum crack opening occurred and vice versa. From these results, the robustness of structural modelling is confirmed according to the crack opening patterns. The different crack pattern can be obtained from the first, the second and so on of calculation using the same concrete properties. In fact, this method requires several numerical simulations (at least three).

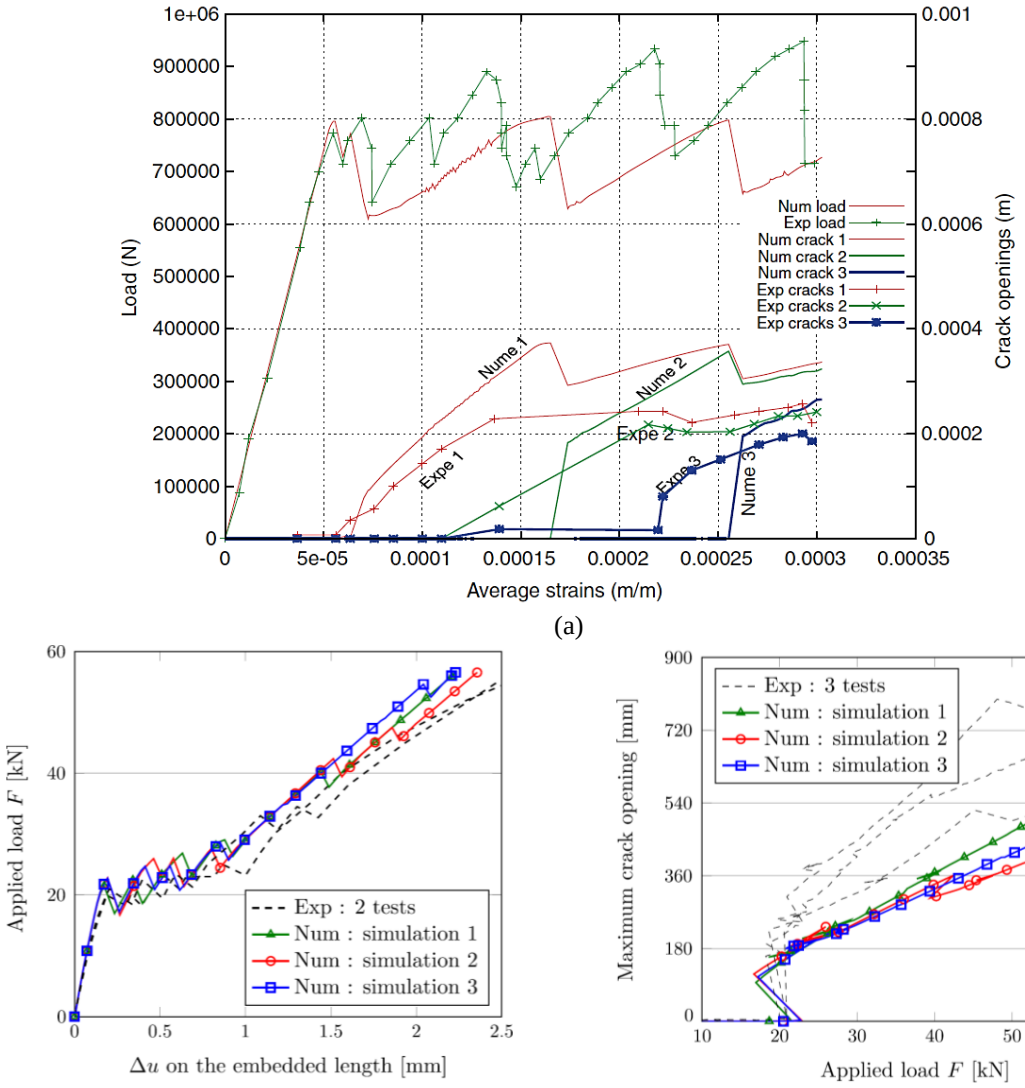

Figure 1. 20. Global response of simulation characterised by the generation of random field using Cast3M finite element codes.

(a). Results from concrete Young's Modulus random field generation on RC tie-beam from Mivelaz (Mivelaz, 1996) (Matallah et al., 2010). (b) and (c). Generation of concrete tensile strength random field on RC tie-beam in global behaviour and crack opening (Michou et al., 2015).

B. Theory of Weibull

The theory of Weibull is usually used in the probabilistic aspects of the fragile materials. The original Weibull's theory is presented in Equation 1.25. All the infinitesimal volumes dV are considered with the same probabilistic weight. These results in the continuous are increasing the probability of finding a defect with the infinitesimal domain of integration. In other words, this theory would lead to a very big strength reduction (almost zero) in case of a very large dimension of structures.

$$\ln\left(1-Pf_v\right)=\int_V \frac{\ln\left(1-Pf_{ref}\right)}{V_{ref}}dV \qquad (1.\ 25)$$

Where:

Pf_v = The probability of failure of a volume V

Pf_{ref} = The probability to assess for a reference volume V_{ref} (the volume of specimen in laboratory)

In (Rossi et al., 1994), the proposed formulation for the concrete tensile strength for 35 MPa ≤ R_c ≤ 130 MPa is expressed as:

$$R_t = a\left(\frac{v_s}{v_a}\right)^{-b} \qquad (1.\ 26)$$

Where:

v_s = The volume total of the tensile test specimen

v_a = The volume of the biggest aggregate in the concrete

$a = 6{,}5$

$b = 0{,}25 - 3{,}6.10^{-3} \times R_c + 1{,}3.10^{-5} \times R_c^2$

Weibull's theory or the weakest link theory is very convenient to assess the tensile strength to be used for the first crack initiation. The expression of Equation 1.26 according to the recommendations CEOS.fr (CEOS.fr, 2015) can be rewritten as:

$$\left(\frac{f_{ctm}^{Veq}}{f_{ctm}^{Vref}}\right)^m = \frac{V_{ref}}{V_{eq}} \qquad (1.\ 27)$$

Where:

f_{ctm} = The concrete average tensile stress for the considered volume V_{ref} or V_{eq}

f_{cm} = The concrete average compressive stress

V_{ref} = The reference volume (volume of the specimens)

V_{eq} = The equivalent volume of the considered structures, for the massive structures, it is limited to 2 m^3.

m = The Weibull's exponent expressed identically as b in Equation 1.26

$m = \left\{0{,}25 - 3{,}6.10^{-3} \times f_{cm} + 1{,}3.10^{-5} \times f_{cm}^2\right\}^{-1}$

The Weakest Link and Localisation theory (WL²)

A newly proposed method by (Sellier and Millard, 2014) conducts a deterministic method that is basically developed from statistical approach Weakest Link Theory of Weibull. This method is able to generate the probability of occurrence of the first crack localisation and supplies the most likely tensile strength field at each time step of the numerical non-linear analysis. So, not only

the first crack initiation, the second, the third and so on will be predicted more accurate.

A noticeable improvement proposed in this method is an enhancement of the domain used for the Weibull integration by applying a probabilistic weighting function in the weakest link formulation. A proposed weighting function to limit the integration domain is written in Equation 1.28 and is depicted in Figure 1.21. This function considers the distance from a given point and the characteristic length of the probabilistic weighting function.

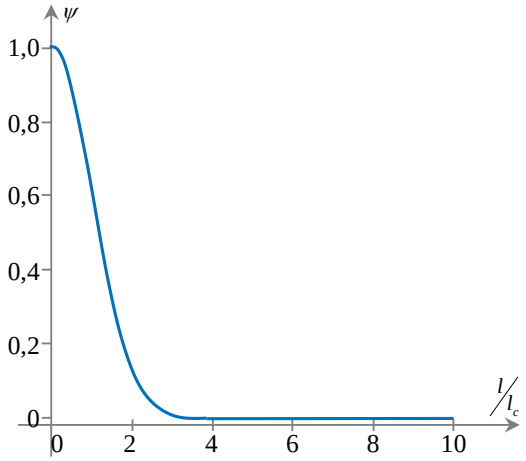

$$\psi = \exp\left(-\frac{1}{2}\left(\frac{l}{l_c}\right)^2\right) \qquad (1.\ 28)$$

Figure 1. 21. Proposed probabilistic weighting function. (Sellier and Millard, 2014)

Where:

l = Represents the distance between two points, the current point and the integrated one.

l_c = Spatial decreases characteristics of the probabilistic weighting function that is obtained from inverse analysis (0,5 metre for concrete and 1,25 metre for larger structures); it is linked to aggregate distribution and the shrinkage amplitude

The proposed deduction of the tensile strength to be used in the non-linear model is written as expressed in Equation 1.28 that can be rewritten as:

$$\frac{f_{ctm}^{Veq}}{f_{ctm}^{Vref}} = \left(\frac{V_{ref}}{V_{eq}}\right)^{1/m} \qquad (1.\ 29)$$

WL² method proposed the estimation of V_{eq} that cannot exceed a volume function of l_c called $V_{\max(M)}$ even in a condition with very large volume of structures ($R_{t/V_{ref}} = f_{ctm}^{Vref}$).

$$V_{eq(M)} = \alpha\left(\frac{\sigma_{\max}}{R_{t/V_{ref}}}\right)^{-m} \text{ with } \alpha = \int_V \left(\frac{\sigma}{R_{t/V_{ref}}}\right)^m \psi\left(l/l_c\right)dV \qquad (1.\ 30)$$

$$V_{\max(M)} = \int_{V\to\infty} \psi\left(l/l_c\right)dV = \left(l_c\sqrt{2\pi}\right)^N \qquad (1.\ 31)$$

The Weibull exponent that depends on the coefficient of variation of experimental results can be found from Equation 1.32 (a) or (b).

$$C = \frac{\sqrt{\Gamma\left(1+\frac{2}{m}\right) - \Gamma^2\left(1+\frac{1}{m}\right)}}{\Gamma\left(1+\frac{1}{m}\right)} \tag{1. 32a}$$

Or simply *m* can be approximated from:

$$m \approx \frac{1}{10}\left(\frac{12}{C} - 2\right) \tag{1.32b}$$

Where:

C = Coefficient of variation of measured tensile strength f_{ctm}^{Vref}

Another way to assess m is to use the empirical relationship found by Rossi or Equation 1.27.

To assess the V_{eq}, the α variable is computed using a Helmholtz differential equation. In the numerical application, the estimation of V_{eq} is calculated during each loading increment to adapt the tensile strength to the current loading. In other words, the crack modelling will always estimate the correspondence tensile stress. Therefore, the crack modelling for the continuing phase after the first initiation will be accurate. An advantage of this method is to consider automatically probabilistic scale effect with a single deterministic calculation (that is basically developed from statistical consideration).

1. 4. Conclusion

In this work, numerical crack modelling on RC structures is the objective of the study. The recent recommendation of the design crack width and spacing from PN Ceos.fr (CEOS.fr, 2015) mentioned three important aspects for RC modelling, such as the steel-concrete bond, the initial stress due to shrinkage and the scale effect due to the concrete's random properties. Thus, these three aspects are the main interest in addition to the concrete damage model in the context of FEM.

Experimentally, the pull-out characteristic seems promising to investigate the local bond behaviour that can be used as the evolution law describing the local degradation. Then, the tensile tests of prism specimen (RC prismatic element) provide great information from the influence of bond properties on the crack behaviour (crack opening, spacing and pattern) for a simple structure. Moreover, four-point bending test on RC beam allows crack observation on the pure bending area for large structural elements.

In term of steel-concrete bond, numerous bond models have been proposed using different

approaches. Analytical model of Eligehausen (Ciampi et al., 1981; Eligehausen et al., 1983) can be applied as the evolution law; or as an alternative, pull-out test results is also appropriate. Elastoplastic model with Von Mises criterion can be employed since in the thick cover concrete (pull-out test), the bond strength is independent of the active confinement (Torre-Casanova et al., 2013). Three dimensional modelling of the interfacial transition zone seems favourable as its robustness to model the progressive degradation and the plastic sliding phenomena proven.

Relating to shrinkage, the presence of steel bar that provokes a restraint to the shrinking action of the concrete in the RC structures induced an initial stress which reduces the first cracking force proportionally. An induced stress can be done from the imposed shrinkage strain using Van-Genuchten formulation in poro-mechanics framework.

Concerning probabilistic scale effects, recent studies showed the structural size effect on the overall behaviour of structures and on the maximum crack opening and the crack spacing. TBM (Turning Band Method) and WL² (Weakest Link and Localization) are two methods that can be utilised.

In this thesis, we are interested in the steel-concrete bond model, the influence of shrinkage via a poro-mechanical framework and the heterogeneity as the origin of the scale. The objectives are to quantify the role of each of these three aspects and their combinations to find the most effective modelling methods.

This page is intentionally left blank

Chapter 2

Importance of Transition Zone between Rebar and Concrete

A method chosen to show the importance of the transition zone between rebar and element consists firstly to identify an interfacial transition zone behaviour law from experimental results in LMDC laboratory and secondly to use it on a simple RC prismatic element. In order to fit the behaviour law of steel-concrete bond, pull-out tests were performed. Then, based on this experimental works, an elasto-plastic law with a Von Mises criterion is used in a volumetric element representing the interfacial zone. Choice of thickness for further cases is explained. Then, the next section aims to prove the importance of this interfacial transition zone between concrete and reinforcements in case of RC prismatic element by comparing experimental and numerical modelling results. In the first step, experimental works to capture the behaviour of RC prismatic elements subjected to a pure tension are conducted using a Digital Image Correlation (DIC) system. A tension test of RC element is then modelled in two different ways: firstly, considering a perfect connection between the concrete and the reinforcements (non-sliding connection), in the Perfect Interface (PI) model and, secondly, considering a plastic sliding interface zone, in the Sliding Interface (SI) model. One layer of solid elements between the concrete and the steel bar is used to represent the interfacial transition zone explicitly according to the results. The SI model provides better crack modelling results than PI model because it limits shear stress in the surrounding concrete.

This page is intentionally left blank

2. 1. Introduction

The interfacial transition zone is induced by the presence of the ribs of the steel bar reinforcement bordering the concrete. This zone is recognised as the most important section in transfer mechanism of stresses from the steel bar to concrete and vice versa. Evolution of cracks on concrete surface certainly relies on this transfer mechanism. The consideration of this zone in finite element modelling of Reinforced Concrete (RC) structures becomes more important as precise and rigorous crack modelling are demanded these days (PN CEOS.fr, 2009). Numerous of interfacial zone behaviour law have been proposed with different techniques in geometry interpretation. Some of the existing models are promising and interesting in the context of FEM. However, some difficulties have been raised while the applications in larger and complicated structures were performed.

Based on preliminary works of Kolani (Kolani, 2012), Leroux (Leroux, 2012) and also (Sellier et al., 2013a), Michou developed an interesting behaviour law adding the heterogeneities of the ribbed bar (Michou, 2015; Michou et al., 2015). In the previous works, a homogenous model using Von Mises or Drucker-Prager criterion was used. The model proposed by (Michou, 2015) considers the heterogeneities by considering the ribs of the steel bar. The heterogeneities are applied periodically along the anchorage length. This condition requires a constraint in size mesh of the interface element; in this case, it has to be at least a half of the width of the rib (2 mm). The mesh size of the concrete follows the mesh in the interface. Local concrete degradation can be investigated at the interface level in a form of inclined cracks. It is possible to apply this last model on a tensile test tie prism which only has one ribbed bar cast inside, but, the application in larger and more complicated structures may be less convenient due to this mesh constraint.

Another model that was proposed by (C Mang et al., 2015) uses the kinematical relationship to relate the slip of one-dimensional bar and the surrounded massive concrete volume. Basically, the sliding is obtained by the duplication of nodes (in the bar and in the concrete) that represent interface. Under slip condition and in a sufficiently finer mesh size of the concrete surrounding the bar, the stress concentration induced by the bar into the concrete can lead to an almost total deterioration of the surrounding concrete. A later development of this method suggested a distribution of the bar's force to four nodes of square elements of concrete. Afterwards, a similar model has been improved thanks to a static condensation method aiming to delocalise the bar force in a sufficient large zone of concrete to avoid concrete damage (Llau, 2016). Also, to better perform simulation using this method, application of sufficiently large size of the concrete element can be used. So, in this model, fine mesh sizes must be avoided otherwise the stress concentration has to be treated.

In this chapter, we start to fit a steel-concrete bond behaviour law inspired from previous works by (Hameed, 2010; Kolani, 2012). According to (Dominguez Ramirez, 2005; Kolani, 2012; Michou, 2015; Tixier, 2013), to this purpose, pull-out tests are performed. Then, the fitted law is used to model a tensile test that is also performed experimentally in the laboratory. The

ribbed steel bar was a 12 mm diameter. The detailed dimension of the experimental specimens used is referring to the previous works of (Hameed, 2010). The interest of tensile test on RC prismatic element is to observe the cracks propagation in concrete on a sufficiently simple structure. It helps to avoid experimental artefacts associated to large size element, such as scale effect, thermal gradient, etc. That is why it is usually used to validate the interface models (Michou et al., 2015).

In the following, a series of experimental works is presented along with the modelling. These series consist of the material characteristic tests (concrete and steel bar reinforcement), pull-out tests and tensile tests of RC Prismatic elements. The same steel bars and concrete material were used. Next, the fitting of the interface zone behaviour law to the pull-out test results is performed. Subsequently, the model is applied to an RC Prismatic element under tensile test to see its effectiveness. Discussion and remarks for further application of interface behaviour law in larger structures terminate this chapter.

2. 2. Material Characterization

Characteristic tests are required to obtain the material properties of concrete and steel bar. In the ideal condition, the pull-out test can be classified as material characterization test as it is conducted to be used to characterise the local behaviour steel-concrete interfacial transition zone. The pull-out test is explained in the sub-chapter 2.3.

2. 2. 1. Concrete

Several cylindrical specimens with 11 cm of diameter and 22 cm in height were cast. Table 2.1 describes the materials used and the conditions of concrete storage in the laboratory LMDC, while Table 2.2 describes the mechanical properties of the concrete. This table shows the average value and the standard deviation for each test. More detailed information of the materials can be found in Appendix B.

Table 2. 1. Mix design of concrete materials.

Type of concrete	C35/45 XF1 normal concrete, exposure classes according to Eurocode 2: Moderate water saturation without a de-icing agent (Eurocode 2, 2005)
W/C	0,6
Type of sand	0/4 mm (830 kg/m^3) - natural silica-calcareous sand
Type of aggregates	4/11 mm (445 kg/m^3) - natural silica-calcareous aggregates
	8/16 mm (550 kg/m^3) - natural silica-calcareous aggregates
Type of Cement	CEM I 52,5 N CE CP2 (320 kg/m^3) (High resistance Portland cement for aggressive environments)
Admixture	Sikaplast Techno 80 Superplasticizer based on modified polycarboxylates (2,4 kg/m^3)
Storage of concrete	Storage room maintained at 20°C and 100% relative humidity

Table 2. 2. Mechanical properties of concrete.

Concrete compressive strength*	R_c	=	56,5 ± 1,6	MPa
Concrete tensile strength* (Brazilian test)	R_t	=	4,0 ± 0,2	MPa
Concrete modulus of elasticity*	E	=	38 500 ± 820	MPa

* Average ± standard deviation value of experimental results from 3 samples at 126 days after casting

2. 2. 2. Steel bar reinforcement

The nominal reinforcing bar diameter used was 12 mm, corresponding to a cross-section of 113 mm^2 (NF EN 10080, 2005). As it was mentioned in the previous work of Tixier (Tixier, 2013), there are two types of the motif on the ribbed bar. The first one is called irregular motif with two kinds of inclinations: around 45° and 60° to the longitudinal axis of the bar. The second one is called regular motif with around 60° of inclination to the longitudinal axis of the bar. So, naturally, this bar can be considered as unsymmetrical and it may possess different behaviour on the two sides. A cutting through the steel bar gives the detail of section A-A and it is illustrated in Figure 2.1 (d). Table 2.3 describes the mechanical properties of the steel reinforcement bar from experimental results in LMDC.

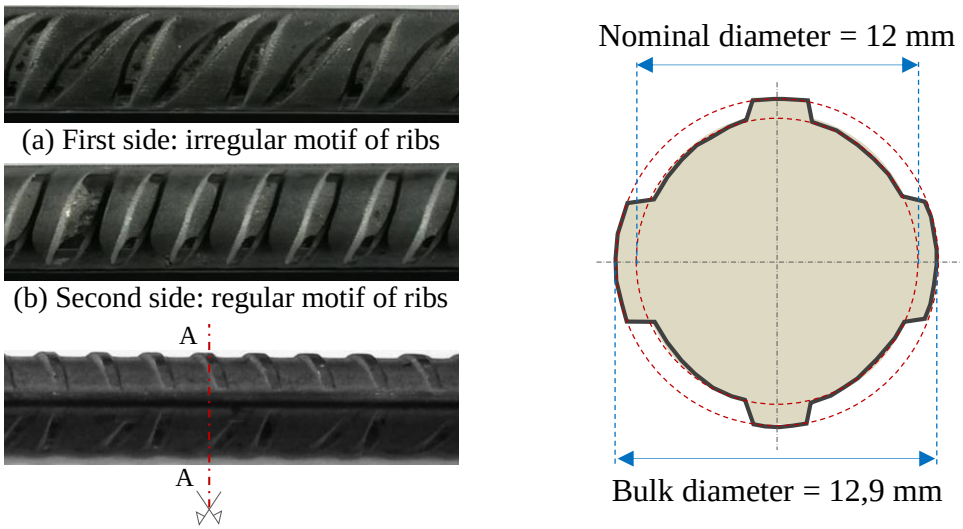

(a) First side: irregular motif of ribs

(b) Second side: regular motif of ribs

(c) Side with horizontal rib

(d) Detail of section A-A

Figure 2. 1. Detail of steel bar reinforcement.

Table 2. 3. Mechanical properties of steel reinforcement bar.

Reinforcing Bar : Fe E 500 HLE (High Strength Steel)				
Nominal diameter of HA steel bar (NF EN 10080, 2005)	ϕ_n	=	12	mm
Yield strength‡	f_y	=	566 ± 4,4	MPa
Modulus of elasticity‡	E	=	190 ± 5,6	GPa

‡Average ± standard deviation value of tensile test results from 3 reinforcement bars

2. 3. Pull-Out Tests and Development of Interfacial Zone Behaviour Law

With the aim of fitting a bond model, standard pull-out tests were performed in LMDC. Two pull-out tests specimens were cast with the cylindrical specimens for concrete characteristic tests and two specimens of RC prismatic elements.

2. 3. 1. Pull-out test

A. Detail of pull-out test specimen

A ribbed steel bar was cast inside a volume of concrete. In accordance with the RILEM recommendation (RILEM, 1970), the effective encasement height of the bar inside the concrete volume was taken as five times the diameter of the bar. The two parts of the bar where it entered/left the concrete were protected by PVC pipes to reduce the influence of the disturbed area and to localise the shear stresses along a relatively short zone. The detailed configuration of the specimen is shown in Figure 2.2. A steel plate was installed between the specimen and loading frame to limit the friction.

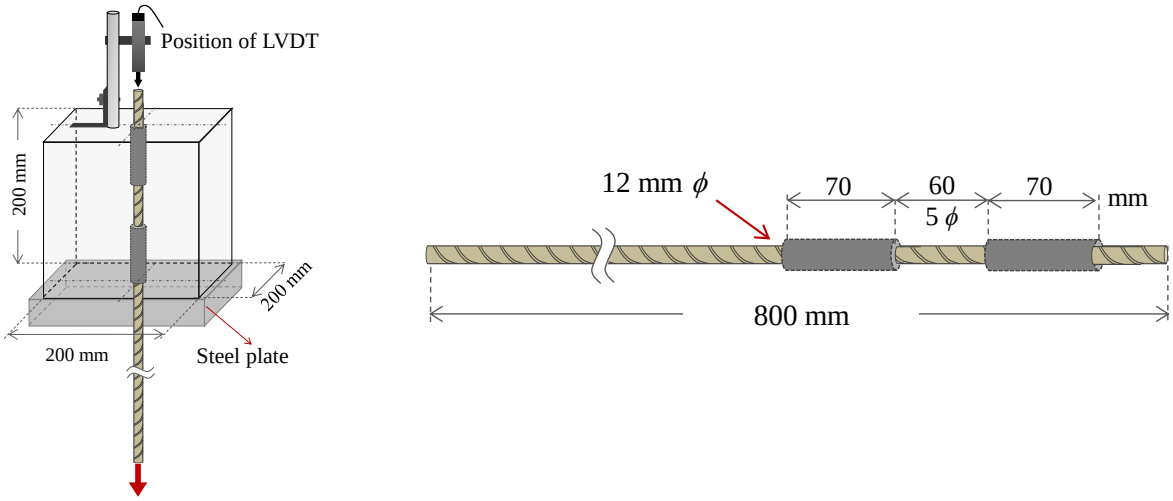

(a) Pull-out test specimen (b) Detail of steel bar cast in concrete volume

Figure 2. 2. Detail of specimen in the Pull-Out test.

(a) (b)

Figure 2. 3. Pull-out test installation on loading frame with 60 kN of maximum capacity.

The installation of the specimen can be seen in Figure 2.3. The block of concrete with one embedded ribbed bar was installed on a loading frame while its end of the bar is fixed between two grips. As the hydraulic jack with a maximum capacity of 60 kN works, the loading frame moves upward and the steel bar is loaded in tension. As expected, the chosen dimension of the specimen allows the pulling out of the bar by sliding mechanism and no visible cracks appeared. A displacement transducer (LVDT) was set up on the upper part of the concrete block to measure the relative movement of the bar from the concrete (slip).

B. Global results

The force (*F*) was measured and transferred to shear stress (τ) using the formulae presented in Equation 2.1. The displacement measured by the LVDT represents the sliding of the bar (slip). Experimental results of this test on two specimens are shown in Figure 2.4. The average curve is derived from the two results. This curve represents the average value along this concrete-steel bar cohesion surface. The maximum shear stress attained was 20,6 MPa.

$$\tau = \frac{F}{\pi \phi l} \qquad (2.1)$$

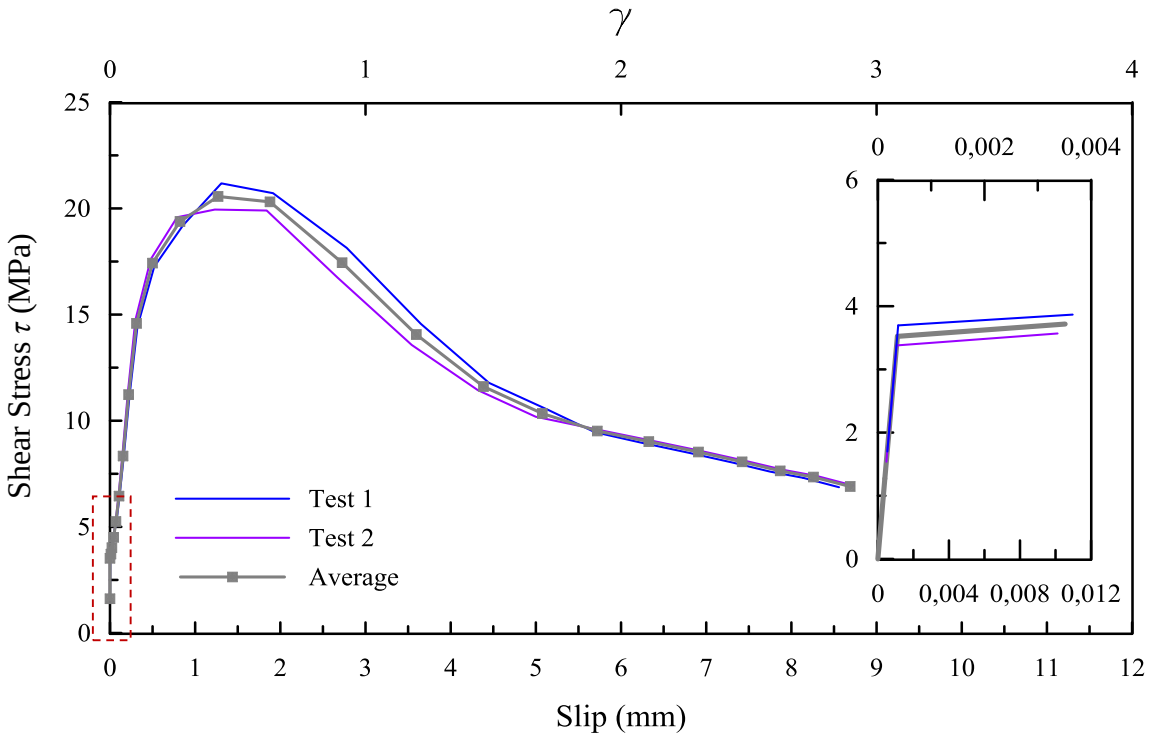

Figure 2. 4. Pull-out test: experimental results.

As seen in the curve, the results emphasised three different behaviours. The first one is elastic linear behaviour with a very small relative displacement between the steel bar and the concrete

(less than 2 µm) up to 3,5 MPa, see the zoomed curves in Figure 2.4. The second one is the progressive loss of stiffness until a maximum bond stress (20 MPa and 21,2 MPa for the first and the second specimen successively). Then, the third one is identified by the decrease of the bond stress as the slip that starts to grow and the degradation of the steel-concrete interface zone.

2. 3. 2. Investigation on the post-test specimen

After the pull-out tests were conducted, a cutting through the concrete was carried out. Without cutting the bar cast in the middle, Figure 2.5 shows the real condition of concrete deterioration around the bar. The concrete cube was cut from two directions up to the lines called *limit of a chainsaw* (see Figure 2.5 (a)). The two almost separated blocks were then split manually. That's why the area between the black dotted line and the red dotted one looked like being cut irregularly. It must be noted that, as the saw has around 2 mm of thickness, the photos displayed in Figure 2.5 are approximately showing a half of cast bar.

Figure 2.5 (b) and (d) show the two separated blocks: one block has attached steel bar and another one does not. These two are respectively called Block 1 and Block 2. The letter A and B indicate which side was separated during the cutting process. After detaching the bar on the Block 1 (Figure 2.5 (c)), the concrete block and its bar are presented in (e). To be noted, some part of dust from the deteriorated concrete around steel bar appeared during the detaching process. The zone in between two ribs may or may not contain concrete. The detail of this attaching concrete can be seen in Figure 2.6. Meanwhile, on the concrete surface Block 1, the motif of the steel bar can be seen (imprinted) on the side close to the direction of pulling test. The two areas between two red dotted lines represent the deteriorated concrete around the steel bar. As we can see in Figure 2.5 (a), some finer aggregates are dominants in the steel-concrete bond area. Apparently, the deterioration is not perfectly in line. Some of the deteriorated concrete occurred within; others took places beyond the PVC pipe.

Figure 2.6 shows the detailed of the bar condition. In Figure (a) and (c), the longitudinal rib that separates the two types of the motif is displayed. Figure (b) and (d) present the side of the irregular and the regular motif successively. Some of the attached concrete remained in between two ribs area, another amount of concrete remained beyond the ribs. Meanwhile, it is also possible that there is no attached concrete in between ribs due to the change of the state to dust (damaged) or concrete is almost undamaged (as can be seen in Figure 2.5 (e), the motif of ribs was imprinted on the concrete). The volume of the damaged concrete during the pull-out process corresponds mainly to the concrete enclosed between ribs. So, the modelling process below is based on the existence of a *plastifiable* zone of concrete with a thickness approximately equals to the rib's height.

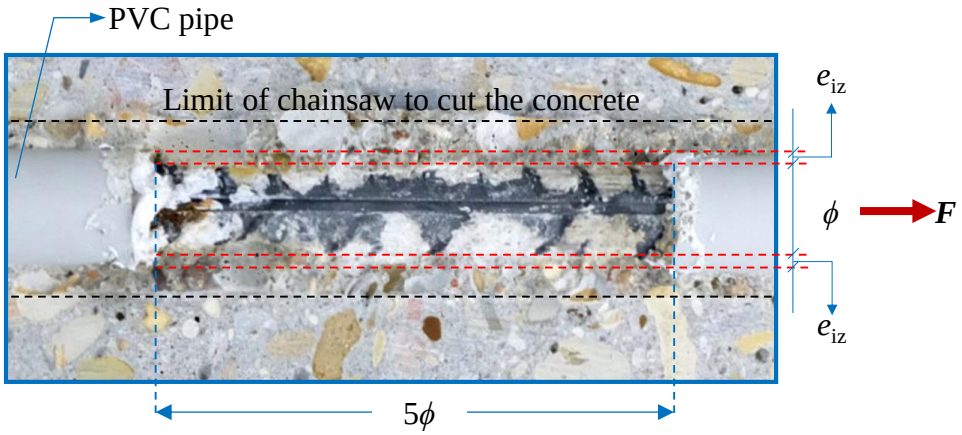

e_{iz} = thickness of deteriorated concrete layer

(a) Zoomed part of blue rectangle in (b)

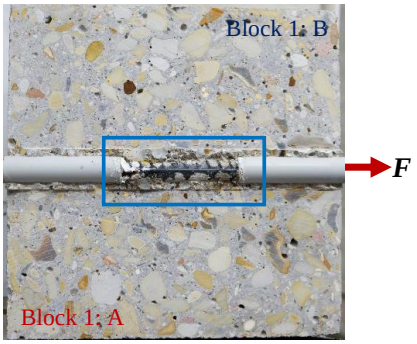

(b) Block 1 with attached steel bar.

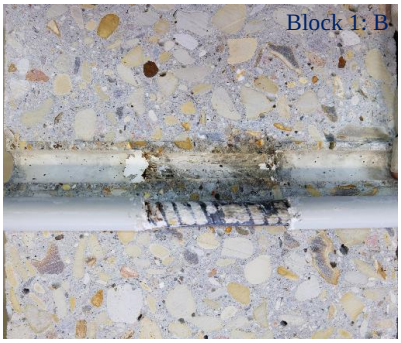

(c) Block 1 with detached steel bar

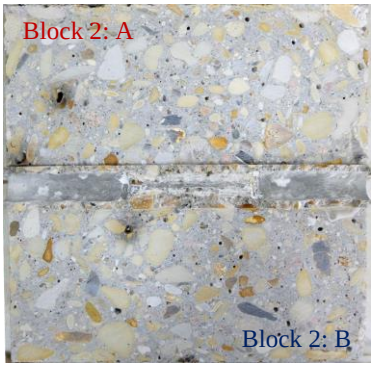

(d) Block 2 without attached bar

(e) Zoomed part of picture (c) Block 1

Figure 2. 5. Cutting through concrete on the pull-out test specimen.

(a) Side with horizontal rib

(b) Side with the irregular motif

(c) Side with horizontal rib

(d) Side with the regular motif

Figure 2. 6. Detail of steel bar reinforcement with attached concrete on the ribs of the bar (four side views).

2. 3. 3. Development of interfacial transition zone behaviour

A. Proposed geometry for interfacial transition zone

Regarding Figure 2.5 (a), the thickness of the *plastifiable* zone was determined from the outside of the nominal diameter up to the undamaged massive concrete. Zero to four millimetres of thickness was measured and 3 millimetres was the mode, the measured value the most often. In the longitudinal direction, locally, the heterogeneities could be considered as suggested by (Michou et al., 2015). However considering heterogeneities properties for each rib seem too much complicated, so a simplification is taken, the homogenous behaviour is decided. Results in Figure 2.4 represent the average sliding behaviour along the anchorage zone of ($5\times\phi$) in the pull-out test specimen. To conclude, a 3 mm of thickness interfacial transition zone with homogenous behaviour developed from the pull-out test is proposed. In Figure 2.7, the proposed geometry of the interfacial transition zone is illustrated.

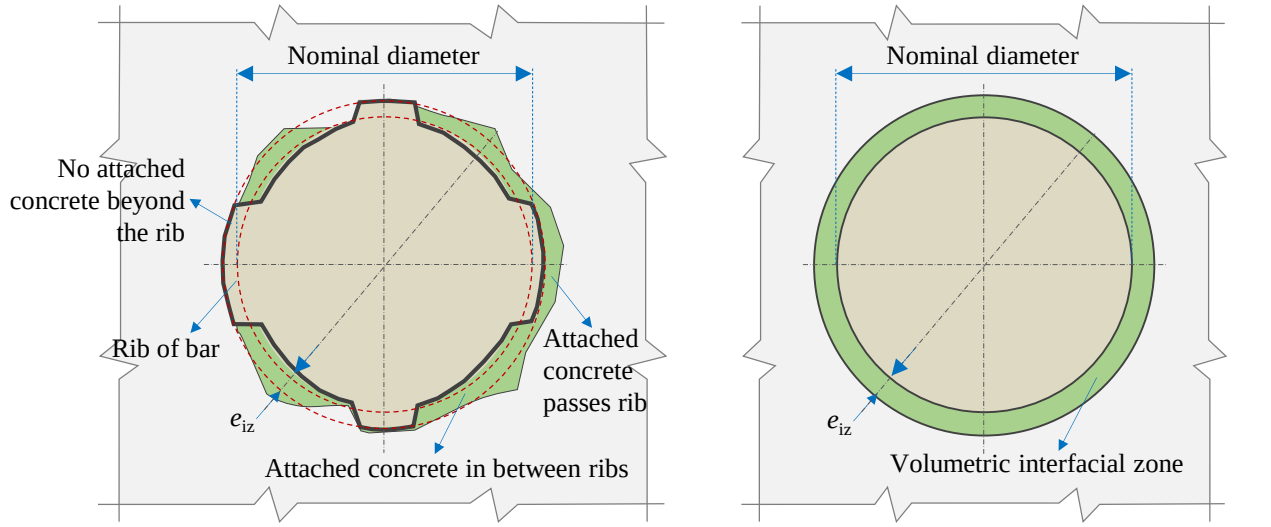

(a) Representative image of the steel bar cross section with attached concrete material

(b) Proposed model to represent steel-concrete bond

Note:

The massive concrete volume

The attached concrete on the steel bar (in between ribs and on the ribs)

The steel bar with ribs

e_{iz} = thickness of interfacial zone

Figure 2. 7. Sketch of the attached concrete around steel bar and the proposed geometry for numerical simulation.

B. Behaviour law

Regarding the experimental results in Figure 2.4, the behaviour of materials in pull-out test shows several tendencies. The first one is observed as *elastic linear* up to 0,0011 mm of displacement (displayed in the zoomed curve). Then, in the second stage, it starts to *yield* until it reaches the peak shear stress at 20,5 MPa. Step three, after passing its peak point, the *softening* behaviour occurs and it is followed by degradation of materials. Since a plastic sliding was

observed experimentally, a ductile materials Von Mises criterion is selected to regulate this behaviour. Moreover, a study performed by (Torre-Casanova et al., 2013) showed that the bond strength is not dependent of the active confinement for the case with a thick concrete cover as in the pull-out test specimen.

Von Mises criterion is basically independent of hydrostatic pressure because it is directly related to the deviatoric strain energy term. In a case of RC structures, even without hydrostatic pressure term in the criterion, a confinement effect may be produced from the decrease of the deviatoric stress. As in the further application the steel bar and the interfacial transition zone is modelled three-dimensionally and explicitly, a confinement effect will be considered indirectly.

There are some possible conditions for further application in structural elements, such as intersection and overlapping of the steel bars. The interfacial transition zone is definitely following the same condition because it encircles the bar. In order to prevent lateral contraction of the interface during elastic part of loading, the Poisson's ratio is simply set to be zero.

In this research, numerical simulations are performed using Cast3M FE code (CEA, 2012). In order to use Von Mises Criterion, elastic-plastic with isotropic[1] softening is selected. This law needs a stress-deformation relationship in the normal direction.

Cast3M uses the Von Mises equivalent uniaxial stress as the input data. It is deduced from measured shear stress as follows:

$$\sigma_{eq} = \sqrt{3\left(\sigma_{12}^2\right)} = \sqrt{3}\,\sigma_{12} \qquad (2.2)$$

And an equivalent uniaxial strain, deduced from the equivalent plastic strain as follows:

$$\varepsilon_{eff} = \frac{1}{3}\sqrt{3}\,\gamma \qquad (2.3)$$

C. Model fitting: Pull-Out Test

In a pull-out test specimen, under pull-out loading, a relative displacement between steel and concrete (simply called slip) occurred, as illustrated in Figure 2.8. The deformation (γ) can be obtained by dividing the slip (s) by the interface thickness (e_{iz}), in this case is 3 mm. On condition of pure shear stress, considering Von Mises criterion as described before in Equation (2.2) and (2.3), the equivalent stress and deformation are shown in Equation (2.4) and (2.5). A reduction coefficient of 1,24 has to be considered to link the numerical analysis and the pull-out test experiment for the equivalent stress. This coefficient could be due to the non-homogeneous strain field in the interface zone.

With the aim of performing the inverse analysis, a numerical simulation fitting test was conducted. The geometry of the pull-out test for modelling and its mesh configuration for

[1] *Mécanique Elasto-Plastique avec écrouissage Isotrope*

simulation are shown in Figure 2.9 whilst the list of selected behaviour law is presented in Table 2.4. The geometrical configuration and boundary conditions were taken from the pull-out specimen. The concrete material is modelled by the LMDC model while the reinforcement is modelled as elastic perfectly plastic. The interface zone is elasto-plastic with isotropic softening behaviour. The mechanical properties in Table 2.2 and 2.3 are employed to define the massive concrete and the steel bar and are summarised in Table 2.5 and 2.6 along with other parameters. For the concrete, the value of fracture energy (G_t^f), which was not measured experimentally, was calculated as proposed by the equation of Ottosen (Dahlblom and Ottosen, 1990), which leads to a value of 154 J/m².

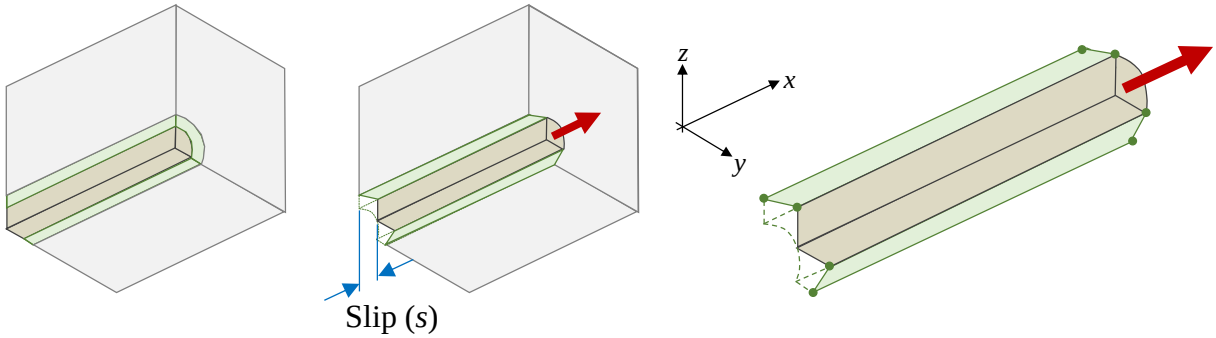

(a) 3D illustration of deformed interfacial transition zone.

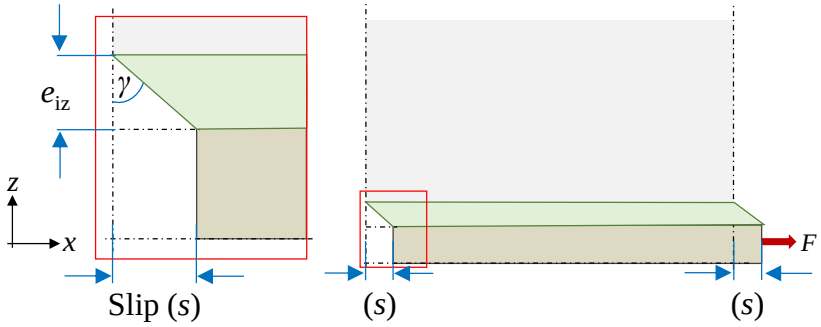

$$\sigma_{eq} = \frac{\sqrt{3}}{1{,}24}\tau \qquad (2.4)$$

$$\varepsilon_{eq} = \frac{1}{3}\sqrt{3}\,\gamma \qquad (2.5)$$

(b) 2D illustration of the deformed interfacial transition zone.

Figure 2. 8. Behaviour of concrete in a pull-out test at plastic sliding state.

Taking advantage of the two axes of symmetry, only a quarter of the specimen was discretized using CUB8 elements. A quarter tube shape of the interface element was obtained (in green colour). In Figure 2.9, the applied boundary condition is presented. The *yz*-plane was set to be fixed in the *x*-direction to represent the position of the specimen on the bearing plate of the machine while the other two planes were set as described in the figure to follow the symmetrical condition. One end of the reinforcement is imposed in the *x*-direction of displacement whereas another one was left free.

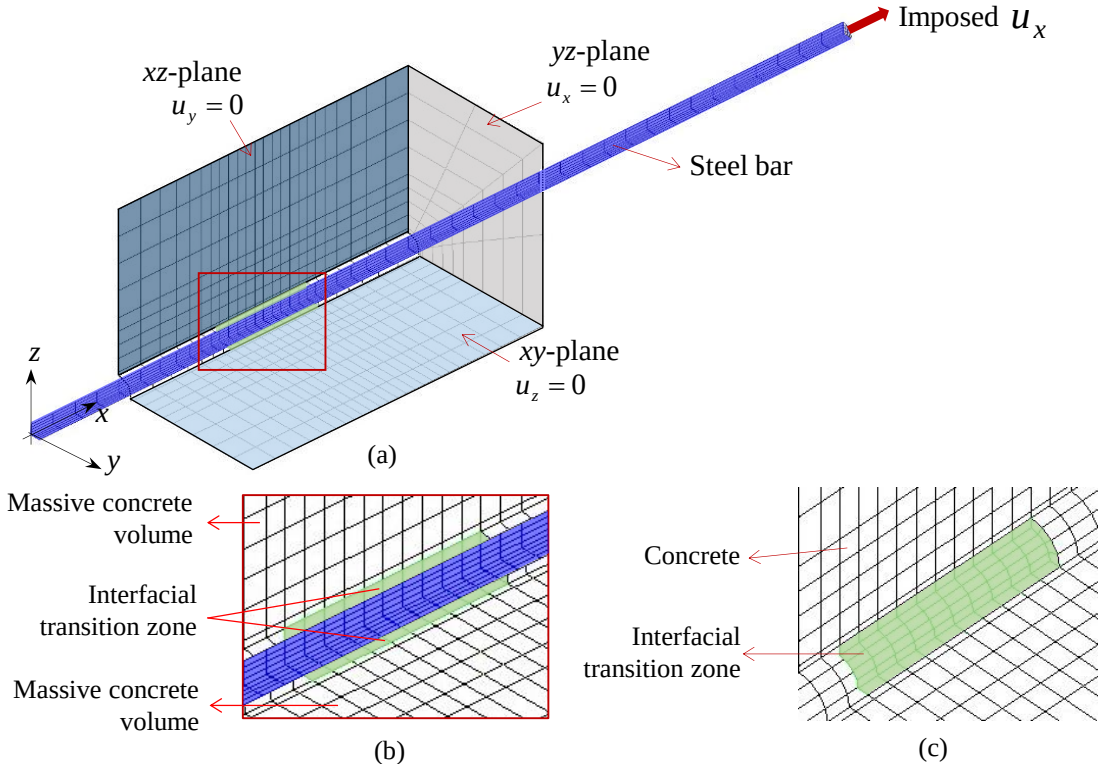

Figure 2. 9. Mesh and boundary conditions for pull-out test modelling (one-quarter of specimen's volume). (a) Mesh and boundary condition. (b) The detail on the anchorage length. (c) Massive concrete and interfacial transition zone along the anchorage length if steel bar does not appear.

Table 2. 4. List of behaviour law for each material in pull-out test modelling.

Model / Elements	Pull-Out Test
Plain concrete	Plain concrete LMDC model
Steel bar	Elasto-plastic model with perfect plasticity
Interfacial transition zone	Elasto-plastic model with hardening curve deduced from pull-out test

Table 2. 5. List of parameters of the reinforcement to be used in the modelling.

Parameters	Symbol	Value	Unit
Young's Modulus of elasticity	E	195	GPa
Poisson's ratio	υ	0,27	-
Yielding	f_y	567,30	MPa

Figure 2.10 shows the equivalent uniaxial behaviour law of a plastic sliding interface to be used in numerical modelling. Several researchers applied the 1,5 MPa of adhesion stress at zero slip as the limit of the initial shear stress referring to PIAF tests (Ouglova, 2004) and from the improvement works by (Tran et al., 2007). In this model, the pull-out experimental test result is used just as it is.

Table 2. 6. List of parameters of concrete materials to be used in modelling using the LMDC Model.

Parameters	Symbol	Value	Unit
Young's Modulus of elasticity	E	38500	MPa
Poisson's ratio	υ	0,27	-
Density	ρ	2400	kg/m^3
Concrete tensile strength	R_t	4	MPa
Strain at peak tension	$\varepsilon_{R_t}^{pk}$	$1{,}03\times10^{-4}$	-
Concrete compressive strength	R_c	57	MPa
Strain at peak uniaxial compression	$\varepsilon_{R_c}^{pk}$	$2{,}0\times10^{-3}$	-
Drucker Prager Confinement coefficient	δ	0,75	-
Dilatancy for non-associated Drucker-Prager plastic flow	β	0,28	-
Characteristic plastic strain for Drucker-Prager associated damage	$\varepsilon^{k,s}$	$8{,}0\times10^{-4}$	-
Fracture energy in tension	G_t^f	154	J/m^2

This curve was then compared with Eligehausen's model (Eligehausen et al., 1983) (fitted on the experimental results). At the very beginning of the curve, the slope of the equivalent stress-deformation is almost half Young's modulus of elasticity of concrete (53%). The following behaviour has less stiffness than the beginning. This means that the interface zone was always weaker than the concrete itself. It is possible because of the porosity around the steel bar that could be greater than in the plain concrete. Eligehausen's model results show the similarities at some points before the peak or the plastic sliding. It can be noted that this Eligehausen's model has some difficulties in capturing the post-peak behaviour (overestimation occurs).

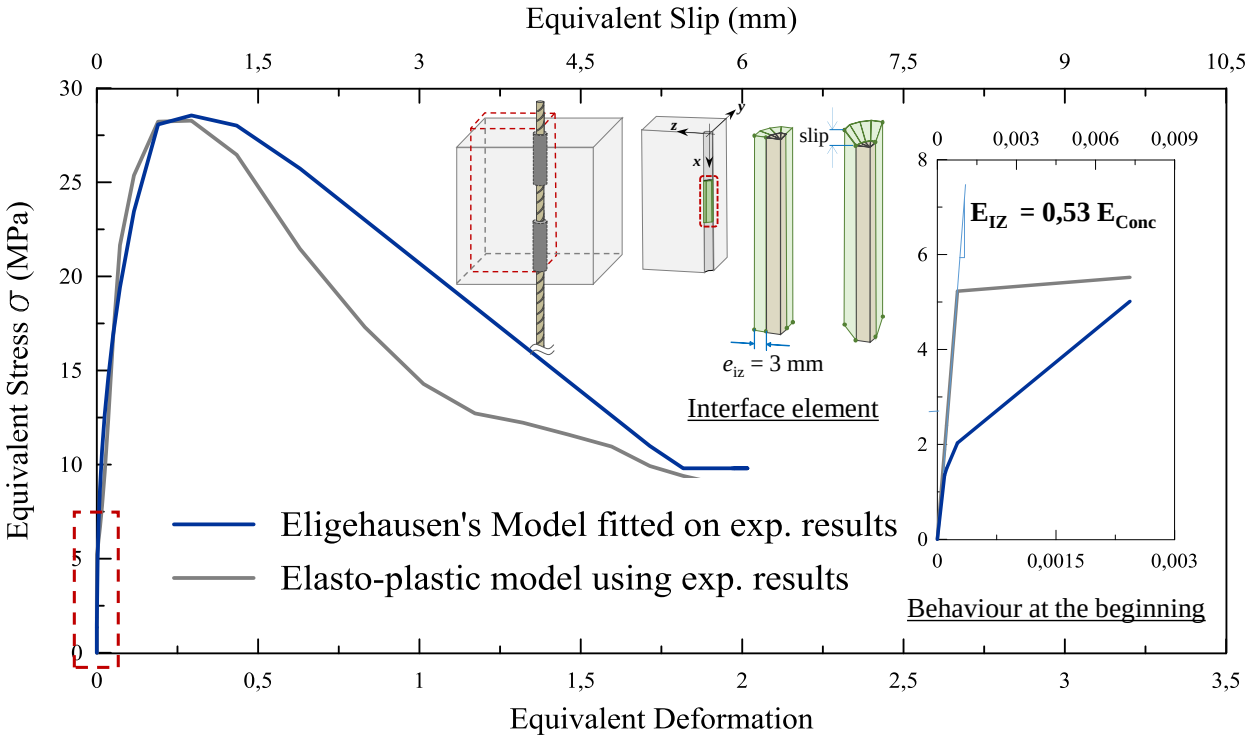

Figure 2. 10. Behaviour law of interfacial zone derived from experimental pull-out tests.

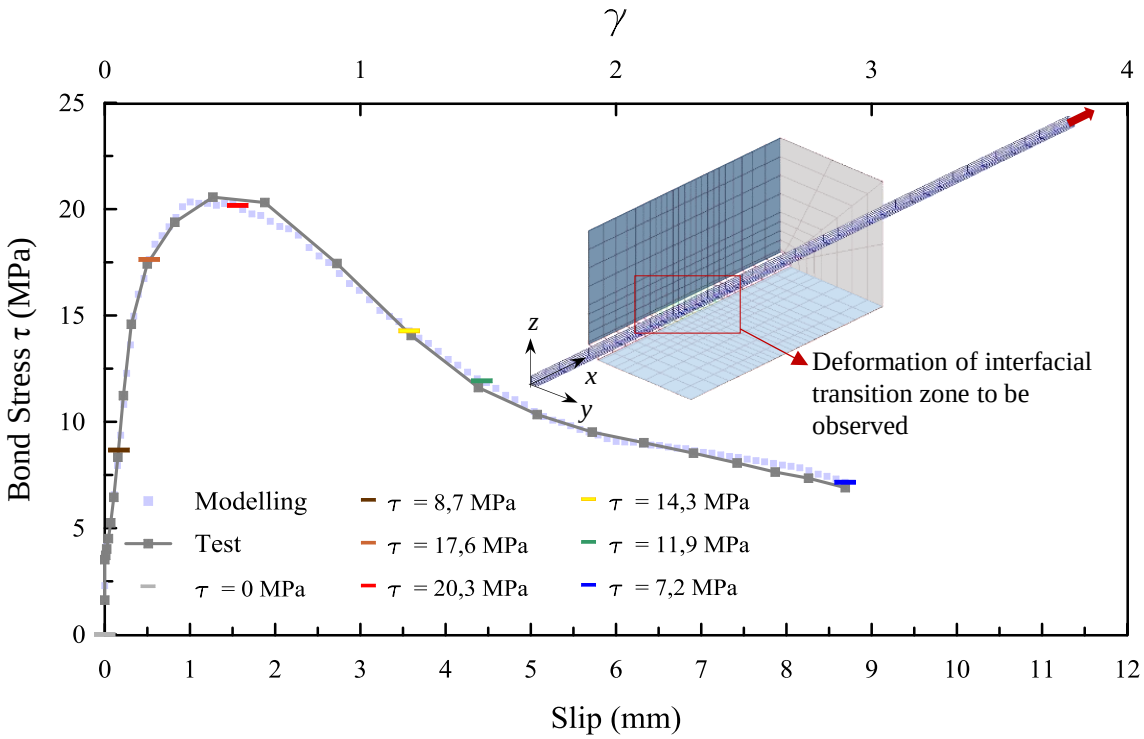

Figure 2. 11. The result of global behaviour obtained from pull-out test modelling and experimental fitting.

The comparison of experimental and modelling results are presented in Figure 2.11. It can be seen that by applying the Equation 2.4 and 2.5 (Von Mises Criterion) to the experimental tests, the similar behaviour can be obtained. The major principal tensile damage occurred in the concrete is presented in Figure 2.12 (a), highlighted on three different stages: the initial condition, the stage at the peak stress and the maximum of slip. In this figure, only the damage on massive concrete volume is shown. The damage occurred only at the area in which the reinforcement was attached (anchorage length). An inclined damage (approximately 45° to the longitudinal direction) occurred along the anchorage length and at the end of the anchorage length, the largest damage occurred. All the damage happened in the first and the second layer of concrete. Experimentally, referring to Figure 2.5 (e), the damage is also concentrated at the end of the anchorage and gradually less damage occurred as the distance to the acting force shortened.

Figure 2.12 (b) illustrates the state of the interfacial zone. At the very beginning, it was non-deformed. Then, respectively to the slip that was measured on the global scale, it started to elongate following the loading application. The deformed zone has the same form as illustrated in Figure 2.8. The shear stress distributions along the anchorage length are presented in Figure 2.13. These seven different colours indicate the different slip as presented in Figure 2.11.

So, a homogeneous behaviour law for three-dimensional interfacial transition zone is developed. In Figure 2.11, 2.12 and 2.13, we can see the responses of modelling on the global scale. This model is used further in the next part for the RC prismatic element modelling.

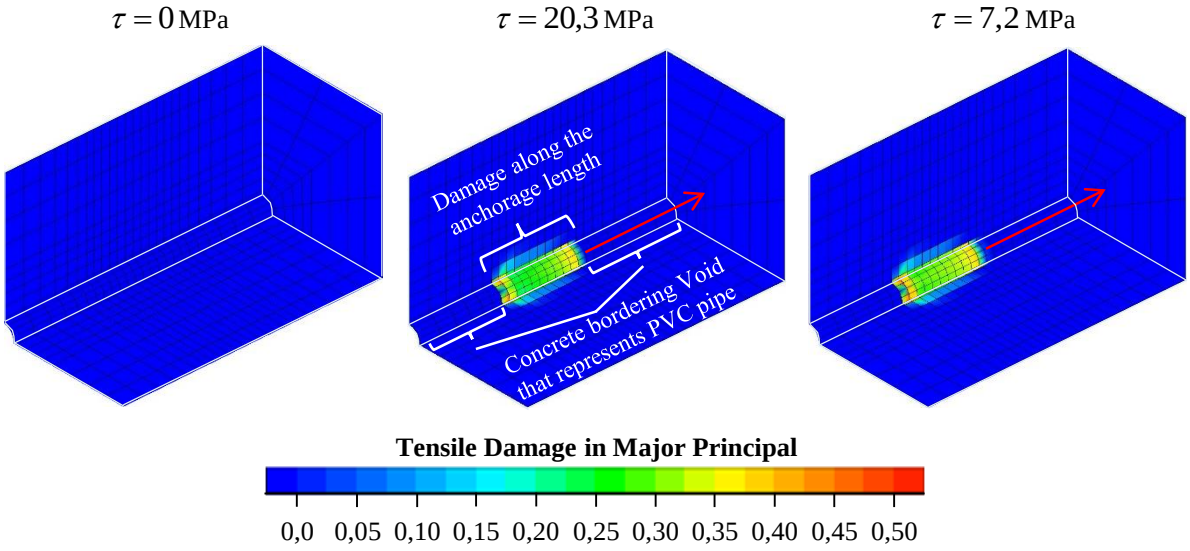

(a) Tensile damage in major principal direction on the **concrete** massive volume. The red arrow shows the loading direction of the pull-out test.

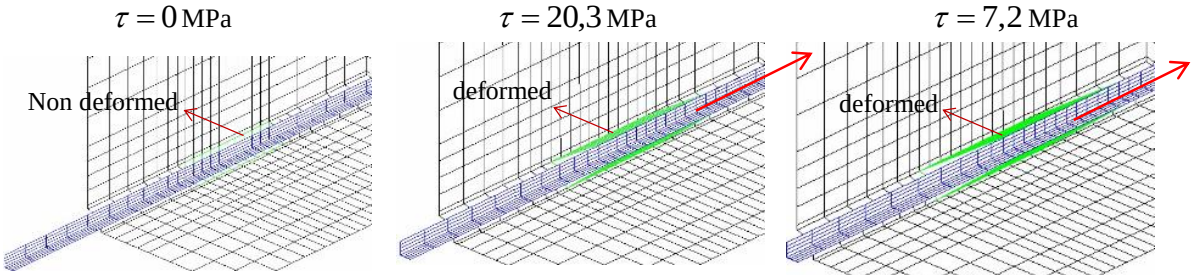

(b) Deformation of interfacial transition zone

Figure 2. 12. Damage occurred in the concrete and deformation in the interface zone.

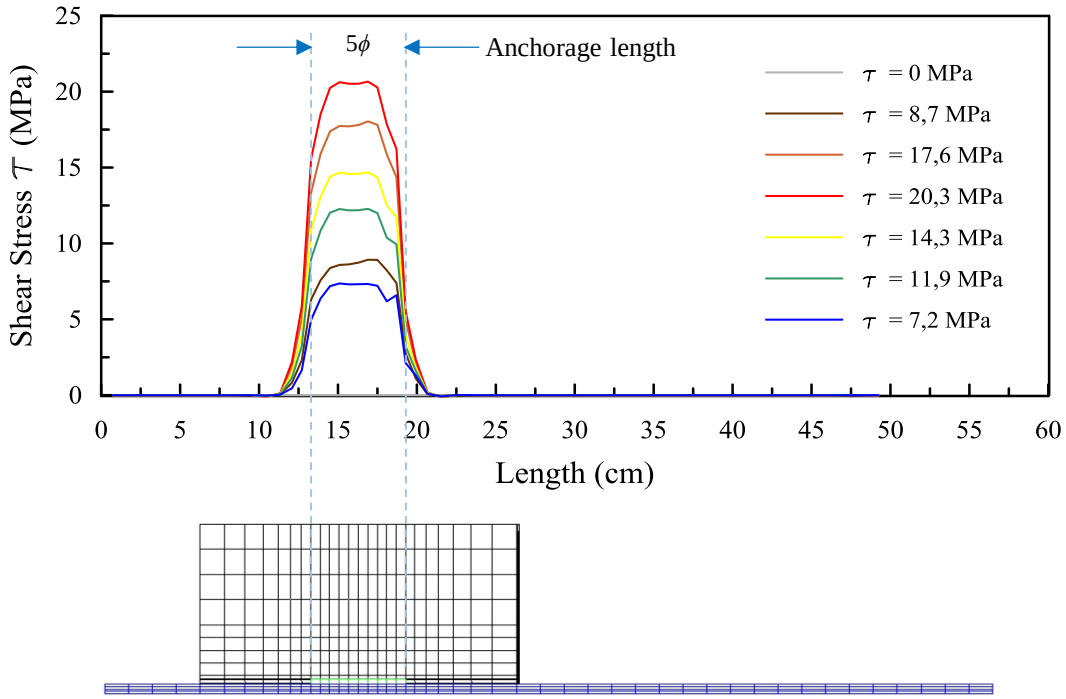

Figure 2. 13. Shear stress along the anchorage length with the colour codes following Figure 2.11.

2. 4. Tensile test on RC Prismatic element

One of the most suitable tests for observing the propagation of cracks in RC structures is a tensile test of a simple prismatic element with one reinforcement bar set in the centre of the concrete volume. As the specimen is subjected to pure tension loading, the effects of the steel and concrete bond, such as stress distribution, tension stiffening reduction and concentration of forces at some local points can be observed (Dominguez Ramirez, 2005; Hameed, 2010). In some works, this structure is called *tie beam* (Jason et al., 2013; Michou et al., 2015).

2. 4. 1. Detail of specimen for tensile test

A concrete prism was cast with one steel reinforcement bar of nominal diameter 12 mm in its centre. The concrete cross section is equal to $10 \times 10 cm^2$.The bar was encased in a PVC pipe at the points where it came out of the ends of the concrete prism in order to prevent a contact between the steel and the concrete during casting and consequently to avoid spall off the concrete during the loading (details are shown in Figure 2.14). So, the bond length is 40 cm. Two specimens were fabricated with the same concrete and the same steel bar as those in the pull-out tests.

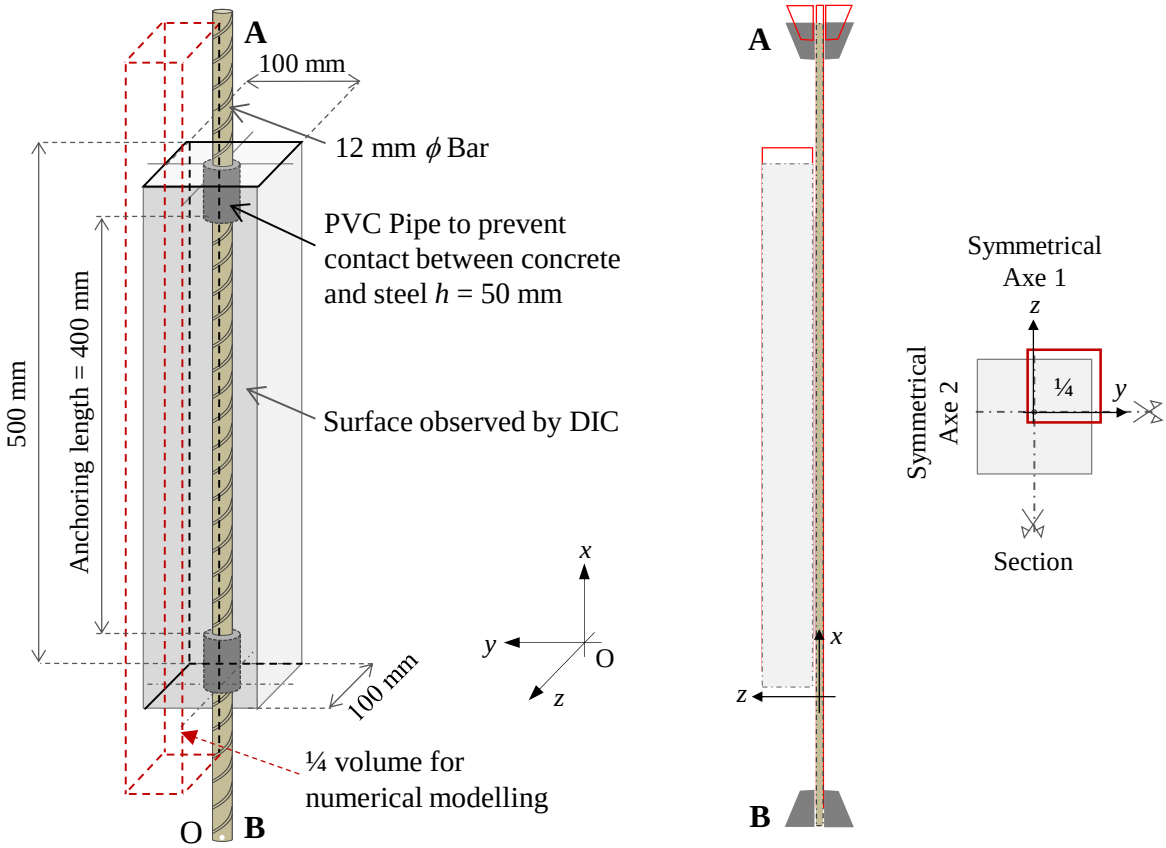

Figure 2. 14. Detail Dimensions of RC tensile test specimen.

Ten centimetres long of steel bar separated each end of the prism from the grip of tension loading machine. One end, B, was clamped while another end, A, was loaded in tension. The rate of the imposed displacement was 1,8 mm/minute according to the previous works by (Ciampi et al., 1981; Eligehausen et al., 1983; Hameed, 2010). The tests were conducted up to the yielding of reinforcement.

The DIC system was used to observe the appearance of cracks on the concrete surface. Two cameras integrated into the system were linked each other with a stereovision technique. This technique allows the displacement field to be measured in three dimensions by using two corresponding images. The basic concept is to obtain the third dimension of the observed specimens at various times during the specimen deformation by stereo correspondence (A et al., 2009; Orteu, 2002), i.e. triangulation of two images that have a common part in their field.

LMDC has a DIC measurement system using 5.0 MP numerical cameras with a pixel size of 3,45 µm. The use of this type of camera helps to obtain more stable pictures without any vibration. Observation using another type of camera, such as DSLR (digital single-lens reflex) camera, may lead to a slight movement since the camera vibrates while capturing the photos. In this experimental work, 2128 x 564 pixels photos were taken every second during the test. Vic-3D software v7.2.4 was used to perform the post-treatment analysis. During the post treatment, every zone of interest of the image is divided into several finite subsets. The chosen size of one subset is 4 mm x 4 mm equivalent to 19 x 19 pixels in this case. The installation of this system is presented in Figure 2.15. The uncertainty of displacement field is 6 µm and 5 µm for the first and the second specimens successively.

The system requires a sufficiently random of the speckle pattern on the studied concrete surface. The speckle pattern was carried out using black paint spray. If it is necessary, white paint can be applied first before the black speckle to obtain the better contrast. In order to obtain the appropriate dimension and also distribution, the surface was not directly sprayed. Direct spray to specimen may lead to a very dense speckle pattern with small dots dimension. Therefore, the black paint was sprayed horizontally parallel to the concrete surface and we let the droplets create the speckle pattern. This technique possesses better distribution and dimension of the speckle pattern (kilonewton Sarl, 2010).

The experimental results are presented in Table 2.9 along with the modelling results. The final cracking patterns after yielding of the reinforcement are presented in displacement field of the studied surface two-dimensionally. One or two cracks localised perpendicularly to the loading axis. Observation in the first specimens shows the second localised crack propagated after the yielding of the steel bar at 7,5 cm from the first crack. When the specimen was unloaded, this second crack was re-closed. Further discussion from experimental works is explained in the part 2.4.3 along with the numerical modelling results.

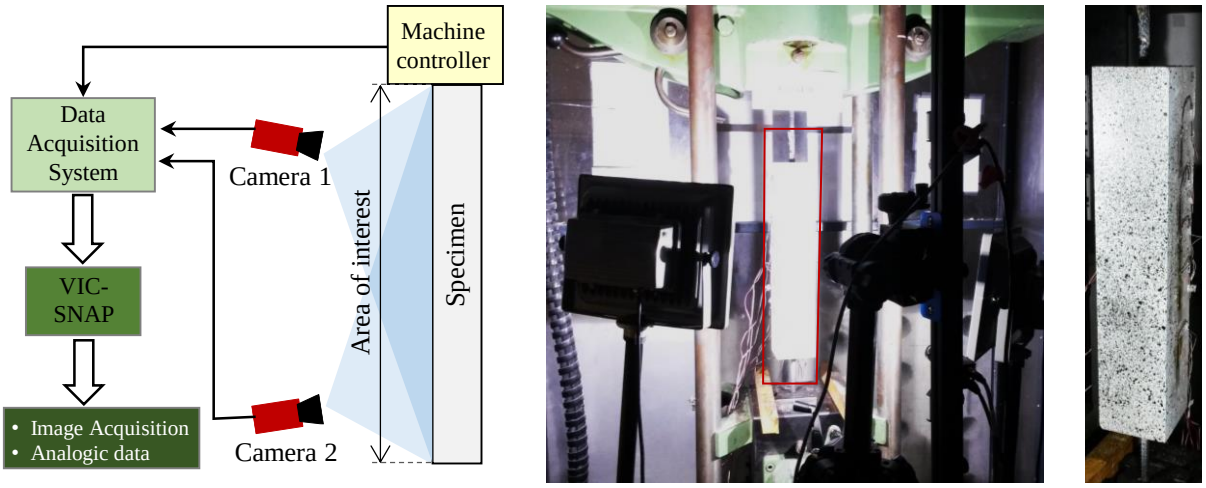

(a) (b) (c)

Figure 2. 15. DIC installation for tensile test on RC Prismatic Element in LMDC.
(a) Sketch of DIC system. (b) Installation of cameras and LED projector. (c) RC prismatic element specimen with the speckle pattern.

2. 4. 2. Numerical modelling of tensile test on RC prismatic element

In this part, the effectiveness of interfacial transition zone is studied. In order to understand better and to investigate the effectiveness of the interface model, the tension test on RC prismatic element is conducted by considering two different conditions: *Perfect Interface* (PI) model and *Sliding Interface* (SI) model. In the PI model, the steel bar is surrounded by the massive concrete volume. This modelled is also called *non-sliding steel-bar connection*. In the SI model, the same configuration of the pull-out test is used in which interface zone is introduced around the bar creating *a plastic sliding connection*. As the two different conditions were considered in the numerical simulation, the three behaviour laws used in the model are presented in this section, for plain concrete, steel bar reinforcement and steel-concrete interfacial transition elements.

A. Geometry and boundary conditions

The finite element mesh configuration for the numerical simulations is presented in Figure 2.16. Similar to the pull-out modelling, only a quarter of the specimen was discretized with CUB8 elements (cube with 8 nodes). The reinforcement bar is meshed three-dimensionally and the interface zone is also taken 3 mm based on the pull-out test. The boundary condition is configured as the experiment worked. In the summary presented in Table 2.9, also in several figures in part 2.4.3, the cracking pattern is observed on the *xz*-plane (with the presence of the reinforcement and the interface); and/or the *xy*-plane at the concrete outer surface (the same surface that was observed by DIC).

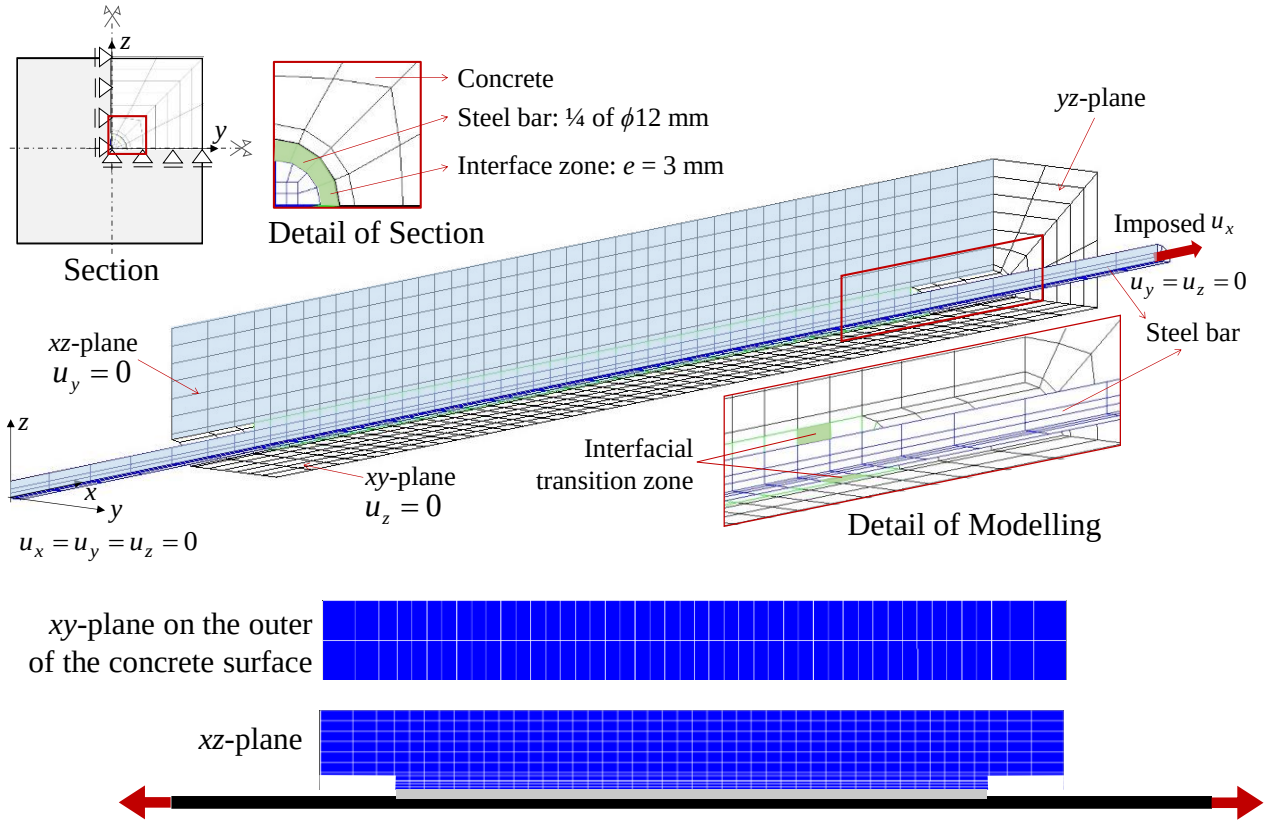

Figure 2. 16. Mesh and boundary conditions for modelling (one-quarter of specimen's volume).

B. Behaviour law

Table 2.7 summarises the behaviour law employed for each material in the two models. For the PI model, only the behaviour of the concrete and steel bar model were used. For the SI case, the plastic sliding interface was introduced to model the interface zone.

Table 2. 7. List of behaviour law for each material in two types of model.

Model / Elements	Perfect Interface (PI)	Sliding Interface (SI)
Plain concrete	Plain concrete LMDC model	Plain concrete LMDC model
Steel bar	Steel bar elasto-plastic model	Steel bar elasto-plastic model
Interfacial transition zone	Plain concrete LMDC model	Elasto-plastic interfacial transition zone model

Behaviour Law of Plain Concrete

The behaviour of plain concrete is modelled by the LMDC concrete damage model. The parameters used in this numerical simulation are already presented in Table 2.6 whilst its behaviour under cyclic loading is presented in Figure 2.17. The behaviour of LMDC model in this figure may slightly different to the one that was explained in Chapter 1 due to the fitting of concrete's parameters.

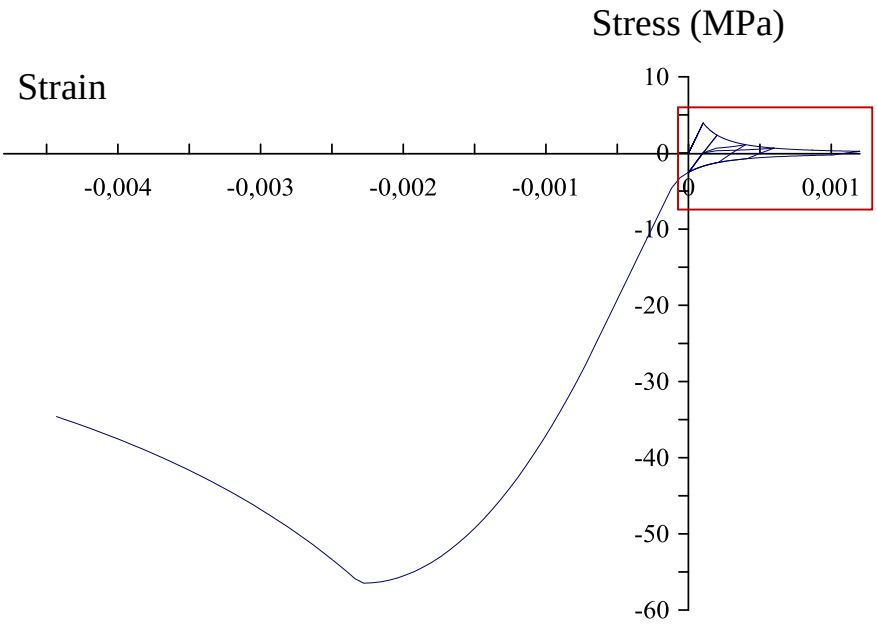

(a) Response under cyclic tension and compression loading.

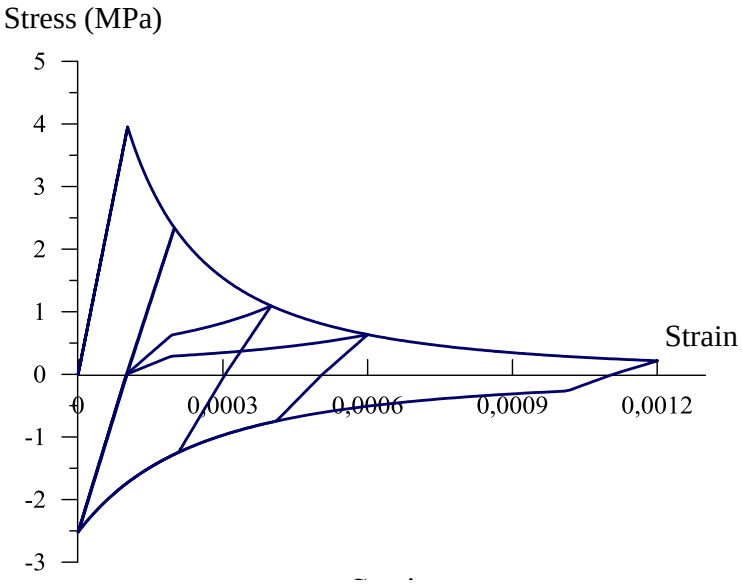

(b) Response under cyclic tension loading.

Figure 2. 17. LMDC model: Stress-strain curve responses under cyclic loading.

Behaviour Law of Steel Reinforcing Bar

The steel reinforcement bar was modelled as elastic-perfectly plastic materials. Based on the experimental tensile test result, the steel bar reached the yield strength of 567,30 MPa and a Young's modulus of 190 GPa.

Behaviour Law of Plastic Sliding Interface

The interface zone thickness was set to 3 mm as explained in Part 2.3.3 C. The behaviour of the plastic sliding interface is presented in Figure 2.10. This equivalent stress-deformation models the interfacial zone up to 5 mm of slip.

Table 2. 8. List of parameters used in the interfacial transition zone.

Parameters	Symbol	Value	Unit
Young's Modulus of elasticity	E	20500	MPa
Poisson's ratio	υ	0	-
Thickness	e_{iz}	3	mm

2. 4. 3. Analysis and discussion: validation of the tensile test on RC prismatic element

In this section, the comparison of the experimental and the two modelling results of the tensile test are discussed. The discussion is highlighting four main stages: before the first localised cracks appear (1), after the first localised cracks appear (2), the beginning of strain hardening (3) and the maximum applied force at F = 65,2 kN (4), all is summarised in Table 2.9. In this table, the sub-sequential phenomena could be seen. As several cracks propagated in PI model, the moments when the nth crack(s) occurred are given.

The comparison at a global scale is discussed firstly. Secondly, displacements along the concrete surface are observed to obtain the crack opening in the concrete surface. The difference of displacement at two end points where steel bar is cast (anchorage length) is presented giving the cumulative crack opening evolution. Then, the stress-strain in the steel bar from the two models is presented. Deriving from the steel stress, shear stress at the interface zone and the steel bar connection is studied for two models. A discussion of the dependency on mesh size ends this part.

A. Comparison at global scale

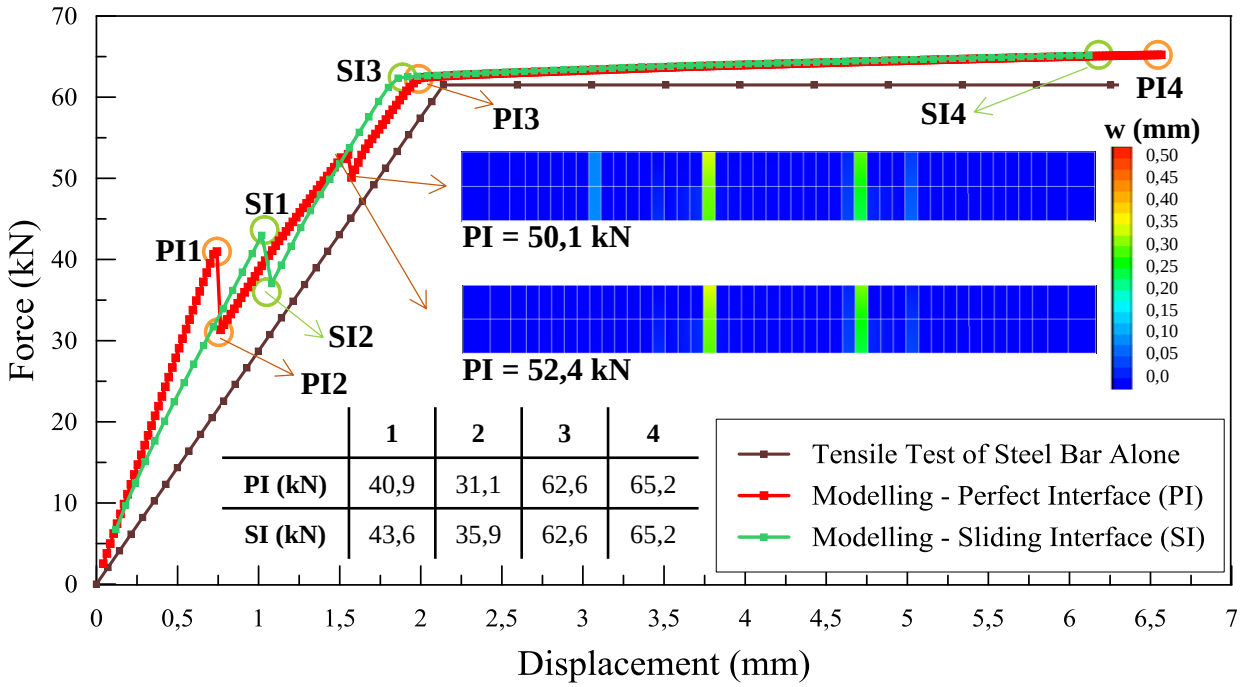

Figure 2. 18. Force-displacement curves (at the global scale).

Figure 2.18 shows two modelling results corresponding to the perfect interface and the sliding interface (PI and SI respectively) of the tensile test on the RC prismatic element compared to the experimental tensile test of only steel bar. Displacements in this curve are measured from the two ends of the steel bar, facing the two grips of the tensile test apparatus; therefore the flexibility of the steel bar influences the results. The difference in stiffness between model curves and the steel bar behaviour represents the contribution of the concrete to the RC element (tension stiffening effect). The first localized crack appears earlier for PI (F = 40,9 kN) than for SI (F = 43,6 kN). Before the first crack, the slope is steeper for PI than SI because of the stiffer behaviour law used in the PI interface zone. This is reasonable as SI uses an equivalent behaviour law in which the Young's modulus is approximately a half that of concrete.

B. Displacement along concrete surface (cumulative displacement, represents cracking in concrete surface)

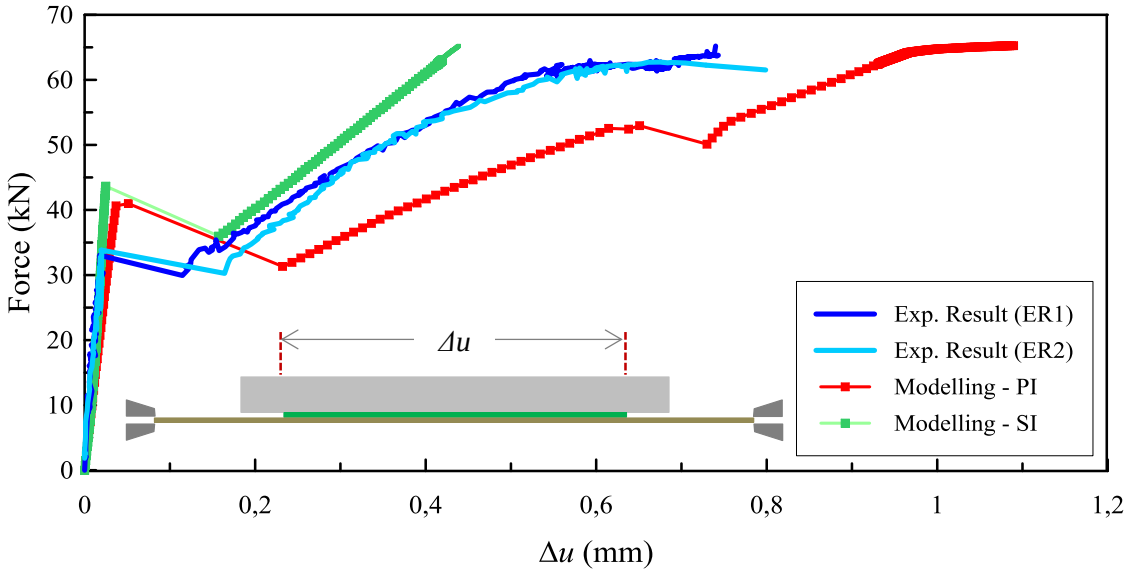

Figure 2. 19. Force-delta displacement in global behaviour.

Regarding the observation of the surface using DIC, the comparison of the experimental tensile prismatic element test results (ER1 and ER2) and the two modelling results (PI and SI) is presented in force – relative displacement (Δu) relation in Figure 2.19. This figure shows relative displacement along the steel bar within the concrete (40 cm of bond length). This relative displacement represents the total crack and the elongation along the measured concrete surface.

On the curve, the beginning stiffness for SI is closer to ER1 and ER2 than the beginning stiffness of PI. The first crack force is overestimated by the model. This phenomenon is due to the direct use of the tensile strength measured in split test (*Brazilian* test). This first problem will be treated in Chapter 3 where we will study the different causes of the first crack's force overestimation by numerical models (material heterogeneity and initial stress heterogeneity are not yet considered at this stage of the work). In the continuing behaviour, the PI modelling

shows a larger displacement after the first crack localisation than the SI results. This large difference in displacement corresponds to the accumulation of localised crack opening in the case of PI. As discussed in the following paragraphs, PI model generated several cracks.

Displacement in the *x*-direction along the concrete surface for Experimental Results (ER) specimen 1 and 2 at the end of the test are presented in Figure 2.20, while PI and SI modelling results are presented successively in Figure 2.21 (a) and (b).

By using VIC-3D, the axial displacement of the concrete surface from experimental results using DIC system was able to reproduce. At the end of the test, the displacement is displayed in Figure 2.20. The abscissa of these displacement gaps gives the positions of cracks. This displacement is the average value measured on three different axes as illustrated by the three white lines. The crack opening evolution can be measured from this gap by using the approach method proposed in (Jason et al., 2013; Michou et al., 2015). Multiple linear regressions were performed on the displacement field on the right and on the left of the gap. Then, its crack width is measured. Furthermore, in Figure 2.22 and 2.23 the evolutions of crack width are summarised in the sum of cracks and the maximum crack.

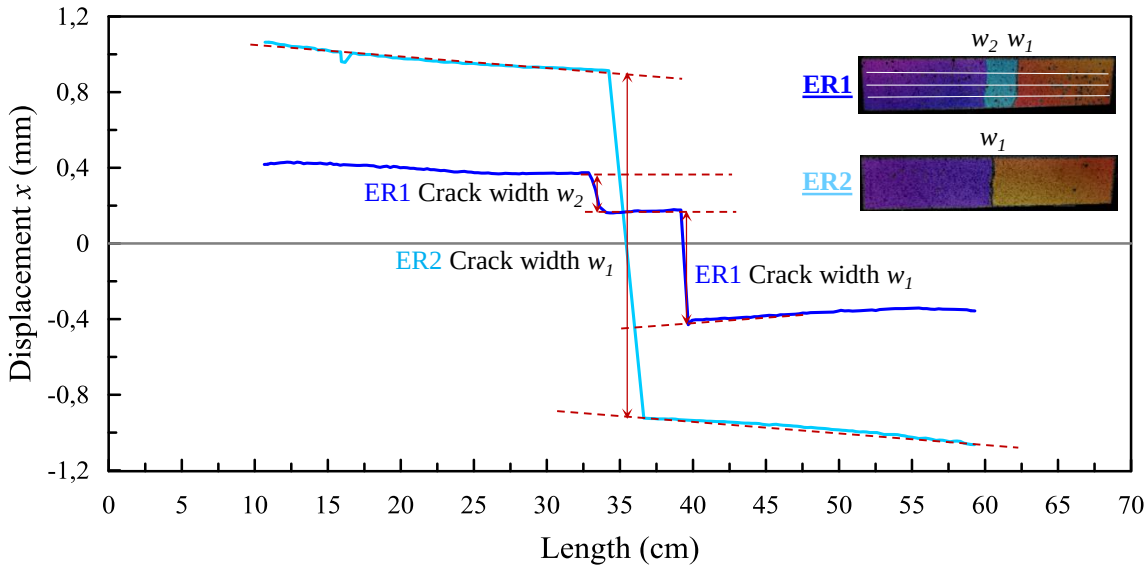

Figure 2. 20. Evolution of displacement along the concrete surface for experimental results at stage 4, the end of the test (65,21 kN for ER1 and 63,95 kN for ER2).

Referring to the highlighted events in Figure 2.16, the cracking pattern from modelling is shown under the curve in Figure 2.21 (a) and (b). This cracking pattern is presented on the *xy*-plane, the same surface that was observed using DIC and it shows the maximum opening measured at stage 4. In these figures, the results of two types of modelling are displayed separately; red represents the PI model and green represents SI model, in four stages (corresponding to the stages mentioned in Figures 2.18 and Table 2.9).

In the PI case, four gaps are captured describing several crack openings that result in around 1 mm of the total crack width along the concrete surface at the end of the test. The SI model shows

only one crack opening, at mid length, which widens from the stage 2 onwards. The evolution of displacement during the test is shown. From stage 3 to stage 4, jumps in values occur as the result of elongation of the bar not set in concrete at the two ends of the RC prismatic elements (the increasing of tensile test can be seen in Figure 2.24, will be discussed in the next part). Continuous loading leads to higher displacement along the RC element.

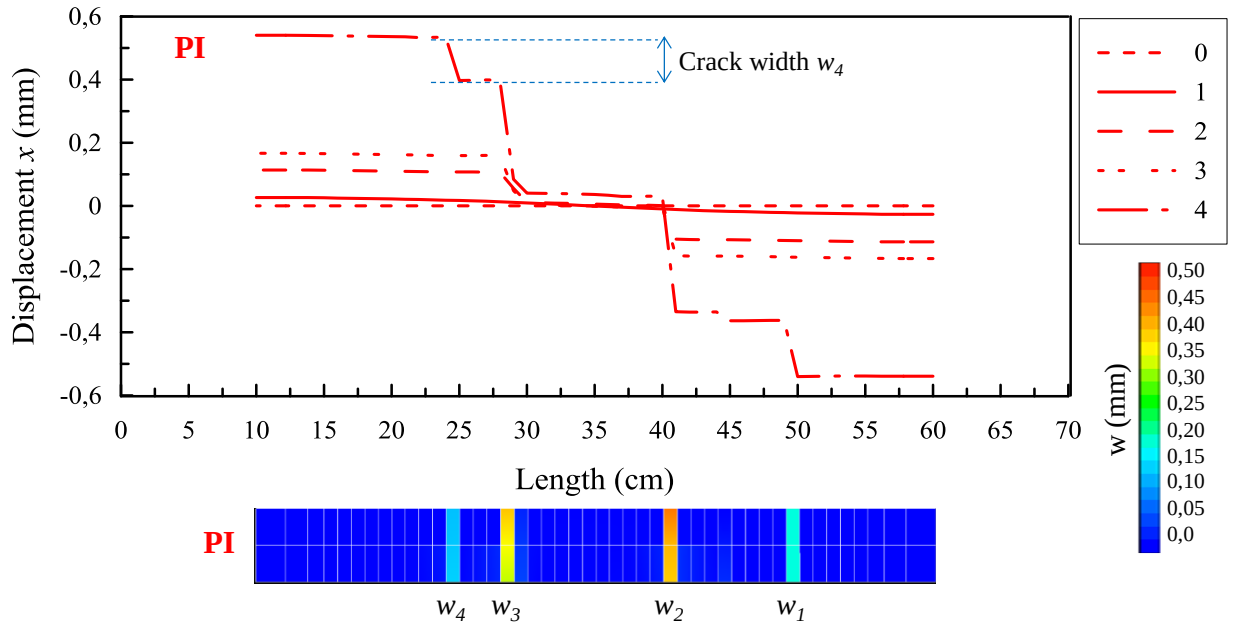

(a) PI model results.

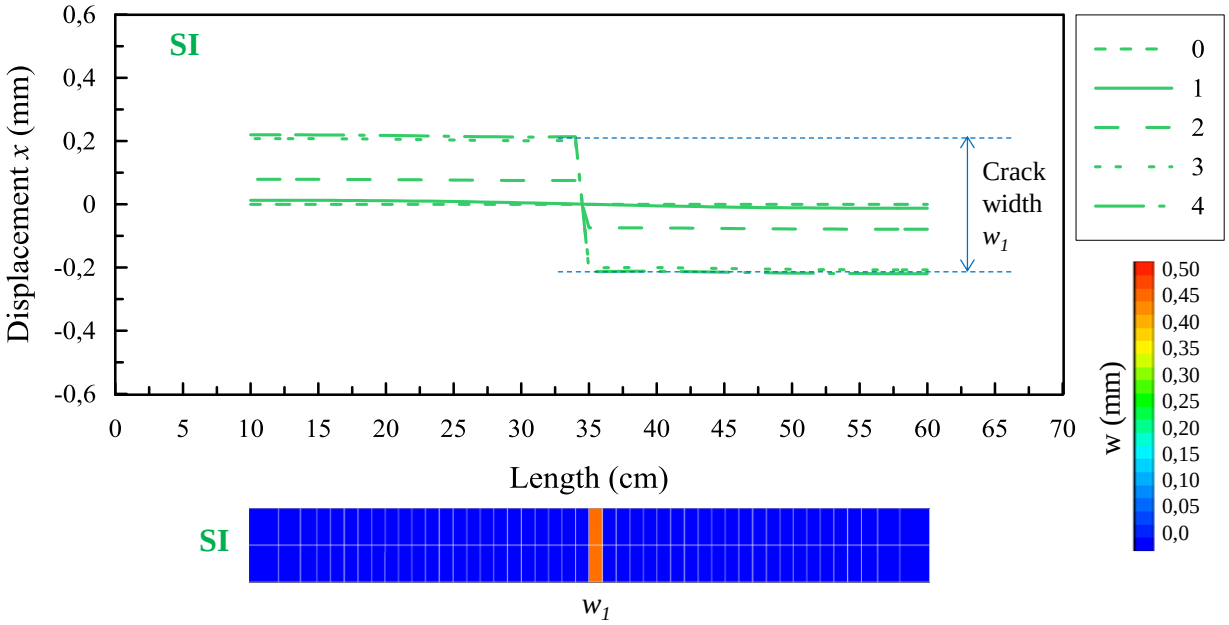

(b) SI model results.

Figure 2. 21. Evolution of displacement along the concrete surface with traces of cracks at stage 4.

Figure 2.22 represents the evolution of crack opening accumulation during the experiment. For PI case, the red curve represents the total opening of four cracks ($w_1 + w_2 + w_3 + w_4$). For the case of ER1, the dark blue curve represents the total opening of two cracks ($w_1 + w_2$). This

figure shows the evolution from the first propagation up to the yielding of the reinforcement. (Michou et al., 2015) proposed this quantitative crack characterization related to elongation of the structure.

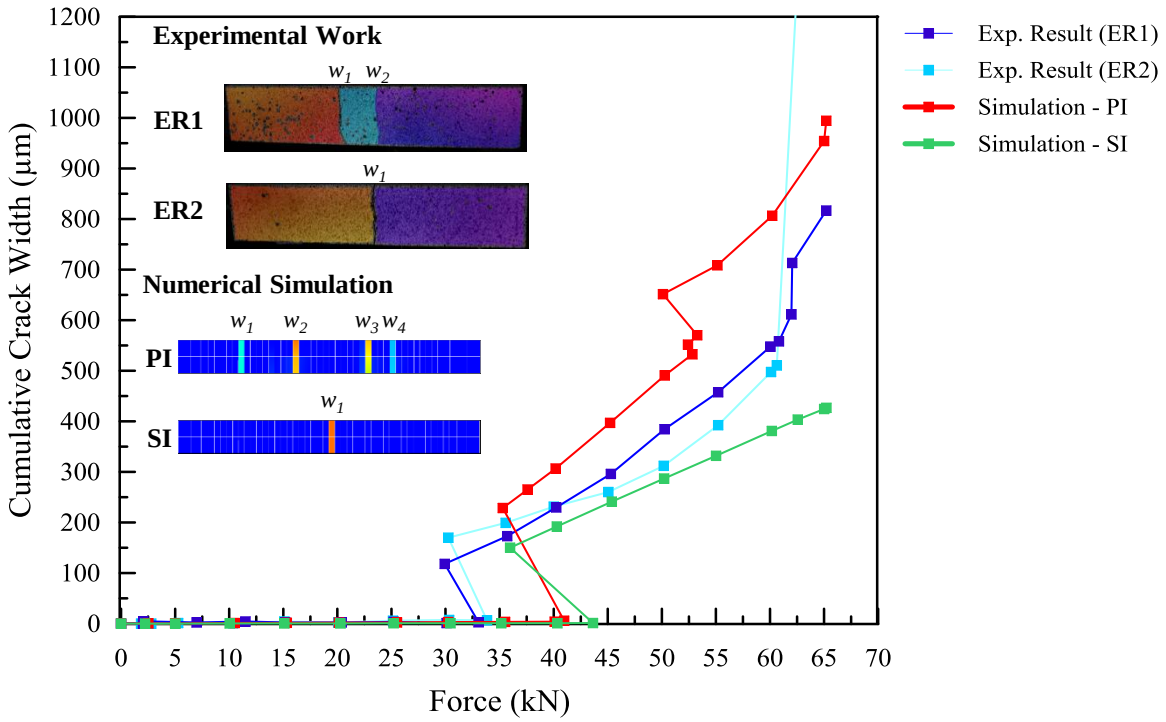

Figure 2. 22. Evolution of cumulative crack width.

It can be seen that the cracks from experimental works were initiated approximately around 33 kN. After that, cracks evolved almost linearly up to strain hardening phase. Observation in specimen 1 shows a second opening of crack when the strain hardening was passed. In Figure 2.23 the opening for each crack is presented. At 62 kN, the second crack opening appeared and it re-closed when the specimen was unloaded. Meanwhile for ER2, after it passed to strain hardening, the one and only crack opening became larger (1,84 mm of crack width at 64 kN).

The SI model propagated the first localised crack later (43,73 kN) than the PI model (40,79 kN). Conforming Figure 2.19, the initiation of the first crack for both cases was late compared to the experiment due to the non-consideration of random field or other causes of heterogeneities of concrete in the initial state. Moreover, the evolution of cumulative crack width from PI model was over-estimated as it produced four cracks while the one from SI model was under-estimated regarding Figure 2.22. The cumulative crack width in the PI model was more than twice of the one obtained by the SI model. So, the model with a perfect interface leads to an overestimation of the crack number. In other words, between PI and SI case, the interfacial transition zone was effectively working in reducing the damage or the crack propagation on concrete.

If the evolution of each crack is investigated (see Figure 2.23), the closest maximum of a single crack to experimental results was obtained from SI model, for example at 50 kN. In general, the evolution of w_{max} produced from modelling is still under-estimated.

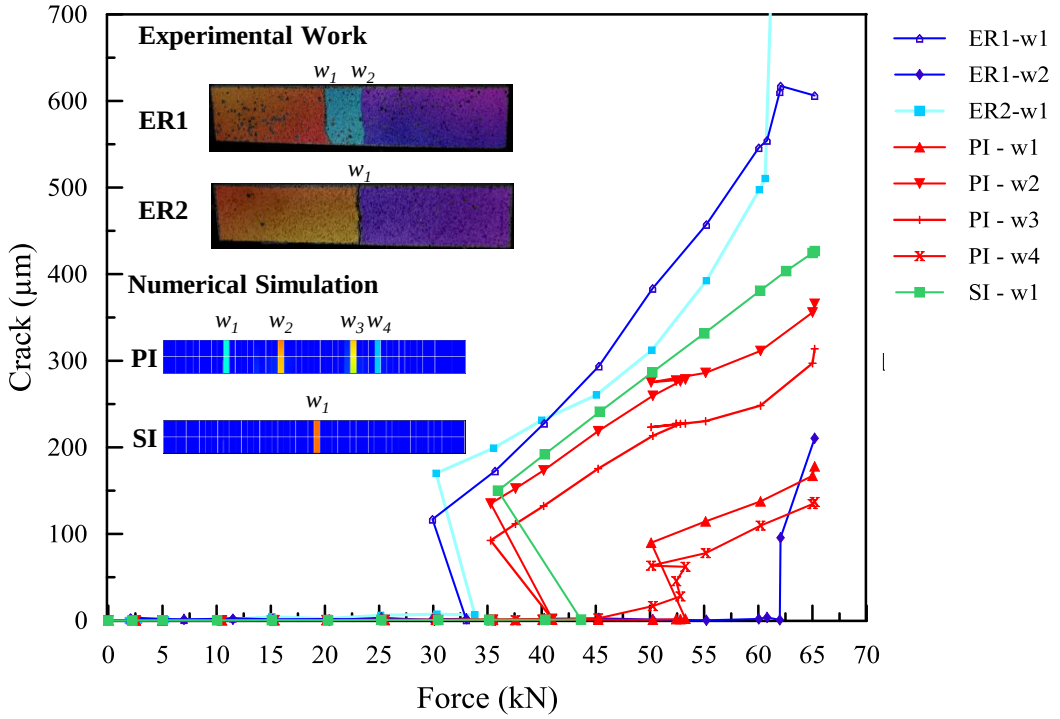

Figure 2. 23. Evolution of crack width for each crack.

Besides the sum of crack, (Michou et al., 2015) also proposed a sum of cubic crack following the Equation 2.6 below to examine the best model. This criterion is related to permeability. In this case, the participation of the large crack opening is increased and the representation is shown in Figure 2.24. The curves are started in the first iteration before the crack localisation.

$$S_{op}^{3} = \sum_{i} \left(w_i^3 \right) \qquad (2.6)$$

The sum of cubic crack width is expressed in the logarithmic axis. Due to the different first crack localisation, the initial conditions are different. The cubic formulation that magnifies the role of the largest crack opening leads the results of SI and PI models close to each other. A slight under-estimated result of modelling compared with the experimental ones is observed after the first crack localisation.

Eurocode 2 (Eurocode 2, 2005) controls the maximum crack opening based on the exposure class of building classification. Therefore, in this RC modelling, the maximum crack is the most important parameter. So, from this point of view, SI model is able to produce better (maximum) crack opening than PI model.

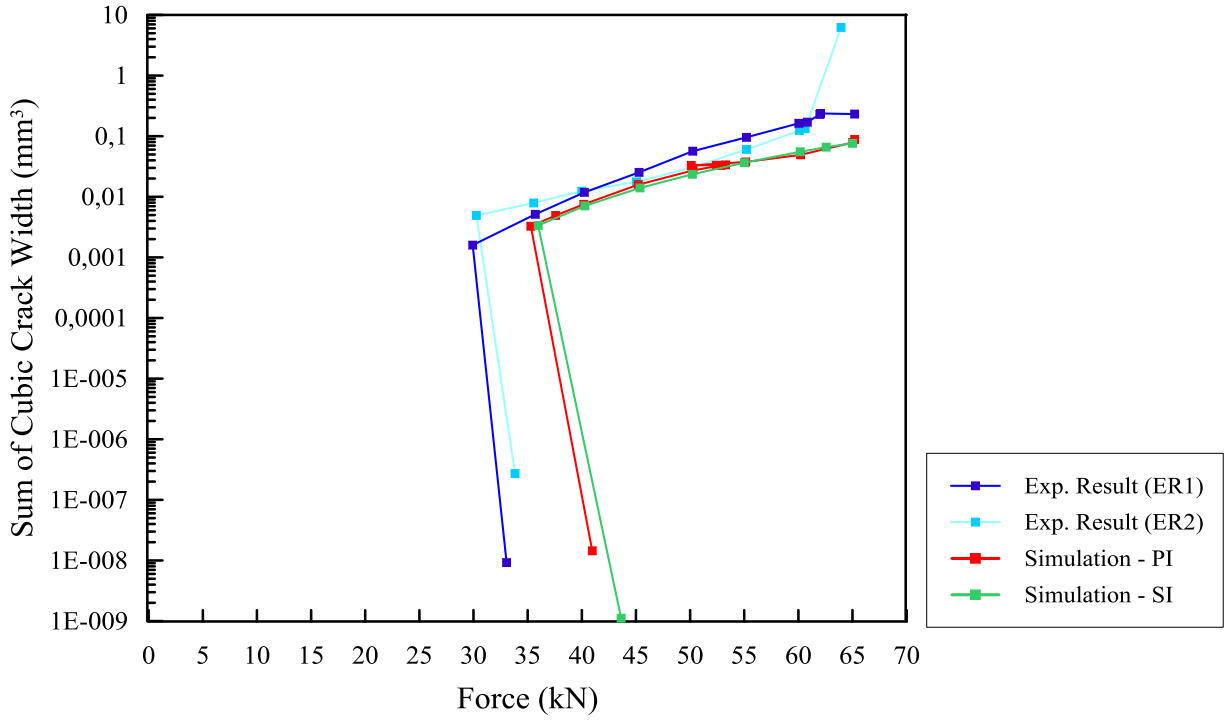

Figure 2. 24. Evolution of crack width for each crack.

C. Comparison of axial stress in steel bar

One of the advantages of using CAST3M (CEA, 2012) is its ability to exploit numerical modelling results, particularly stresses. Figure 2.25 displays the distribution of axial stress in the reinforcing steel bar from modelling results with the cracking pattern presented on the *xz*-plane below the curves.

For the PI model, just before the first localised cracks appear, the distribution of axial stress follows a U-shaped curve. Axial stress in the bar without concrete reaches 375 MPa while the axial stress at x = 35 cm is 30 MPa. When two localised cracks appear at x = 28 cm and 42 cm (at stage 2), axial stress in the mid-length of the bar increases (reaching almost the same stress as in the steel outside the concrete) because deterioration of the concrete reduces its contribution to the bearing of the external load. Further loading applications show the same trend: when crack opening occurs, the steel axial stress increases. At the final load, four cracks occur on the concrete surface and the steel stress reaches its elastic limit.

Unlike the previous results, the SI model shows one crack at the end of test. Before the first localised crack occurs (stage 1), the distribution of the axial stress in the steel has a tendency to decrease towards the mid-length, resulting in a V-shaped curve. At stage 2, one crack appears in the mid-span followed by increasing axial stress in the bar. To be noted, at stage 4, at the two ends of anchorage, there is imprecision of axial stress from FE analysis. This condition resulted in augmentation of stress passing the 566 MPa of yield stress despite employing the elastic perfectly plastic model for reinforcement.

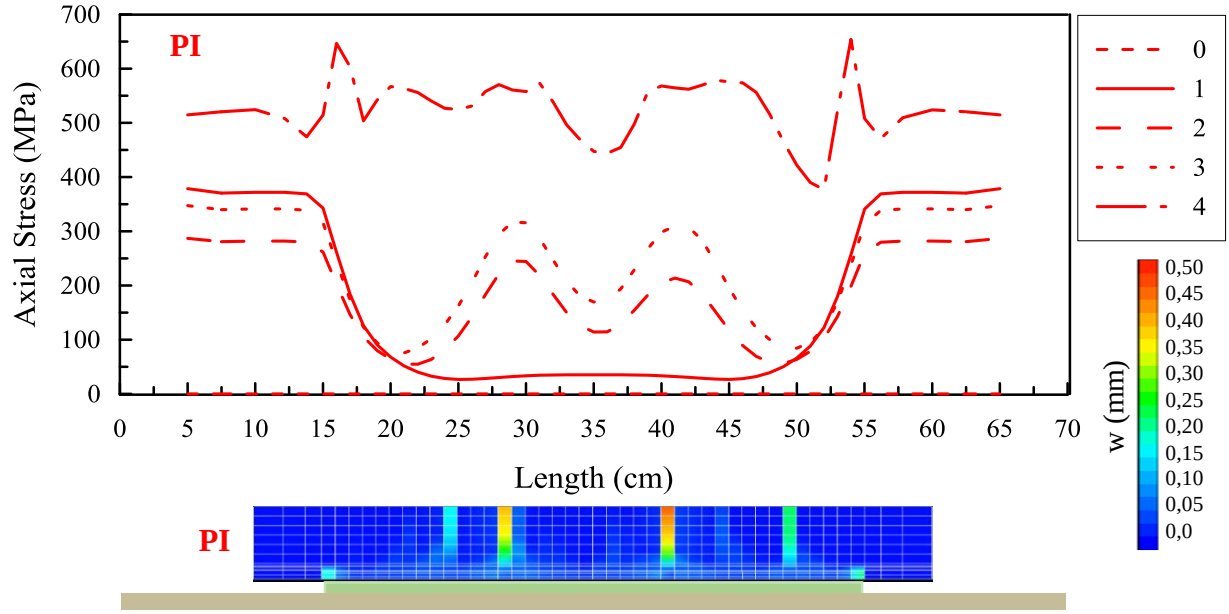

(a)

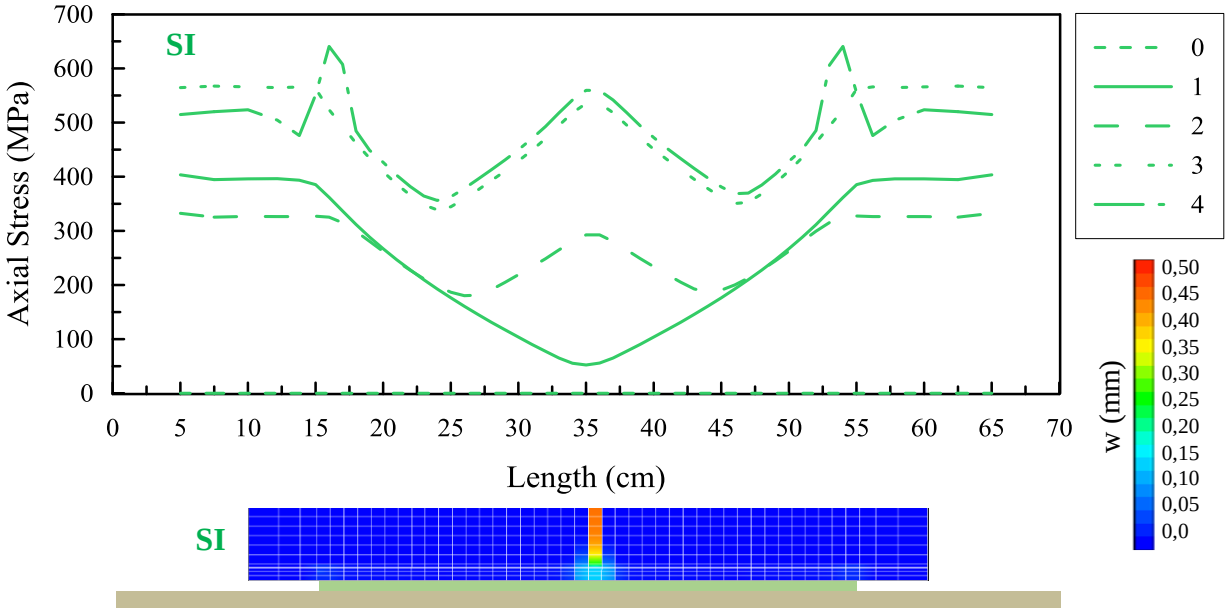

(b)

Figure 2. 25. Evolution of axial stress in the steel bar. (a) PI model. (b) SI model.

D. Comparison of shear stress at the interfacial transition zone

When the axial stress on the steel bar is known, it is possible to derive the shear stress on its boundary with the interface zone. The axial stress obtained in the previous part is in the centre of the steel bar. So, by considering the nominal diameter and the area of its surface in contact with the concrete (πd), the approximate value of the shear stress can be obtained (as detailed in Equation 2.7) where $F_s = \sigma_s 0{,}25\pi d^2$, σ_s represents axial stress of the reinforcement, d represents nominal diameter of reinforcement and Δx represents the size of the mesh.

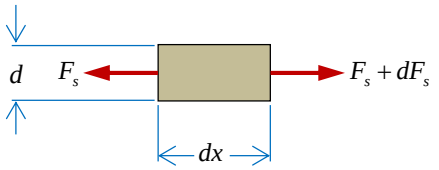

Figure 2. 26. Force in one element of reinforcement.

$$\tau \, \pi d \, dx = dF_s$$

$$\tau = \frac{dF_s}{dx} \frac{1}{\pi d}$$

$$\tau \approx \frac{1}{\pi d} \frac{\Delta F_s}{\Delta x} \qquad (2.7)$$

Figure 2.27 shows the shear (bond) stress results for both cases at stage 4. Shear stress has reverse behaviour on both sides of the crack. It is positive on the left of the crack and it is negative on the right. Moreover, bond stress variation along the steel bar between two cracks forms a sine-like curve. Zero shear stress occurs at crack zones as no stress is transferred to the concrete, and a second zero value also occurs between two cracks. This has the same form as explained by (Michou et al., 2015; Wight and MacGregor, 2011).

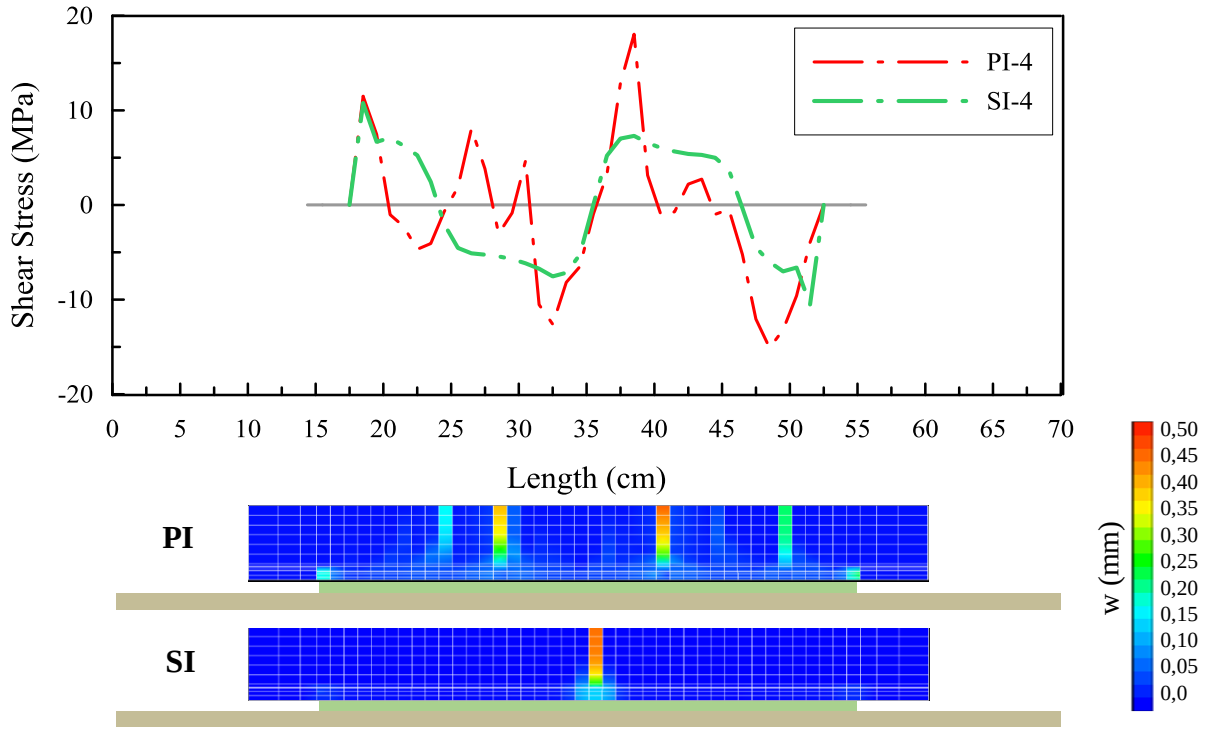

Figure 2. 27. Shear stress at steel bar interface for PI and SI model at F = 65.2 kN (stage 4).

E. Table of comparison

In the following, a comparison table presents the experimental and the modelling results sequentially. Numerical simulations are presented in crack opening (*w*) colour gradient. On the other hand, experimental results are presented in two-dimensional displacement colour gradient.

Table 2. 9. Comparison of displacement and crack opening obtained from experimental and modelling highlighted in four events.

	Numerical modelling results	**Experimental results (ER)**		**Numerical modelling results**
	Perfect Interface (PI)	**ER-1**	**ER-2**	**Sliding Interface (SI)**
0. Start Point	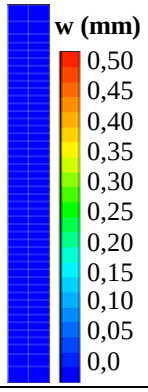	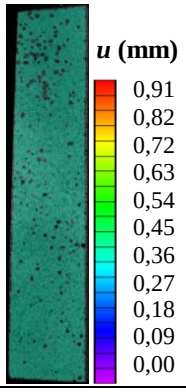	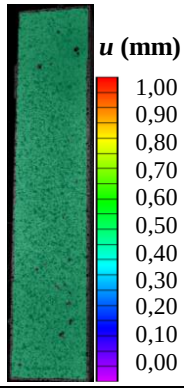	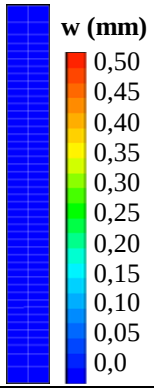
1. Before the first localised cracks appear	F = 40,8 kN 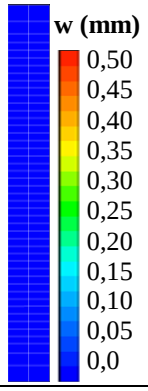	F = 33,1 kN 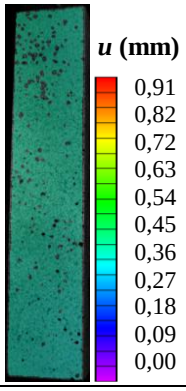	F = 33,8 kN 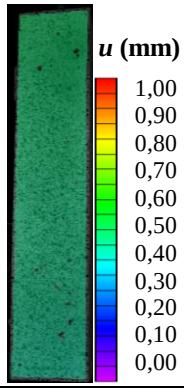	F = 43,7 kN 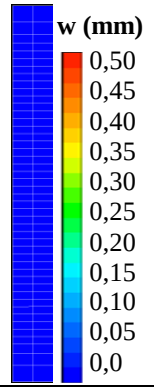
2. a After the first localised cracks appear	F = 29,9 kN 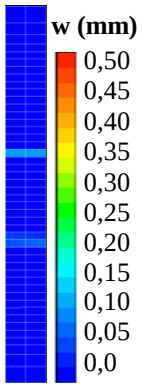	F = 29,9 kN 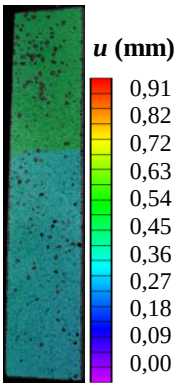	F = 30,3 kN 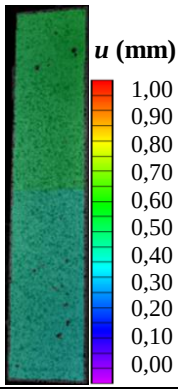	F = 36,1 kN 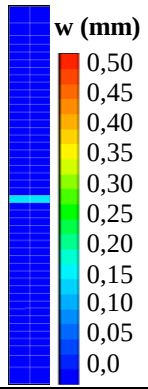
2. b After the second localised cracks appear	F = 52,4 kN	F = 62,1 kN	-	-

	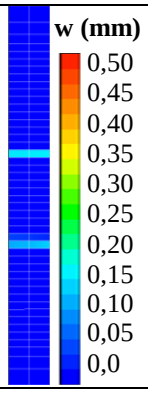	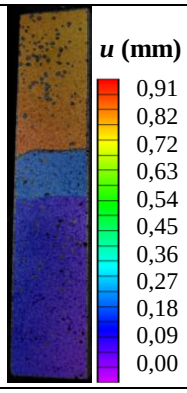		
2. c After the third localised cracks appear	F = 50,1 kN 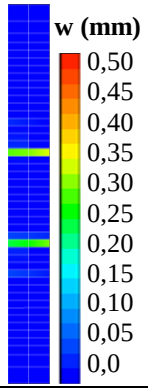	-	-	-
3. Beginning of strain hardening (F = 62 kN)	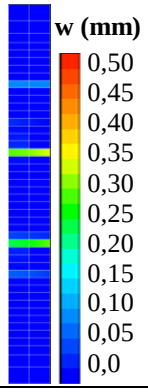	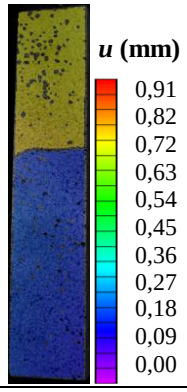	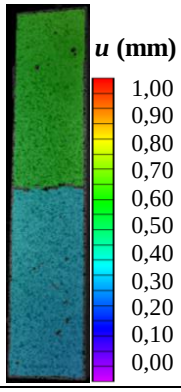	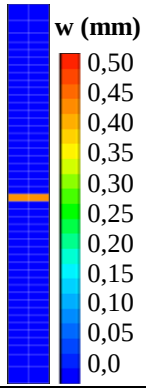
4. Maximum applied force	F = 65,2 kN 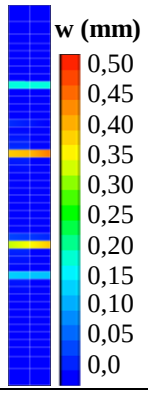	F = 65,2 kN 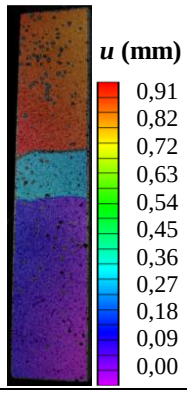	F = 64,1 kN 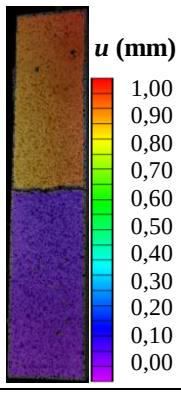	F = 65,2 kN 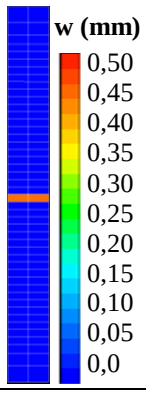

F. Mesh sensitivity

In order to verify the independence of the model results with respect to mesh size, modelling was performed with coarser element size for both cases. In the previous sections, the modelling for both PI and SI were implemented by using 1 cm of concrete element size. In this section, 2 cm of one element was taken.

In the PI case, despite the fact that the plain concrete model was regularised, crack propagation was dependent on mesh size. Nevertheless, the first crack localisation occurred at almost the same time for finer and coarser mesh size. This is due to the fact that, in PI case, the regularisation method of concrete model acts also in the interface zone where damage is not localised, so the dissipated energy increases with the mesh refinement of this zone. This is the main reason why the regularised model has to be replaced by a non-regularised plastic behaviour in this zone.

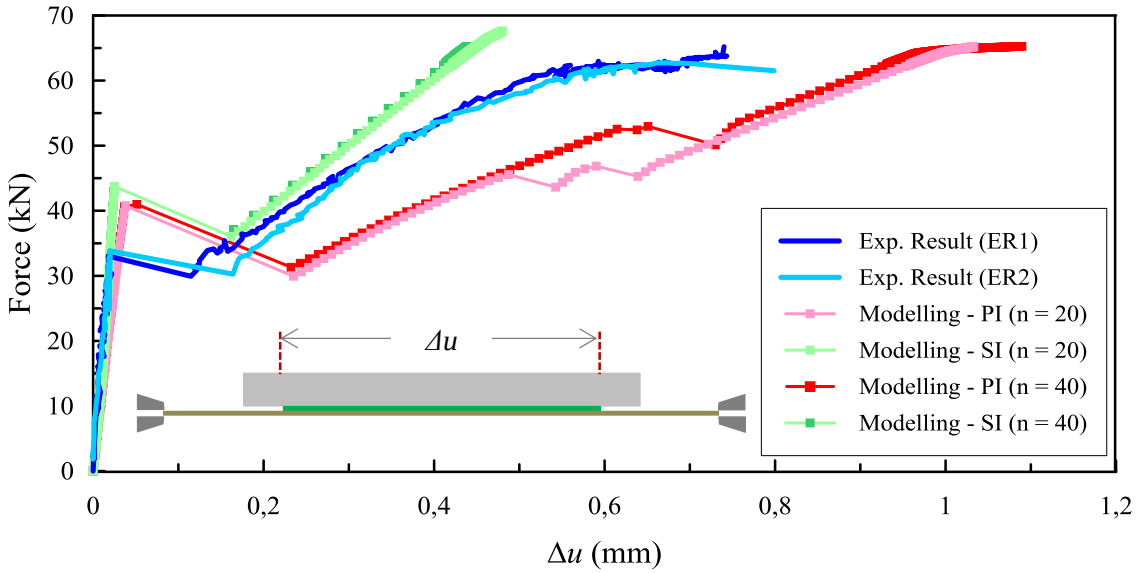

Figure 2. 28. Force-delta displacement in global behaviour with *n* represents the number of mesh in along the anchorage length.

And effectively, in contrast to the previous condition, SI showed almost no dependency on mesh size. Applying a coarser mesh did not change the steel bar sliding. In Figure 2.29, the evolution of the cumulative crack opening of all cases is presented.

Finally, the sensitivity analysis confirms that the interface element is necessary (together with the regularisation of plain concrete surrounding this interface) to ensure a finite element model response that is independent of the mesh refinement.

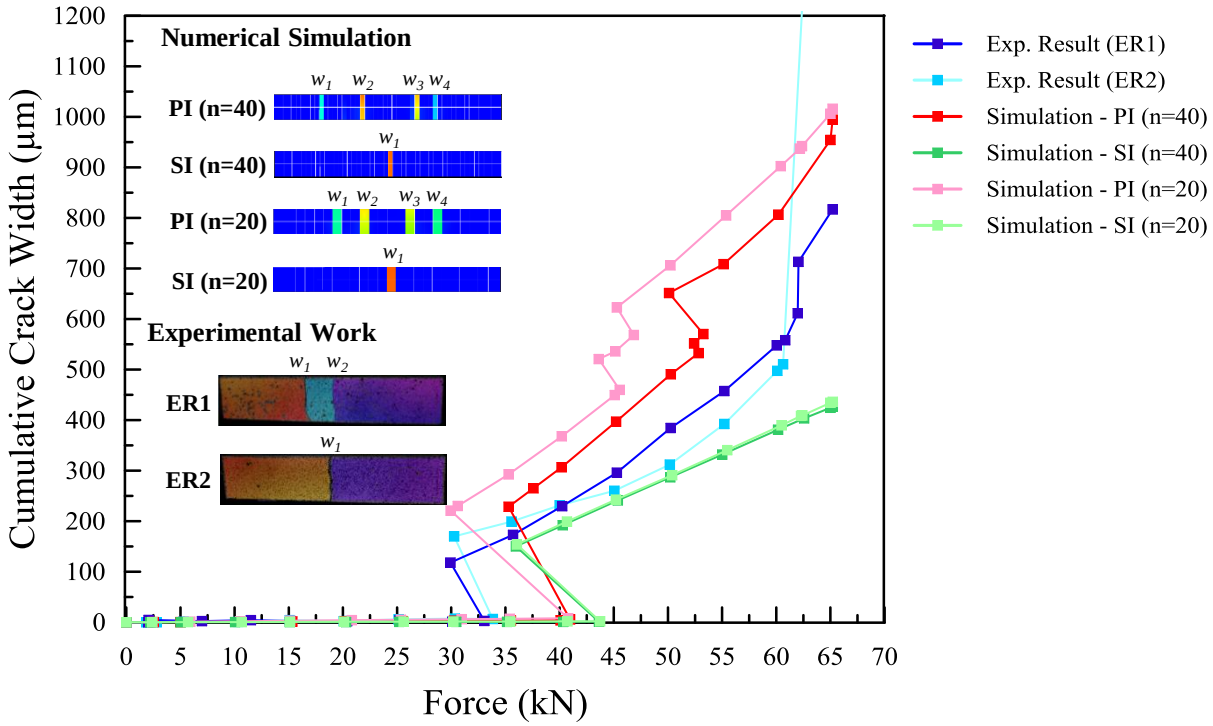

Figure 2. 29. Evolution of cumulative crack width with *n* represents the number of mesh in along the anchorage length.

2. 5. Remarks and discussions for further application

This chapter has discussed the development of the steel-concrete bond behaviour and its interest for RC FE modelling. First, the pull-out tests were performed to characterise the behaviour of interface zone. The investigation on the specimen post-test conditions shows the deterioration of the concrete up to certain thickness from the reinforcement. Then, based on this condition the geometry of interfacial transition zone was proposed. Later on, based on the average behaviour along the anchorage length, an elasto-plastic behaviour law is adopted. Practically, a Von Mises criterion can be used with a hardening derived from a pull-out test. A numerical modelling fitting test on pull-out experimental results was executed to calibrate the correspondence between the interface model and the pull-out test results.

Next, two tensile test specimens were cast from the same mix design along with the two pull-out test specimens and some cylindrical specimens for concrete characteristic tests. The steel bar reinforcements were also from the same fabrication. The first crack localisation for both cases propagated almost at the same force which was 33 kN. Even so, the two specimens have different continuing results, such as cracking pattern, the number of cracks, and certainly, crack opening evolution. At the end, the first specimen has two cracks whilst the second one has only one crack that opened widely. This condition shows us that even though a great effort was made to create almost the similar experiments for both specimens, the results were different. It may come from concrete random nature properties (Fenton, 1990; Van der Have, 2015).

Numerically, the application of interface model (sliding interface) on RC prismatic element

was conducted. The results are then compared to another numerical modelling with a perfect bond. It shows the need of interfacial transition zone. Nevertheless, there are some remarks to be discussed and improved.

In general, the comparison with DIC results showed that SI gave more realistic results than PI. The assumption of a perfect interface PI (non-sliding behaviour law) led to an exaggerated number of cracks along the specimen even if a realistic and regularised behaviour law for the plain concrete is used. On the other hand, SI model has a better agreement with the experimental results in term of the initial stiffness before the localisation of crack than PI model (see Figure 2.19). Also in the crack opening, SI model had only one crack at the end of the test. Nevertheless, this model needs some improvements, notably in the localisation of the first cracks and the crack opening. Moreover, the mesh sensitivity analysis demonstrates that the use of the regularised model in the interface zone (PI) is counterproductive since the mesh dependency exists only in this configuration and disappears in case of SI with non-regularised plastic behaviour.

Another aspect concerns the first localisation which arrived lately regardless the interface condition (around 10,7 kN of delayed over the experimental results). Apparently, it is not due to the interface but to the concrete properties which are overestimated in this first simulation due to the non-consideration of random nature of concrete.

In the next chapter, the SI method proposed will be applied in a larger structure in order to investigate the role of the random nature of concrete (probabilistic scale effect) and the initial state of concrete (shrinkage-induced stress). In fact, the objective stays to quantify progressively the role of each phenomenon in the FE modelling of RC structures cracking.

This page is intentionally left blank

Chapter 3

Shrinkage and Random Mechanical Properties Effects on Reinforced Concrete Beams Behaviour

A finite element modelling of reinforced concrete (RC) structures is necessary to assess special structures nowadays. Despite using interfacial transition zone between steel bar and concrete, numerical modelling still requires other aspects to obtain better results in term of crack opening and global behaviour. In this chapter, experimental and modelling results of an RC beam with a rectangular section are studied. Experimentally, the Digital Image Correlation technique is employed to observe crack properties. Numerically, pre-damage due to shrinkage and random mechanical properties (using Turning Band Method or Weakest Link and Localization Theory) are envisioned for RC modelling. Their relative importance is discussed. To this purpose, the modelling considers first these phenomena independently and then their combinations are progressively examined.

This page is intentionally left blank

3. 1. Introduction

In the previous chapter, the development of the steel-concrete bond behaviour was discussed step by step from the pull-out test experimental results. An interface model was needed if the sliding behaviour between steel and concrete was to be considered properly. An application in RC prismatic element under pure tension loading led to some remarks that are necessary to be discussed and to be improved. The volumetric interfacial transition zone that was applied to the surrounding concrete along the steel bar has shown its capabilities in limiting the concrete damage diffusion around the steel bar without resorting to a localised damage limiters for the interfacial concrete as in (Llau, 2016).

In the study by Michou et al (Michou et al., 2015), drying shrinkage was considered in the modelling of RC tie with one reinforcement bar in the middle. Delayed strain due to shrinkage was considered in numerical modelling and resulted in the better first crack localisation than the disregard condition. Also, this consideration showed better agreement in global behaviour of RC tie structures, particularly its initial stiffness. Another modelling in RC structures performed by (Jason et al., 2013) in a case of RC beam modelling using interface behaviour law also proved the importance of shrinkage in RC modelling. The absence of this phenomenon resulted in an overestimation of Force-Displacement curve, specifically during the pre-cracking and at the first cracking stages.

Furthermore, three random field simulations for RC tie were performed based on experimental results of concrete tensile strength (R_t) especially for the continuing behaviour after the first crack localisation (Michou et al., 2015). Another application of *Turning Band Method* (TBM), as a random field generator, was performed by (Matallah et al., 2010). In this case, generation of a spatially correlated concrete Young's Modulus using TBM was conducted. This method led to different cracking pattern results and led as for shrinkage effect to an earlier cracking. Random fields are also able to explain that, as mentioned before, experimental works may have different results despite the fact that great efforts were performed to obtain the same outcome (Fenton, 1990; Van der Have, 2015). These discrepancies are due to the underlying random mechanical properties of concrete which appear to be intrinsic to this material.

Based on several studies conducted for (CEOS.fr, 2015), large dimension of structures conducted to specific cracking pattern involving the *random scale effect* factor. This scale effect exists due to the difference of dimension used in the laboratory to measure the concrete tensile strength and the large dimension of structures. It can be explained as an effect of weakest link phenomenon, which reduces the apparent strength with the increases of solicited volume (Weibull, 1939). Normally this scale effect should be considered by the random field method

This chapter aims first to quantify the influence of initial shrinkage and random field of mechanical properties on cracking occurrence. Secondly, to test a determinist method (WL^2) which is able to consider the probabilistic scale effect without resorting to large numerical sampling plan with numerous random fields (which are too much time consuming for real

application).

In this research, the study of structure element was initially oriented towards two types of RC beam: a beam with a rectangular section under four-point of flexural load and a beam with a T-shaped section under three-point flexural load. To be clear, the geometrical configuration of the beam with a T-shaped section was adjusted for experimental works that depends on the capacity of the loading machine in LMDC laboratory. Therefore, the dimension of the T-beam was not in accordance with the standard building Eurocode 2. Furthermore, it is possible that there were some uncertainties in the position of the steel bar reinforcement (due to the casting difficulties) which led to instability in the crack pattern (for some T-beams, a crack started from one support, while some others were not in the same case although the two beams were assumed to be the same). So, the numerical study of such a T-beam is explained and discussed in Appendix A, but their exploitation in the present chapter was finally not considered. Thus, the present chapter is focussed on the RC beam with a rectangular section only.

In this Chapter, the steel-concrete bond model method that was previously proposed in Chapter 2 is applied on RC beam with a rectangular section. In addition, *pre-damage* due to shrinkage and *random properties of concrete* in RC modelling are also considered. In Figure 3.1 below, the stages of the studies are presented.

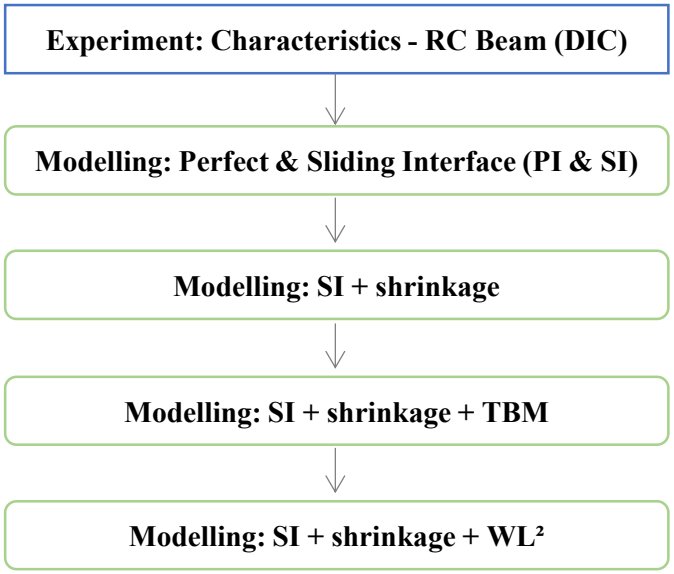

Figure 3. 1. The steps of studies on RC beam with a rectangular section.

To start by understanding the cracking behaviour, in the first step, material characteristics and experiment to capture the behaviour on RC beam subjected to four-point flexural loading were performed. The DIC technique is used to determine the crack features, such as crack opening and crack spacing on the RC beam. In the second step, this flexural test was modelled in two ways, Perfect Interface without sliding (PI) and Sliding Interface (SI) connection. Some important remarks in this first set of modelling are shown in the global scale and in the cracking features. In the second set of modelling, a pre-damage state in the concrete due to shrinkage was taken into account. Then, two methods to consider the probabilistic scale effect were considered along

with the SI model and shrinkage. In the third set of modelling, the Turning Band Method (TBM) was employed to generate random field on concrete. And in the last set of modelling, the Weakest Link and Localisation (WL^2) method was used.

3. 2. Material Characterisation

Characteristic tests for each material were, of course, performed to obtain the properties of concrete, steel bar and also interface zone. Characteristic tests were required to obtain the material properties and determine the local behaviour law of the interface zone. The concrete for the beam and the characteristic test specimens were mixed and cast at the same time.

3. 2. 1. Concrete

Table 3.1 describes the concrete materials used in LMDC (more detailed information of the materials can be found in Appendix B), while Table 3.2 describes the mechanical properties of the concrete. After concrete casting, RC beam was let hardened inside a room without special treatment. After two days, it was removed from the mould and exposed to ambient combinations from January to Avril 2015 (approximately 20°C, 60% HR). Properties of fracture energy were obtained from three-point bending tests on prismatic concrete element according to (RILEM, 1985). The obtained average fracture energy is 124,50 ± 3 J/m².

Table 3. 1. Mix design of concrete materials.

Type of concrete	Normal concrete
W/C	0,5
Type of sand **Type of aggregates**	0/4 mm (700 kg/m^3) - silica alluvial sand Garonne 4/10 mm (1100 kg/m^3) - silica alluvial aggregates Garonne
Type of Cement	CEM I 52,5 R CE CP2 (350 kg/m^3) (High resistance Portland cement for aggressive environments)

Table 3. 2. Mechanical properties of concrete materials.

Concrete compressive strength*	R_c	=	51,37 ± 0,18	MPa
Concrete tensile strength* (Brazilian test)	R_t	=	3,68 ± 0,48	MPa
Concrete modulus of elasticity*	E	=	35620 ± 712	MPa
Concrete fracture energy	G_t^f	=	124,50 ± 3,1	J/m²

* Average ± standard deviation value of experimental results from 3 samples at 87 days after concrete casting

3. 2. 2. Steel bar reinforcement

The nominal bar diameters were 6 mm and 14 mm, corresponding to a cross section of 28,26 mm² and 154 mm^2 (NF EN 10080, 2005).

Table 3. 3. Mechanical properties of steel reinforcement bar.

Reinforcing Bar : Fe E 500 HLE (High Strength Steel)				
Nominal diameter of HA steel bar (NF EN 10080, 2005)	ϕ_n	=	14	mm
Yield strength‡	f_y	=	520,06 ± 4,52	MPa
Modulus of elasticity‡	E	=	198,50 ± 1,33	GPa

‡ Average ± standard deviation value of tensile test results from 3 reinforcement bars

3. 2. 3. Interface by pull-out test

The pull-out tests were carried out to determine the behaviour of the interfacial zone between concrete and steel bar. The results and the details of specimen used in this test are shown in Figure 3.2. Grey curve represents the average value along this concrete-steel bar cohesion surface (anchorage length). The maximum shear stress was 22 MPa.

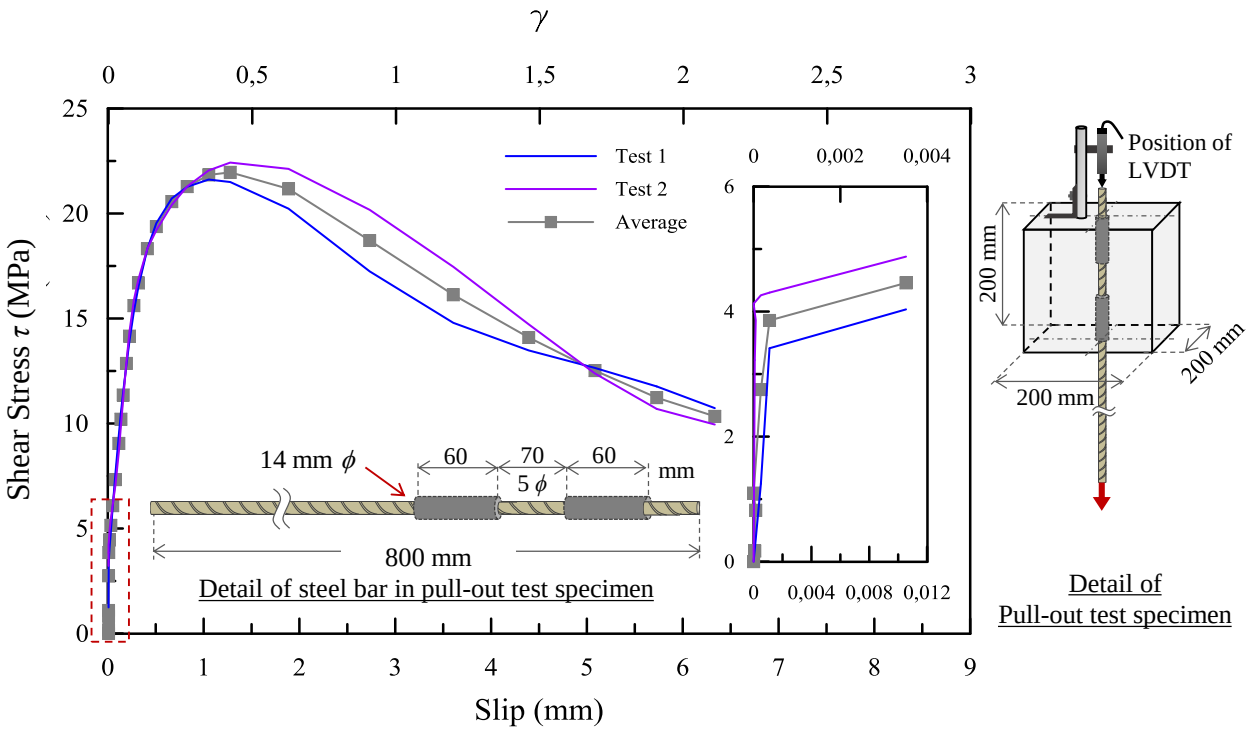

Figure 3. 2. Pull-out test: experimental results and details of the specimen for RC beam with a rectangular section.

3. 3. Experimental Campaign

The experimental works performed within the context of this study is a four-point flexural test in an RC beam with a rectangular section. A special attention is devoted to the pure bending area between the two points of loading.

3. 3. 1. Detail of experiment

Detail and configuration of RC beam dimensions and steel bar reinforcement are presented in Figure 3.3. After 87 days, a four-point load test was conducted on a rectangular beam with the depth of 28 cm, the thickness of 15 cm, the length of 300 cm that led to an effective span equals to 280 cm. With the capacity of loading up to 20 tonnes, the hydraulic actuator loading application was distributed into two points of loading within 1,2 metre. The apparatus used for this modelling is able to be controlled whether in imposed load or in imposed displacement. Imposed load of 0,10 kN/s was performed at the beginning until it reached 90% of its Ultimate Limit State (ULS). Then, in order not to lose the data, imposed displacement of 0,07 mm/s was applied up to the rupture of the beam. Area of interest for crack observation is located between two points of loading, A and C, in which behaviour of pure bending of RC beam occurred.

Moreover, an LVDT extensometer is employed to measure the displacement in the vertical direction at point B (mid-span of the beam) to be compared to DIC results.

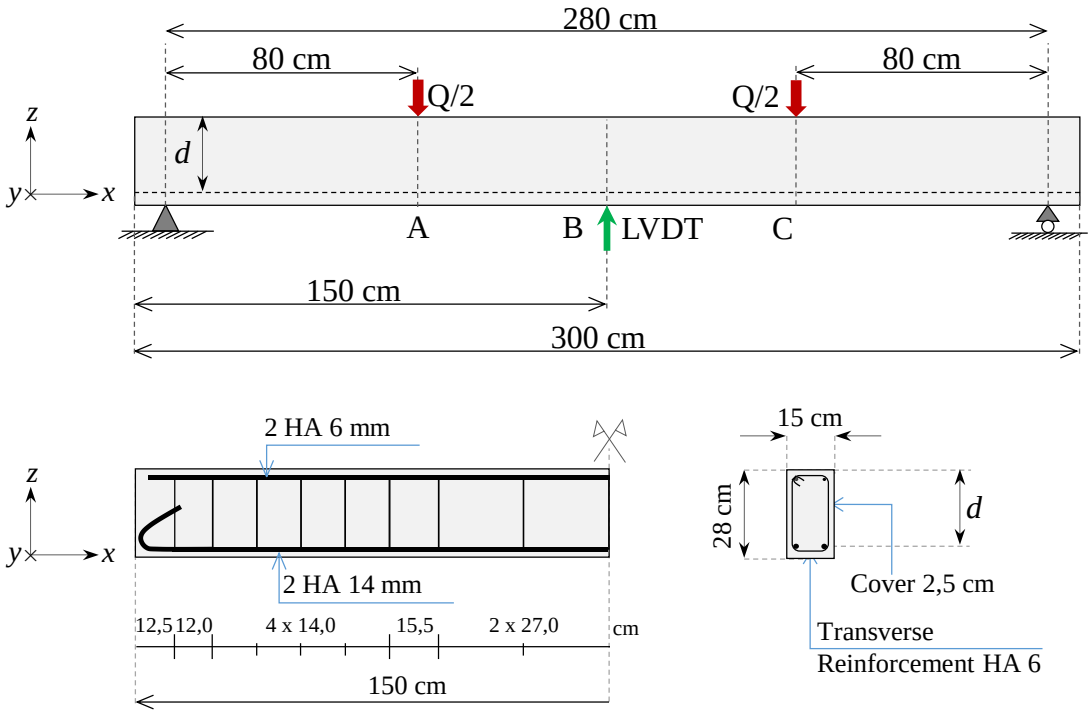

Figure 3. 3. Detail dimensions of RC beam and its loading application.

3. 3. 2. Installation of DIC system

Using the same technique as in Chapter 2, the DIC system was employed to observe the appearance of cracks on the concrete surface. Two cameras integrated into the system were installed to observe the behaviour of the specimen throughout the duration of the test as schematically shown in Figure 3.4(a). In this experimental work, 2432 x 755 pixels photos were taken with a rate of one frame per second using 5,0 MP cameras with 8,0 mm of focal length. Two LED projectors of 50 W were used to adjust the brightness to prevent the variation of the ambient luminous that can disturb the DIC calculation.

As the pure bending zone is the area of interest, two third of RC beam surface was treated as presented in Figure 3.4(a). A black and white speckle pattern is projected onto the sample surface with contrast enhancement for better precision in images processing. The size of the black speckle is 5-11 mm, obtained from the function of the opening of the two cameras' focal length, the dimension of the area of interest, the distance between two cameras, the longest and the closest distance from the camera to the edge of the area of interest (kilonewton Sarl, 2010). The same technique to apply speckle as explained in the previous chapter was used. The complete working condition using DIC in LMDC is presented in Figure 3.4 below.

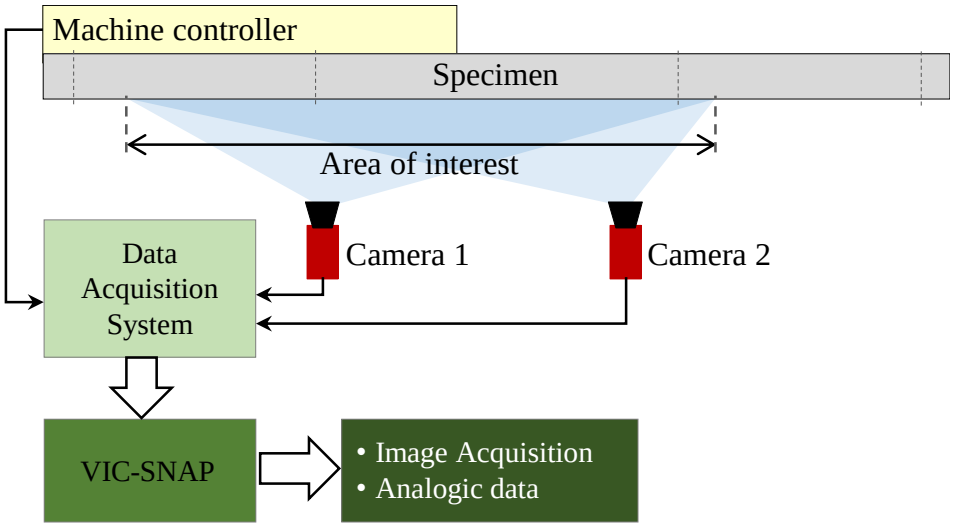

(a) Schema of Digital Image Correlation Technique (seen from above).

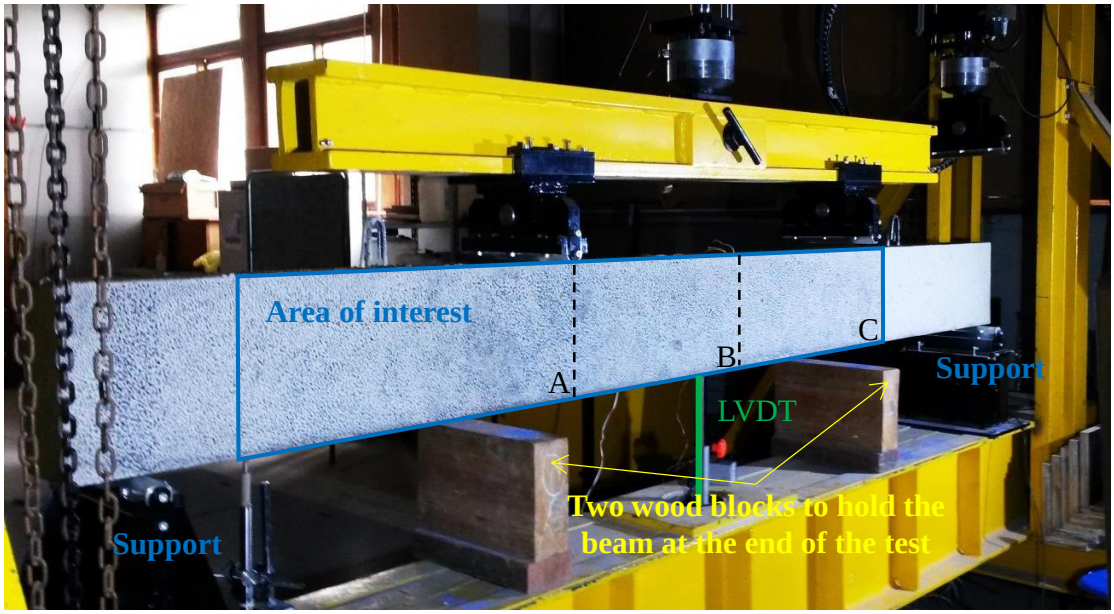

(b) Photo of the specimen.

Figure 3. 4. Installation of RC beam and DIC system in LMDC laboratory.

3. 3. 3. Experimental results

During the post treatment, every zone of interest of the image is segmented into several finite subsets (or sub-images). The chosen size of one subset is 11 mm x 11 mm or 21 x 21pixels in the reference image (2432 x 755 pixels). In other words, one pixel represents approximately 520 µm. Uncertainty in displacement field that determines the error is around 1,7% pixels. Thus, the uncertainty of displacement field is 9 µm.

A. Global Behaviour: Force-Vertical Displacement

To ensure the results from DIC system, global behaviour of RC beam measured by LVDT and DIC are compared in Figure 3.5. Global results from LVDT are presenting the loading application (Force) of the hydraulic jack in a function of vertical displacement (u_z) at the mid-

span of the beam (green arrow). The results from DIC measurement system show the evolution of the lowest point of the bottom part in the mid-span. Both measurement systems show the same results. So, DIC was able to reproduce the same measurement in vertical displacement. In the next part, DIC system is used to observe the cracks.

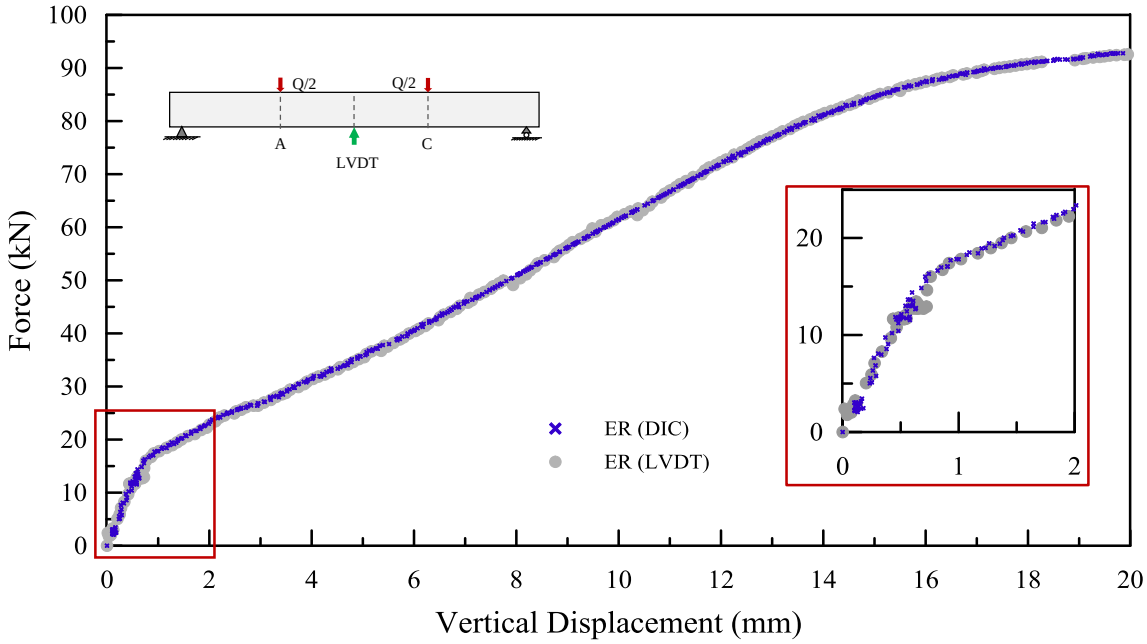

Figure 3. 5. Global behaviour, the evolution of force-vertical displacement *Uz* at mid-span of RC beam measured by LVDT extensometer and DIC.

B. Cracking pattern and opening

Our interest is to measure the crack opening and to observe the crack pattern on the displacements fields reproduced from DIC technique at each loading time. Indeed, cracks propagated vertically in the beam (*z*-direction). So, their respective opening is defined along the horizontal direction of the beam (*x*-direction). Figure 3.6 (a) shows how to extract the crack width from the displacement field in the area between A and B. The jump value in the displacement field shows the evidence of a discontinuity (crack).

The sketch of the beam with the measurement point using LVDT and the position of loading points is superposed with the displacement field (U_x) from DIC (see Figure 3.6 (b)). The observation area of DIC is shown as bordered by two red dash-lines. This figure shows stair-stepped shape of colour gradation in the displacement field on the studied surface. The choice of the vertical position is at *d* that represents the distance from the upper edge of the beam to the centre of gravity of the longitudinal steel bar reinforcement HA14 (see Figure 3.3.). The extraction result shows the stair-stepped shape curve that defines the crack width (*w*) by using the same method used in Chapter 2. As we can see from the image, along with this dash line there are some colour gradations ranging from 0 to -3 mm. Another way to identify visually the

location of cracks more easily is using the deformation field as shown in Figure 3.7 and 3.8.

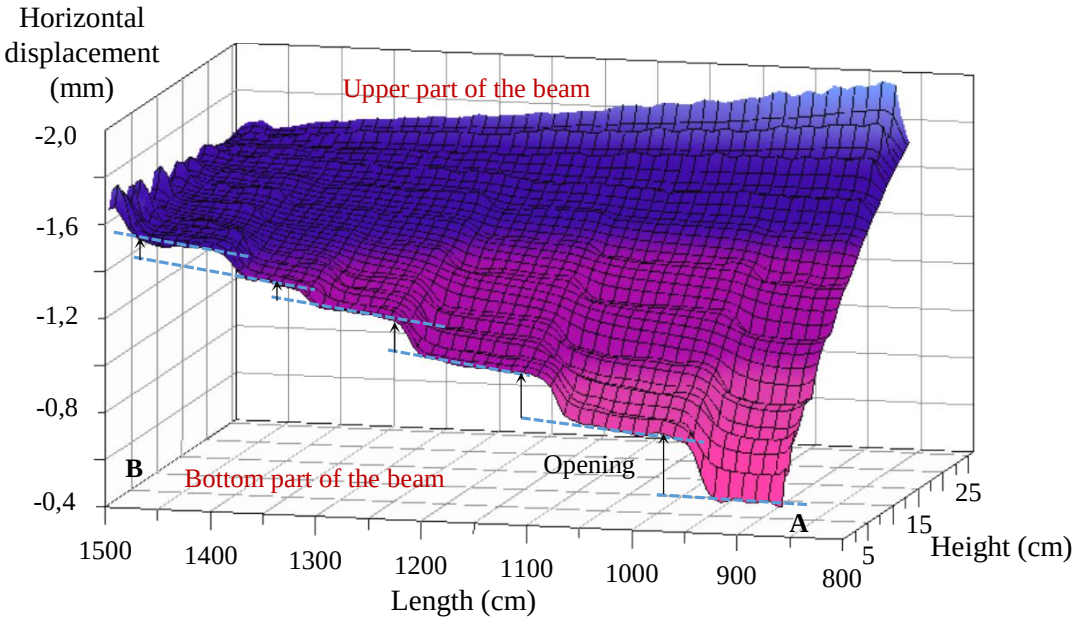

(a) Extraction of the crack width on the surface between A and B.

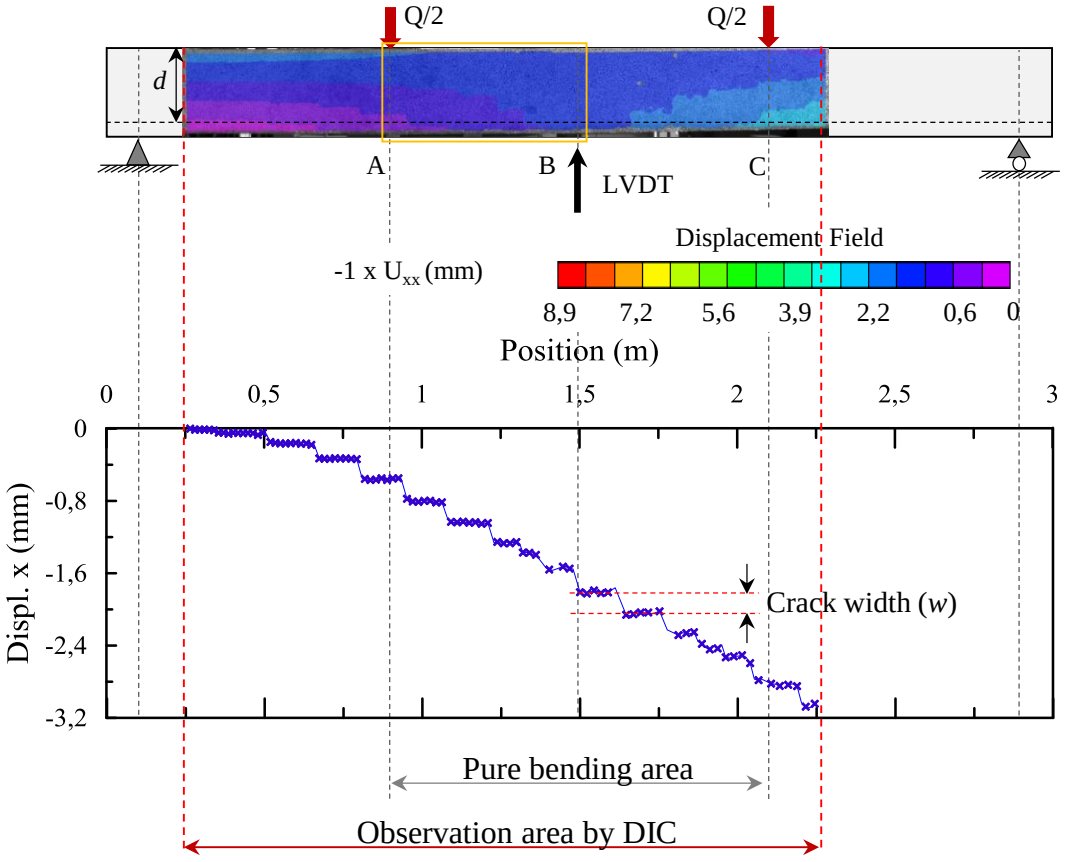

(b) Extraction at level *d* from the upper part of the beam.

Figure 3. 6. Extraction of crack opening on displacement field in the *x*-direction at 50,5 kN.

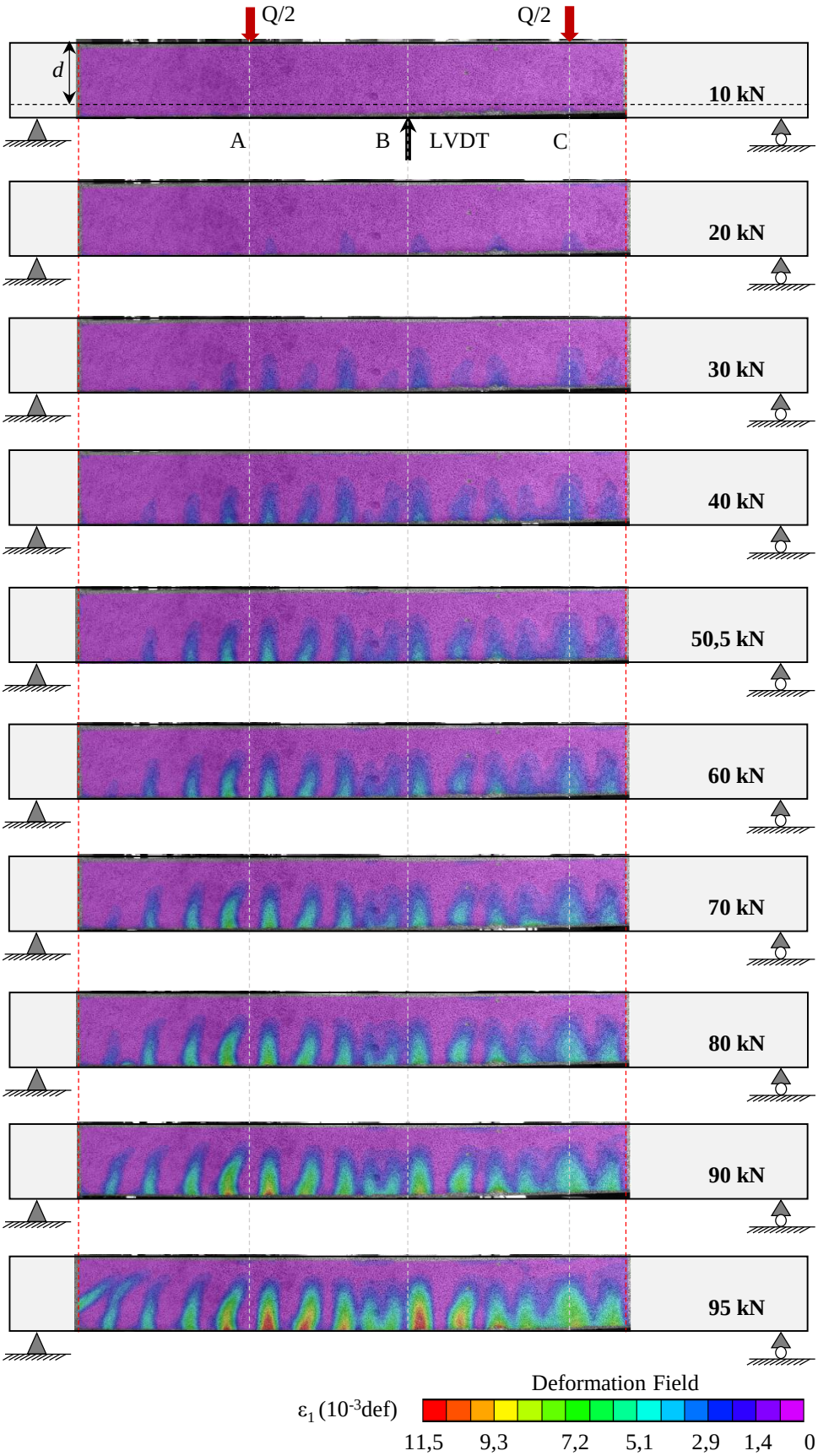

Figure 3. 7. Experimental results (DIC): evolution of cracking pattern observed on deformation field in major direction (ε_1).

In Figure 3.7, the evolution of crack is displayed using the deformation field in major principal direction ε_1. Even if the deformation field around a crack has none physical meaning, since the crack displacement is localised, it is convenient to use it as a crack position indicator. The amplitude of the deformation plotted by Vic-3D around a given crack results from the DIC algorithm which built a "non-local" strain field corresponding schematically to the speckle's displacement divided by the distance between two speckles. Purple colour means the area with deformation relatively small or tends to zero.

In Figure 3.8, the evolution of crack opening is presented in µm with the strain field at 50,5 kN. Crack observation is presented in eight different stages of forces: 20 kN, 30 kN, 40 kN, 50,5 kN, 60 kN, 70 kN, 80 kN and 90 kN. For each corresponding cracks, their width and their position are shown. The stabilised cracks were opened wider in a function of force. At 60 kN of force, some small cracks spread again at the bottom part of the beam. As soon as the cracks get stabilised, the width is growing.

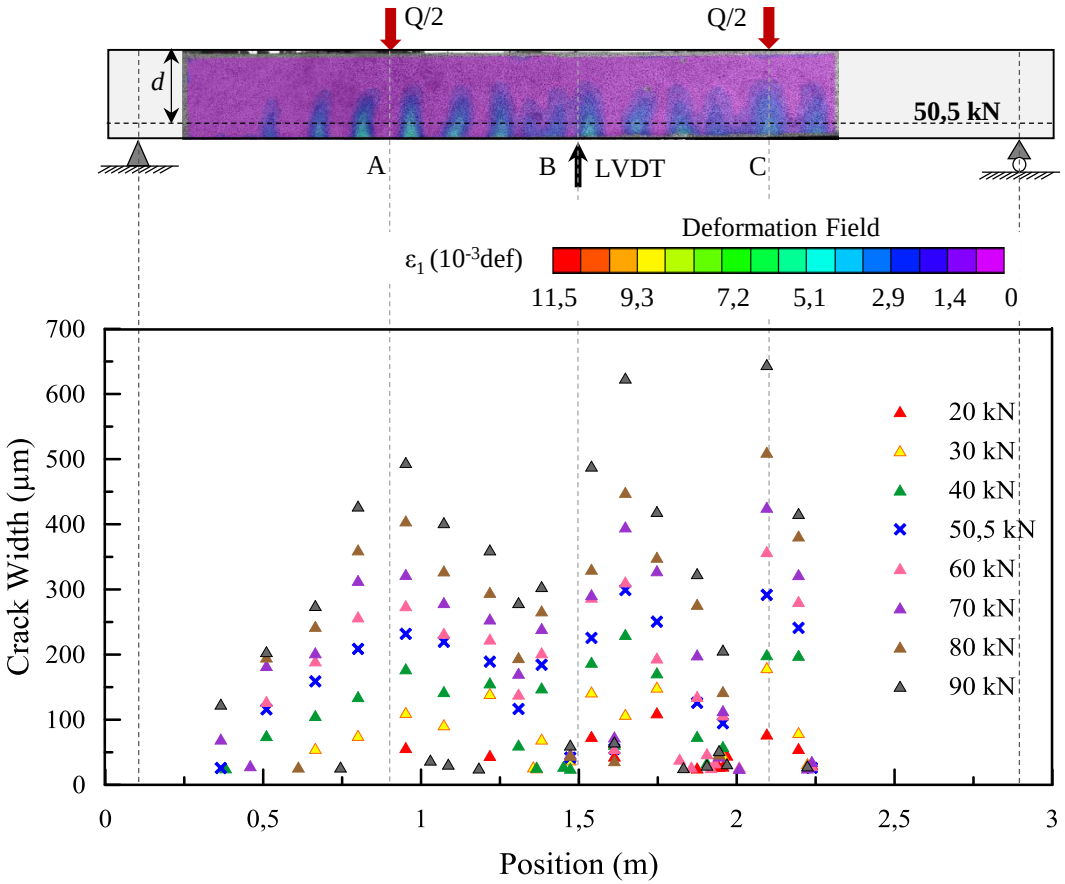

Figure 3. 8. Experimental Results (DIC): deformation field (direction ε_1) at 50,5 kN and the evolution of crack opening (*x*-direction) up to 90 kN.

To be noted, the experimental results show an unsymmetrical crack pattern for the right and the left side of the mid-span since it has different support as presented in the figure. On the left, pinned support was employed whilst on the other side, roller support was used. So, the beam can move to the right.

At a distance of 1,6 metre from the left, the maximum crack opening occurred (299 µm) when the force was 50,5 kN. This point (50,5 kN) then will be used to compare the numerical modelling results in the following sub-chapters. According to Eurocode 2, 300 µm is the maximum crack opening for structure element with exposure classes XC2, XC3 and XC4 (exposure to air and moisture) under the action of the quasi-permanent load combination of SLS (Eurocode 2, 2005; Mosley et al., 2007).

3. 4. Numerical Modelling Campaign on RC Beam with a rectangular section

The numerical simulations carried out within the context of this study were made by using the Finite Element code CAST3M (CEA, 2015). The geometry of the RC beam modelling is presented in detail as the first step. Then, secondly, the three behaviour laws used in the model are presented. Those are the behaviour law of plain concrete, steel bar reinforcement and steel-concrete interface elements.

3. 4. 1. Detail of geometry and boundary conditions

In the real condition (see Figure 3.3), reinforcements were attached one to another using fine wire (ligature). In this numerical work, the volumetric sliding interface will be meshed around each steel bar. The round shape geometrical condition is not easy to be configured and to be meshed numerically. So, equivalent area method is used to model the steel bar in a square shape. This method really facilitated the meshing process. By using the same area (circle with ϕ_n of diameter), we obtain the dimension for "square" reinforcement as shown in Figure 3.9 (b) below.

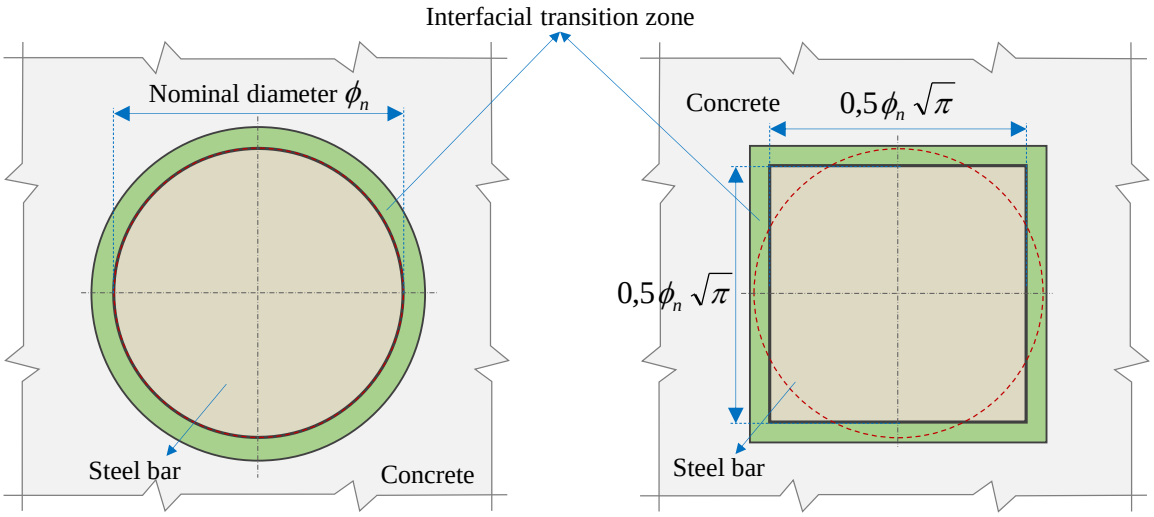

(a) Proposed model to represent the steel-concrete bond. (b) Equivalent area method application on bars.

Figure 3. 9. Application of equivalent area method on the steel bar reinforcement.

The detail of the finite element mesh configuration for the numerical simulations is presented in Figure 3.10. Taking advantage of the two axes of symmetry, only a quarter of the specimen

was discretized with CUB8 elements (cubical solid element with 8 nodes). In Figure 3.10 (a), the transverse reinforcements are modelled fully. To represent a simple beam, a surface at the mid-span (plane of symmetry 1) is blocked in the *x*-direction, and a support is used to block in *y*- and *z*-directions. So, it allows a movement in the *x*-direction on the support. Another plane of symmetry is blocked in the *y*-direction to represent symmetrical condition.

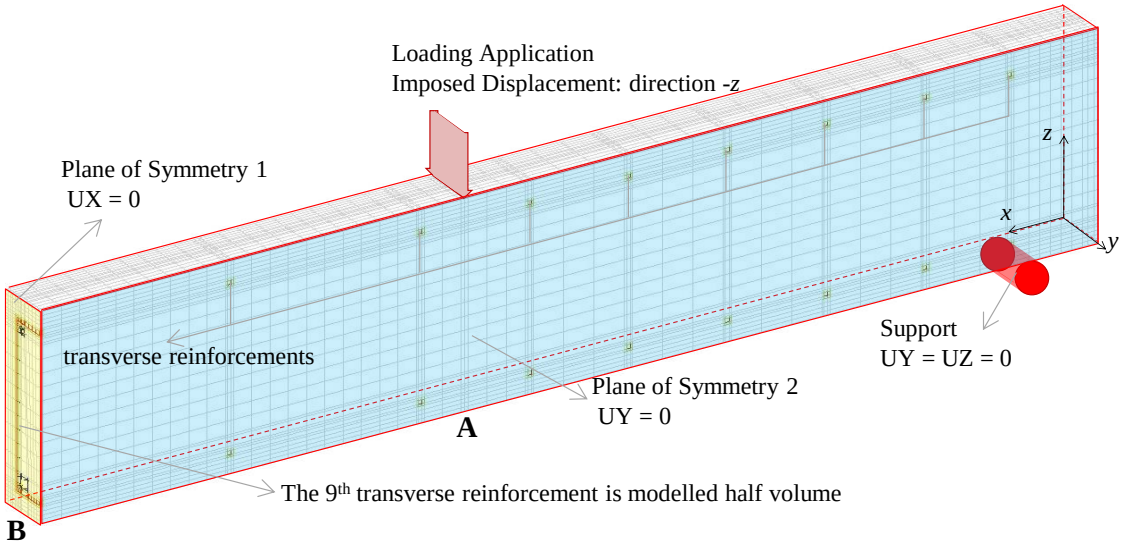

(a) Detail of one-quarter volume of RC beam. A-B indicates the pure bending area.

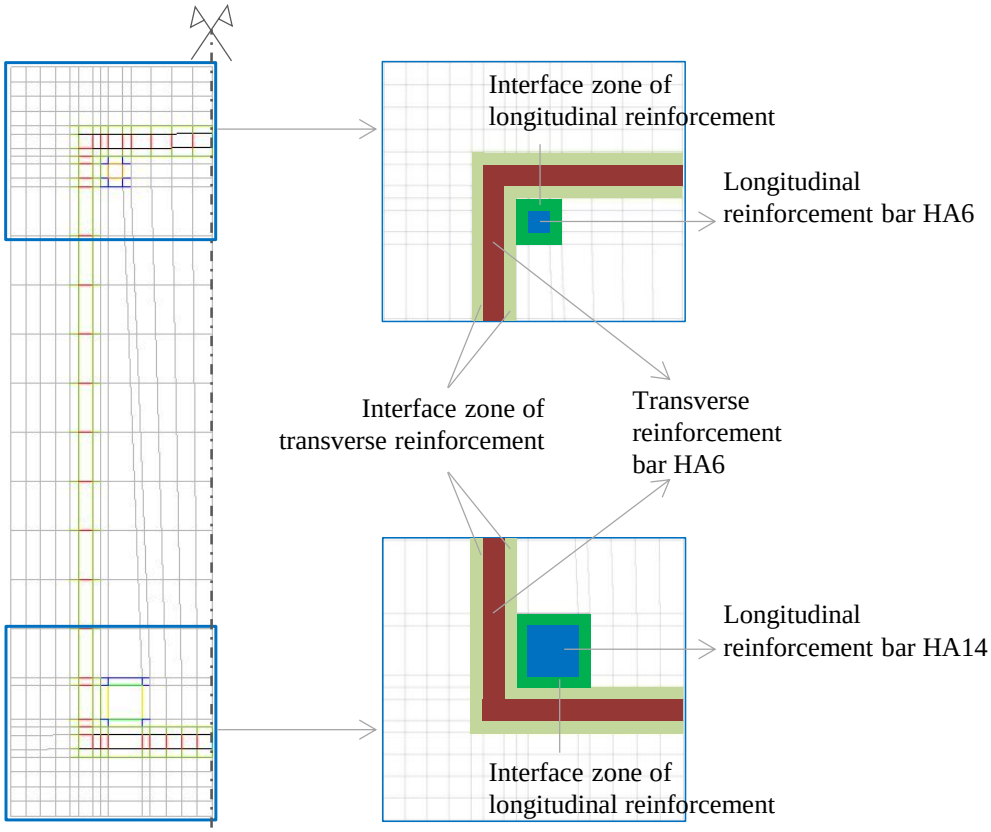

(b). Detail of a half rectangular section.

Figure 3. 10. Mesh and boundary conditions for numerical modelling (one-quarter of specimen's volume).

All the configuration of reinforcement bars is considered in detail. As described in Figure

3.10 (b), interface zone is meshed around the entire steel bar used in this RC beam. It means that not only the longitudinal bars (HA 6 and HA 14) but also the transverse reinforcements (HA 6) are surrounded by this interfacial zone. All interface zones were meshed with 3 mm of the thickness. Loading application was also located at the exact same point as in the experimental works and was applied in imposed displacement in the direction -*z*.

It was proven in the previous chapter that the modelling using interfacial transition zone is independent of the size mesh. So, as it is considered more important in pure bending area, in the A-B area along the *x*-direction (see Figure 3.10 (a)), one element has 2,7 cm of width. In the *yz*-plan, the mesh size is sufficiently finer following the size of the interface element and the steel bar that are meshed only with one layer.

3. 4. 2. Behaviour Law

As mentioned before, the plastic sliding connection between the concrete and the steel bar is used. So, there are three behaviour laws in this RC beam modelling: behaviour law of concrete, behaviour law of steel bar and behaviour law of interface zone as mentioned in Table 3.4.

Table 3. 4. List of behaviour law for each material in two types of model.

Model / Elements	Sliding Interface (SI)
Plain concrete	Plain concrete LMDC model
Steel bar	Steel bar elasto-plastic model
Interface Zone	Elasto-plastic interface zone

C. Behaviour Law of Plain Concrete

The behaviour of plain concrete is modelled by the LMDC concrete damage model. The parameters used in this numerical simulation are already presented in Table 3.5 whilst its behaviour under cyclic loading is presented in Figure 3.11. The behaviour of LMDC model in this figure may be slightly different to the one that was explained in Chapter 1 due to the fitting of concrete's parameters.

Table 3. 5. List of parameters of concrete materials to be used in modelling using the LMDC Model.

Parameters	Symbol	Value	Unit
Young's Modulus of elasticity	E	35620	MPa
Poisson's ratio	υ	0,27	-
Density	ρ	2400	kg/m^3
Concrete tensile strength supplied by split test (Brazilian test)	R_t	3,68	MPa
Strain at peak tension	$\varepsilon_{R_t}^{pk}$	$1{,}23\times10^{-4}$	-
Concrete compressive strength	R_c	51	MPa
Strain at peak uniaxial compression	$\varepsilon_{R_c}^{pk}$	$2{,}0\times10^{-3}$	-
Drucker Prager Confinement coefficient	δ	0,75	-
Dilatancy for non-associated Drucker-Prager plastic flow	β	0,28	-
Characteristic plastic strain for Drucker-Prager associated damage	$\varepsilon^{k,s}$	$8{,}0\times10^{-4}$	-
Fracture energy in tension	G_t^f	124,5	J/m^2

Van Genuchten modulus	M_{shr}	40	MPa
Van Genuchten exponent	m_{vg}	0,5	-

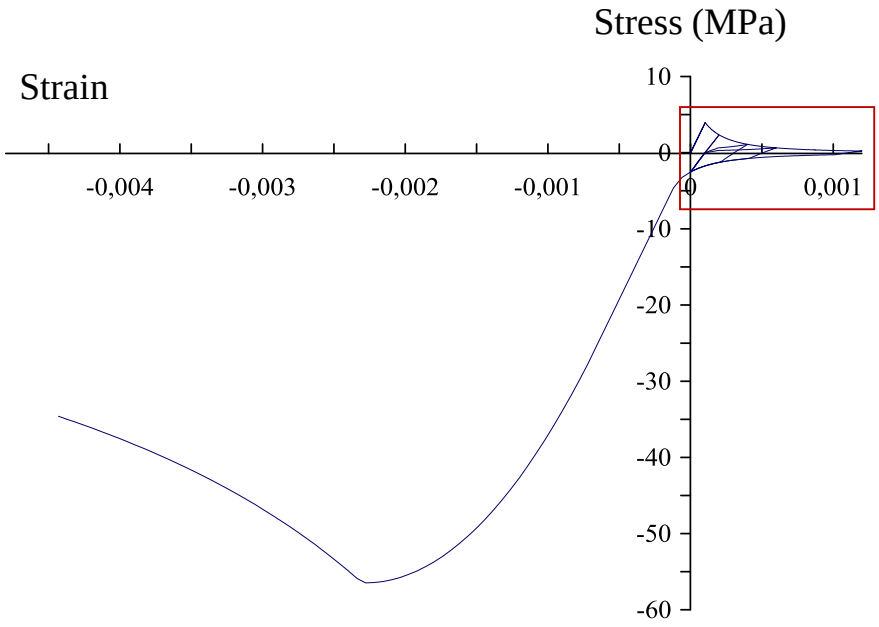

(a) Response under cyclic tension and compression loading.

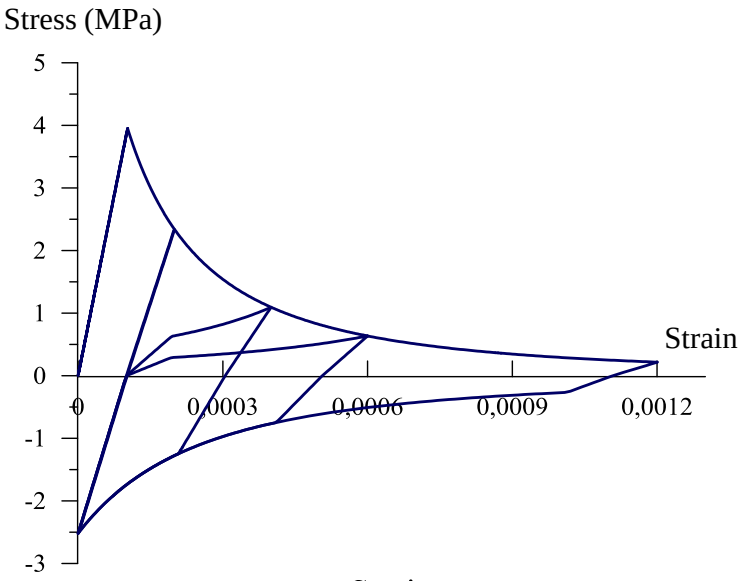

(b) Response under cyclic tension loading.

Figure 3. 11. LMDC model: Stress-strain curve responses under cyclic loading.

D. Behaviour Law of Plastic Sliding Interface

The interface zone thickness was set to 3 mm as explained in Part 2.3.3 C. The same method developed in the previous chapter is applied to obtain the behaviour of the interfacial transition zone. The formula of Equations (2.4) and (2.5) in Chapter 2 were applied to the pull-out test results in Figure 3.2 to obtain the equivalent stress-deformation used as the hardening law of the

plastic model in the interface zone presented in Figure 3.12. Using the same correction, the interfacial zone has around 74% of the concrete modulus. This equivalent stress-deformation regulates the interfacial zone. The model is fitted up to 3,7 mm of slip. Regarding the application of the equivalent model from Eligehausen (Eligehausen et al., 1983) to the experimental results, the same tendency can be obtained. The continuing behaviour beyond 3,7 mm of slip is constant. Eligehausen's model results show the similarities at some points before the peak or the plastic sliding. It can be noted that the Eligehausen's model has some difficulties in capturing the post-peak behaviour (overestimation occurs). Also, in the beginning, Eligehausen's model leads to nonlinearities faster than the model from experimental works (see zoomed part in Figure 3.12).

Table 3. 6. List of parameters used in the interfacial transition zone.

Parameters	Symbol	Value	Unit
Young's Modulus of elasticity	E	26100	MPa
Poisson's ratio	υ	0	-
Thickness	e_{iz}	3	mm

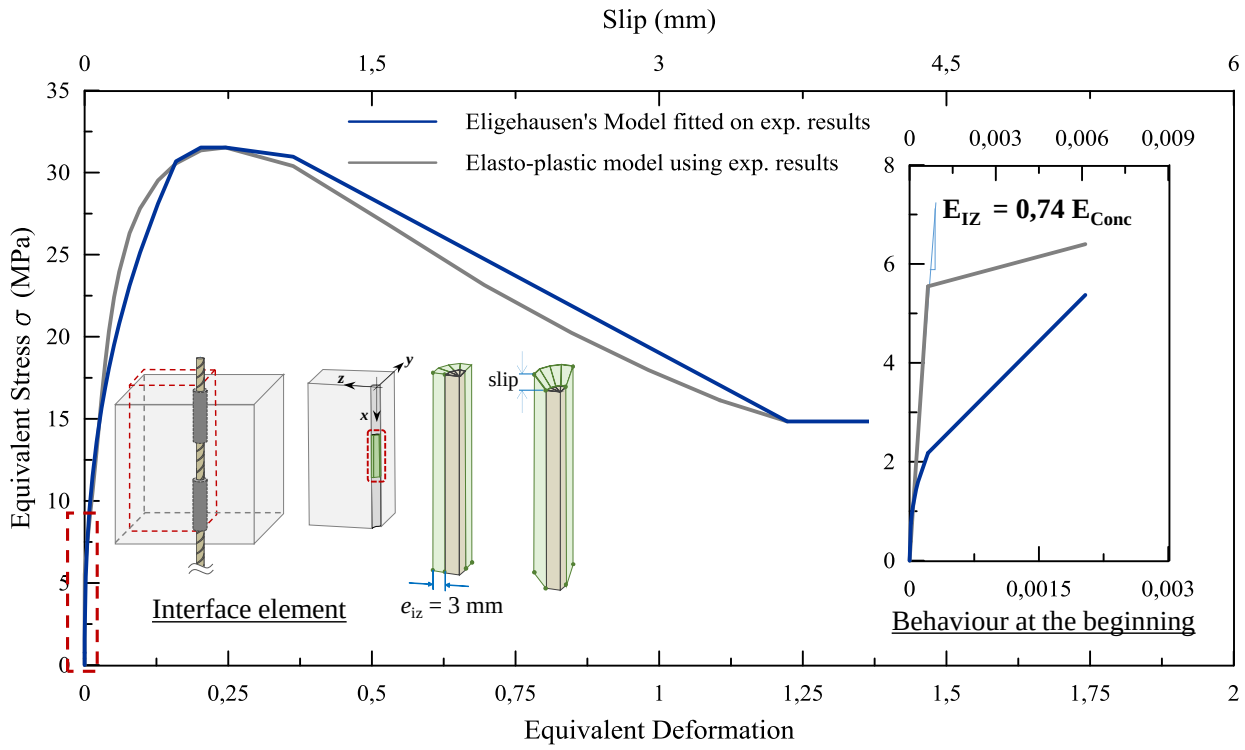

Figure 3. 12. Behaviour law interface zone fitted with pull-out experimental results.

3. 5. Numerical Modelling 1: PI and SI comparisons

In this first step of modelling, a solid layer is meshed volumetrically to represent the interfacial transition zone as described in Chapter 2. This zone is regulated by the elastoplastic behaviour law as presented in Section 3.4.2.C.

3. 5. 1. Detail of numerical simulation

As examined in the previous chapter, there are also two kinds of modelling in this section, *Perfect Interface* (PI) model and *Sliding Interface* (SI) model. In the PI model, only two materials are considered: concrete and steel bar while in the SI model, the third material called interfacial transition zone is employed and is governed by the plastic sliding behaviour law presented before. This numerical simulation was conducted in imposed displacement up to 22 mm. Up to 1,2 mm of the displacement, the measurement was performed denser than thereafter in order to observe clearly the initial stiffness.

3. 5. 2. Modelling results: Global behaviour

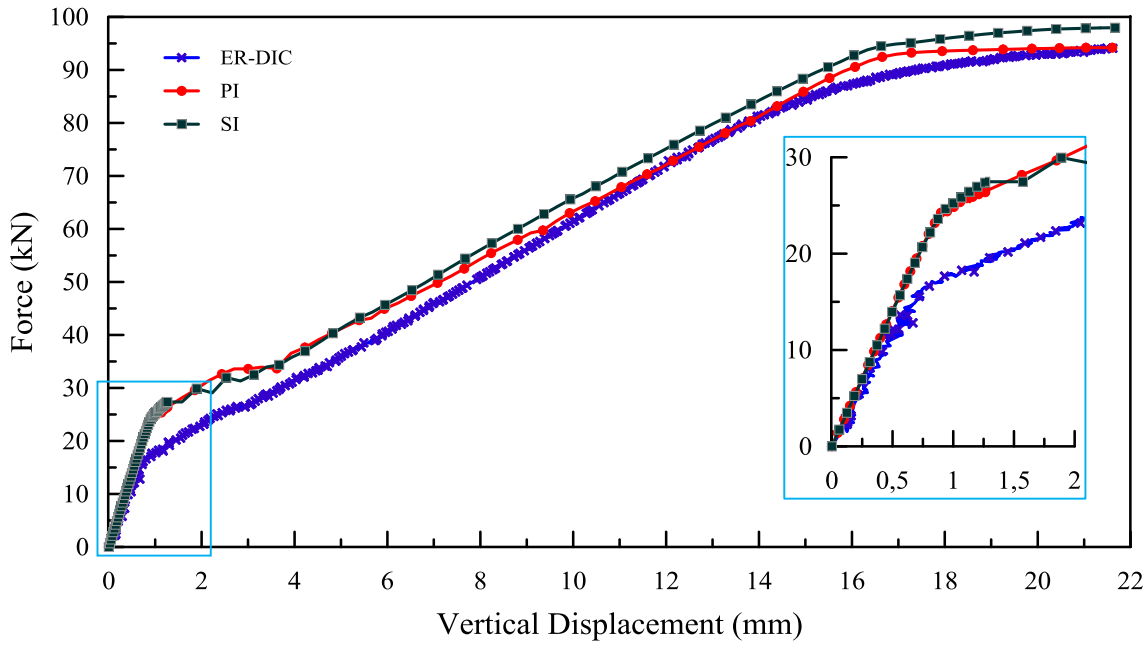

Figure 3. 13. Global behaviour: Experimental (ER-DIC), Modelling PI (Perfect Interface, without sliding) and SI (Sliding Interface) results.

Figure 3.13 shows the global behaviour of experimental and modelling results. Both modelling PI and SI are able to simulate the experimental global behaviour. The PI results are presented in a red curve whilst the SI ones are presented in a black curve. At the beginning, both PI and SI cases do not have the same stiffness comparing with the experimental results. A simple elastic calculation with the same geometric and boundary condition was performed, and it showed the same results, always an overestimation of initial stiffness by the models (whatever the interface condition).

The first crack localisation appeared at around 25 kN for PI and SI model while experimentally cracks appeared earlier at 17 kN. Numerically, almost 1,5 times of the experimental results to start this propagation. Reaching 45 kN of loading force application, both PI and SI model have approximately the same tendency. Beyond this point, PI model is less strong than SI model. At 70 kN, PI model reaches the same value displacement as the experiment.

Despite employing the behaviour law of plastic sliding in interfacial zone, using the exact material properties obtained from experimental results in the laboratory, a detailed modelling (geometric, boundary condition, etc.) using solid element in Finite Element Method, the good correlation of the initial elastic stiffness of load-vertical displacement at the beam mid-span was never reached. In this case, a significant overestimation of the first crack propagation occurred for 8 kN of difference. This same tendency also arrived in other works performed by (Jason et al., 2013; Michou et al., 2014). Further behaviour shows an overestimation of force, which means, it needs higher force to attain a certain value of displacement, the modelled structure resisted better than the actual one. Regarding this condition, the problem comes from the materials properties that are applied in the numerical simulation.

3. 5. 3. Modelling results: Cracking pattern and opening

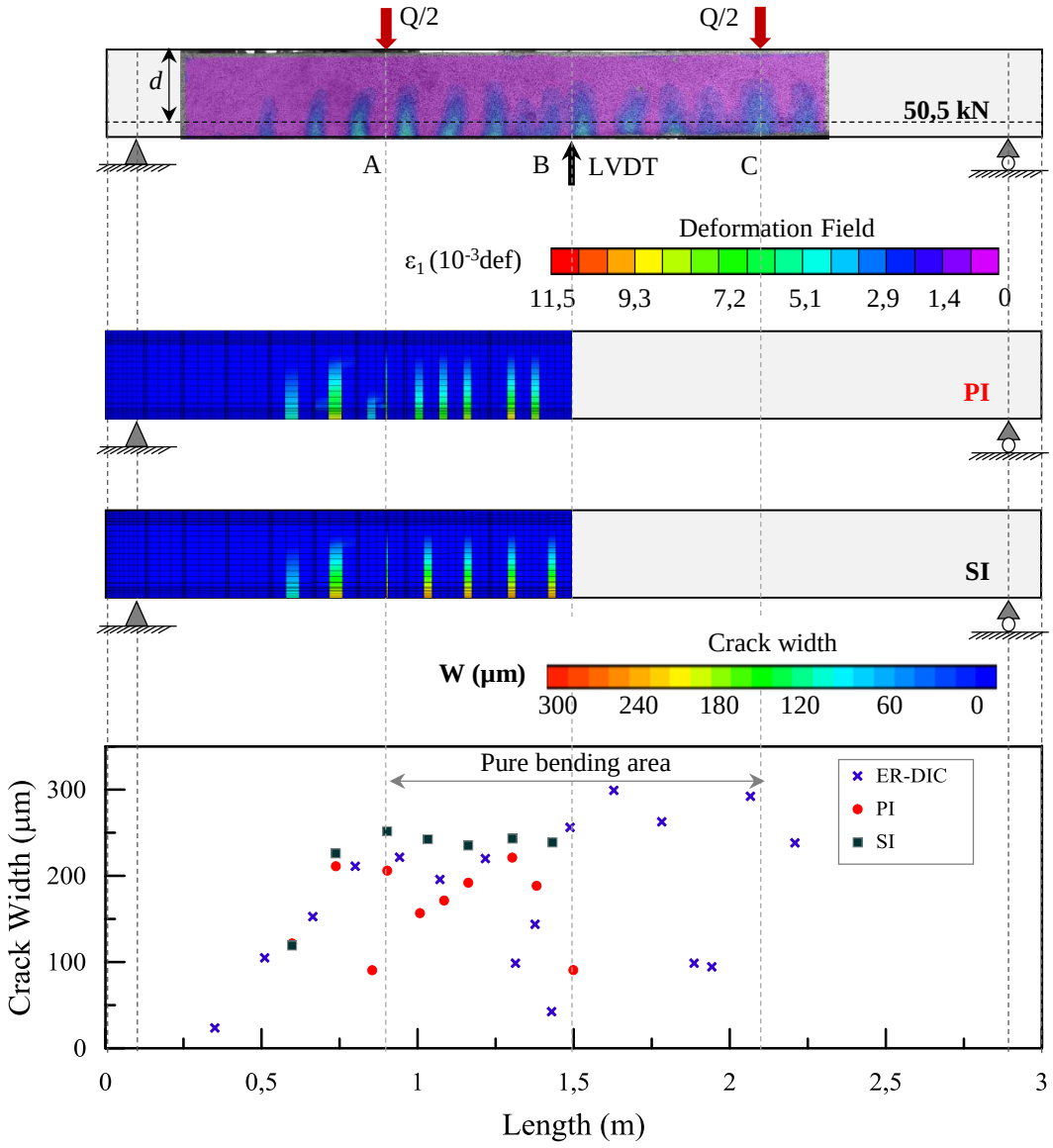

Figure 3. 14. Cracking pattern and opening at 50,5 kN: Experimental (ER-DIC), Modelling PI (Perfect Interface, without sliding) and SI (Sliding Interface) results.

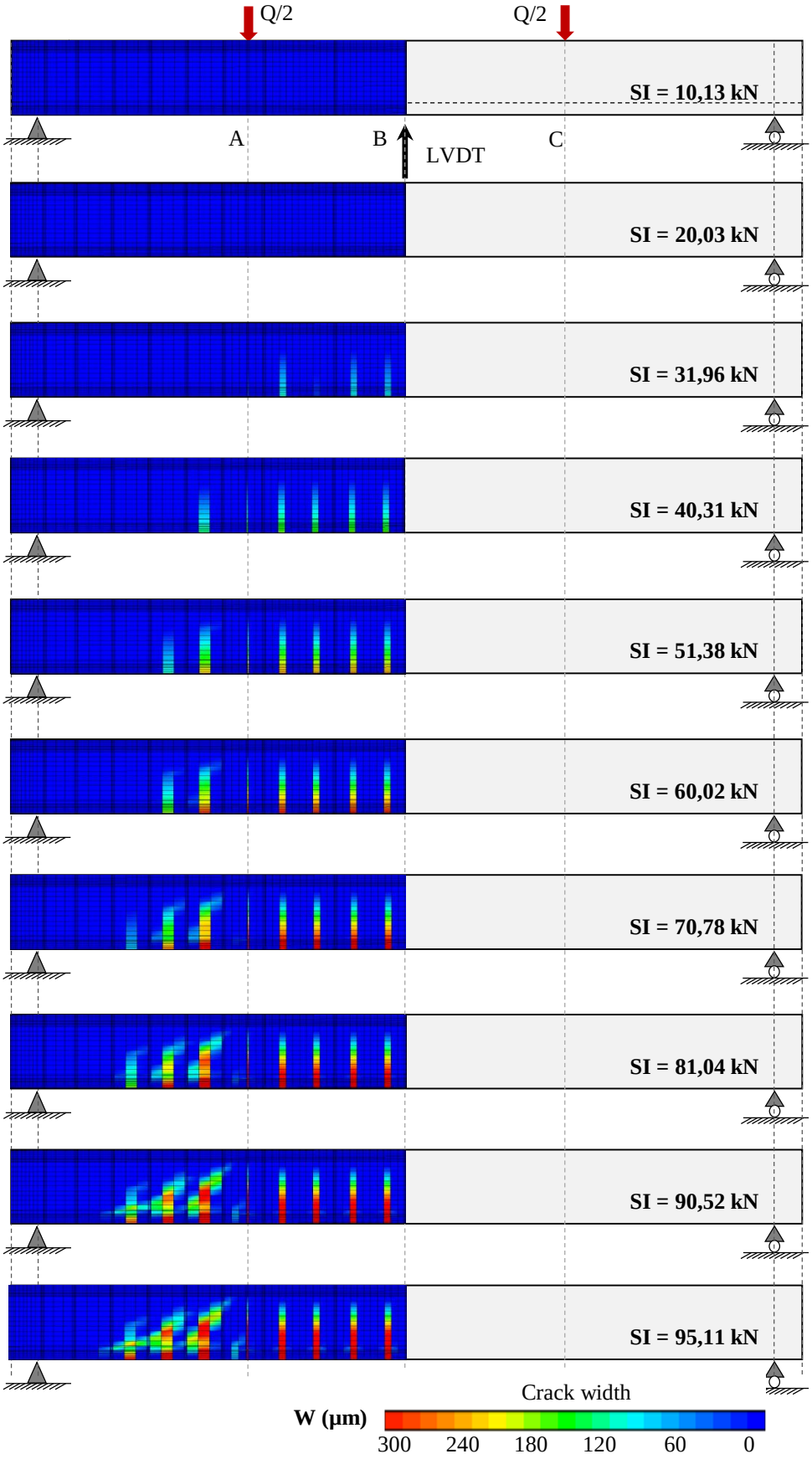

Figure 3. 15. SI (Sliding Interface) results for the evolution of the cracking pattern blocked in 300 µm of crack opening.

The obtained crack opening from these simulations at 50,5 kN of loading are compared to the experimental results in Figure 3.14. To remind, this point is chosen because the maximum crack opening on concrete surface reached 299 µm experimentally. The crack opening is measured at a height *d*, the distance from upper beam to the centre of gravity of longitudinal steel bar HA 14 for experimental and modelling results.

Numerically, in the pure bending area, PI model has six cracks and SI model has five cracks. SI model result had approximately 252 µm of the maximum crack opening under the loading point while PI model 221 µm at 1,3 meter from the left (See Figure 3.14). Experimentally, the maximum crack opening of RC beam was observed at 1,6 m from the left support. So, the introduction of the sliding interface model to RC modelling has a tendency to make a larger crack opening than the one with the perfect interface, conforming to the conclusion in Chapter 2.

The evolution of cracking patterns from SI modelling is shown in Figure 3.15 for every 10 kN, in which, cracks started to propagate at 30 kN. Three big cracks and one small crack appeared on the pure bending area. Then, small crack propagated at 40,31 kN under the loading point application. These cracks are considered as bending cracks and they were growing along with the loading. At around 60 kN, the bending-shear crack started to appear, with an inclined crack appear beyond the pure bending area. At the end of the test, the bending-shear cracks were merged. In reality, this merging condition was proven as the spalling off the concrete cover.

Although modelling step 1 reached the crack opening adequately (48 µm of difference), the global behaviour shows different results in its stiffness including a very significant difference of the first crack localisation (8 kN). It is confirmed in Figures 3.7 and 3.15 that the experimental crack initiations appeared faster than the simulated one (SI).

Later on, two other aspects are taken into account and the calculation will only be conducted using sliding interface (SI) model. Pre-damage due to shrinkage phenomenon and scale effect representing the variation of mechanical properties in the concrete volume are taken into account. These two conditions will be considered in RC modelling since they are recommended in (CEOS.fr, 2015) and were employed in (Michou et al., 2015).

3. 6. Numerical Modelling 2: Shrinkage consideration

So, as we can see in Figure 3.13, the initial stiffness is not correct comparing to the experimental results, in this section shrinkage is employed in RC modelling. Consideration of shrinkage in RC modelling was performed by (Michou et al., 2015) that proved better agreement in the obtained initial stiffness for the tensile test of tie beam cases. It was notified in (Gilbert, 2001) that the reduction of stiffness is the main consequence of the shrinkage phenomena in RC structure.

As RC beam was cast in winter 2015 and was exposed to room temperature and humidity, shrinkage occurred during the concrete ageing before loading application. To consider this

phenomenon, an approximation of the shrinkage was taken into account for this second set of simulation. The shrinkage amplitude is applied differently in the cover and in the internal (core) concrete and these rates are fitted to explain the stiffness loss. The state of concrete at the end of this imposed stage of shrinkage is later called *pre-damage*. Detail of shrinkage simulation is described in the following sub-sections. The method imposed shrinkage consists to use the capillary pressure in the framework of poro-mechanics as described in Figure 1.18; the capillary pressure depends on the imposed water saturation degree through Van-Genuchten Equation 1.20 in Part 1.3.2. The parameters M_{shr} and m_{vg} are listed in Table 3.5 as used in (Sellier et al., 2016).

3. 6. 1. Detail of numerical simulation considering shrinkage on concrete

A. Test in a cubic specimen configured as one element

As explained in Chapter 1, water capillary pressure model of Van-Genuchten (Van-Genuchten, 1980) is implanted in the concrete damage LMDC model. Its application in the model for example by simulating the water mass loss virtually in concrete will generate stress in its massive volume. In order to understand, initially, a simple numerical calculation of shrinkage in a cubical specimen with $10\times10\times10\,\mathrm{cm}^3$ of dimension was performed. One area on the bottom was blocked in the vertical direction while another one was set on small displacement and was also blocked during the shrinkage simulation. It was meshed as one element using CUB8 (cubical solid element with 8 nodes).

In the concrete volume, a porosity of 12% is considered. In moist concrete, almost 100% of this void is supposed to be filled with water. The simulation of shrinkage effect on behaviour law was performed by reducing the water content virtually that will induce stresses in concrete volume. For instance, 50 µm/m of imposed shrinkage was applied. This imposed shrinkage strain can be obtained by applying water mass loss using Van-Genuchten's model (Van-Genuchten, 1980) in the poro-mechanics framework. The detail loading application is explained in the next paragraph.

The first step was applying a very small imposed displacement (from zero to 1×10^{-5} mm) to generate a small tensile stress in the concrete. In the second step, 50 µm/m of imposed shrinkage strain was applied during 900 calculation steps. Finally, in the third step, the imposed shrinkage was set to constant and the imposed displacement is set to increase up to 0,1 mm. This loading configuration illustrates the model response under a hydro-mechanical loading.

In Figure 3.16 the response of the material to the combination of shrinkage and mechanical loading is presented. To be clear, these curves are presenting the response only under mechanical loading (displayed in stress-strain curves). The brown curve represents the response to exclusively mechanical loading application, which means, the loading application is performed without shrinkage simulation. On the other hand, the purple one represents the response to the shrinkage and the mechanical loading combination. The maximum stress is 3,67 MPa which corresponds to the concrete tensile strength (R_t). Then, the post-pic behaviour follows the regularisation of fracture energy from Hillerborg (Hillerborg et al., 1976).

As we can see, at the beginning of the mechanical loading, the purple curve has already had an initial tensile stress that was induced by imposed shrinkage in the concrete volume. It means that at the end of the shrinkage simulation, the concrete is already in tension, of course, if a similar phenomenon occurs in the surrounding zone of a beam, the corresponding tensile stress will conduct to damage more quickly than in the condition without shrinkage.

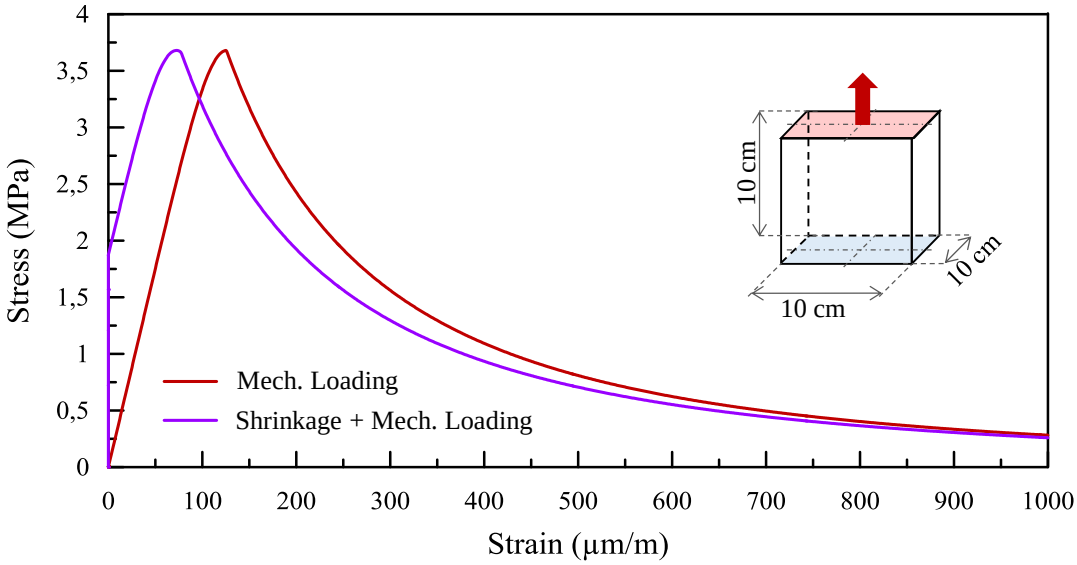

Figure 3. 16. The response of material under shrinkage and mechanical loading in the force-displacement curve: comparison of the pre-dried cube (purple) to the moist cube (brown).

In the interest of comprehending the behaviour during the shrinkage simulation, Figure 3.17 shows the stress-iteration number for both cases. 50 µm/m of imposed shrinkage led to a shrinkage which generated 1,9 MPa of tensile stress in the concrete. Then, under mechanical loading (imposed displacement), the maximum tensile stress was reached faster than without initial drying.

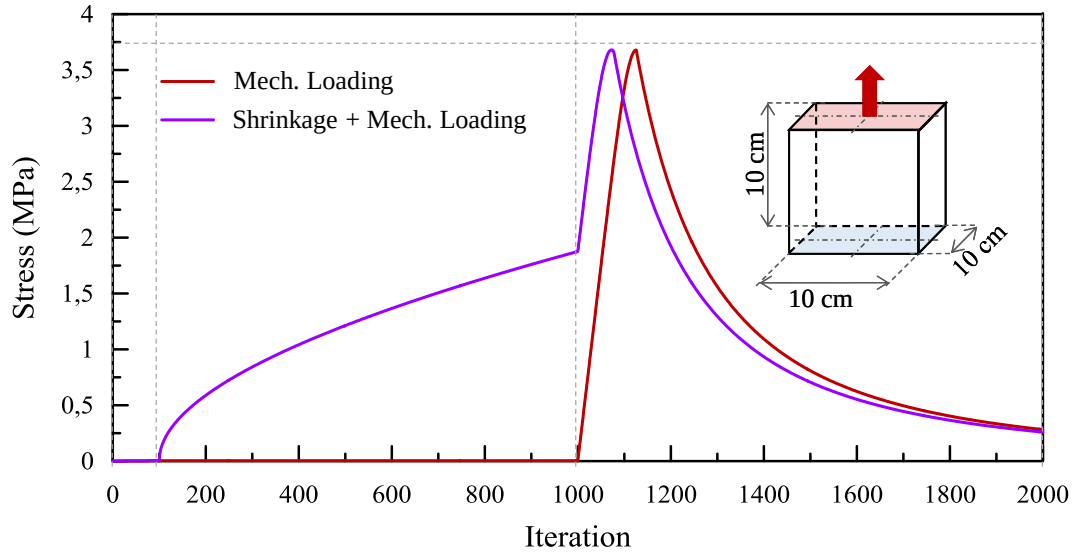

Figure 3. 17. The response of material under shrinkage and mechanical loading in force-iteration number curve: comparison of the pre-dried cube (purple) to the moist cube (brown).

B. Shrinkage test in RC beam

As explained in Chapter 1, there is a gradient profile of hygrometry on a plain concrete specimen subjected to drying shrinkage. Water loss is greatest at the outer surface and it decreases towards the interior. This hydric gradient creates a different deformation in a function of water content. This circumstance creates induced tensile stress on the surface and compressive stress in the internal concrete (Ollivier and Vichot, 2008). These stresses are the results of auto-equilibrium of stress because of the hydric gradient. Moreover, there is a restraining action from steel bar against the shrinking action.

A mass loss numerical simulation could be done with a mass transfer model followed by the mechanical simulation but our objective is simply to find the magnitude order of imposed shrinkage to be able to explain the stiffness reduction observed in the previous section. Therefore, we processed with a simple configuration for which the imposed shrinkage in the concrete is the main fitting parameter. Moreover, to consider the gradient effect in a simplified way, the water mass loss is considered in two homogeneous zones: the cover concrete zone (the concrete outside of the transverse reinforcement) and the concrete inside the transverse reinforcement (hereafter it is called *core concrete*). The cover concrete had direct contact with the atmosphere while inside the transverse reinforcement (hoop), the core concrete was not exposed directly to the environment. In addition, by modelling three-dimensionally, the restraining action induced by the bars and the core concrete will be considered automatically.

After performing inverse analysis to fit the modelling results to the experimental ones, we found the suitable imposed shrinkage strain; the cover concrete and the core concrete were subjected to 350µm/m and 50µm/m of shrinkage successively. In Part 3.6.2, the global behaviour is presented. The first eighty-six days of curing correspond to the first 2064 hours. After that, the imposed displacement is performed up to 24 mm, corresponding to the mechanical test.

As an illustration, the tensile stress field on the concrete volume is given in Figure 3.18 which presents the one-quarter volume of RC beam at the end of the shrinkage stage. Two points of view are presented in order to see the condition at the outer surface and on the inside and for each, the cover concrete, the core concrete and both are presented separately. The core concrete is in compression while the cover one is in tension.

There is a tensile stress concentration in the concrete cover zone reaching 2,21 MPa (see Figure 3.18 (a)). It corresponds to restraint action of the steel bar and of the core concrete. To be noted the arrow that is specified in Figure 3.18 (c) indicates the location of point A (mechanical load) and B (mid-span).

In such way, the interaction of different imposed shrinkage strain in the core and in the cover concrete, the effect of restraining from the reinforcements, and the not fully restrained concrete, all generated a compression state (around -1,5 MPa) in the core concrete and a tension state in the cover concrete (an auto-equilibrium of stress mechanism). The cover concrete is completely under tension except for the end part that has support. In the neighbouring zone to reinforcement, as the concrete shrink, the reinforcement was in compression. The corresponding stress field in the steel bar reinforcement is presented in Figures 3.19 and 3.20. Due to the difference in

section, the HA6 reinforcement is compressed higher (-18 MPa) than the HA14 bar (-16 MPa). In these two reinforcements, at the overlapping point to the transverse reinforcements, the axial stress is smaller than in the rest of the bar. The vertical bar (*z*-direction) in the transverse reinforcement has -16 MPa of axial compression stress. The concrete state after shrinkage effects is qualified as *pre-damage*. Moreover, there was no crack at the end of shrinkage. The behaviour of the beam on the continuing mechanical loading is explained in the next section.

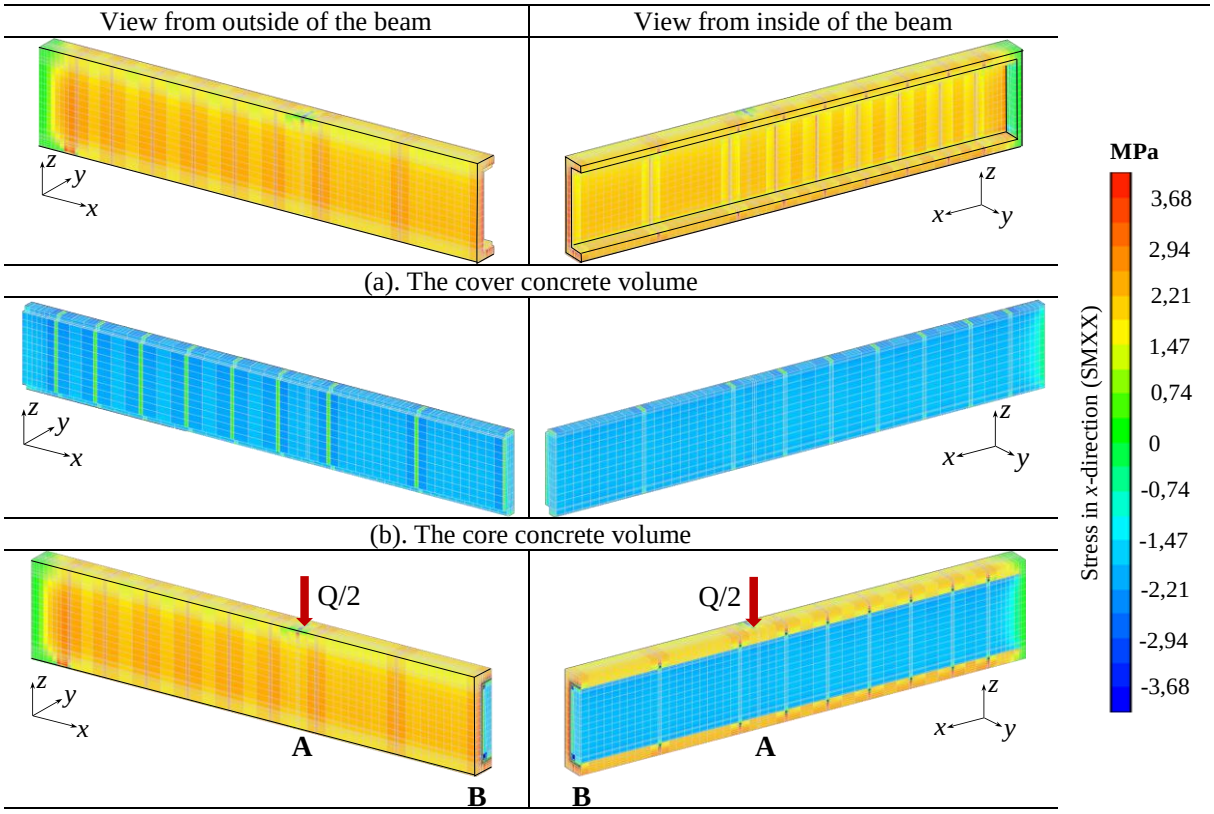

(c). A quarter volume of RC beam

Figure 3. 18. Stress field of concrete volume at the end of shrinkage.

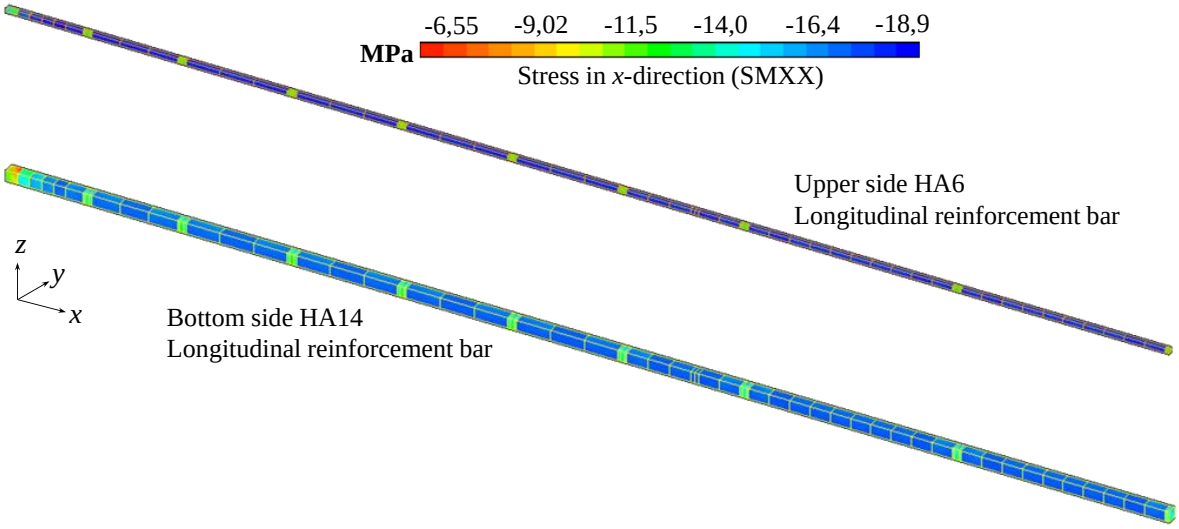

Figure 3. 19. Stress field of longitudinal reinforcement at the end of shrinkage.

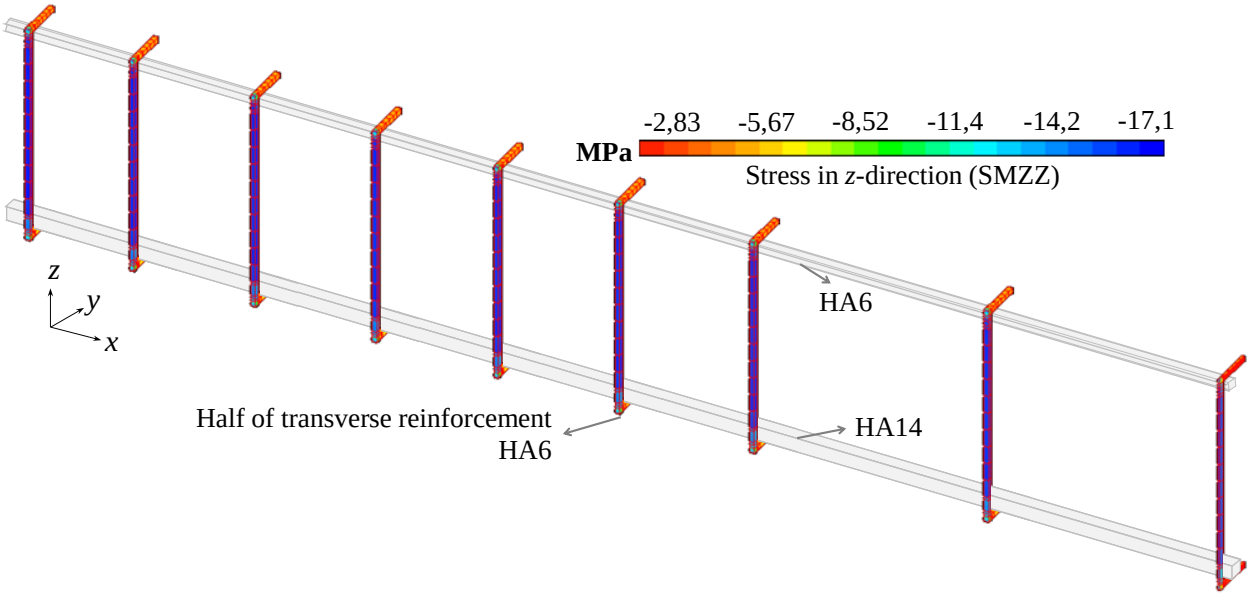

Figure 3. 20. Stress field of transverse reinforcement at the end of shrinkage.

3. 6. 2. Modelling results: Global behaviour

Figure 3.21 shows the global behaviour comparison of modelling with Sliding Interface (SI), SI + shrinkage and the experimental results. A better agreement in the initial rigidity is obtained for the modelling with shrinkage consideration. Clearly, pre-*damage* state due to shrinkage results in a reduction of the initial rigidity of RC structures due to an advanced damage as described in (Gilbert, 2001).

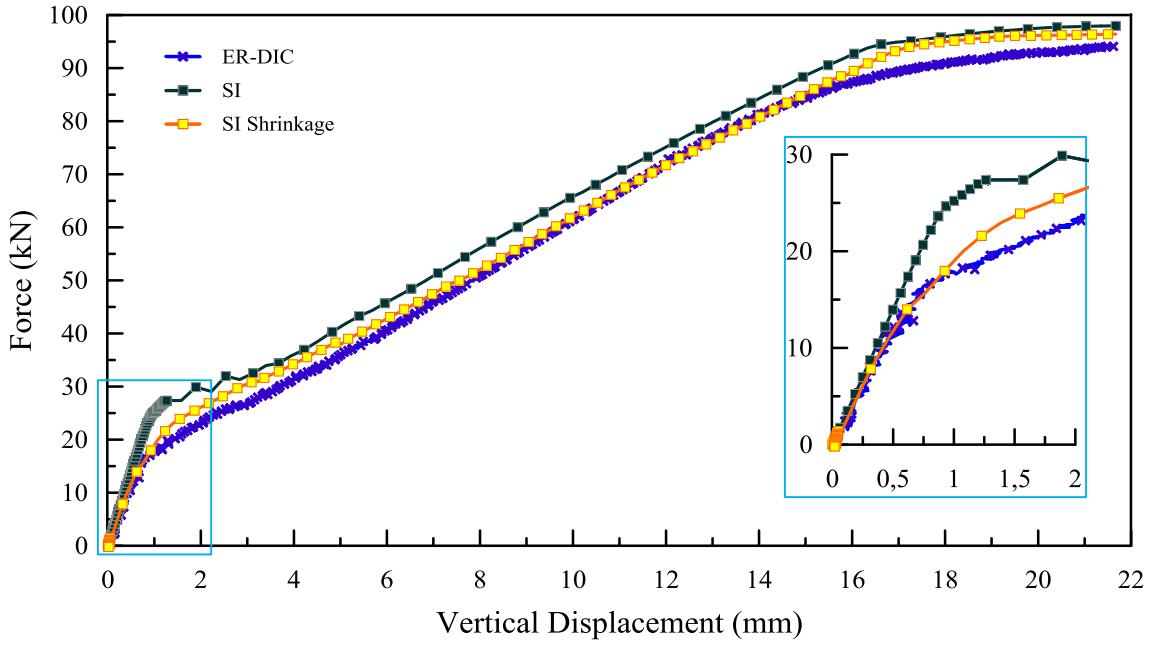

Figure 3. 21. Global behaviour: Experimental (ER-DIC), Modelling SI (Sliding Interface) and SI + Shrinkage results.

To be noted, the shrinkage amplitude in the cover zone has been fitted exactly to match with the experimental initial stiffness of the beam. As a consequence, the first crack localisation can

be reached faster (approximately 18 kN) than the SI results without shrinkage. Nevertheless, overestimation results were still obtained for the first cracking and the further behaviour. On the other hand, the crack opening has different distribution as shown in Figure 3.22.

3. 6. 3. Modelling results: Cracking pattern and opening

Consideration of shrinkage numerically produced more cracks in the pure bending area. Seven cracks are observed and the maximum one is reaching 277 µm, which is larger than the maximum crack in the case of SI model (five cracks with 252 µm of crack width maximum). Observing Figure 3.22, apparently, the cracks mostly appeared beside the transverse reinforcement, also some small cracks propagated on the concrete surface where the transverse reinforcement was installed. As we can see in Figure 3.18, the stress concentration around the stirrups affected the propagation of cracks. So, the shrinkage simulation that produces stresses in the concrete before mechanical loading application works well in generating cracks or damages thereafter.

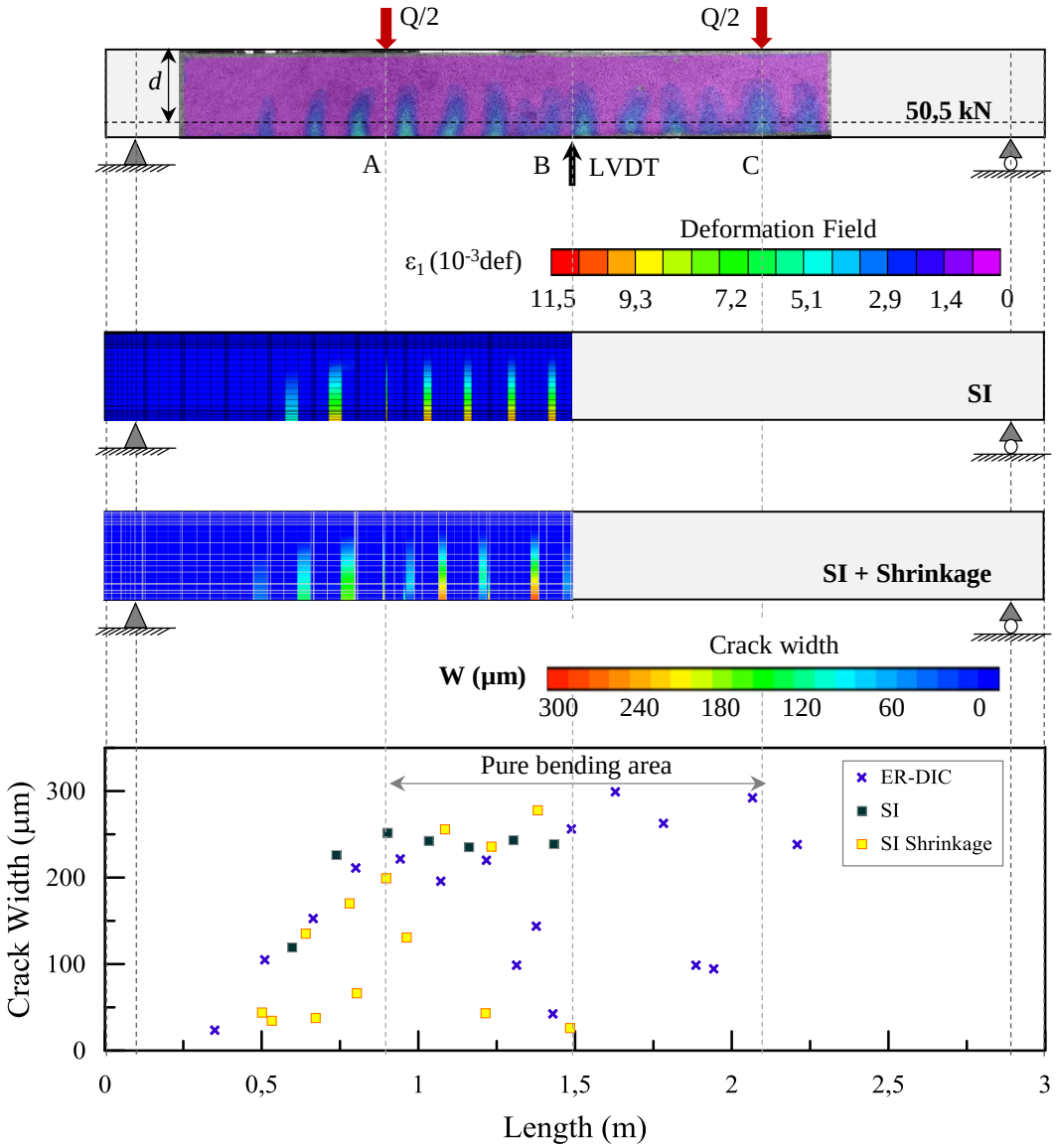

Figure 3. 22. Cracking pattern and opening at 50,5 kN: Experimental (ER-DIC), Modelling SI (Sliding Interface) and SI + Shrinkage results.

So, in this step of numerical modelling, we can obtain a closer behaviour at the beginning (initial stiffness) but the further performance is still considered overestimated. Also, cracks were not opened exactly as they were in the experiment. Apparently, consideration of pre-damage due to shrinkage is able to explain the initial stiffness loss and the crack initiation close to the stirrup but not sufficient to model RC beam accurately during the crack propagation. It might need another aspect to precisely simulate the behaviour.

3. 7. Numerical Modelling 3: Shrinkage and random mechanical properties consideration using TBM

In the previous segment, the shrinkage consideration gave better results for initial stiffness in global behaviour. Nevertheless, the first cracks localisation still arrived a little late than the experimental ones. Also, the continuing behaviour was overestimated. This lack of accuracy in the first localisation of crack and the continuing behaviour might come from the disregards to concrete random nature properties. Random properties of concrete may affect the measured concrete properties in the laboratory, for example, R_t and E_c. Then, numerical application of these measured properties on the entire concrete larger structures will definitely prejudice the first crack localisation.

The concrete tensile strength property determines the first crack propagation. Considering the fact that the concrete homogeneity is not perfect, the R_t property might be modified in the application to large structures (Sellier and Millard, 2014). This property must be adapted as a function of the structures configuration and/or dimension (CEOS.fr, 2015). Decreasing of this property was artificially performed to adjust to the experimental results (Mivelaz, 1996). A good compromise regarding this condition is an implementation of a probabilistic scale effect method that considers concrete random properties in RC modelling. In this section, this method is employed on the beam.

There are several statistical approaches to consider a variation of material properties to represent the concrete heterogeneities. One of the methods is called Turning Band Method (TBM). It is implemented in Cast3M as an operator called ALEA (CEA, 2015).

3. 7. 1. Detail of numerical simulation

In the previous works by (Matallah et al., 2010), random fields were generated to create a spatially correlated concrete Young's Modulus. The chosen evolution law of the concrete damage model was controlled by strain. Another research performed by (Michou et al., 2015) to generate concrete tensile property on the tensile tests of tie beam by employing coefficient of variation 5% and 6 cm of correlation length. In the case of LMDC model, as the model is governed by stress, it was first decided to generate a random field of concrete tensile strength R_t.

So R_t of concrete is engendered randomly based on the variance of the measured properties from Brazilian test in the laboratory.

In this section, three random samplings were generated by the author to create spatially correlated tensile strength in concrete. In this modelling, 5 cm correlation length and 13% the coefficient of variation (corresponding to the measured value of R_t in Table 3.2) are applied. Using the same average value and standard deviation in Cast3M, three random fields of concrete strength were generated in one-quarter of the concrete volume. It must be noted that only one-quarter of the volume is modelled. The generated random draw field might be different if the entire volume of RC beam was modelled.

In the first stage, three random fields were generated and noted respectively RF1, RF2 and RF3. Then, in the second stage, the imposed shrinkage was applied (as explained in section 3.6). At the end of shrinkage modelling, the stress field in the concrete for the three random field cases was obtained identically as in Figure 3.18. Then, finally, in the third stage, the mechanical loading on RC beam was employed.

To check the conformity to the input variables, thanks to the possibility in Cast3M, the standard deviation and the average value of these three random fields were calculated as summarised in Table 3.7 below. Average value is obtained from integration of the generated tensile strength field in the concrete volume, while the standard deviation is obtained from the square root of its variance as written in Equations (3.1) and (3.2).

$$\text{Average} = \frac{1}{vol}\int Rt \; dvol \tag{3. 1}$$

$$\text{Standard Deviation} = \sqrt{\frac{1}{vol}\int \left(Rt - \text{Average}\right)^2 \; dvol} \tag{3. 2}$$

Table 3. 7. Recapitulation of three random samplings compared to the input value.

Random Draw		**Average R_t (MPa)**	**Coefficient of Variation (%)**
INPUT		3,68	13,00
RF1	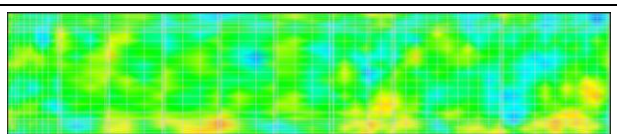	3,70	12,49
RF2	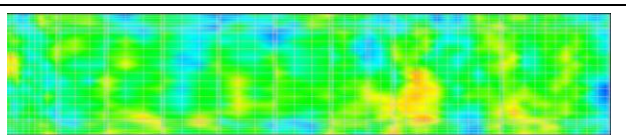	3,67	12,30
RF3	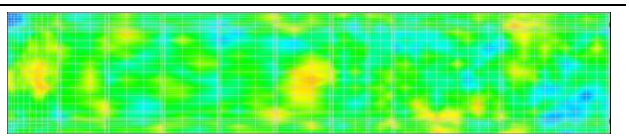	3,65	12,53

3. 7. 2. Modelling results: Global behaviour

In the global scale, the behaviour of RC beam after the first cracks varies as a function of average R_t and the coefficient of variation. From Table 3.7 and Figure 3.23, the closest global behaviour to the experimental results was obtained for the case of RF2, (See RF2, in a cross symbol). This case had the second lowest average value of R_t and the lowest coefficient of variation. The continuing behaviour after the first crack localisation of the three different calculations was still slightly overestimated. Around 75 kN, the three calculations were reaching the close value to the experimental ones. Beyond 85 kN, the modelling results were overestimated again. The three random fields did not have a significant influence on this scale.

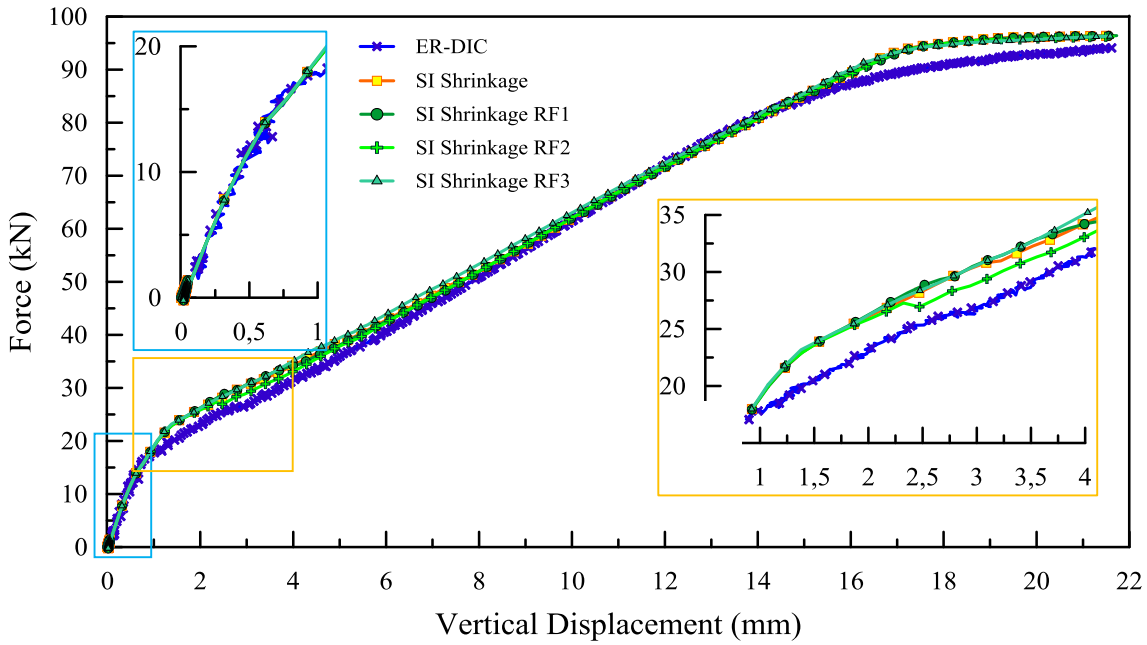

Figure 3. 23. Global behaviour: Experimental (ER-DIC), Modelling SI (Sliding Interface) + Shrinkage; and SI + Shrinkage + TBM results.

3. 7. 3. Modelling results: Cracking pattern and opening

Observation at 50,5 kN on the concrete surface as displayed in Figure 3.24 shows the different cracking pattern for each random sampling case. On the bottom of this figure, the crack width is plot as it appeared in RC beam (crack width and its position in the *x*-direction). Six to seven cracks (larger than 25 µm) were developed in the pure bending area. RF3 case has the least number of crack openings and the largest maximum crack width (326,3 µm) among all cases. The more crack number occurs, the smaller the maximum of crack width is developed. Also, according to Table 3.7, RF3 has the highest coefficient of variation and the lowest average of R_t.

Regarding Table 3.7, the scale of generated R_t in one-quarter concrete volume is varying from 1,6 up to 5,95 MPa. If the random field had been generated in one volume of RC beam, it might have produced a larger maximum crack opening. As consequence, random fields should be used

only with the complete structure to have a realistic value of the weakest and the strongest zones.

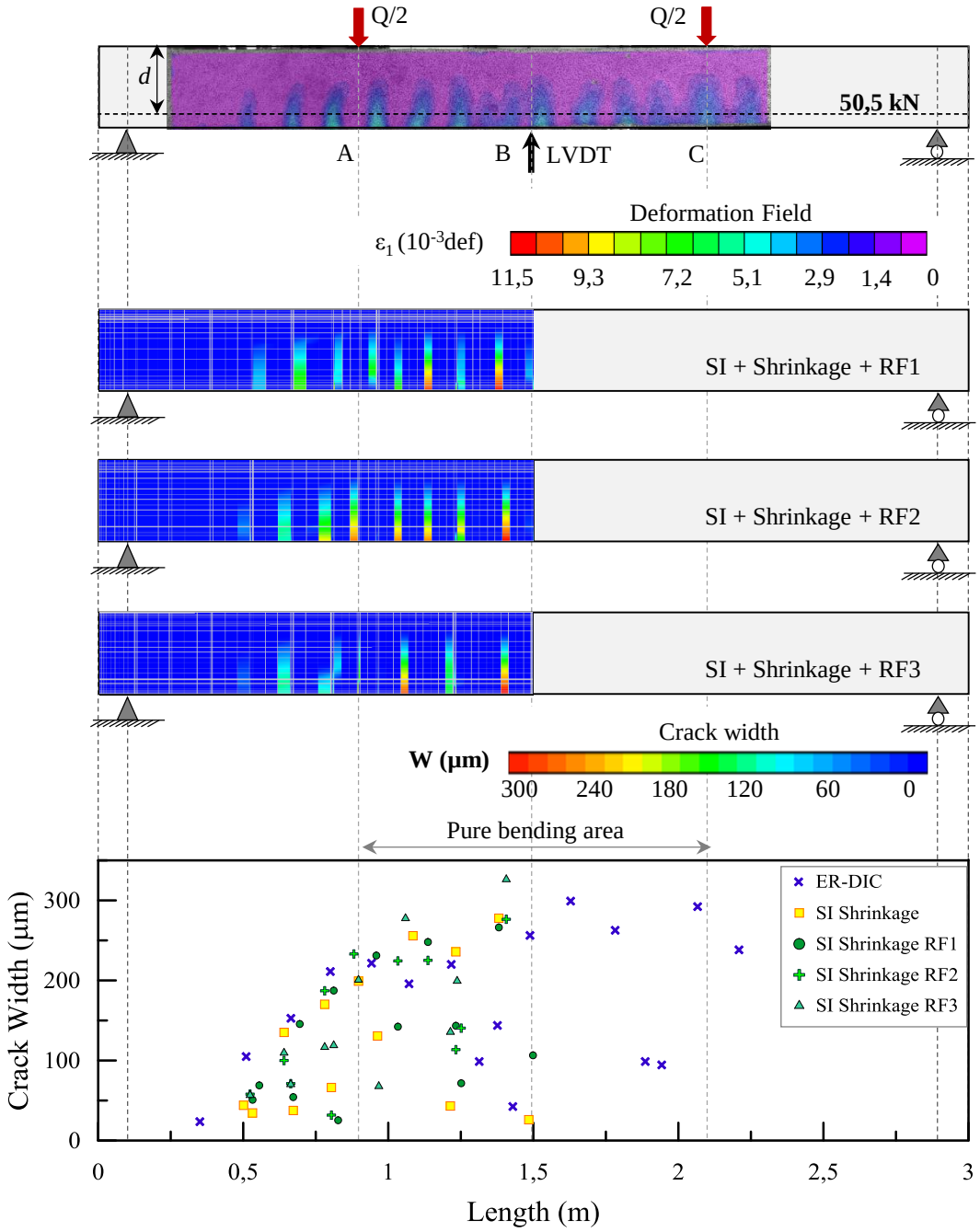

Figure 3. 24. Cracking pattern and opening at 50,5 kN: Experimental (ER-DIC), Modelling SI (Sliding Interface) + Shrinkage; and SI + Shrinkage + TBM results.

In this set of modelling, three cases using random field were performed to obtain the three cracking patterns that would happen in the real condition. The same number of simulations was also performed by (Michou, 2015). Another work generated two random fields (Matallah et al., 2010). Briefly said this method needs several simulations which are computational-time-consumers. In the next section, using a deterministic method that was developed basically from statistical results, the Weakest Link and Localization theory (WL² method proposed by (Sellier and Millard, 2014)) will be applied to the beam.

3. 8. Numerical Modelling 4: Shrinkage and random mechanical properties consideration using WL²

A newly proposed method called Weakest Link and Localization theory (WL²) by (Sellier and Millard, 2014) is able to consider the heterogeneity of material in a deterministic way which avoids resorting to random sampling. As explained in Chapter 1, once calculation performed, the most likely cracking pattern can be obtained directly. In this section, this method is applied on RC Beam.

3. 8. 1. Detail of numerical simulation

WL² method permits to assess the equivalent loaded volume $V_{eq(M)}$ for every time step of calculation. This volume represents the actual concrete volume in tension and determines the most likely tensile strength of concrete as presented in Equation (3.3) below, recall Equation 1.29 in Chapter 1. For each iteration, the tensile stress on RC structure is evaluated based on the loaded volume of concrete. So, scale effect is determined not only at the first time of calculation when the damage had not yet occurred.

$$\frac{R_{t(M)}}{R_{t/V_{ref}}} = \left(\frac{V_{ref}}{V_{eq(M)}} \right)^{1/m} \tag{3. 3}$$

In order to ensure the scaling effect of the concrete tensile strength, a probabilistic weighting function is employed to limit the decreasing value of tensile strength. As shown in Equation (3.3), R_t depends on $V_{eq(M)}$. Another unit of volume called $V_{\max(M)}$ represents the maximum volume that can be reached by $V_{eq(M)}$. When $V_{eq(M)}$ tends to $V_{\max(M)}$, thanks to the applied weighting function, the tensile strength will not be reduced anymore. This condition is ruled by the following equations, recall of Equations 1.30 and 1.31 in Chapter 1. The recommended value for characteristic length (l_c) of the probabilistic weighting function is 0,50 metre according to (Sellier and Millard, 2014).

$$V_{eq(M)} = \alpha \left(\frac{\sigma_{\max}}{R_{t/V_{ref}}} \right)^{-m} \text{ with } \alpha = \int_V \left(\frac{\sigma}{R_{t/V_{ref}}} \right)^{m} \psi\left(l / l_c \right) dV \tag{3. 4}$$

$$V_{\max(M)} = \int_{V \to \infty} \psi\left(l / l_c \right) dV = \left(l_c \sqrt{2\pi} \right)^N \tag{3. 5}$$

To employ this method, the user needs to define some parameter, such as $V_{\max(M)}$ and the reference volume V_{ref}. The $V_{\max(M)}$ can be determined as presented in Equation (3.6) giving a constant value whilst the reference volume V_{ref} may be taken as 300 cm^3. It represents the portion of the test piece subjected to the splitting force of a cylindrical concrete in Brazilian test

specimen with the diameter of 11 cm and the height of 22 cm. More detail recommendation of this method is explained in (CEOS.fr, 2015; Sellier and Millard, 2014).

$$V_{\max(M)} = \min(1{,}25; l) \times \min(1{,}25; b) \times \min(1{,}25; h_{eff}) \quad (3.6)$$

Where:

l, b, h_{eff} = Length, width and effective height of RC structure under tensile stress loading.

In this numerical simulation, the first step was determining the volume $V_{\max(M)}$ to control the maximal reduction value of R_t. Then, in the second step, the imposed shrinkage strain was applied (as explained in section 3.6). Finally, in the third step, the mechanical loading on RC beam was performed. At every time step calculation of shrinkage and mechanical loading, the equivalent loaded volume ($V_{eq(M)}$) is determined as well as the most likely R_t to be used. Using the same values as in the previous section, 350µm/m and 50 µm/m of imposed shrinkage strain in the cover concrete and in the core concrete respectively were applied. The results in global are presented below in Figure 3.25.

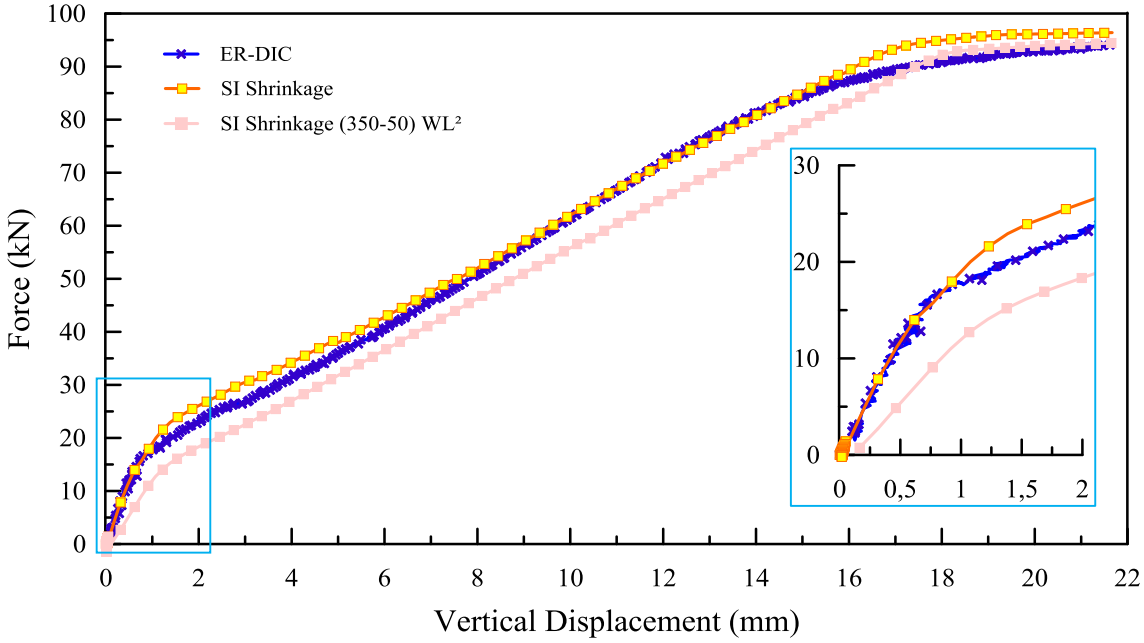

Figure 3. 25. Global behaviour: Experimental (ER-DIC), Modelling SI (Sliding Interface) + Shrinkage (350µm/m-50µm/m); and SI + Shrinkage (350µm/m-50µm/m) + WL² results.

The underestimation behaviour is obtained by using the same imposed shrinkage strain. Apparently, the determination of the most likely R_t for every time step calculation influences the induced stress at the end of shrinkage. The initial stiffness became weaker (almost one-third of loss). This phenomenon can be due to the fact that in the present study the volume $V_{\max(M)}$ was imposed constant all over the mesh, while in the original method clarified by (Sellier and

Millard, 2014), this volume was obtained by a non-local integral procedure which leads to a non-homogeneous field of the most likely R_t, even in case of quasi-homogeneous stress field (as it is the case in the cover zone during the shrinkage state). It is probable that the initial stiffness reduction observed here could disappear if the original procedure was applied. More discussions are available in Section 3.9. Unfortunately, this procedure initially was developed in Cast3M12 is not yet available in Cast3M15. It could be interesting to re-implement it in the current version of the software to avoid this type of problem. But time is missing to do this work in the framework of this PhD study.

3. 8. 2. Modelling results: Global behaviour

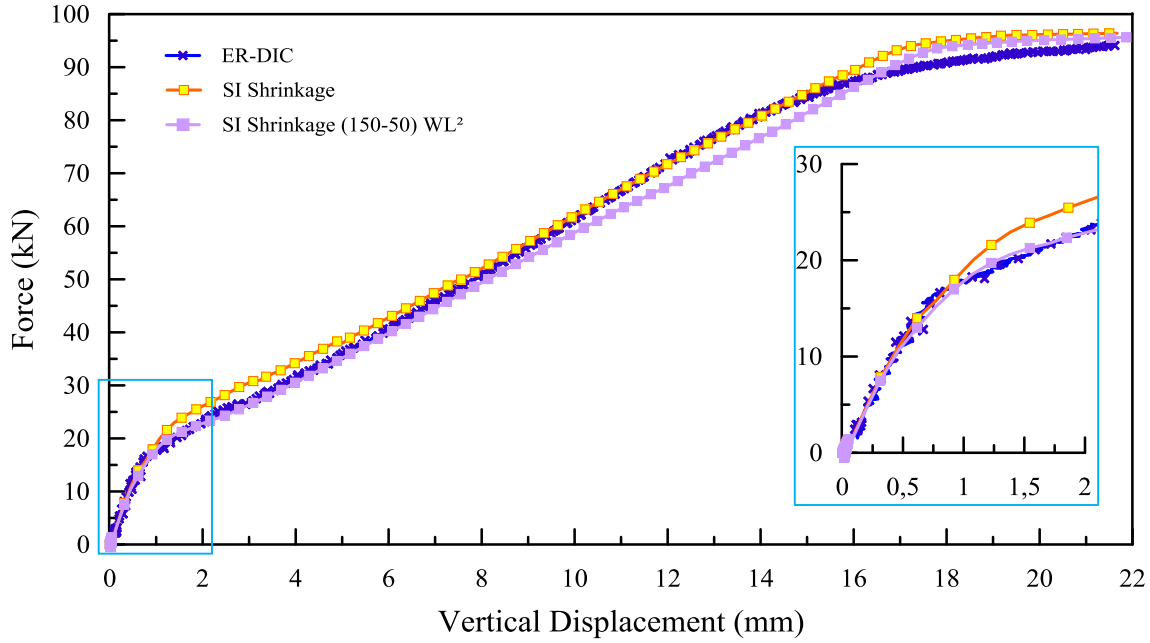

Figure 3. 26. Global behaviour: Experimental (ER-DIC), Modelling SI (Sliding Interface) + Shrinkage (350µm/m-50µm/m); and SI + Shrinkage (150µm/m-50µm/m) + WL² results.

Using 150µm/m and 50 µm/m of imposed shrinkage strain in the cover concrete and in the core concrete respectively limits the consequence of $V_{\max(M)}$ homogeneity pointed out previously, these imposed shrinkage strains combined with the WL² method allows to fit the numerical responses on the experimental ones. Figure 3.26 displays the global results. A good agreement can be obtained up to 50,5 kN of force clearly. Unfortunately, beyond this force, the behaviour obtained remained underestimated. At around 85 kN, the modelling results reached overestimation results. The accuracy loss beyond 50 kN can also be due to the $V_{\max(M)}$ assessment problem mentioned previously. Even so, other explanations can be proposed, for instance, the interface zone is supposed homogeneous while the surrounded concrete is supposed heterogeneous. If the interface was also considered heterogeneous, the maximal shear stress would vary along the rebar and would change the crack's spacing, and consequently the global response in the cracked regime.

3. 8. 3. Modelling results: Cracking pattern and opening

The crack opening at 50,5 kN is presented in Figure 3.27 along with the other two cases (SI and SI + Shrinkage). The maximum crack is observed in line with the load application. The maximum crack opening from the WL² method (275 µm) is not so different from the SI + Shrinkage modelling (277 µm). The consideration of the most likely tensile strength for each numerical step iteration results in better crack localisation without altering the initial stiffness.

When the first crack appeared, the equivalent loaded volume changed. The tensioned zone was decreased, and according to Equation (3.3), R_t increased for the not yet damaged zones. It definitely could affect the initiation of the second crack that appeared a little farther from the first one than if the concrete was homogeneous. This condition continued until larger damage occurred at the end of the test. This large spacing between cracks was expected to generate larger crack opening.

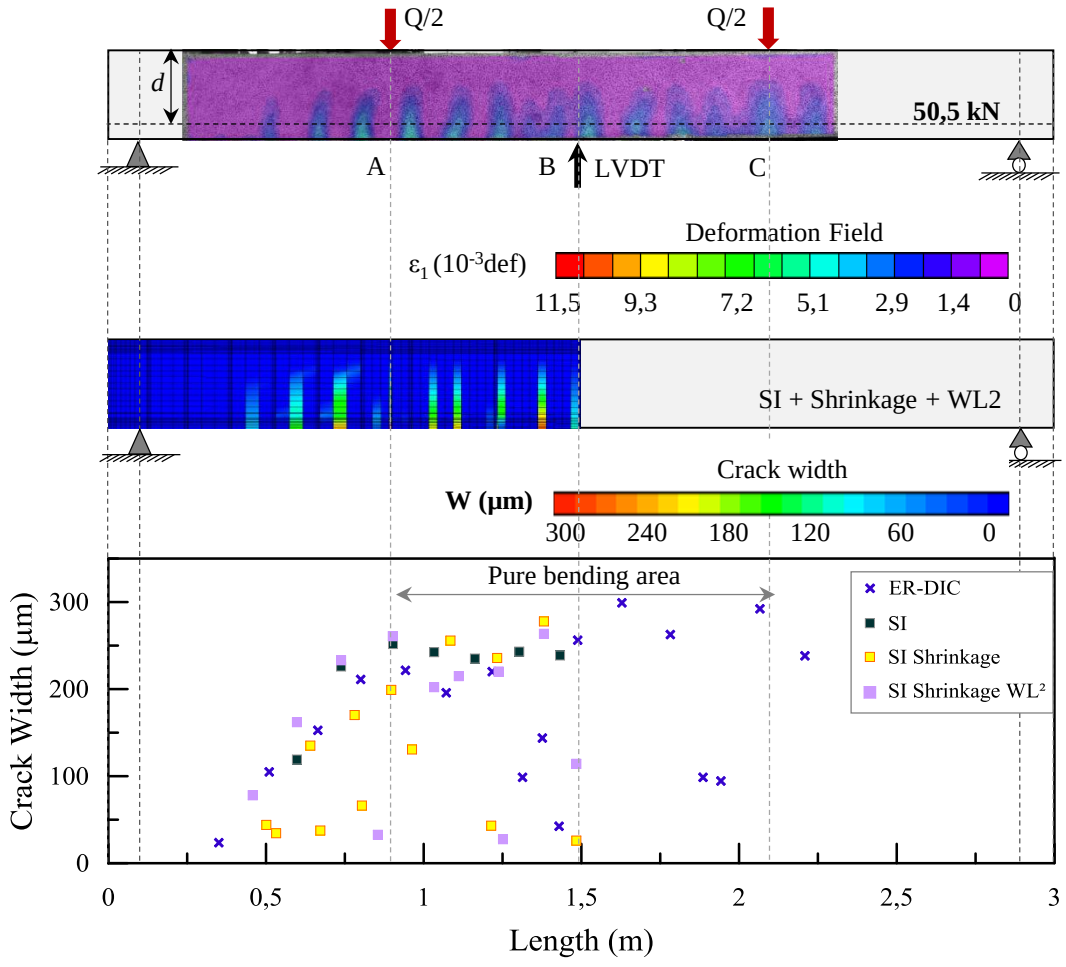

Figure 3. 27. Cracking pattern and opening at 50,5 kN: Experimental (ER-DIC), Modelling SI (Sliding Interface) + Shrinkage (350µm/m-50µm/m); and SI + Shrinkage (150µm/m-50µm/m) + WL² results.

3. 9. Comparative study of numerical simulations

In section 3.7 and 3.8, we noticed some different responses of RC beam by using two

different methods to consider random concrete properties. It may come from the different approach to determining the R_t variation of each method. The cracking pattern at 50,5 kN presented in Figure 3.26 and 3.29 are showing the crack opening just beside the transverse reinforcement for both cases. This situation may be due to the restraining action of the transverse reinforcement to shrinkage loading. In this part, RF2 result (Section 3.7) is compared with WL² results (Section 3.8).

Observation in global behaviour (Figure 3.28) shows that the results from WL² method (the initial stiffness of force application and the first crack localisation) are in accordance with the experimental ones up to 50,5 kN. Beyond this point forward, WL² underestimated the force; while on the other hand, RF2 has a better estimation. These earlier behaviours of both cases are very interesting to be discussed in a more detail observation, for example at the end of the shrinkage simulation.

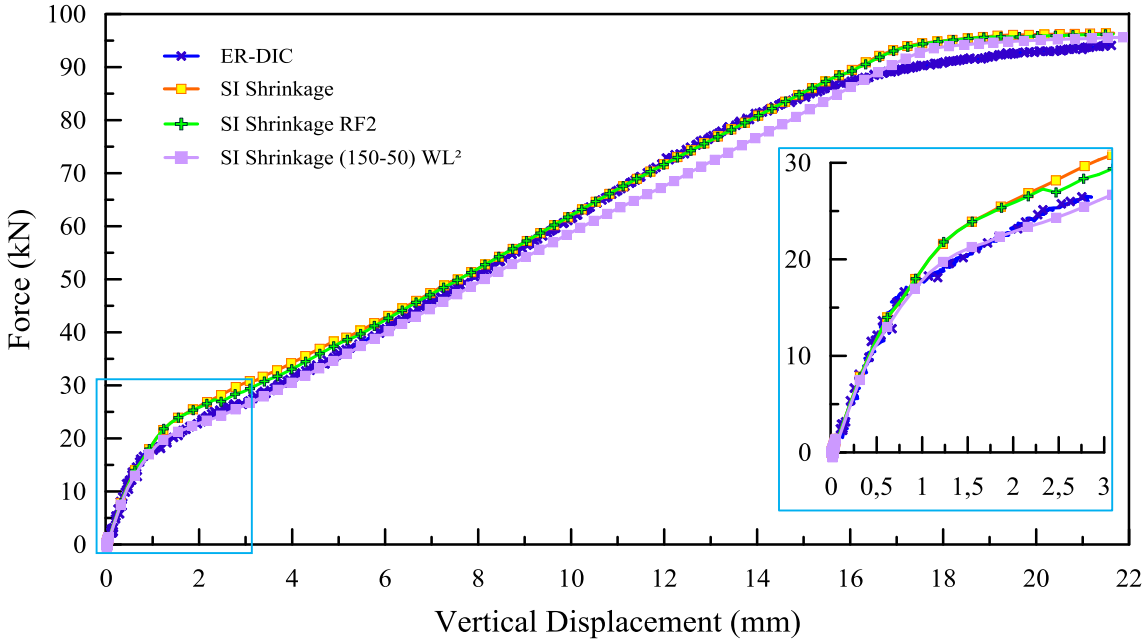

Figure 3. 28. Global behaviour: Experimental (ER-DIC), Modelling SI (Sliding Interface) + Shrinkage (350µm/m-50µm/m); SI (Sliding Interface) + Shrinkage (350µm/m-50µm/m) + TBM; and SI + Shrinkage (150µm/m-50µm/m) + WL² results.

The shrinkage was different for these two cases. In the case of RF2, 350 µm/m of imposed shrinkage strain was needed in the cover concrete whilst only 150 µm/m of imposed shrinkage was used for WL² case. These values were chosen to adjust the initial stiffness of force-vertical displacement. Even if the two values remain realistic, their difference is probably due to a miss estimation of $V_{\max(M)}$ which should be non-homogeneous and was considered constant due to a lack in the current version of software as previously mentioned.

Moreover, the application of WL² used the constant $V_{\max(M)}$ of an **entire volume** (one beam). In the original suggestion (Sellier and Millard, 2014), a non-local integral procedure (Equation (3.5)) considers the total volume from the symmetrical axes of the model to estimate $V_{\max(M)}$.

Even though the mesh was only made for one-quarter of volume, the R_t estimation for each iteration step considered the whole volume, which is one of the advantages of WL². Meanwhile, for TBM case, the generation of the random field was only for one-quarter of volume which means a complete structure must be modelled. So, the strongest and the weakest zone estimation was not the same for these two cases.

In Table 3.8, the loaded beam at the end of shrinkage simulation for both cases is presented. At the end of shrinkage, due to a different imposed shrinkage strain, the induced stress in the concrete for the RF2 case is larger than the one in the WL² case. Nevertheless, the same tendency occurs, with a concentration of stress on the concrete surface where transverse reinforcements are present.

Table 3. 8. Comparison of TBM (RF2) and WL² results.

SI + Shrinkage (350µm/m-50µm/m) + TBM (RF2)	**SI + Shrinkage (150µm/m-50µm/m) + WL²**
Generated tensile strength field on concrete	
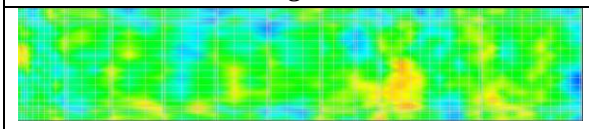 (recall from Table 3.7)	
At the end of shrinkage simulation	
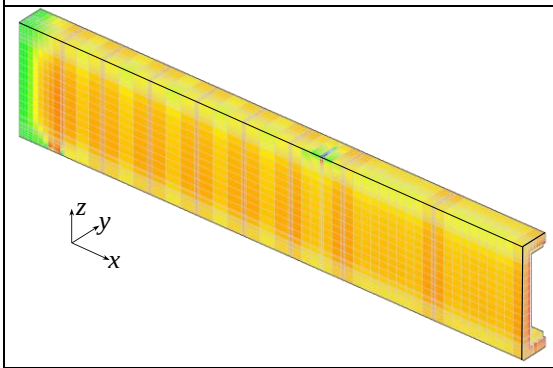	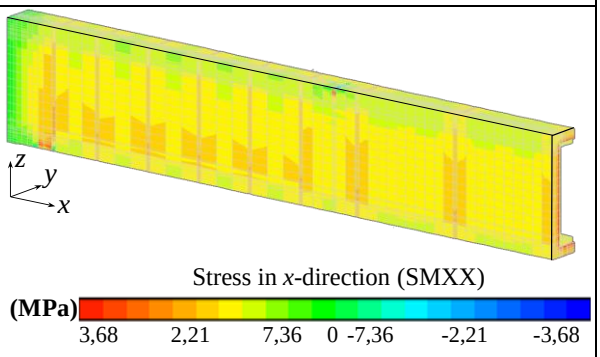
Cracking pattern at F = 27,5 kN (half-length of beam)	
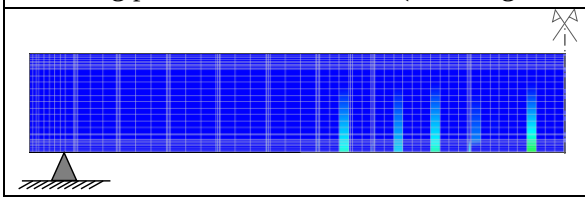	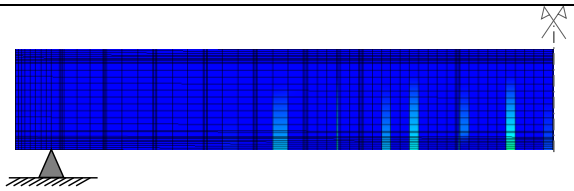
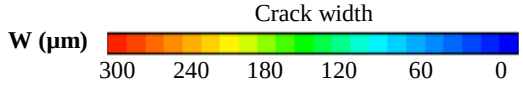	

Recall Equation (3.3), in WL², the actual value of R_t can be estimated as in Equation (3.7). In the cover concrete, the shrinkage simulation causes the concrete volume to be charged under tension that increases the equivalent loaded volume ($V_{eq(M)}$), and in turn decreases the tensile strength homogeneously in the cover concrete according to Equation (3.7).

$$R_{t(M)} = \sqrt[m]{\frac{V_{ref}}{V_{eq(M)}}}\, R_{t/V_{ref}} \qquad (3.\ 7)$$

Therefore, at the end of shrinkage, in the cover concrete, the residual R_t in WL² is smaller than in the TBM. As consequences, in the further mechanical loading, the damage on concrete will be attained quickly and the crack localisation will propagate earlier. That's also why smaller imposed shrinkage strain was sufficient to attain the same initial stiffness.

This phenomenon is due to the fact that in the WL² method, the localised crack initiation is more difficult than in the TBM. In fact, in the WL², only $V_{\max(M)}$ and the stress field control together the first crack initiation. If they are both homogeneous, the localisation is delayed and a short period of homogeneous damage occurs, leading to a global decrease of R_t in the cover zone. In order to avoid this problem, it is necessary to resort to the $V_{\max(M)}$ determination proposed in (Sellier and Millard, 2014), instead of using a constant $V_{\max(M)}$ all-over the beam. Another solution that could be used is a very slight random field to prevent a non-localised damage in the case of the homogeneous stress field. This solution could preserve the advantage of WL² (a single calculus without random sampling based on the large standard deviation of R_t) without resorting systematically to the method advised by (Sellier and Millard, 2014) for $V_{\max(M)}$.

3. 10. The maximum crack width evolution

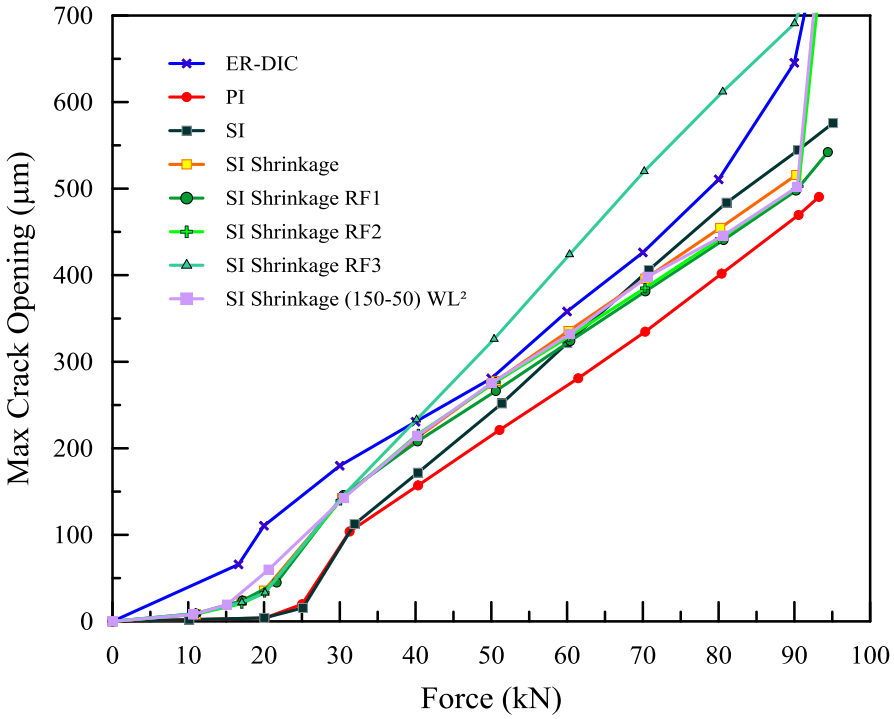

Figure 3. 29. The evolution of $w_{\max}$ during loading, experimental and simulations comparison.

The evolution of the maximum crack opening ($w_{\max}$) is presented in Figure 3.29. The $w_{\max}$

evolutions from numerical simulations are generally underestimated. To be noted, in these curves, it is not necessarily the same crack for each appearance of the maximum one.

Experimentally, crack opening started earlier, showed in blue colour (ER-DIC). At 10 kN, 70 µm of crack was opened. Numerically, the application of interfacial transition zone influences positively the crack propagation. PI model had the most underestimated crack width maximum while SI model reproduced better crack opening. The first crack localisation arrived lately for both cases; up to 20 kN, no significant crack opening occurred. Even so, when the force reached 50 kN, the crack width was getting close to the experimental ones. It is confirming the global behaviour presented in Figure 3.13. So, it also proved that we need to consider other aspects on RC Modelling. Interface zone is not enough to obtain the corresponding experimental results.

Then, shrinkage was considered in the simulation (SI + Shrinkage, in orange-yellow colour). A better crack opening evolution was reproduced. Crack propagated earlier and the continuing crack behaviour was not bad. Application of three random sampling using TBM showed a variation of crack width for each case (in green colours with different symbols). The three results are identical in crack opening maximum up to 30 kN. Afterwards, RF3 had larger crack opening comparing to experimental results. The other two RF1 and RF2 did not exhibit a significant difference crack opening compared with SI + shrinkage results. This condition shows the variation of TBM application. So, it is proven also the previous conclusion mentioned in Section 3.7 that several random draws are needed to be performed to obtain several behaviours in global scale and in cracking behaviour.

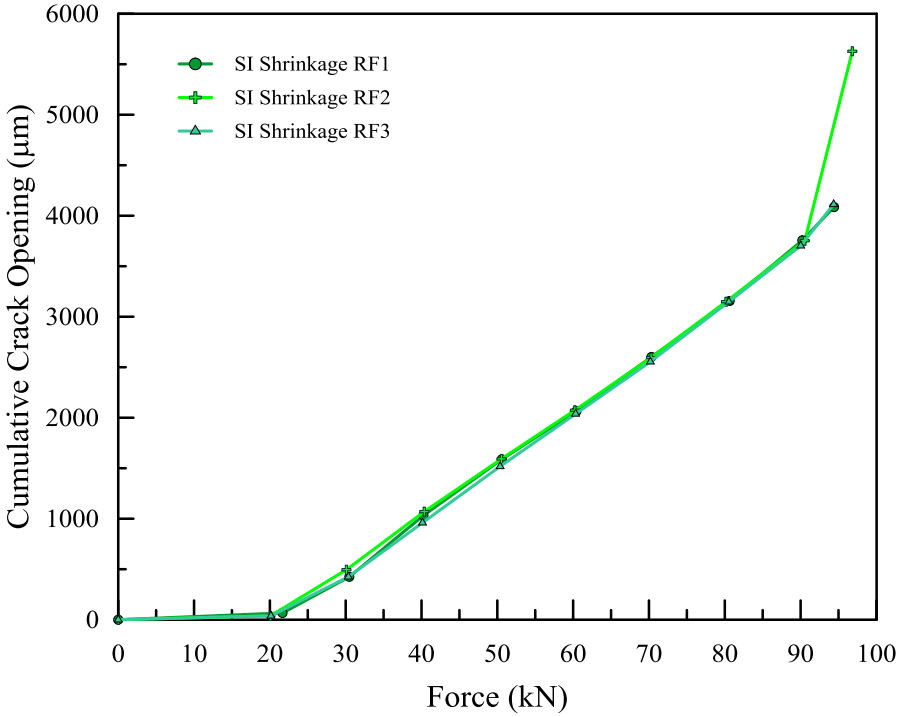

Figure 3. 30. The evolution of cumulative crack opening for the three cases of TBM.

As a curiosity, let see the cumulative crack opening along the beam for these three random field applications (Figure 3.30). Even though in Figure 3.29 the three samplings have a

significant different of crack opening maximum, the cumulative cracks for three cases are the same.

The application of the second scale effect method, WL^2 is shown in purple colour (SI Shrinkage WL^2). Apparently, the first crack localisation and the crack propagation up to 50 kN are the best among the others. The evolution of crack for RC beam according to formulation of Eurocode 2 can be found in Appendix C.

The location of crack opening max on the RC beam for each case is presented in Figure 3.31. Experimentally the maximum crack occurs between 1,5 and 1,75 metre. As it was modelled one-quarter volume, it is normal that numerically the crack width maximum is found between 1,25-1,5 metre except for SI model. The SI + Shrinkage case, the three cases of SI + Shrinkage + TBM and the SI + Shrinkage + WL^2 case have the maximum crack opening in approximately the same location. As expected, WL^2 method gives directly the maximal opening at the mean position of random samplings. To be noted, this position is symmetric to the real one (ER-DIC); from a statical point of view, this is the same position.

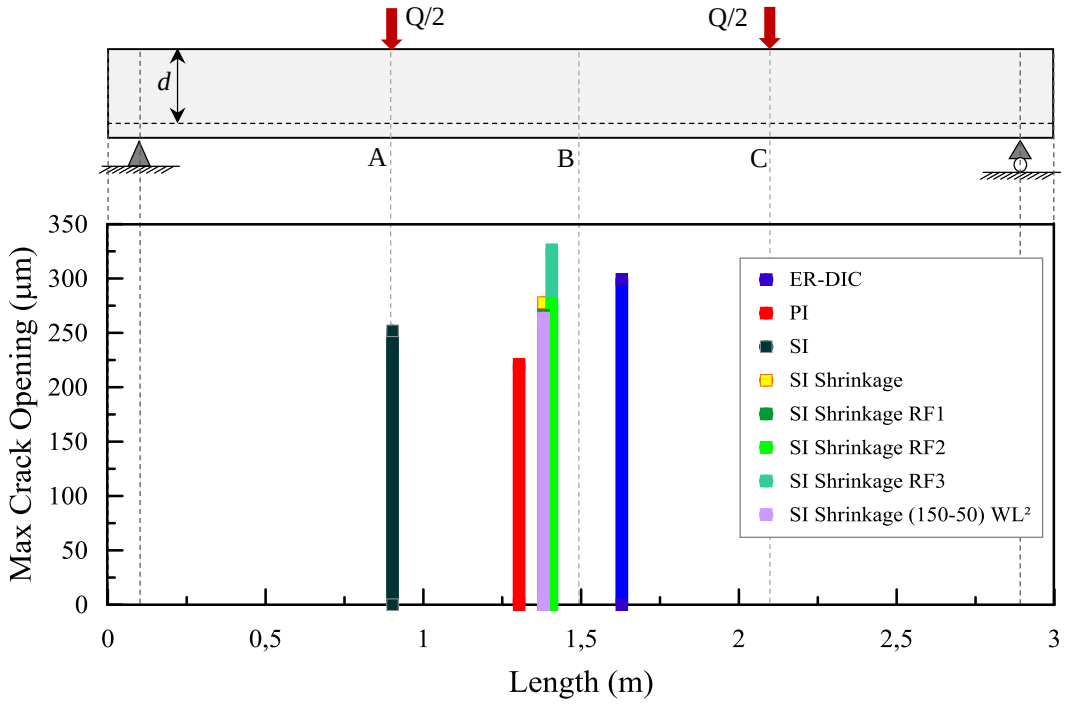

Figure 3. 31. The position of the maximum crack opening for each case of calculation at 50,5 kN.

3. 11. Statistical interpretation on crack opening in the pure bending area

The crack opening in the pure bending area (the area from A to B) for each case of numerical modelling and experimental results are studied in this section in a form of a normal distribution. The recapitulation of crack is shown in Table 3.9 below.

Following Equation (3.8) of Normal Density Function, in the succeeding figures, normal

distribution of numerical modelling and experimental results are compared.

$$f(x,\mu,\sigma)=\frac{1}{\sqrt{2\pi}\,\sigma}e^{-\left(\frac{(x-\mu)^2}{2\sigma^2}\right)} \quad (3.\ 8)$$

Table 3. 9. Recapitulation of crack opening at 50,5 kN in the pure bending area of the beam.

	DIC	SI Shrinkage RF1	SI Shrinkage RF2	SI Shrinkage RF3	SI Shrinkage RF All	SI Shrinkage WL²
Number of cracks	7	7	7	5	19	6
Maximum (µm)	256,290	266,171	276,399	326,328	326,328	263,542
Minimum (µm)	42,488	71,509	30,071	67,786	30,071	27,529
Average crack opening (µm)	168,387	172,692	151,139	201,287	172,276	173,765
Standard Deviation	71,008	69,939	87,293	93,360	85,378	79,221

In Figure 3.32 (a), the normal distribution for three random draws (RF1, RF2 and RF3), WL² and experimental results are compared. RF1 has the closest distribution to DIC. Three random field draws have different distributions. This condition confirms the previous idea that random field may result in a very different way for each sampling. Then, we can see that the result of WL² is between the experimental and the random sampling ones.

To be more precise, in Figure 3.32 (b), the cumulative crack properties in the pure bending from three RF sampling (RFAll), WL², and DIC are compared. It seems that WL² can represent the three random field draws. If more random field draws are generated, the result will closer to WL². If experimental results are considered as a random field realisation, the fact that WL² is in between is effectively representing the most likely situation. So, to conclude, one calculation using WL² can represent the several calculations using TBM. The effectiveness of WL² remains interesting despite the fact that crack initiation problem mentioned above should be clarified.

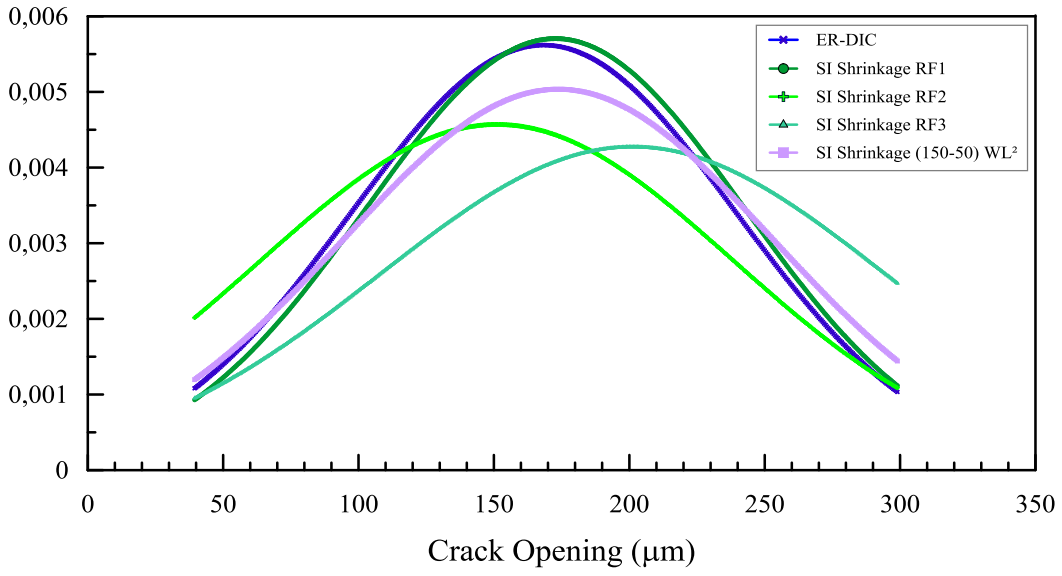

(a)

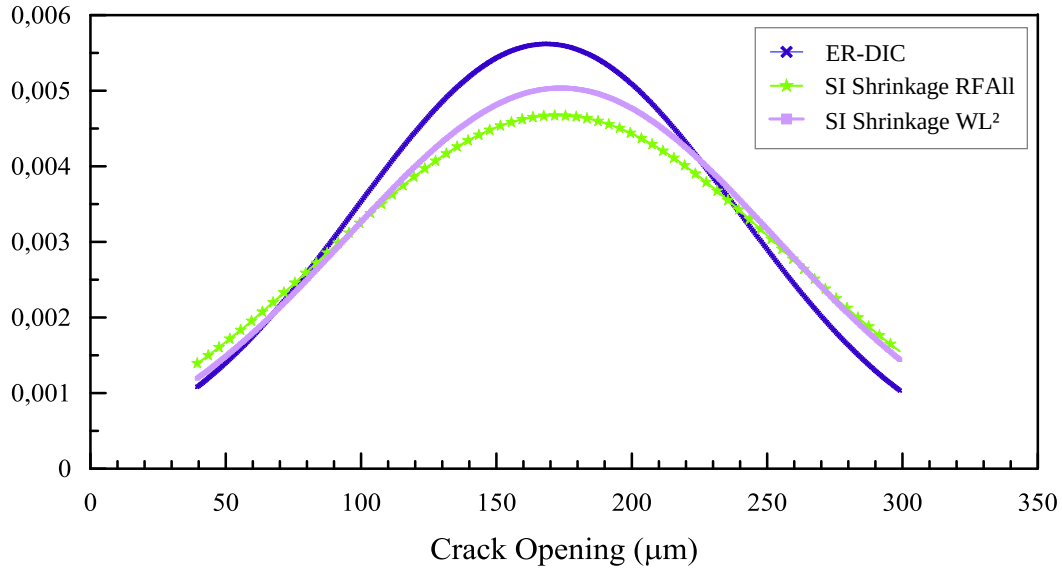

(b)

Figure 3. 32. Gaussian's normal distribution for cracks obtained at 50,5 kN in the pure bending area.

3. 12. Conclusion

In this chapter, the proposed model of the interfacial transition zone in Chapter 2 was applied to an RC beam with a rectangular section under four-point flexural test. All the reinforcements were modelled surrounded with one layer of interfacial transition zone element. The RC modelling should be evaluated both on the global scale and in the term of crack properties, such as its pattern, evolution, width and also space one to the others.

In *the first set of modelling*, the sliding interface model consideration (SI) has a tendency to make a better crack opening than the one with the perfect interface (PI) model. Nevertheless, a significant different of the initial stiffness and the crack propagation remained. Then, in *the*

second set of modelling, the imposed shrinkage strain was introduced and was combined with the interface application. This consideration is able to explain the initial stiffness loss and the crack initiation close to the stirrups.

In *the third step of modelling*, a random field generator called TBM was combined with the previous set of modelling to represent the random mechanical behaviour of concrete. Three random samplings were performed and resulted in three different cracking patterns. As an alternative, *in the fourth set of modelling*, another method to represent random properties called WL² was used. Despite using a constant $V_{\max(M)}$ all-over the beam, this model was able to reproduce the most likely cracking pattern on RC modelling. Furthermore, WL² considers the entire volume of structures even the modelling was only performed on its one-quarter volume of the original size. Thus a WL² application is very practical especially for large structures which are modelled simply by considering the symmetrical axes.

So, in order to assess cracking behaviour on RC structure elements, the interfacial transition zone between concrete and steel bar, the shrinkage on the concrete volume and the concrete random properties consideration are necessary to be taken into account. Otherwise, the nonconformity to the experimental results could happen whether in the global behaviour or in the crack properties.

This page is intentionally left blank

General Conclusion

The objective of this thesis was to find the most effective methods of crack modelling of Reinforced Concrete (RC) structures using finite elements. Inspired from the recently proposed recommendation by PN Ceos.fr (CEOS.fr, 2015), there are three parameters required, which are the specificity of the steel-concrete bond, the self-stress due to shrinkage, and the probabilistic scale effect due to the heterogeneity of concrete.

Chapter 1 was devoted to studying the experimental works and crack modelling on RC structures from the literature review.

Based on the recommendation of PN Ceos.fr, the three main parameters previously mentioned are needed to be clarified in crack modelling for RC large structures in the context of finite elements method. In term of the steel-concrete bond, an analytical model of Eligehausen (Ciampi et al., 1981; Eligehausen et al., 1983) or from the pull-out test results can be applied as hardening law of a plasticity criterion. Von Mises criterion seems promising since in the thick cover concrete (pull-out test), the bond strength is independent of the active confinement (Torre-Casanova et al., 2013). Using this model in the context of a volumetric finite element with a few millimetres thickness around steel bars allows to model realistically the degraded zone observed in pull-out tests. Relating to shrinkage, the presence of steel bar that provokes a restraint to the concrete shrinking action induced an initial stress which lessens the first cracking force proportionally. The initial stress induced by shrinkage can be modelled via a poro-mechanical framework, such as Van-Genuchten's formulation resulting in a pre-damage state at the end of shrinkage. This state explains the initial stiffness reduction observed experimentally on reinforced concrete elements. Regarding the probabilistic scale effects, recent studies showed the structural size effect on the overall behaviour, on the maximum crack opening and on the crack spacing. TBM (Turning Band Method) has been used to consider the concrete's random tensile strength. Another method, WL² (Weakest Link and Localization) can be an alternative to take into account the scale effect in a deterministic way.

Hence, we are interested, firstly, in modelling the steel-concrete bond; secondly, the influence of shrinkage; and thirdly, the heterogeneity at the origin of the scale effect that had to be clarified in the context of crack modelling of RC structures. The objectives are to quantify the importance of each of these three aspects and their combinations to find the most effective modelling methods.

Chapter 2 was focused on the importance of the steel-concrete bond.

This chapter was started by performing material characteristic tests for concrete, steel bar and interface zone. Pull-out tests were performed to obtain the behaviour of the steel bar and the surrounding concrete connection. Next, tensile tests using Digital Image Correlation system were performed to observe the crack behaviour on RC prism. Concerning the numerical simulations, primarily, based on the results of the pull-out test, an elasto-plastic law with a Von Mises criterion is used in a volumetric element representing the interfacial zone observed experimentally. Then, the application was carried out on the tensile test of RC prismatic element. The comparison with experimental results, it showed the importance of sliding interface behaviour that gave better results in the crack opening, the force-relative displacement behaviour and independence to mesh size. Nonetheless, this model needs some improvements, especially for the localisation of the first cracks and the crack opening, leading to Chapter 3.

Chapter 3 demonstrated that the interface model on RC beam has to be completed by consideration of concrete shrinkage and probabilistic scale effect to obtain realistic numerical results both at global and local scale.

A four-point bending test was performed on RC beam with a rectangular section. Then, the proposed model of the interfacial transition zone clarified in Chapter 2 was applied to this beam. All the reinforcements were modelled surrounded with one layer of interfacial transition zone element. In the first set of modelling, the necessity to apply the interfacial transition zone with sliding behaviour was confirmed but a larger initial stiffness and an overestimation of the first crack force propagation were obtained. In the second set, an imposed shrinkage strain was added to the concrete to obtain an initial stress state. The results show that shrinkage is able to explain the initial stiffness loss and the crack near the stirrup but it was not sufficient to model the crack propagation accurately. In the third set of modelling, the concrete's random nature property was taken into account along with the imposed shrinkage strain and interface. Turning Band Method (TBM) and Weakest Link and Localization (WL^2) were successively tested. With the TBM, three random fields were generated that resulted in different cracking pattern and variation of the crack opening which were more realistic than in the previous modelling. However, it required several random samplings to have a representative behaviour of a real structure. This application showed also that the TBM should be always used with the total volume of concrete to have a realistic weakest zone for each sampling.

The WL^2 avoid resorting to several random samplings and allowed to consider the weakest link even with a simplified model for which the total volume was replaced by a quarter volume and symmetry conditions. The method resulted in a better agreement of force-displacement relationship than the TBM cases. Despite a simplified version of WL^2 using constant $V_{\max(M)}$ all-over the beam, this model was able to reproduce the most likely cracking pattern on RC modelling, as shown in the crack opening probability density function which was the closest to

the experimental one.

So, this study shows the importance of three aspects essential in concrete crack modelling: the interfacial transition zone between concrete and steel bar which can be fitted in pull-out test results, the shrinkage of concrete which controls mainly the initial stiffness, and the concrete random properties which has to be taken into account to have a realistic evolution of cracking forces and then cracks spacing and openings.

This page is intentionally left blank

Perspectives

1. Application of WL² method along with the sliding interface behaviour and the shrinkage

The application of this method in Chapter 3 was taking in a simplified way which consisted of a constant value of $V_{\max}$. In the original model (Sellier and Millard, 2014), this $V_{\max}$ was obtained by a non-local integral procedure which leads to a non-homogeneous field of the most likely R_t. It is useful to provoke a localisation in the case of homogeneous stress field. So, application of WL² method as proposed in the original work should be implemented in the current version of finite element software.

2. Delayed strain and random heterogeneities in the interfacial transition zone

The proposed model of interface zone used homogeneous properties along the steel bar while the surrounded concrete was set in random. For this condition, random field in the interface can be generated by using a correlation between the interface zone and the surrounding concrete material properties. So, in the zone where concrete is weak, the interface zone nearby is also weak. Moreover, considering non-homogenous interface according to casting condition could be also an improvement for sliding interface properties.

In term of shrinkage, initial stress is induced in the concrete during the hardening and the drying concrete phase before the loading application. Also, the surrounding concrete (forming interface zone with the ribs) is affected by this shrinkage. So, imposed shrinkage strain can be applied in the interface zone before the mechanical loading application.

3. T-beam (see Appendix A)

The study of T-beam relegated in Appendix A for representability problems, highlights the sensitivity of crack pattern to the steel bar reinforcement's arrangement and position in the RC structures. Perhaps, a probabilistic apprehension of this type of problem should be investigated to avoid such configurations in real structures.

Moreover, the capability of the model for the case of active reinforcements could also be investigated, in order to use the proposed methodology to the prediction of cracking in pre-stressed structures.

This page is intentionally left blank

References

A, M.A.M., Orteu, J.-J., Schreier, H.W., 2009. Introduction, in: Image Correlation for Shape, Motion and Deformation Measurements. Springer US, pp. 1–12.

ACI 408R-03, 2003. ACI 408R-03: Bond and Development of Straight Reinforcing Bars in Tension [WWW Document]. URL https://www.concrete.org/store/productdetail.aspx?ItemID=40803&Format=DOWNLOAD (accessed 9.13.16).

Acker, P., 2003. Sur les origines du retrait et du fluage du béton. Rev. Fr. Génie Civ. 7, 761–776. doi:10.1080/12795119.2003.9692521

Aïtcin, P.-C., Mindess, S., 2013. Écostructures en béton: comment diminuer l'empreinte carbone des structures en béton. Editions Eyrolles.

Alam, S.Y., 2011. Experimental Study and Numerical Analysis of Crack Opening in Concrete (Ph.D Thesis). Ecole Centrale de Nantes (ECN).

Alam, S.Y., Loukili, A., Grondin, F., Rozière, E., 2015. Use of the digital image correlation and acoustic emission technique to study the effect of structural size on cracking of reinforced concrete. Eng. Fract. Mech. 143, 17–31. doi:10.1016/j.engfracmech.2015.06.038

C Mang, L Jason, L Davenne, 2015. A new bond slip model for reinforced concrete structures: Validation by modelling a reinforced concrete tie. Eng. Comput. 32, 1934–1958. doi:10.1108/EC-11-2014-0234

Casanova, A., Jason, L., Davenne, L., 2012. Bond slip model for the simulation of reinforced concrete structures. Eng. Struct. 39, 66–78. doi:10.1016/j.engstruct.2012.02.007

CEA, 2012. Description of the finite element code Cast3m [WWW Document]. URL http://www-cast3m.cea.fr/ (accessed 3.16.16).

CEOS.fr, 2015. Recommandations pour La Maîtrise des Phénomènes de Fissuration CEOS.fr.

Chamseddine, F., 1996. Caractérisation des propriétés de la peau des bétons de structures (Ph.D Thesis in French). Université Lille 1.

Choi, S., Shah, S.P., 1997. Measurement of deformations on concrete subjected to compression using image correlation. Exp. Mech. 37, 307–313. doi:10.1007/BF02317423

Ciampi, V., Eligehausen, R., Bertero, V.V., 1981. Analytical Model for Deformed Bar Bond under Generalized Excitations (IABSE reports of the working commissions No. 34).

Corr, D., Accardi, M., Graham-Brady, L., Shah, S., 2007. Digital image correlation analysis of interfacial debonding properties and fracture behavior in concrete. Eng. Fract. Mech., Fracture of Concrete Materials and Structures 74, 109–121. doi:10.1016/j.engfracmech.2006.01.035

Cox, J.V., Herrmann, L.R., 1998. Development of a plasticity bond model for steel reinforcement. Mech. Cohesive-Frict. Mater. 3, 155–180. doi:10.1002/(SICI)1099-1484(199804)3:2<155::AID-CFM45>3.0.CO;2-S

Dahlblom, O., Ottosen, N.S., 1990. Smeared Crack Analysis Using Generalized Fictitious Crack Model. J. Eng. Mech. 116. doi:10.1061/(ASCE)0733-9399(1990)116:1(55)

De Larrard, F., 2009. Concrete Optimisation with Regard to Packing Density and Rheology. LCPC Nantes Cent.

Dominguez Ramirez, N., 2005. Etude de la liaison acier-béton : de la modélisation du phénomène à la formulation d'un élément fini enrichi "béton armé" (Ph.D Thesis in French). École normale supérieure de Cachan - ENS Cachan.

Eligehausen, R., Popov, E.P., Bertero, V.V., 1983. Local Bond Stress-Split Relationships of Deformed Bars under Generalized Excitations (No. University of California, Report No. UCB/EERC-82/23 of the National Science Foundation). California, USA.

Eurocode 2, 2005. Eurocode 2, EN 1992-1-1. October 2005: Design of concrete structures - Part 1-1: General rules and rules for buildings. Eur. Comm. Stand. CEN.

Farra, B., 1995. Influence de la résistance du béton et de son adhérence avec l'armature sur la fissuration (Ph.D Thesis in French). Ecoàle Polytechnique Federale de Lausanne.

Fenton, G.A., 1990. Simulation and analysis of random fields (Ph.D Thesis).

fib, C.-F., 2000. Bond of Reinforcement in Concrete.

Gambarova, P.G., Rosati, G., 1996. Bond and splitting in reinforced concrete: test results on bar pull-out. Mater. Struct. 29, 267. doi:10.1007/BF02486361

Gilbert, R.I., 2001. Shrinkage, Cracking and Deflection-the Serviceability of Concrete Structures [WWW Document]. EJSE Homepage Electron. J. Struct. Eng. Vol 1 No1 2001 2-14. URL http://www.ejse.org/Archives/Fulltext/200101/02/20010102.htm (accessed 5.2.16).

Goto, Y., 1971. Cracks Formed in Concrete Around Deformed Tension Bars. J. Proc. 68, 244–251.

Hameed, R., 2010. Apport d'un renfort de fibres sur les performances des structures en béton armé pour les applications parasismiques (Ph.D Thesis). Université de Toulouse III - Paul Sabatier.

Hillerborg, A., Modeer, M., Petersson, P.-E., 1976. Analysis of crack formation and crack growth in concrete by means of fracture mechanics and finite elements. Cem. Concr. Res. 6, 773–782.

Jason, L., Torre-Casanova, A., Davenne, L., Pinelli, X., 2013. Cracking behavior of reinforced concrete beams: experiment and simulations on the numerical influence of the steel-concrete bond. Int. J. Fract. 180, 243–260. doi:10.1007/s10704-013-9815-6

Kachanov, L.M., 1958. Time of the rupture process under creep conditions. Isv Akad Nauk SSR 1958 8 26–31 26–31.

kilonewton Sarl, 2010. Techniques de corrélation d'images. Commer. Doc. Court. Kilonewton.

Kolani, B., 2012. Comportement au jeune âge des structures en béton armé à base de liants composés aux laitiers (Ph.D Thesis in French). Université de Toulouse, Université Toulouse III - Paul Sabatier.

Lemaitre, J., 1971. Evaluation of dissipation and damage in metals In ICM Kyoto, 1971.

Lemaitre, J., Chaboche, J.-L., Benallal, A., Desmorat, R., 2009. Mécanique des matériaux solides - 3ème édition. Dunod.

Leroux, A., 2012. Modèle multiaxial d'endommagement anisotrope : gestion numérique de la rupture et application à la ruine de structures en béton armé sous impacts (phdthesis). École normale supérieure de Cachan - ENS Cachan.

Llau, A., 2016. Méthodes de simulation du comportement mécanique non linéaire des grandes structures en béton armé et précontraint: Condensation adaptative en contexte aléatoire et représentation des hétérogénéités (Ph.D Thesis in French). Université Grenoble Alpes, Grenoble, France.

Lutz, L.A., Gergely, P., 1967. Mechanics of Bond and Slip of Deformed Bars in Concrete. J. Proc. 64, 711–721.

Makani, A., 2011. Influence de la nature minéralogique des granulats sur le comportement mécanique différé des bétons. (Ph.D Thesis in French). Toulouse, INSA.

Mantoglou, A., Wilson, J.L., 1982. The Turning Bands Method for simulation of random fields using line generation by a spectral method. Water Resour. Res. 18, 1379–1394. doi:10.1029/WR018i005p01379

Matallah, M., La Borderie, C., Maurel, O., 2010. A practical method to estimate crack openings in concrete structures. Int. J. Numer. Anal. Methods Geomech. 34, 1615–1633. doi:10.1002/nag.876

Matheron, G., 1973. The Intrinsic Random Functions and Their Applications. Adv. Appl. Probab. 5, 439–468. doi:10.2307/1425829

Mazars, J., 1986. A description of micro- and macroscale damage of concrete structures. Eng. Fract. Mech. 25, 729–737. doi:10.1016/0013-7944(86)90036-6

MC 2010, fib, 2013. fib Model Code for Concrete Structures 2010.

Mensi, R., Acker, P., Attolou, A., 1988. Séchage du béton: analyse et modélisation. Mater. Struct. 21, 3–12. doi:10.1007/BF02472523

Michou, A., 2015. Analyse expérimentale et modélisation du comportement de structures précontraintes (Ph.D Thesis in French). Université Pierre et Marie Curie - Paris VI.

Michou, A., Hilaire, A., Benboudjema, F., Nahas, G., Wyniecki, P., Berthaud, Y., 2015. Reinforcement–concrete bond behavior: Experimentation in drying conditions and meso-scale modeling. Eng. Struct. 101, 570–582. doi:10.1016/j.engstruct.2015.07.028

Michou, A., Hilaire, A., Desodt, C., Benboudjema, F., Nahas, G., Wyniecki, P., Berthaud, Y., 2014. Drying Shrinkage Effect on Cracking and Structural Strength of Reinforced Concrete Structures. CONMOD 2014 - RILEM Int. Symp. Concr. Model.

Millard, A., Vivier, M., 2006. Modelling of tests performed in order to evaluate the residual strength of corroded beams in the framework of the benchmark of the rance beams. J. Phys. IV Proc. 136, 151–158. doi:10.1051/jp4:2006136016

Mivelaz, P., 1996. Etanchéité des Structures en Béton Armé : Fuites au Travers d'un élément fissuré (Ph.D Thesis in French). Ecole Polytechnique Fédérale de Lausanne.

Moës, N., Dolbow, J., Belytschko, T., 1999. A finite element method for crack growth without remeshing. Int. J. Numer. Methods Eng. 46, 131–150. doi:10.1002/(SICI)1097-0207(19990910)46:1<131::AID-NME726>3.0.CO;2-J

Mosley, B., Bungey, J., Hulse, R., 2007. Reinforced Concrete Design, Sixth Edition. ed. Palgrave Macmillan.

NF EN 10080, 2005. NF EN 10080: 2005-09 Aciers pour l'armature du béton - Aciers soudables pour béton armé - Généralités.

Ollivier, J.-P., Vichot, A., 2008. La Durabilité des Bétons Bases scientifiques pour la formulation des bétons durables dans leur environnement, 2è Edition. ed. Presses de l'école national des Ponts et Chaussées, Paris.

Orteu, J.-J., 2002. Mesure 3D de formes et de déformations par stéréovision. Tech. Ing.

Ouglova, A., 2004. Etude du comportement mécanique des structures en béton armé atteintes par la corrosion. Cachan, Ecole normale supérieure.

PN CEOS.fr, 2009. PN CEOS.fr [WWW Document]. URL http://www.ceosfr.irex.asso.fr/en/ (accessed 3.16.16).

Rashid, Y.R., 1968. Ultimate strength analysis of prestressed concrete pressure vessels. Nucl. Eng. Des. 7, 334–344. doi:10.1016/0029-5493(68)90066-6

RILEM, 1985. Determination of the fracture energy of mortar and concrete by means of three-point bend tests on notched beams. Mater. Struct. 18, 287–290. doi:10.1007/BF02472918

RILEM, 1970. RILEM, Essais portant sur l'adhérence des armatures du béton: 2: Essai par traction. Mat. Struct 3, 175–178.

Rossi, P., Wu, X., 1992. Probabilistic model for material behaviour analysis and appraisement of concrete structures. Mag. Concr. Res. 44, 271–280. doi:10.1680/macr.1992.44.161.271

Rossi, P., Wu, X., Maou, F.L., Belloc, A., 1994. Scale effect on concrete in tension. Mater. Struct. 27, 437–444. doi:10.1007/BF02473447

Rots, J.G., Blaauwendraad, J., 1989. Crack Models for Concrete: Discrete or Smeared Fixed, Multi-directional or Rotating? HERON 34, 59.

Roux, S., Réthoré, J., Hild, F., 2009. Digital image correlation and fracture: an advanced technique for estimating stress intensity factors of 2D and 3D cracks. J. Phys. Appl. Phys. 42, 214004. doi:10.1088/0022-3727/42/21/214004

Sellier, A., Bary, B., 2002. Coupled damage tensors and weakest link theory for the description of crack induced anisotropy in concrete. Eng. Fract. Mech. 69, 1925–1939. doi:10.1016/S0013-7944(02)00069-3

Sellier, A., Buffo-Lacarrière, L., 2009. Vers une modélisation simple et unifiée du fluage propre, du retrait et du fluage en dessiccation du béton. Eur. J. Environ. Civ. Eng. 13, 1161–1182. doi:10.1080/19648189.2009.9693184

Sellier, A., Casaux-Ginestet, G., Buffo-Lacarrière, L., Bourbon, X., 2013a. Orthotropic damage coupled with localized crack reclosure processing: Part II: Applications. Eng. Fract. Mech. 97, 168–185. doi:10.1016/j.engfracmech.2012.10.016

Sellier, A., Casaux-Ginestet, G., Buffo-Lacarrière, L., Bourbon, X., 2013b. Orthotropic damage coupled with localized crack reclosure processing. Part I: Constitutive laws. Eng. Fract. Mech. 97, 148–167. doi:10.1016/j.engfracmech.2012.10.012

Sellier, A., Millard, A., 2014. Weakest link and localisation WL2: a method to conciliate probabilistic and energetic scale effects in numerical models. Eur. J. Environ. Civ. Eng. 18, 1177–1191. doi:10.1080/19648189.2014.906368

Sellier, A., Multon, S., Buffo-Lacarrière, L., Vidal, T., Bourbon, X., Camps, G., 2016. Concrete creep modelling for structural applications: non-linearity, multi-axiality, hydration, temperature and drying effects. Cem. Concr. Res. 79, 301–315. doi:10.1016/j.cemconres.2015.10.001

Solutions, C., 2012. Vic-3D v7 Testing Guide. www.CorrelatedSolutions.com.

Sutton, M., Wolters, W., Peters, W., Ranson, W., McNeill, S., 1983. Determination of displacements using an improved digital correlation method. Image Vis. Comput. 1, 133–139. doi:10.1016/0262-8856(83)90064-1

Theiner, Y., Hofstetter, G., 2009. Numerical prediction of crack propagation and crack widths in concrete structures. Eng. Struct. 31, 1832–1840. doi:10.1016/j.engstruct.2009.02.041

Tixier, A., 2013. Analyse du comportement de l'interface acier-béton pas essai push-in. Mesures par fibres optiques et modélisation par éléments finis (Ph.D Thesis in French). Grenoble.

Torre-Casanova, A., Jason, L., Davenne, L., Pinelli, X., 2013. Confinement effects on the steel–concrete bond strength and pull-out failure. Eng. Fract. Mech. 97, 92–104. doi:10.1016/j.engfracmech.2012.10.013

Tran, B.H., Berthaud, Y., Ragueneau, F., 2007. Essais PIAF : Pour Identifier l'Adhérence et le Frottement. 18 Ème Congrès Fr. Mécanique Grenoble.

Van der Have, R.C., 2015. Random Fields for Non-Linear Finite Element Analysis of Reinforced Concrete (Master Thesis). TU Delft: Civil Engineering and Geosciences: Structural Engineering, Delft, Germany.

Van-Genuchten, M.T., 1980. A Closed-form Equation for Predicting the Hydraulic Conductivity of Unsaturated Soils. Soil Sci. Soc. Am. J. 445 892–898. doi:10.2136/sssaj1980.03615995004400050002x

Weibull, 1939. Ingeniørs Vetenskaps Akademien Handlingar 1–45.

Wight, J.K., MacGregor, J.G., 2011. Reinforced Concrete: Mechanics and Design, 6 edition. ed. Prentice Hall, Upper Saddle River, N.J.

This page is intentionally left blank

Appendix A

Interfacial Transition Zone Application on RC T-Beam

In this section, another application of the volumetric interfacial transition zone behaviour on structural element of Reinforced Concrete (RC) structures is analysed. This work consists of experimental and modelling of RC beam with a T-shaped section.

This page is intentionally left blank

A. 1. Introduction

In the second chapter, the development of the steel-concrete bond behaviour was discussed. Then, in the third chapter, the consideration of shrinkage and random mechanical properties on RC modelling were discussed. Their importance in RC modelling to obtain the better agreement to the experimental results was proven. In this section, another application of interfacial transition zone is studied. This time is an application on RC beam with a T-shaped section (T-beam) subjected to three-point flexural load. To be clear, the geometrical configuration of the beam is oriented in experimental works that depend on the capacity of the loading machine in LMDC laboratory. Therefore, the dimension of the beam was not in accordance with the standard building Eurocode 2.

A. 2. Material Characterisation

Characteristic tests for each material were performed to obtain the material properties of concrete and steel reinforcement bar, also to determine the local behaviour law of the interface zone by performing the pull-out test.

A. 2. 1. Concrete

Table A. 1. Mix design of concrete materials.

Type of concrete	Normal concrete
W/C	0,6
Type of sand **Type of aggregates**	0/4 mm (700 kg/m^3) - silica alluvial sand Garonne 4/10 mm (1100 kg/m^3) - silica alluvial aggregates Garonne
Type of Cement	CEM I 52,5 R CE CP2 (350 kg/m^3) (High resistance Portland cement for aggressive environments)

Table A. 2. Mechanical properties of concrete.

Concrete compressive strength*	R_c	=	40,73	MPa
Concrete tensile strength* (Brazilian test)	R_t	=	2,98	MPa
Concrete modulus of elasticity*	E	=	29750	MPa
Concrete fracture energy	G_t^f	=	122,47	J/m²

* Average value of experimental results at 67 days of concrete casting

A. 2. 2. Steel bar reinforcement

Table A. 3. Mechanical properties of steel reinforcement bar.

Reinforcing Bar : Fe E 500 HLE (High Strength Steel)				
Nominal diameter of HA steel bar (NF EN 10080, 2005)	ϕ_n	=	16	mm
Yield strength‡	f_y	=	520,06 ± 4,52	MPa
Modulus of elasticity‡	E	=	198,50 ± 1,33	GPa

‡ Average ± standard deviation value of tensile test results from 3 reinforcement bars

A. 2. 3. Interface by pull-out test

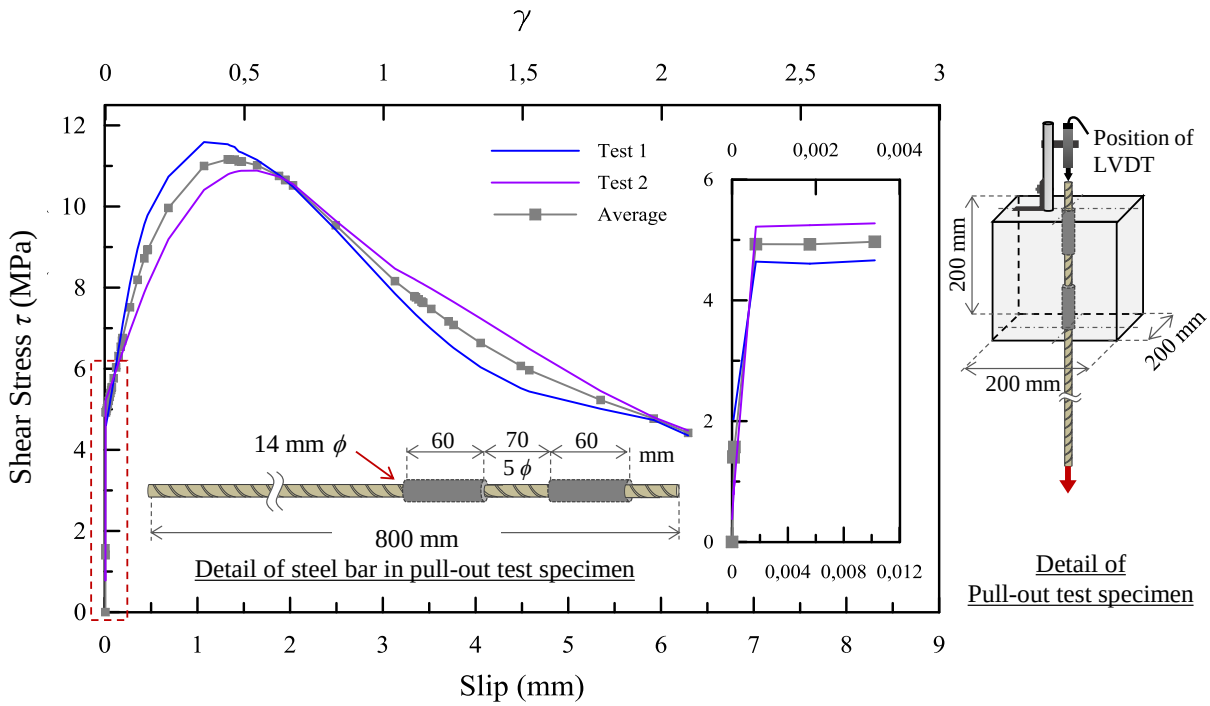

Figure A. 1. Pull-out test: experimental results and details of the specimen.

A. 3. Experimental Campaign

The experimental works performed within the context of this study is a three-point flexural test in an RC beam with a T-shaped cross section. The detail of experiment and the installation of DIC systems are presented.

A. 3. 1. Detail of experiment

In Figure A.2, the detail and the configuration of RC beam are presented. There were three steel bars cast as one packet (bundled) with only one bar on the bottom that went to the both ends of RC beam. After 67 days, a three-point flexural test was conducted on a T-beam with the depth of 40 cm, the thickness of flange 4 cm, the length of 232 cm that led to an affective span equals to 228 cm. The photo of its installation in the loading frame is presented in Figure A.4. With the capacity of loading up to 600 tonnes, the hydraulic actuator loading machine was applied at the distance 90 cm from support A. An imposed load was performed up to the rupture of the RC beam. Area of interest for crack observation is located between two points A and B due to the condition in the laboratory (see Figure A.4). Then, an LVDT extensometer is employed to measure the displacement in the vertical direction at point B (90 cm from support A) to be compared to DIC results. This experiment allowed us to observe the shear crack propagation.

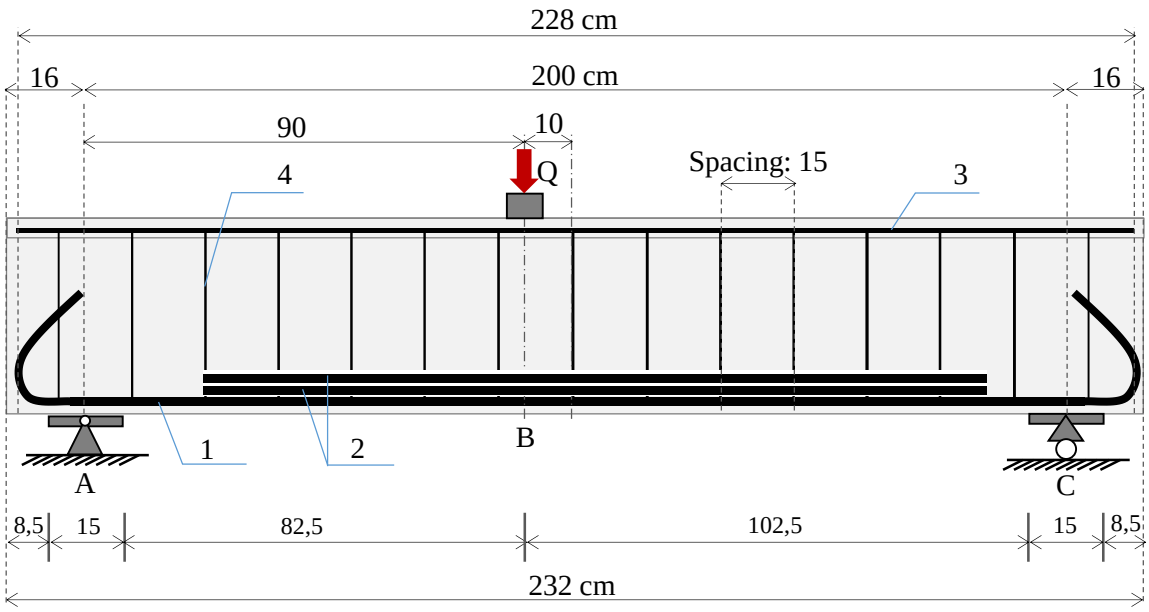

Figure A. 2. Detail dimensions of RC T-beam and its loading point.

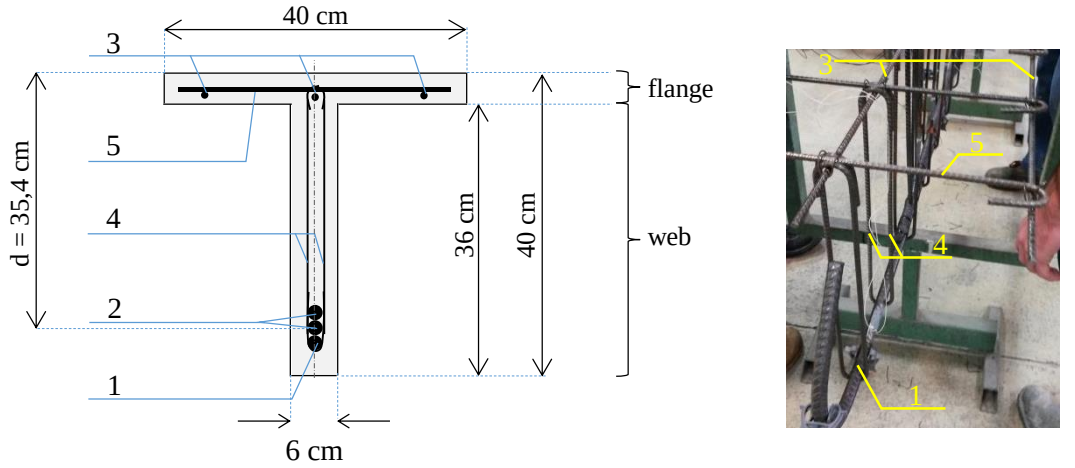

(a) Detail of section.

(b) Photo of reinforcements.

Figure A. 3. Detail of T-shaped section.

Table A. 4. Detail of steel reinforcement bar.

No.	Name	Number	Type	φ (mm)	Length (mm)	Spacing (cm)
1	Longitudinal bar	1	Ribbed bar	16	2688	-
2	Longitudinal bar	2	Ribbed bar	16	1600	-
3	Longitudinal bar	3	Ribbed bar	6	2280	-
4	Closed-hook	15	Ribbed bar	6	839	15
5	Opened-hook	15	Ribbed bar	6	470	15

A. 3. 2. Installation of DIC system

Using the same technique as presented in Chapter 2 and 3, the DIC system was used to observe the appearance of cracks on the concrete surface. Two cameras integrated into the system were installed to observe the behaviour of the specimen throughout the duration of the test as schematically shown in Figure A.4. The LMDC DIC measurement system has 5,0 MP

cameras with relatively small focal length (8,0 mm). In this experimental work, 2444 x 1332 pixels photos were taken at a rate of two frames per second.

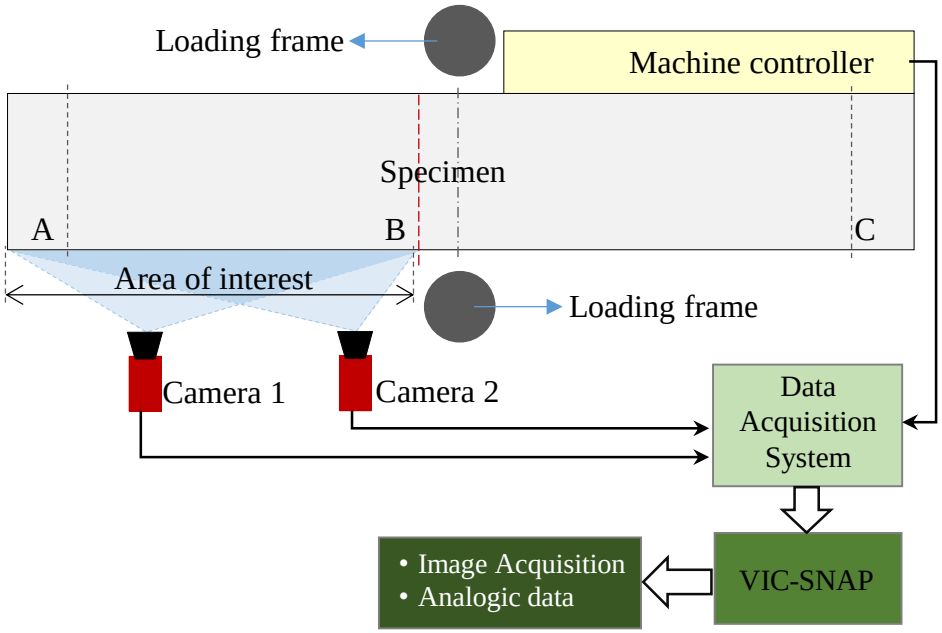

(a) Schema of DIC system installation for RC T-beam (seen from above).

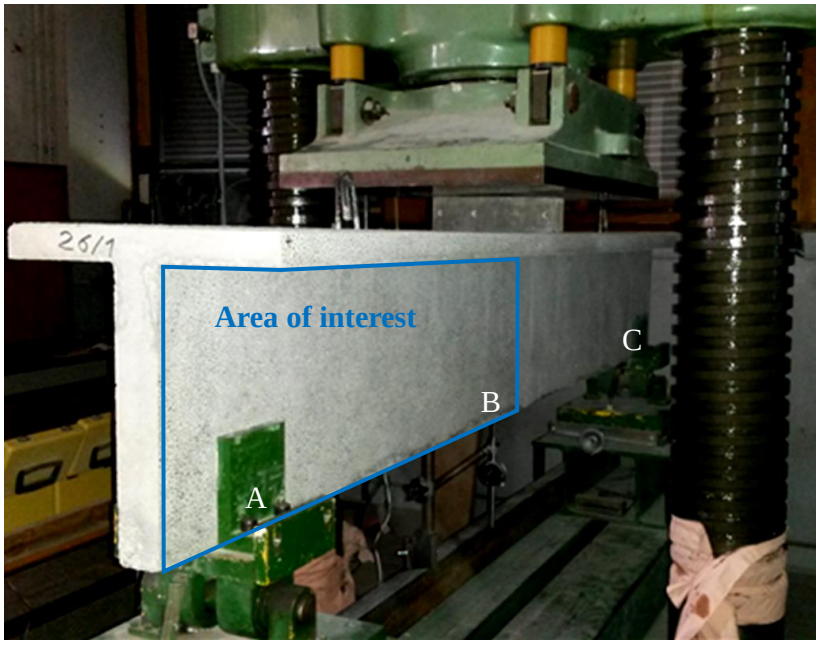

(b) Photo of T-beam: entire volume and the hydraulic jack system.

(c) Support A: Pin support.

(d) Support C: Roller support.

Figure A. 4. Installation of RC T-beam in LMDC laboratory.

Since the area of interest of this test was from A to B (indicated in the figure), a half of RC beam surface was treated with a black and white speckle pattern as presented in Figure A.4 (b). The size of the black speckle is 3,5 - 7 mm that was obtained from the function of the opening of the two cameras' focal length, the dimension of the area of interest, the distance between two cameras, the longest and the closest distance from the camera to the edge of the area of interest (kilonewton Sarl, 2010). The same technique to apply speckle as explained before was employed.

In the post treatment, every zone of interest of the image is divided into several finite subsets (or sub-images). The chosen size of one subset is **7 mm x 7 mm or 21 x 21 pixels** (one pixel represents approximately 350 µm.). Uncertainty in displacement field that determines the error is around 2,1% pixels. Thus, the uncertainty of displacement field is 7,5 µm.

A. 3. 3. Experimental results

In this section, the global behaviour and crack pattern from experimental results are presented. The correspondence of image correlation and LVDT in measuring the vertical displacement under the loading point application is also presented.

a. Global Behaviour: Force-Vertical Displacement

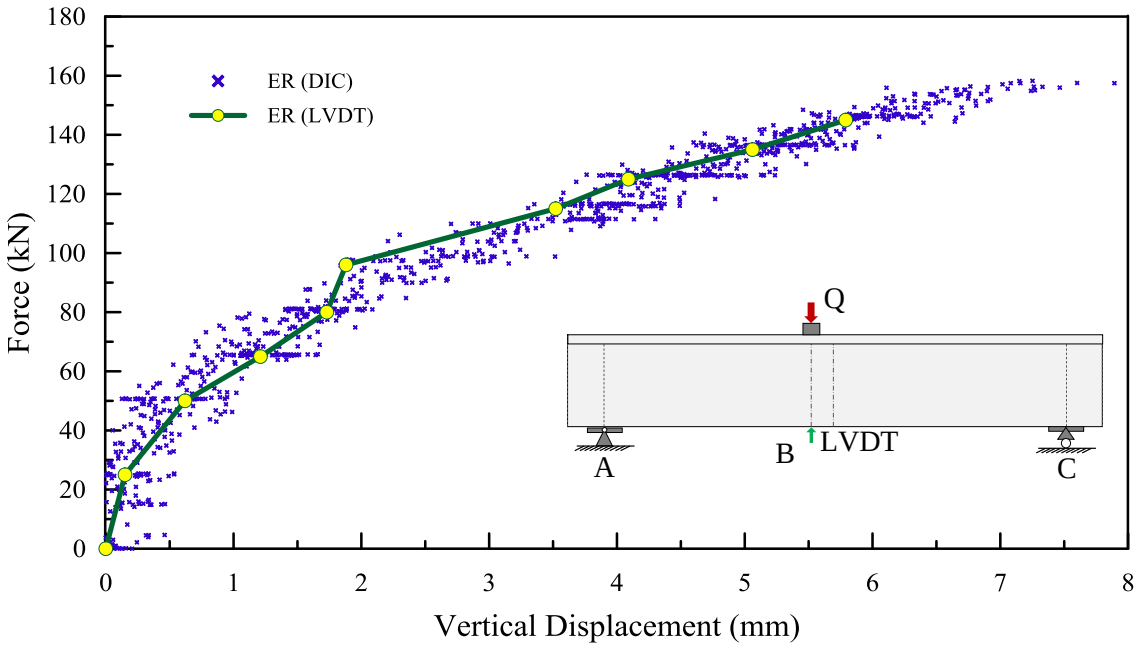

Figure A. 5. Global behaviour, vertical displacement *Uz* under the loading application of T-beam measured by LVDT extensometer and DIC.

In Figure A.5 global behaviour of T-beam measured by LVDT and DIC under the loading point are compared. Although noises occurred on DIC system results, this system was able to produce the same measurement in vertical displacement. In the next part, DIC system is used to observe the cracking pattern and the local crack opening.

b. Cracking pattern and opening

The sketch of the beam with the measurement point using LVDT and the position of loading points is superposed with the displacement field reproduced by DIC system (see Figure A.6). The same colour represents the same range of displacement.

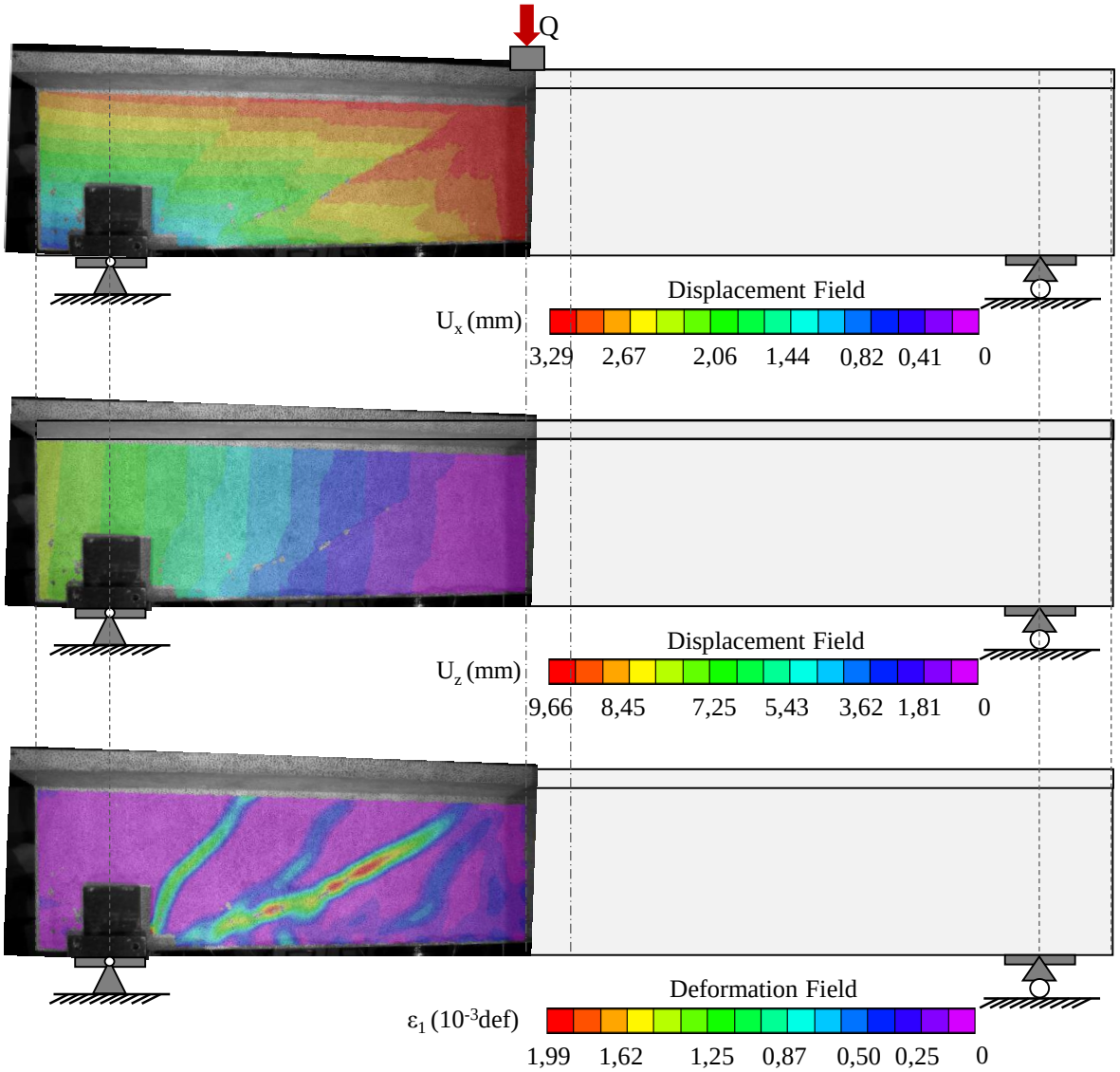

Figure A. 6. Experimental Results using DIC at 145 kN.
(a) and (b) Displacement field in Ux and Uz to visually show crack opening. (c) Deformation Field and crack opening evolution in major direction.

In Figure A.7, the evolution of crack is displayed from the deformation field in major principal direction ε_1. Even if the deformation field around a crack has none physical meaning, since the crack displacement is localised, it is convenient to use it as crack positions indicator.

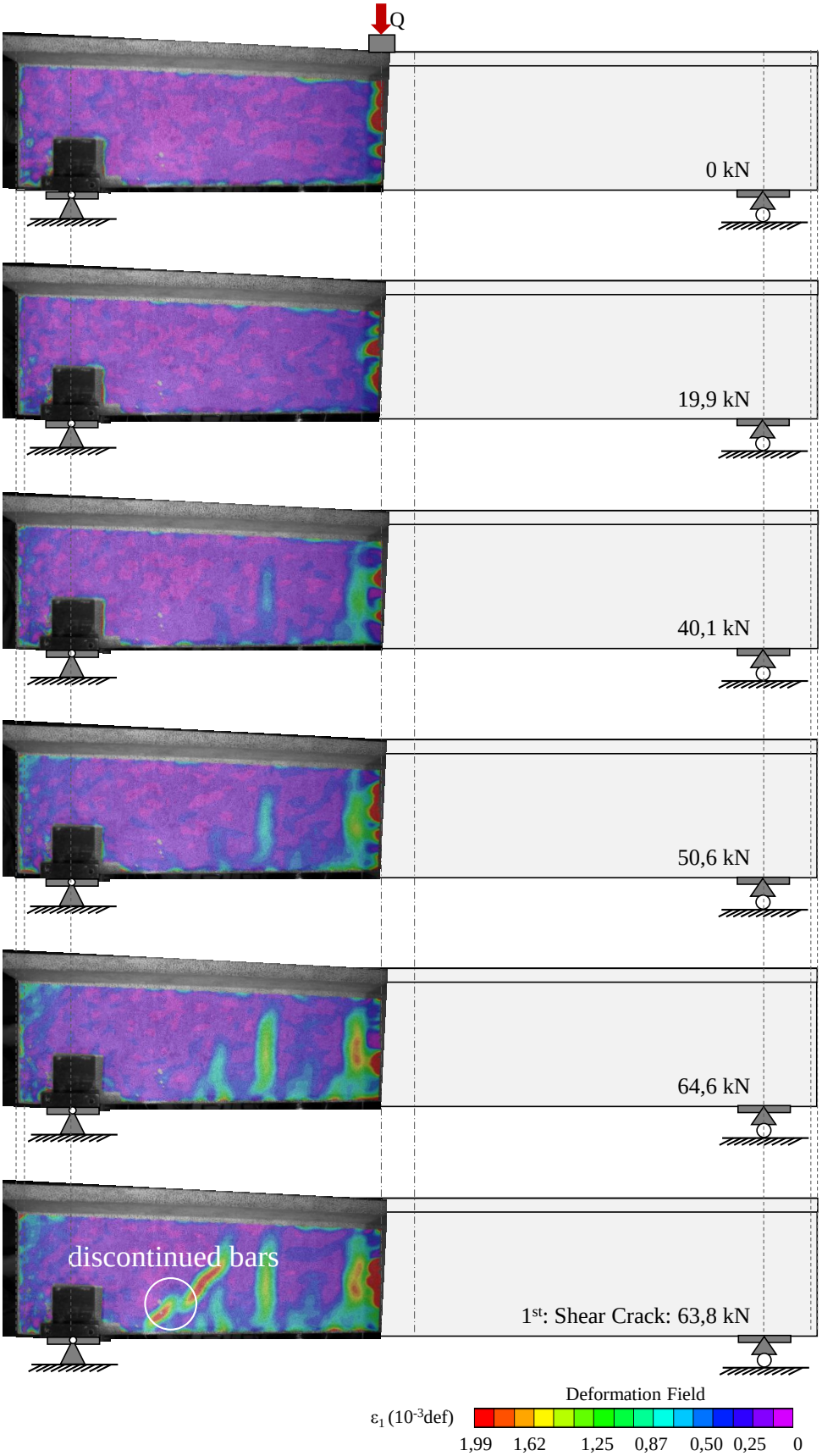

(a). Evolution from 0 to 63,8 kN (1st Shear Crack).

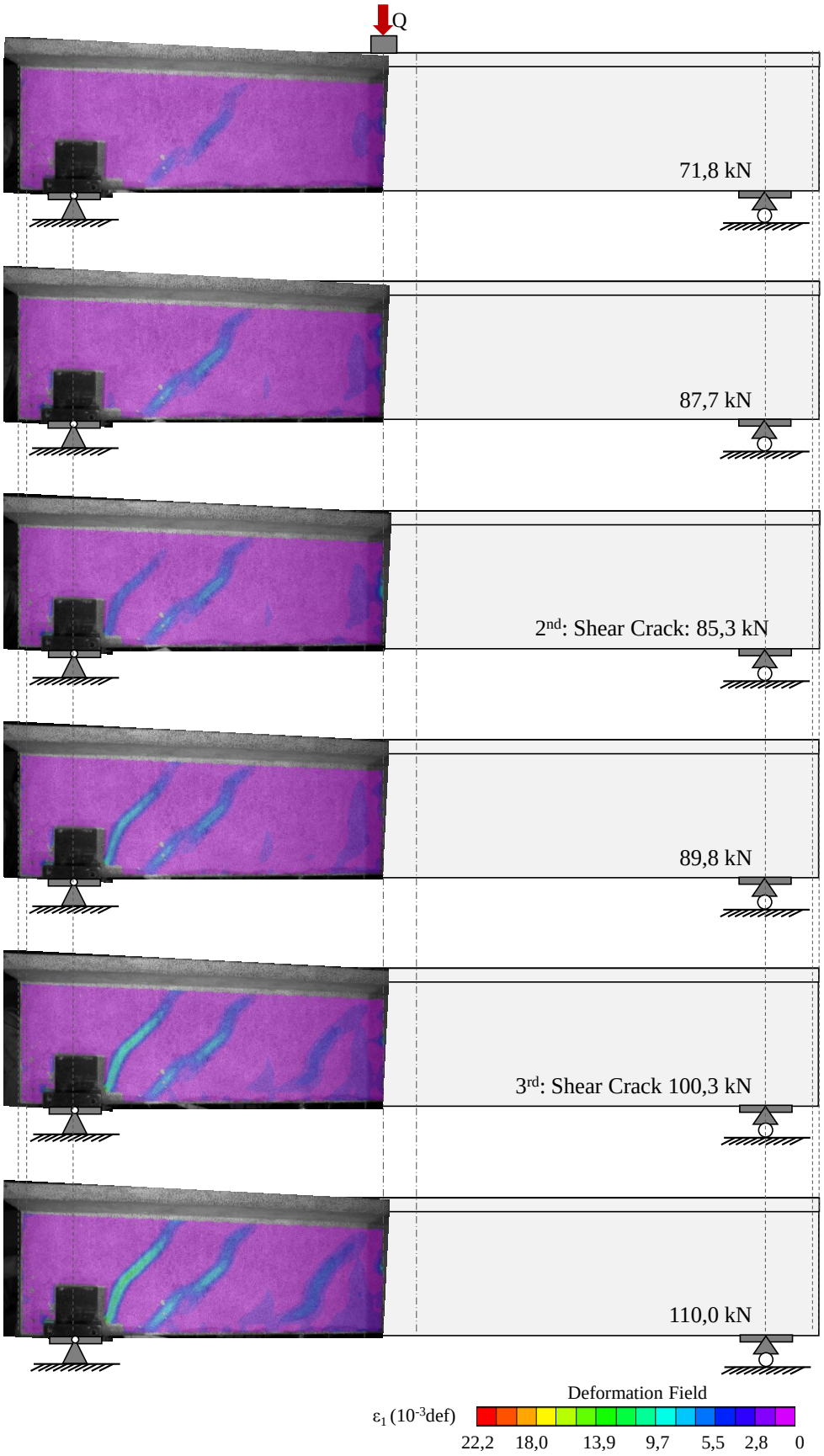

(b). Evolution from 71,8 to 110,0 kN.

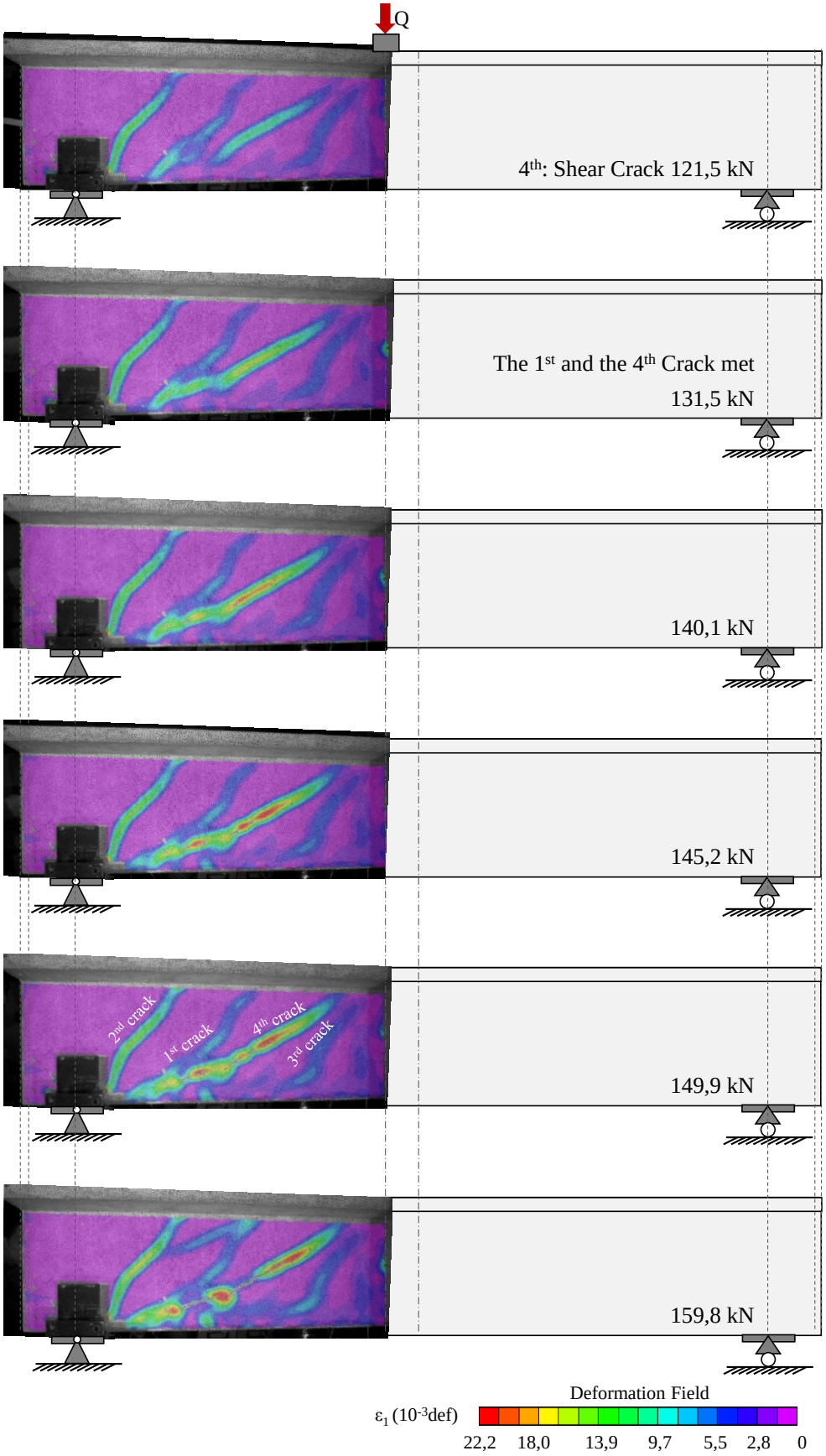

(c). Evolution from 121,5 to 159,8 kN.

Figure A. 7. Experimental results (DIC): evolution of cracking pattern observed on deformation field in major direction (ε_1).

As presented in the previous figures, at least four shear cracks propagated at 121 kN of loading application on the observation surface. The first shear crack appeared at 63,8 kN and was initiated on the discontinued longitudinal bars. Very close to the support A, the second shear crack appeared at 85,3 kN. Moreover, at 100,3 kN, the third shear crack appeared. And it was followed by the appearance of the fourth one at 121 kN. The fourth shear crack collided to the first one and was forming larger crack and spall off the concrete on the further loading application. The horizontal space between the first and the third crack was around 32 cm.

The crack opening was extracted from five different locations. Their measurements and their evolutions are shown in Figure A.8 below superposed with the formation of the crack opening at 145 kN. From these curves, we can see the moment of the crack propagation for each crack. This evolution confirms the crack initiation as mentioned in the previous paragraph and observed in Figure A.7.

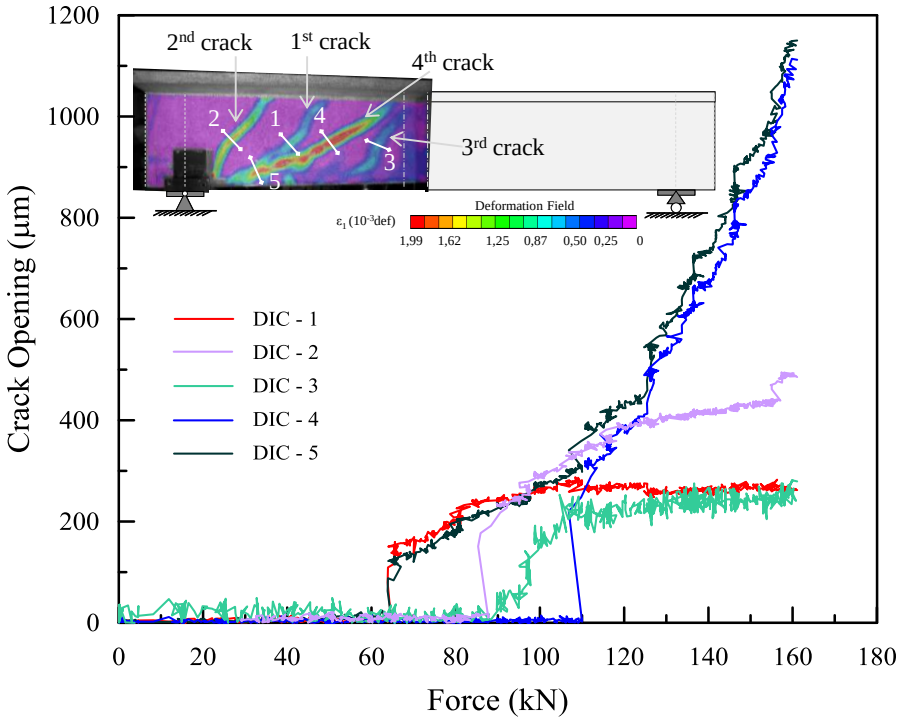

Figure A. 8. The evolution of crack opening observed at five different locations.

A. 4. Numerical Modelling

A. 4. 1. Detail of geometry and boundary conditions

Same as in Chapter 2, the equivalent area method is applied to model the steel bar in a square form to facilitate the meshing process. By using the same area (circle with ϕ_n of diameter), we obtain the dimension for square-formed reinforcement. Half of T-beam volume was modelled numerically. All the configuration of reinforcement bars was considered in 3D. As described in Figures A.9 and A.10, interfacial transition zone was meshed around the steel bar

reinforcements, except for the three longitudinal bars in the flange (HA 6, indicated as number 3 in Figures A.2 and A3). The thickness of interfacial zone was set 3 mm. Loading application was also located at the exact same point as in the experimental works (90 cm from support A) and was applied in imposed displacement in the direction of -z.

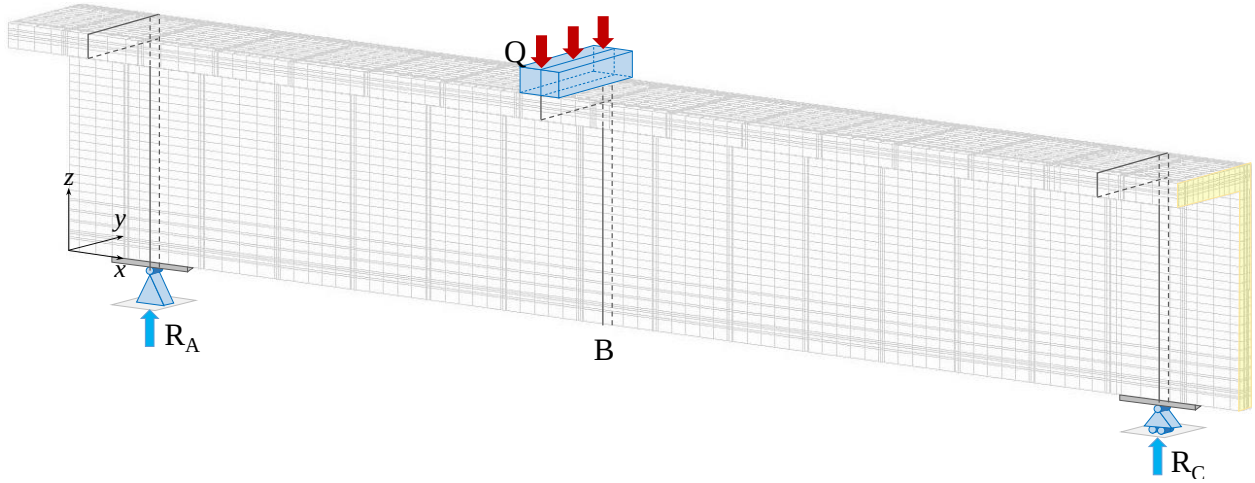

(a). Detail of a half RC T-beam volume: 1st point of view.

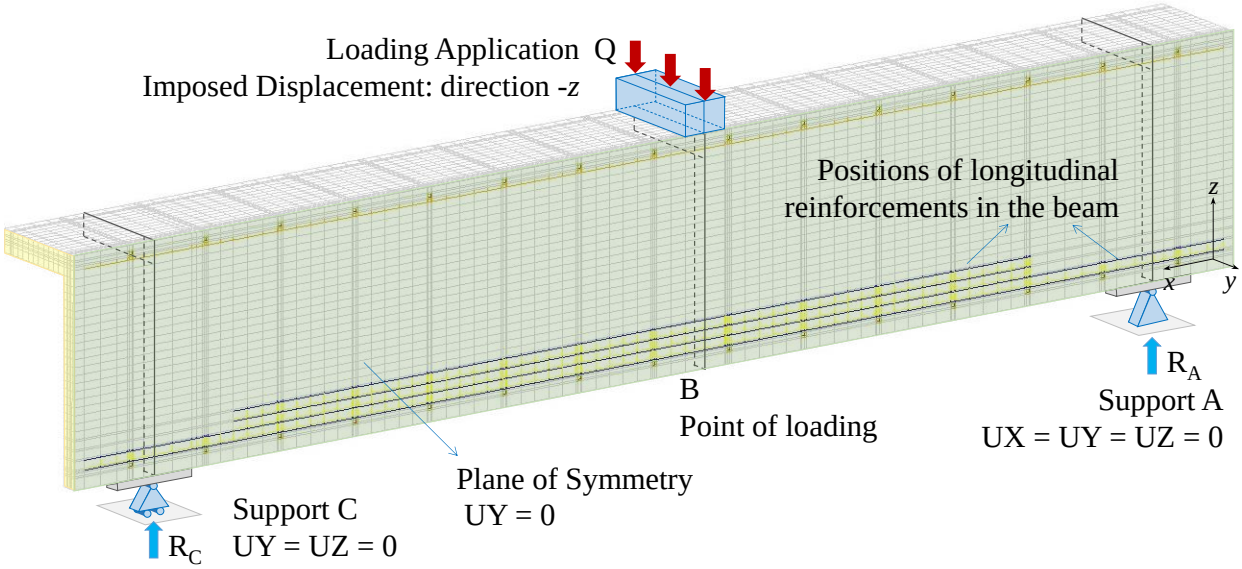

(b). Detail of a half RC T-beam volume: 2nd point of view.

Figure A. 9. Mesh and boundary conditions for modelling: a half of specimen's volume.

The three longitudinal reinforcements (HA16) on the bottom part (web) were numerically configured with one layer of interface zone in between. Two reinforcements number 2 were meshed started from the third stirrup as it was experimentally and created a discontinuity near the third stirrup. The closed and the opened-hook were meshed as one unit (see Figure A.10). Interfacial zone from longitudinal bars and transverse reinforcement are modelled side by side. In the real condition, these two types of reinforcement were attached by fine wires (ligature) that might create voids in between. Interface zone also represents these voids.

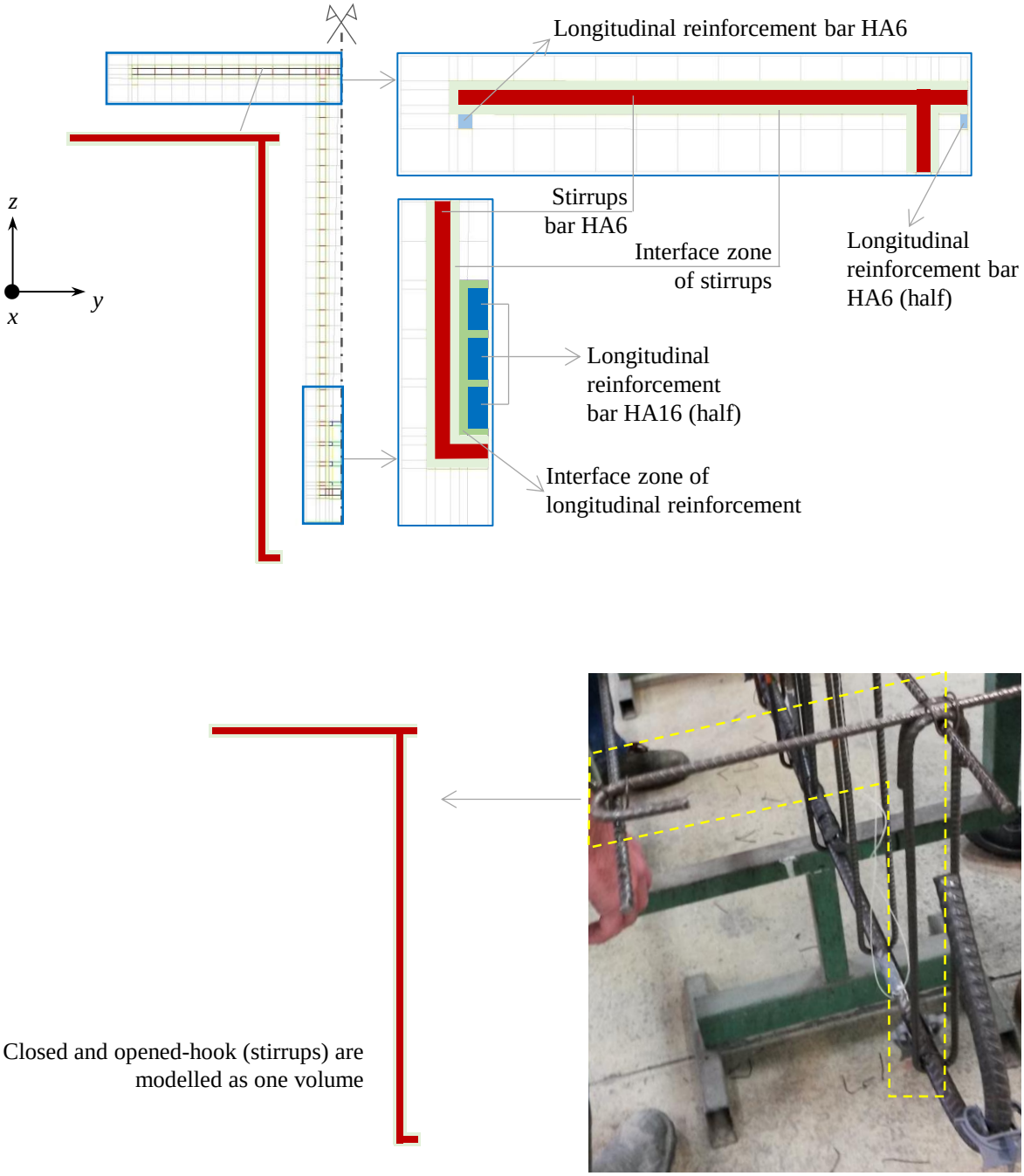

Figure A. 10. Mesh and boundary conditions for modelling: a half of specimen's T-shaped section.
Note: All steel reinforcement bars are meshed in square form (equivalent area method).

A. 4. 2. Behaviour Law

a. Behaviour Law of Plain Concrete

Table A. 5. List of parameters of the concrete materials to be used in modelling using the LMDC Model.

Parameters	Symbol	Value	Unit
Young's Modulus of elasticity	E	29750	MPa
Poisson's ratio	υ	0,27	-
Density	ρ	2400	kg/m^3
Concrete tensile strength	R_t	2,98	MPa
Strain at peak tension	$\varepsilon_{R_t}^{pk}$	$1{,}03\times10^{-4}$	-
Concrete compressive strength	R_c	40,73	MPa
Strain at peak uniaxial compression	$\varepsilon_{R_c}^{pk}$	$2{,}0\times10^{-3}$	-
Drucker Prager Confinement coefficient	δ	0,75	-
Dilatancy for non-associated Drucker-Prager plastic flow	β	0,28	-
Characteristic plastic strain for Drucker-Prager associated damage	$\varepsilon^{k,s}$	$8{,}0\times10^{-4}$	-
Fracture energy in tension	G_t^f	122,47	J/m^2

b. Behaviour Law of Steel Reinforcing Bar

The steel reinforcement bar was modelled as elastic-perfectly plastic materials. Based on the experimental tensile test result, the steel bar reached the yield strength of 520,06 MPa and Young's modulus of 198,50 GPa.

c. Behaviour Law of Plastic Sliding Interface

Table A. 6. List of parameters used in the interfacial transition zone.

Parameters	Symbol	Value	Unit
Young's Modulus of elasticity	E	19040	MPa
Poisson's ratio	υ	0	-
Thickness	e_{iz}	3	mm

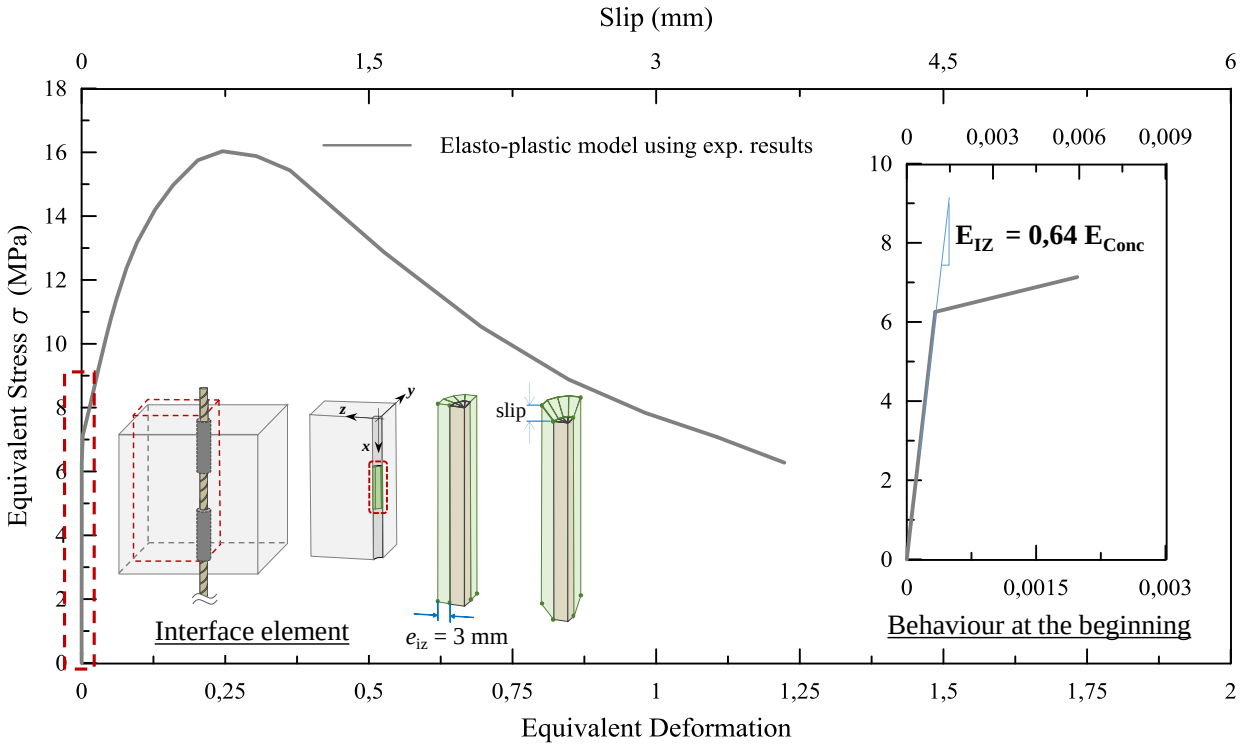

Figure A. 11. Behaviour law interface zone fitted with pull-out experimental results.

The same method developed in Chapter 2 is applied to obtain the behaviour of the interfacial transition zone. The behaviour of the plastic sliding interface is presented in Figure A.11. Using the same correction, the interfacial zone has around 64% of the concrete Young's modulus. This equivalent stress-deformation models the interfacial zone.

A. 5. Numerical Modelling: Application of Sliding Interface

A. 5. 1. Global behaviour

In this section the application of the interfacial zone model is performed, called *Sliding Interface* (SI) model. This numerical simulation was conducted in imposed displacement up to 8 mm. The global result in force – displacement curve is presented in Figure A.12 while the cracking pattern is shown in Figure A.13. We can see in the global behaviour that the initial stiffness of T-beam numerically reached the same results as in the experiment.

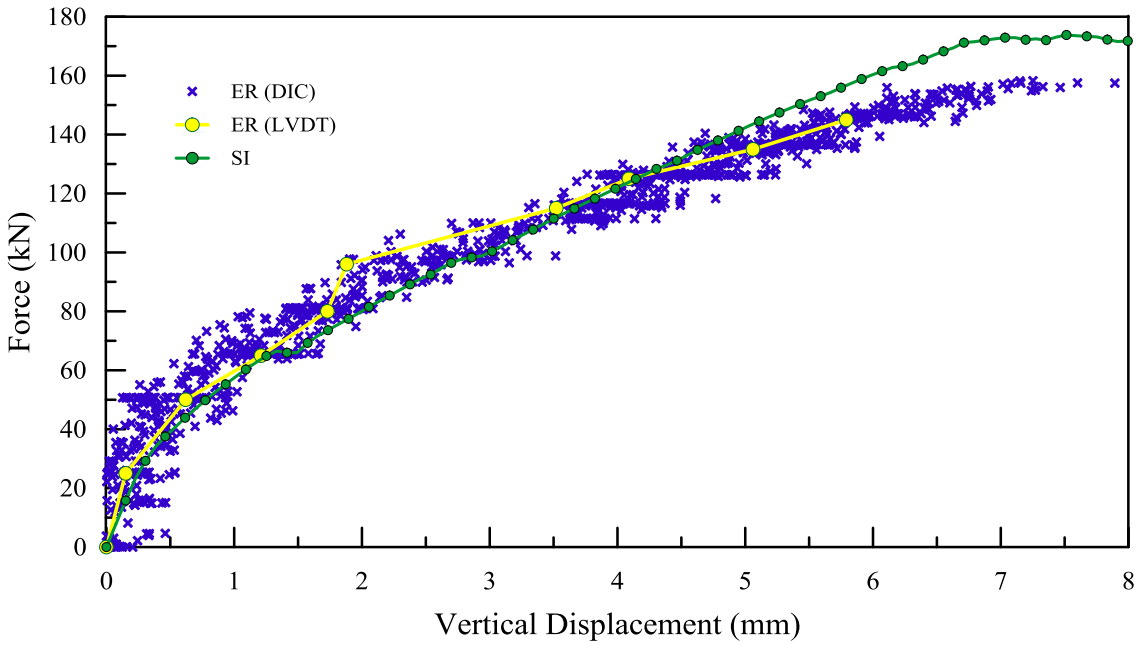

Figure A. 12. Global behaviour: Experimental (ER-DIC and ER-LVDT), Modelling SI (Sliding Interface) results.

A. 5. 2. Crack behaviour (spacing, opening, number, etc.)

As shown in Figure A.13, the cracking pattern of the structure at the end of the test which was obtained experimentally was not exactly the same as the ones from numerical modelling. One shear crack did not propagate numerically. Although the loading was not performed symmetrically, the observation on the other point of view (Figure A.13 (c)) shows that there was also a shear crack close to the support B. From experimental observation, the corresponding cracks close to the two supports did not arrive at the same time. The crack near to support A initiated faster than the one close to support B. To be noted, the red lines in Figure A.13 (c) represent the cracking pattern and the thickness of the line does not represent the crack width.

Application of sliding interface for three longitudinal bars on the bottom part of RC beam was very complicated. Three overlapped bars might be considered as one bar with one interfacial transition zone around. Or, another possibility is to apply one area of interfacial transition zone for each bar. The second proposition that was used in the modelling led to a dependence of the second bar from the first one and so on.

The discontinuities of the two bars (indicated as bar number 2 in Figures A.2 and A3) led to a critical slip condition between concrete and steel bar. These bars were installed between the third stirrup (see Figure A.13) and the fourteenth stirrup with 160 cm in length. This discontinuity became the start point of the first crack initiation (see Figure A.7).

Furthermore, in numerical modelling, the anchorage length of the lowest longitudinal reinforcement was not meshed. The absence of the shear crack near the support A might be caused by this condition. Therefore, a numerical simulation was performed by making the both end of the beam very stiff to represent the anchorage in the second stage. This consideration did not generate the shear crack close to the support A.

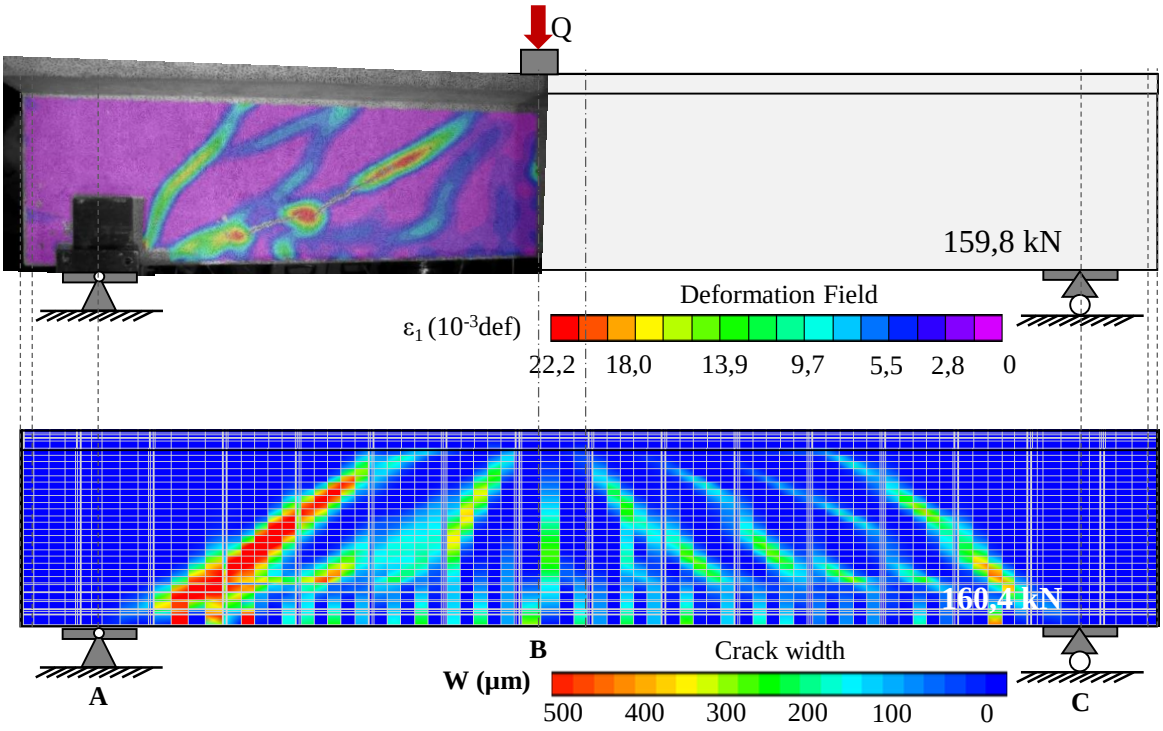

(a) Experimental and Modelling results from point of view 1 at 160 kN.

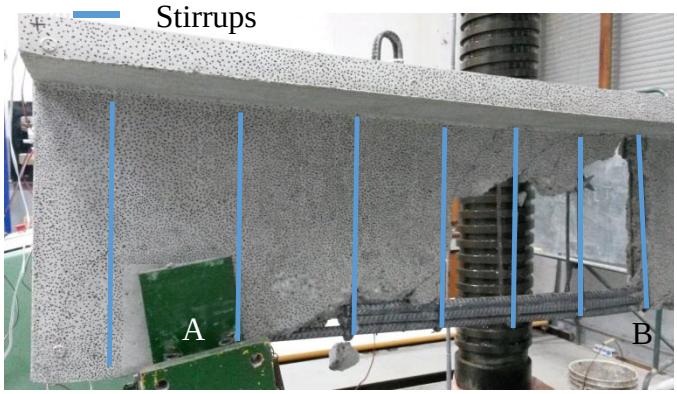

(b) Point of view 1 at the end of the test and after removing the spall off the concrete and the stirrups were already deformed.

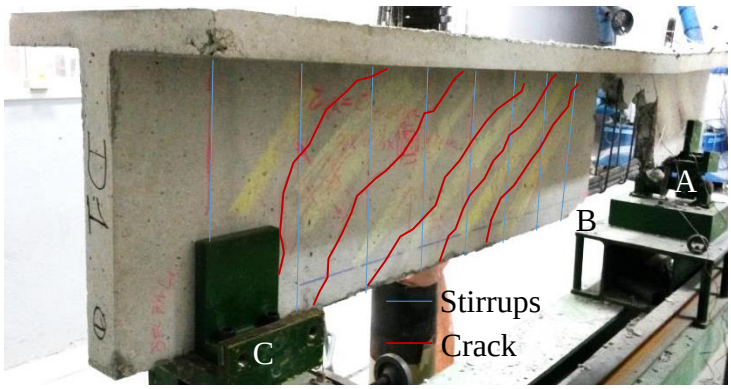

(c) Point of view 2 at the end of the test and after removing the spall off the concrete.

Figure A. 13. Crack pattern: experimental and modelling results.

Another aspect was also considered. Regarding the supports of the T-beam (see Figure A.4 (c)

and (d)), it is possible that there was an effect of friction on the bottom of the beam touching the support. So, in this third stage, a consideration of friction on the support was taken to simulate the boundary condition using an operator called RELA in Cast3M (CEA, 2015). This consideration did not trigger the shear crack close to the support either.

A. 6. Other results of cracking pattern from three-point load on RC T-beam

As it was designated for experimental classes, four other identical T-beams were observed. In this section, the different cracking patterns from experimental classes are shown. The cracking patterns were not the same for these four other samples. We can see that the shear crack near the support might or might not propagate. It is possible that there were some uncertainties in the position of the steel bar reinforcement which led to this instability of the cracking pattern.

Sample 2: There was no shear crack close to the support A.

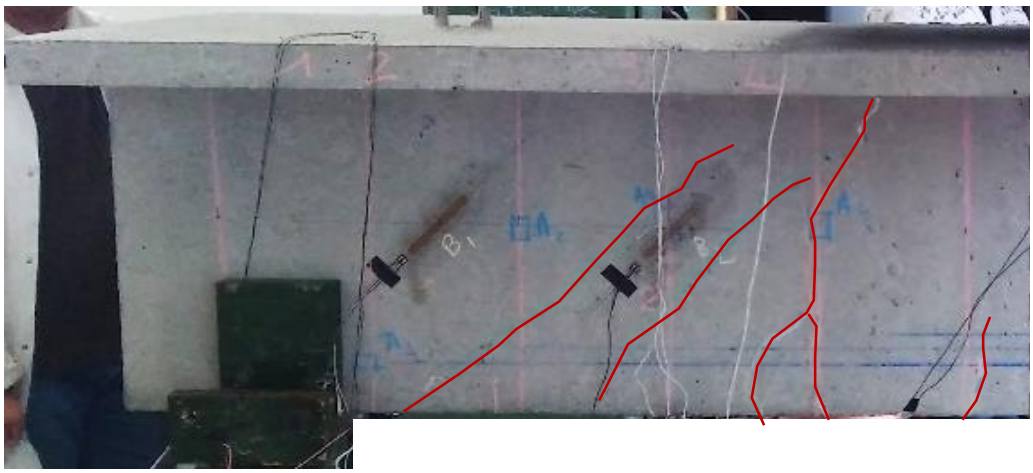

Figure A. 14. Cracking pattern Sample 2.

Sample 3: There was a flexural-shear crack close to the support A.

Figure A. 15. Cracking pattern Sample 3.

Sample 4: There was no shear crack close to the support C (from point of view 2).

Figure A. 16. Cracking pattern Sample 4.

Sample 4: There was one shear crack close to the support A (from point of view 1) but there was no crack near the support C

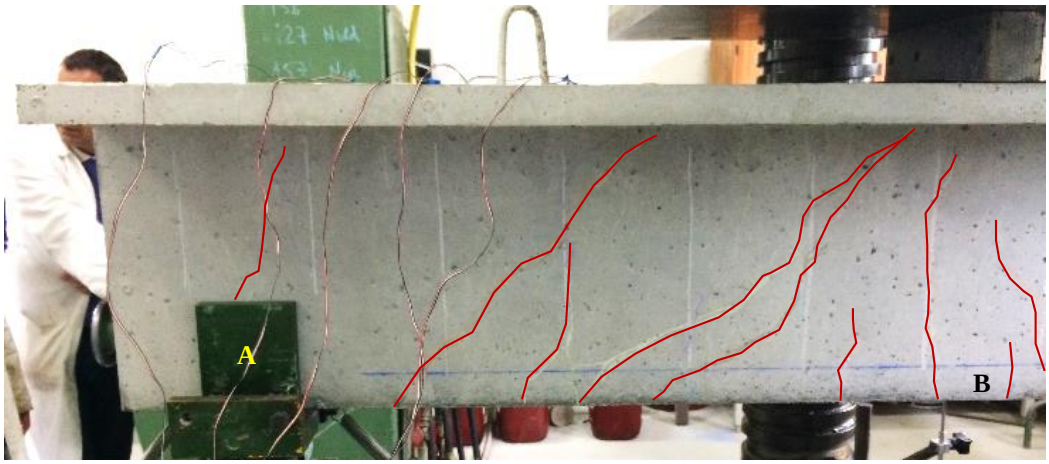

Figure A. 17. Cracking pattern Sample 5: A to B.

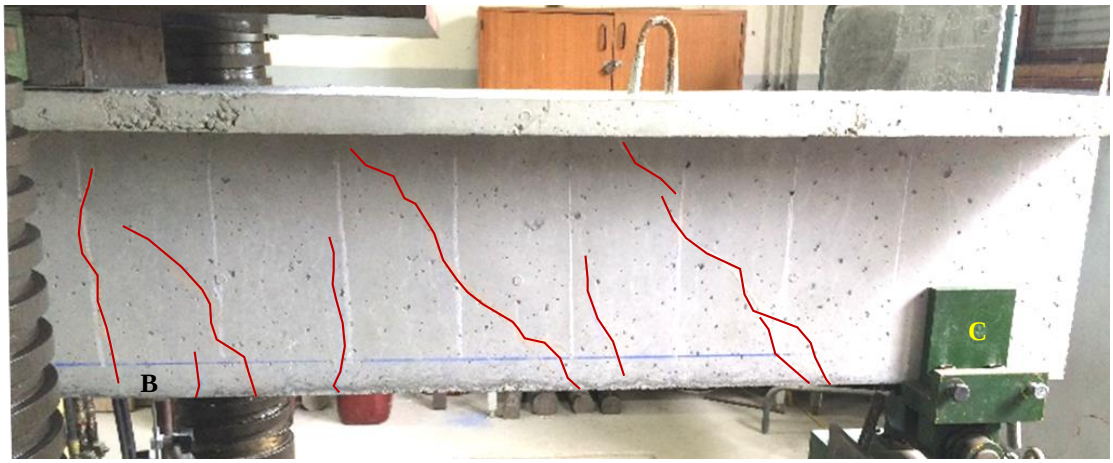

Figure A. 18. Cracking pattern Sample 5: B to C.

A. 7. Conclusion

Application of interfacial transition zone on the T-beam was performed and was able to reproduce a global behaviour quite well. The interfacial might represent the presence of air void in between two reinforcements, especially on the connection between longitudinal bar HA 16 and the closed-hook.

Instability of cracking pattern occurred on this T-beam. Observation from five different samples showed that sometimes shear crack near the support A appeared and some other times it did not appear. On the other hand, a shear crack always occurred on the discontinuity of the bars number 2 (installed near the stirrup number three). The considerations of friction on the supports and the simplified method to model anchorage zone were not successful to reproduce the crack near the support.

A. 8. Perspectives

There are some remarks from the application of homogeneous steel-concrete bond model on T-Beam.

- The detail configuration of the beam shows a bundled of the bars (a package of three bars) in the mid area of the beam (see the configuration in Figure A.2 and A.3), the mesh configuration in the bundled bars is shown in Figure A.19 below.

  The fact that sliding interface was developed from the pull-out tests with a single bar, the numerical application for bundled bars remains questionable. In the present studies, the sliding between bars is assumed to be the same as the sliding of the bars to the concrete materials in the present works. More detailed studies can be performed by changing the behaviour of the interface between the bars. Characteristic tests using bundled bars should be investigated to develop the appropriate interface zone model.

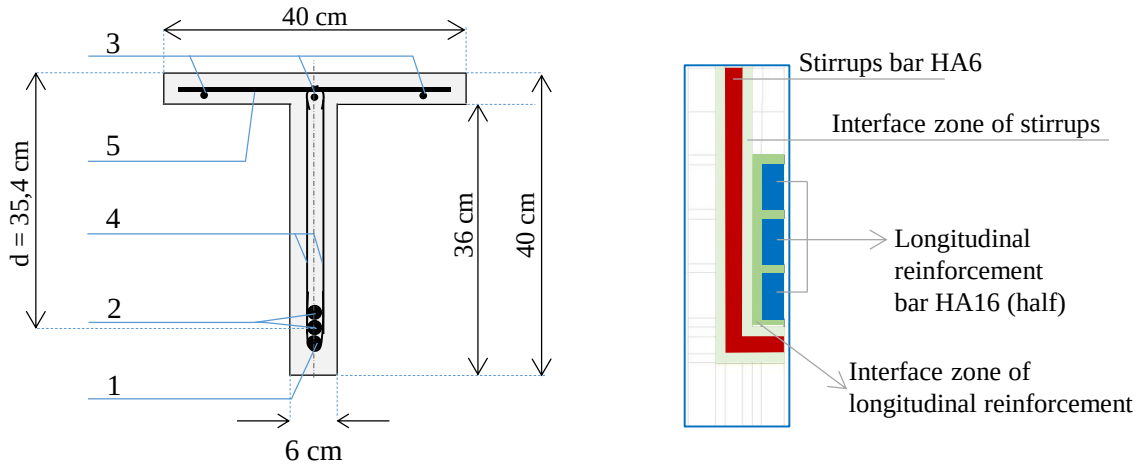

(a) The detail of T-beam section. (b) The configuration in modelling.

Figure A. 19. Detail of T-shaped section.

- Only one longitudinal bar that went to the both end creating a discontinuity of the bundled longitudinal bars (see Figure A.20 (a)). This discontinuity became the start point of the crack propagations. Furthermore, this one bar was curved creating anchorage length. The anchorage length for T-beam beyond the two ends of supports was not modelled exactly as it is (see Figure A.20 (b)).

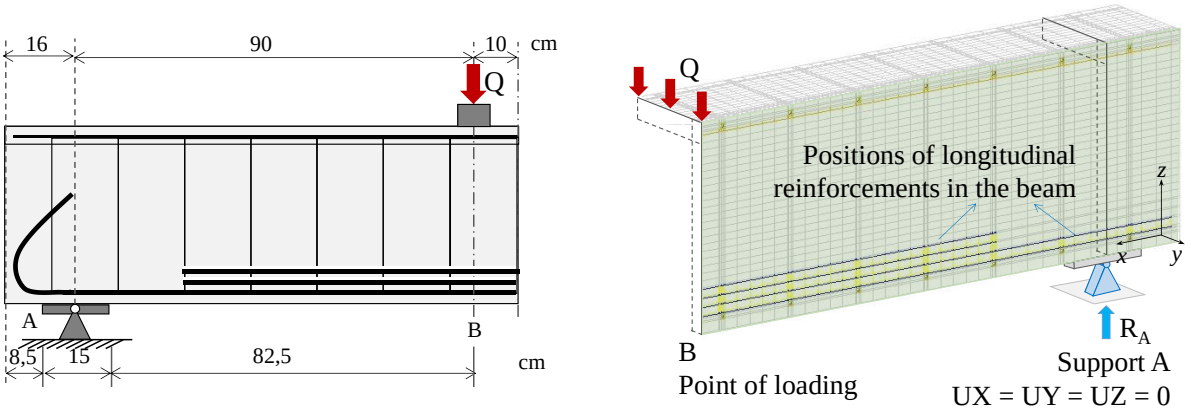

(a) The detail of T-beam from support A to mid-span. (b) The configuration in modelling.

Figure A. 20. Detail of T-shaped beam.

Therefore, more comprehensive studies for the case of T-beam are needed, such as a more detailed configuration of the steel bar inside the beam and a more precise steel-concrete bond for bundled bars that is able to represent the realistic behaviour.

Appendix B

Materials description

In this section, the references of material descriptions are presented.

This page is intentionally left blank

B. 1. Materials used for RC prismatic elements

LAFARGE CIMENTS
Usine du TEIL

CEM I 52,5 N CE PM-ES-CP2 NF

NF EN 197-1 NF P 15-317 XP P15-319 NF P 15-318

NF EN 196-10

Fiche produit technique

CE NF

N°de certificat CE : 0333-CPD-1203

• **Constituants et composition du ciment**

Principaux (%)				Secondaires (%)		Sulfate de calcium (%)		Additifs (g/t)		
Clinker			97	Calcaire (LL)	3	Gypse	2,7	Agent de mouture	AMA 14	1100
C3S	67,9	C4AF	7,9							
C3A	4,05	C2S	19,9							

• **Caractéristiques physiques et mécaniques**

	Valeur usine moyenne	Limites applicables à chacun des résultats (Réf : NF EN 197-1) minimum	Limites applicables à chacun des résultats (Réf : NF EN 197-1) maximum	Limites applicables à chacun des résultats (Réf : annexe 1 du règlement de certification NF002) minimum	Limites applicables à chacun des résultats (Réf : annexe 1 du règlement de certification NF002) maximum
Résistance à la compression 1 jour (MPa)	18,9				
Résistance à la compression 2 jours (MPa)	32,1	18		18	
Résistance à la compression 28 jours (MPa)	67,5	50		50	
Retrait à 28 jours (µm/m)	624,3				
Début de prise (min)	181	40		60	
Stabilité (mm)	0,7		5		5
Masse volumique (g/cm3)	3,16				
Surface spécifique Blaine (cm²/g)	3524,53				
Q12h (J/g)	199,3				
Q41h (J/g)	294,26				
L*	61,6				

• **Caractéristiques chimiques (%)**

MAXI : Valeurs limites applicables à chacun des résultats (Ref : NF EN 197-1, NF P 15-318, NF P 15-317, XP P 15-319)

	Valeur usine moyenne	MAXI			Valeur usine moyenne	MAXI		Valeur usine moyenne	MAXI
SiO2	22,71		S--	<	0,10	0,20	Insolubles	0,35	0,75
Al2O3	3,03	8,00	Cl-	<	0,10	0,10	CO2	0,84	
Fe2O3	2,33		Perte au feu		1,33	3,00	CaO libre	0,54	
CaO	67,00		TiO2		ND			Valeur usine moyenne	Coef var (%)
MgO	0,95	3,00	Cr VI	<	2 PPM	2 PPM			
K2O	0,17		P2O5		0,08		Alcalins actifs	0,21	0,1
Na2O	0,10		Non dosé		-0,03		Na2OEq	0,21	
SO3	2,13	2,50	IS		< 23,5	23,50			
Total : 100									

Ces valeurs, extraites de notre autocontrôle, permettent de vérifier la conformité de notre produit aux spécifications normatives et donnent une indication pour les caractéristiques complémentaires. Elles ne constituent pas un engagement sur les résultats à venir.

■ : Caractéristique modifiée / fiche précédente ND : non dosé ***Révision du 18/03/2011***

Le Teil : livraison en sac et en vrac

GSM Italcementi Group

La Grande Paroisse

Lieu dit les Prêtres de Pinouvent
77130 VARENNES SUR SEINE
Tel 01.60.73.61.70 Fax 01.60.96.15.02 pdegembe@lgp-granulats.fr

Fiche Technique de Produit

Engagement du 08/04/2014 au 08/10/2014
Page 1/1, imprimé le mardi 8 avril 2014

0/4 Reconstitué mixte LGP1

Pétrographie : Alluv.silico-calcaire + chailles — *Utilisateur :* EXTERNE
Elaboration : Roulé

Partie contractuelle

Valeurs spécifiées sur lesquelles le producteur s'engage

Classe granulaire		Norme	Code
0	4	NF P 18-545 Article 10	A

	0.063	0.125	0.16	0.25	0.315	0.5	1	2	4	5.6	8	SE(10)	FM	WA24
V.S.S.+U	7			47			89		100	100	100		3.15	3.00
V.S.S.	6			45			86		99	100	100		3.00	2.50
V.S.I.	0.0			5			45		89	95	100	65.00	2.40	
V.S.I.-U	0.0			3			41		87	94	100	60.00	2.25	
Ecart-type max	1.82			12.12			12.12		3.03	1.52			0.18	

Partie informative

Résultats de production

du 10/10/13 au 04/04/14

	0.063	0.125	0.16	0.25	0.315	0.5	1	2	4	5.6	8	SE(10)	FM	WA24
Maximum	1	10	17	33	42	61	77	89	99	100	100	85.50	2.97	0.70
Xf+1.25xEcart-types	1	8	14	29	39	58	74	86	98	100	100	83.42	2.78	0.73
Moyenne Xf	1	6	12	26	35	53	70	83	97	100	100	77.50	2.64	0.59
Xf-1.25xEcart-types	1	5	10	23	32	49	65	80	96	100	100	71.58	2.49	0.42
Minimum	1	3	9	21	30	47	62	76	96	99	100	67.50	2.42	0.45
Ecart-type	0.1	1.3	1.7	2.4	2.8	3.8	3.5	2.4	0.7	0.1	0.00	4.736	0.120	0.125
Nombre de résultats	46	46	46	46	46	46	46	46	46	46	46	41	46	2

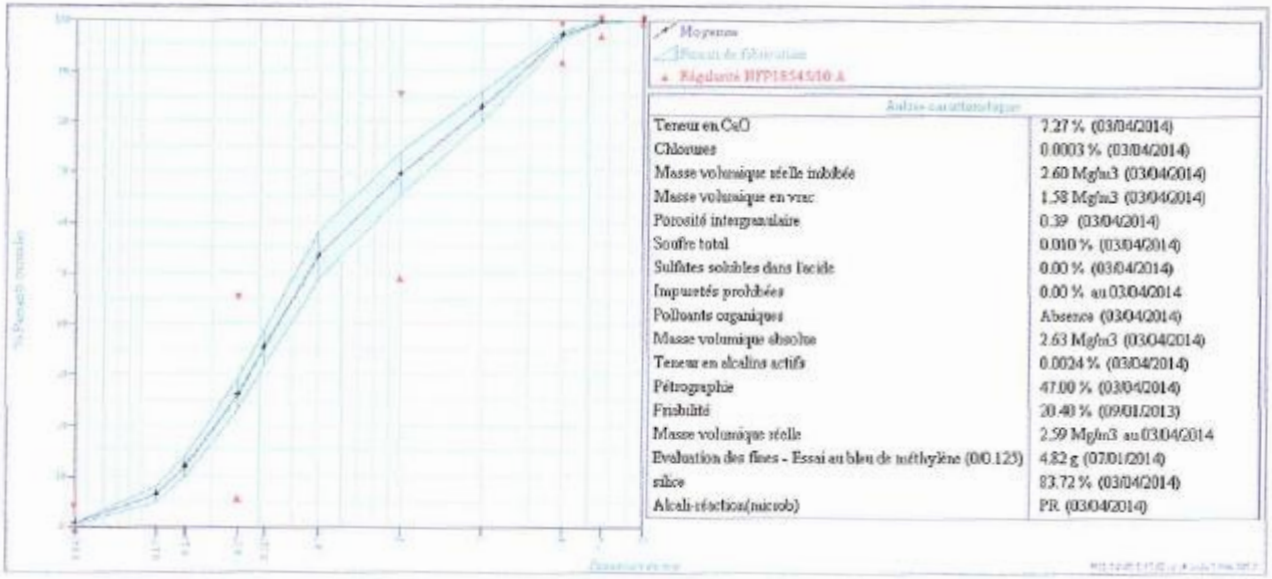

GSM Italcementi Group

La Grande Paroisse

Lieu dit les Pièces de Pinouvert
27130 VARENNES SUR SEINE
Tel 01.60.73.51.70 Fax 01.60.66.13.02 pdegombert@gsm-granulats.fr

Fiche Technique de Produit

Engagement du 03/04/2014 au 09/10/2014
Page 1/1, imprimé le mardi 8 avril 2014

4/11 roulé LGP1

Pétrographie : Alluvionnaire silico/calcaire
Elaboration : Roulé

Utilisateur : EXTERNE

Partie contractuelle

Valeurs spécifiées sur lesquelles le producteur s'engage

Classe granulaire		Norme	Code
4	11.2	NF P 18-545 Article 10	A sauf FI et WA24 code B

	2	4	5	6.3	8	10	11.2	16	22.4	FI	LA(8/11.2)	f	WA24
V.S.S.+U	6	20					100	100	100	39.0	33.00	1.80	5.50
V.S.S.	5	15					99	100	100	35.0	30.00	1.50	5.00
V.S.I.	0.0	0.0					84	98	100				
V.S.I.-U	0.0	0.0					79	97	100				
Ecart-type max	1.52	4.55					4.55	0.61					

Partie informative

Résultats de production

du 10/10/13 au 02/04/14

	2	4	5	6.3	8	10	11.2	16	22.4	FI	LA(8/11.2)	f	WA24
Maximum	2	11	28	53	76	91	97	100	100	29.9		0.94	2.65
Xf+1.25xEcart-types	1	9	26	52	76	91	97	100	100	30.2		0.44	2.65
Moyenne Xf	1	6	20	44	67	85	94	100	100	28.8	25.20	0.21	2.65
Xf-1.25xEcart-types	0	4	15	35	59	80	91	100	100	27.4		0.00	2.65
Minimum	0	3	10	24	46	74	88	100	100	27.0		0.00	2.65
Ecart-type	0.3	1.9	4.5	7.1	7.1	4.2	2.2	0.00	0.00	1.10		0.182	0.002
Nombre de résultats	29	29	29	29	29	29	29	29	29	6	1	28	2

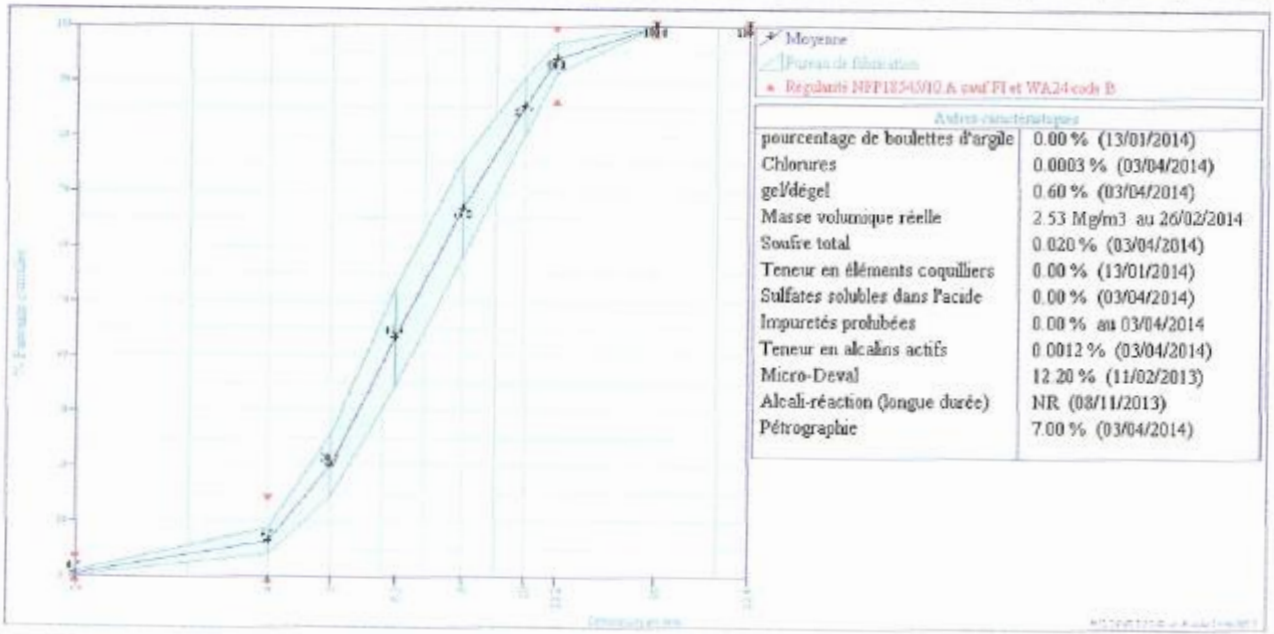

Autres caractéristiques	
pourcentage de boulettes d'argile	0.00 % (13/01/2014)
Chlorures	0.0003 % (03/04/2014)
gel/dégel	0.60 % (03/04/2014)
Masse volumique réelle	2.53 Mg/m3 au 26/02/2014
Soufre total	0.020 % (03/04/2014)
Teneur en éléments coquilliers	0.00 % (13/01/2014)
Sulfates solubles dans l'acide	0.00 % (03/04/2014)
Impuretés prohibées	0.00 % au 03/04/2014
Teneur en alcalins actifs	0.0012 % (03/04/2014)
Micro-Deval	12.20 % (11/02/2013)
Alcali-réaction (longue durée)	NR (08/11/2013)
Pétrographie	7.00 % (03/04/2014)

GSM
Italcementi Group

GSM
Italcementi Group
IDFE

Fiche Technique de Produit

8/16 roulé BALLOY

Producteur : Balloy
Utilisateur : EXTERNE
Pétrographie : Alluvionnaire silico/calcaire
Elaboration : Roulé

Partie contractuelle

Valeurs spécifiées sur lesquelles le producteur s'engage

Classe granulaire		Norme	Code
8	16	NF P 18-545 Article 10	A sauf FI code D

	4	8	9	11.2	12.5	14	16	20	22.4	31.5	f	WA24	LA	FI
V.S.S.+U	6	20					100		100	100	1.80	3.00	33.00	54.0
V.S.S.	5	15					97		100	100	1.50	2.50	30.00	50.0
V.S.I.	0.0	0.0					82		98	100				
V.S.I.-U	0.0	0.0					77		97	100				
Ecart-type max	1.52	4.55					4.55		0.61					

Partie informative

Résultats de production

	du 14/10/13 au 31/03/14											du 28/08/13 au 28/02/14		
	4	8	9	11.2	12.5	14	16	20	22.4	31.5	f	WA24	LA	FI
Maximum	2	17	29	62	77	89	96	100	100	100	0.84			39.7
Xf+1.25xEcart-types	1	15	27	59	74	86	96	100	100	100	0.54			38.1
Moyenne Xf	1	11	21	49	65	80	92	99	100	100	0.28	2.50	26.40	35.0
Xf-1.25xEcart-types	0	6	15	38	55	74	89	98	100	100	0.03			31.9
Minimum	0	5	11	31	48	69	86	97	99	100	0.00			31.7
Ecart-type	0.5	3.4	4.8	8.2	7.5	5.0	2.7	0.9	0.2	0.00	0.202			2.60
Nombre de résultats	35	35	35	35	35	35	35	32	35	34	35	1	1	6

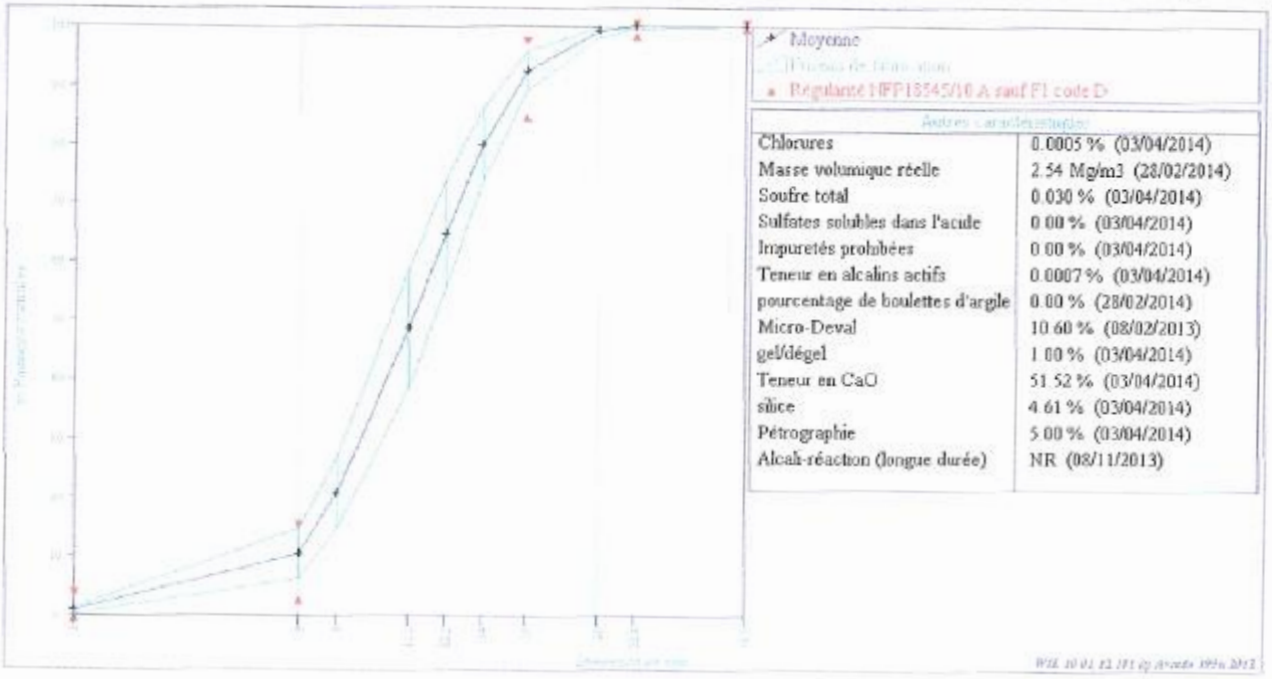

Chlorures	0.0005 % (03/04/2014)
Masse volumique réelle	2.54 Mg/m3 (28/02/2014)
Soufre total	0.030 % (03/04/2014)
Sulfates solubles dans l'acide	0.00 % (03/04/2014)
Impuretés prohibées	0.00 % (03/04/2014)
Teneur en alcalins actifs	0.0007 % (03/04/2014)
pourcentage de boulettes d'argile	0.00 % (28/02/2014)
Micro-Deval	10.60 % (08/02/2013)
gel/dégel	1.00 % (03/04/2014)
Teneur en CaO	51.52 % (03/04/2014)
silice	4.61 % (03/04/2014)
Pétrographie	5.00 % (03/04/2014)
Alcali-réaction (longue durée)	NR (08/11/2013)

Construction

SIKAPLAST® TECHNO 80

Plastifiant/Réducteur d'eau de nouvelle génération pour bétons prêts à l'emploi.

Conforme à la Norme NF EN 934-2

CE NF

Présentation

Le SIKAPLAST® TECHNO 80 est un plastifiant réducteur d'eau non chloré, à base de polycarboxylates modifiés, qui se présente sous la forme d'un liquide jaune clair.

Domaines d'application

SIKAPLAST® TECHNO 80 est un plastifiant/réducteur d'eau qui a été développé spécifiquement pour l'utilisation de granulats concassés dans les bétons de consistance S3 et S4. SIKAPLAST® TECHNO 80 confère aux bétons un bon maintien rhéologique (>1h30) sans effet retard sur les résistances initiales.

SIKAPLAST® TECHNO 80 permet la fabrication de :

- bétons de consistance S3 et S4,
- bétons composés de sable et gravillon concassés,
- bétons utilisant des eaux chargées,
- bétons pompés sur longues distances.

SIKAPLAST® TECHNO 80 confère, pour des bétons S3 et S4, une consistance onctueuse permettant d'utiliser des granulats concassés.

Caractères généraux

Le SIKAPLAST® TECHNO 80 est un plastifiant réducteur d'eau qui confère au béton les propriétés suivantes :

- maintien prolongé de la rhéologie (> 1h30min),
- haute réduction d'eau,
- stabilité et homogénéité des bétons composés de sable et gravillon concassés,
- bonnes résistances initiales et finales,
- bel aspect de parement au décoffrage.

CLASSIFICATION 3 R :

Caractéristiques

Aspect	Liquide jaune clair
Conditionnement	■ Vrac ■ Conteneur perdu de 1000 litres ■ Fût de 220 kg
Stockage	Dans un local fermé, à l'abri de l'ensoleillement direct et du gel, entre 5 et 30 °C. Le produit peut geler, mais, une fois dégelé lentement et réhomogénéisé, il retrouve ses qualités d'origine. En cas de gel prolongé et intense, vérifier qu'il n'a pas été déstabilisé.
Conservation	1 an dans son emballage d'origine intact

Sika®

Construction

Données techniques	
densité	1,055 ± 0,010
pH	4,5 ± 1,0
Teneur en ions Cl^-	≤ 0,1 %
Teneur en Na_2O Eq.	≤ 1,5 %
Extrait sec	24 ± 1,2 %

Conditions d'application	
Consommation / Dosage	Plage d'utilisation recommandée 0,3 à 2% du poids de liant selon les performances recherchées.
Mise en œuvre	Le SIKAPLAST® TECHNO 80 est ajouté, soit, en même temps que l'eau de gâchage, soit en différé dans le béton préalablement mouillé avec une fraction de l'eau de gâchage.
Précautions d'emploi	En cas de contact avec la peau, laver abondamment à l'eau. Consulter la fiche de données de sécurité accessible sur Internet www.sika.fr
Mentions légales	Produit réservé à un usage strictement professionnel Nos produits bénéficient d'une assurance de responsabilité civile «Les informations sur la présente notice, et en particulier les recommandations relatives à l'application et à l'utilisation finale des produits SIKA, sont fournies en toute bonne foi et se fondent sur la connaissance et l'expérience que la Société SIKA a acquises à ce jour de ses produits lorsqu'ils ont été convenablement stockés, manipulés et appliqués dans des conditions normales. En pratique, les différences entre matériaux, substrats et conditions spécifiques sur site sont telles que ces informations ou toute recommandation écrite ou conseil donné n'impliquent aucune garantie de qualité marchande autre que la garantie légale contre les vices cachés. Nos agences sont à votre disposition pour toute précision complémentaire. Notre responsabilité ne saurait d'aucune manière être engagée dans l'hypothèse d'une application non conforme à nos renseignements. Les droits de propriété détenus par des tiers doivent impérativement être respectés. Toutes les commandes sont acceptées sous réserve de nos Conditions de Vente et de Livraison en vigueur. Les utilisateurs doivent impérativement consulter la version la plus récente de la fiche technique correspondant au produit concerné, qui leur sera remise sur demande.»

B. 2. Materials used for RC Beam with a rectangular cross section and T-Beam

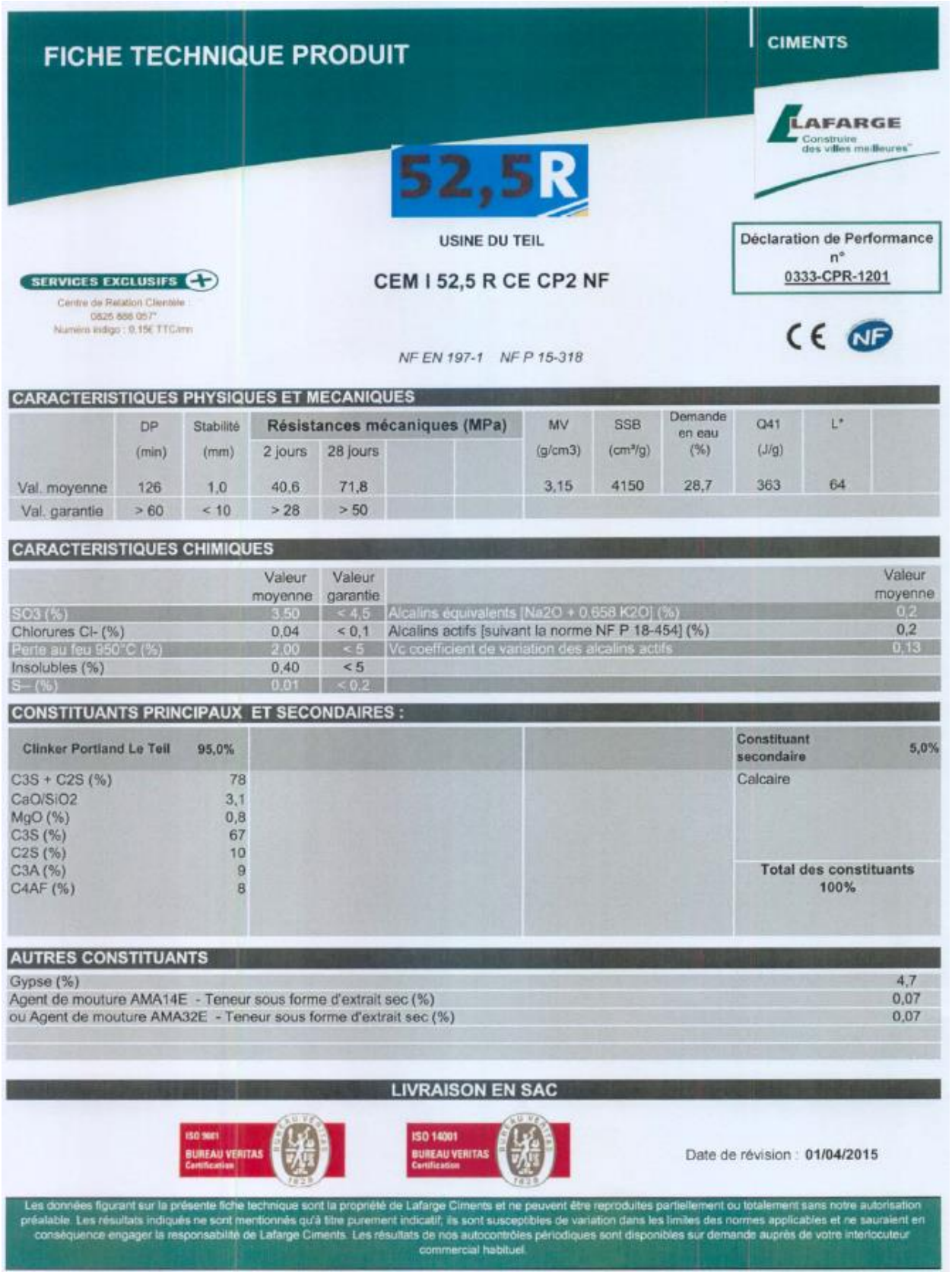

FICHE TECHNIQUE PRODUIT

CIMENTS

LAFARGE
Construire des villes meilleures

52,5R

USINE DU TEIL

CEM I 52,5 R CE CP2 NF

NF EN 197-1 NF P 15-318

Déclaration de Performance n° 0333-CPR-1201

SERVICES EXCLUSIFS
Centre de Relation Clientèle : 0825 886 057* Numéro indigo : 0,15€ TTC/mn

CE NF

CARACTERISTIQUES PHYSIQUES ET MECANIQUES

	DP (min)	Stabilité (mm)	Résistances mécaniques (MPa) 2 jours	28 jours			MV (g/cm3)	SSB (cm²/g)	Demande en eau (%)	Q41 (J/g)	L*	
Val. moyenne	126	1,0	40,6	71,8			3,15	4150	28,7	363	64	
Val. garantie	> 60	< 10	> 28	> 50								

CARACTERISTIQUES CHIMIQUES

	Valeur moyenne	Valeur garantie		Valeur moyenne
SO3 (%)	3,50	< 4,5	Alcalins équivalents [Na2O + 0,658 K2O] (%)	0,2
Chlorures Cl- (%)	0,04	< 0,1	Alcalins actifs [suivant la norme NF P 18-454] (%)	0,2
Perte au feu 950°C (%)	2,00	< 5	Vc coefficient de variation des alcalins actifs	0,13
Insolubles (%)	0,40	< 5		
S-- (%)	0,01	< 0,2		

CONSTITUANTS PRINCIPAUX ET SECONDAIRES :

Clinker Portland Le Teil	95,0%			Constituant secondaire	5,0%
C3S + C2S (%)	78			Calcaire	
CaO/SiO2	3,1				
MgO (%)	0,8				
C3S (%)	67				
C2S (%)	10				
C3A (%)	9			Total des constituants 100%	
C4AF (%)	8				

AUTRES CONSTITUANTS

Gypse (%)	4,7
Agent de mouture AMA14E - Teneur sous forme d'extrait sec (%)	0,07
ou Agent de mouture AMA32E - Teneur sous forme d'extrait sec (%)	0,07

LIVRAISON EN SAC

ISO 9001 BUREAU VERITAS Certification

ISO 14001 BUREAU VERITAS Certification

Date de révision : 01/04/2015

SABLIERES MALET - Site de PORTET

27 avenue de Palarin
31120 Portet sur Garonne
Tel:0561728080

Fiche Technique - NOV 2014 / 01
Engagement du 29/11/2014 au 28/05/2015

Sable 0/4RL code 22 SMP

CE

Pétrographie : Alluvionnaire Siliceux de Garonne
Elaboration : Roulé Lavé
Site de production : PORTET SUR GARONNE

Partie normative

Valeurs spécifiées sur lesquelles le producteur s'engage

Classe granulaire : 0 / 4

Norme : *NFP18-545 Art 10 - EN12620/EN13139 - Granulats pour bétons hydrauliques,mortiers*

Spécification : *Code A*

							D	1.4D	2D		
	0.063	0.125	0.25	0.5	1	2	4	5.6	8	FM	MB
Etendue e	6		40		40		10			0.6	
Incertitude U	1		2		4		2	1		0.15	0.5
V.S.S.+U	7.0		42		88		100	100		3.52	2.00
V.S.S.	6.0		40		84		99	100	100	3.37	1.50
V.S.I.	0.0		0		44		89	95	100	2.77	
V.S.I.-U	0.0		0		40		87	94		2.62	
Ecart-type max			12.12		12.12					0.18	

Partie informative

Résultats de production

	du 11/06/14 au 24/11/14										
	0.063	0.125	0.25	0.5	1	2	4	5.6	8	FM	MB
Maximum	2.8	9	19	43	68	85	99	100	100	3.33	0.50
Xf+1.25xEcart-types	2.1	8	18	41	64	83	99	100	100	3.26	0.55
Moyenne Xf	1.5	6	16	37	59	77	95	99	100	3.10	0.43
Xf-1.25xEcart-types	0.9	5	13	33	54	72	91	98	100	2.93	0.30
Minimum	0.8	5	13	32	52	70	89	97	100	2.80	0.22
Ecart-type	0.51	1.0	1.7	3.1	4.1	4.4	2.9	1.0	0.0	0.130	0.100
Nombre de résultats	26	26	26	26	26	26	26	26	26	26	26
Norme											NFEN 933-9
Dernier	24/11/2014	24/11/2014	24/11/2014	24/11/2014	24/11/2014	24/11/2014	24/11/2014	24/11/2014	24/11/2014	24/11/2014	24/11/2014

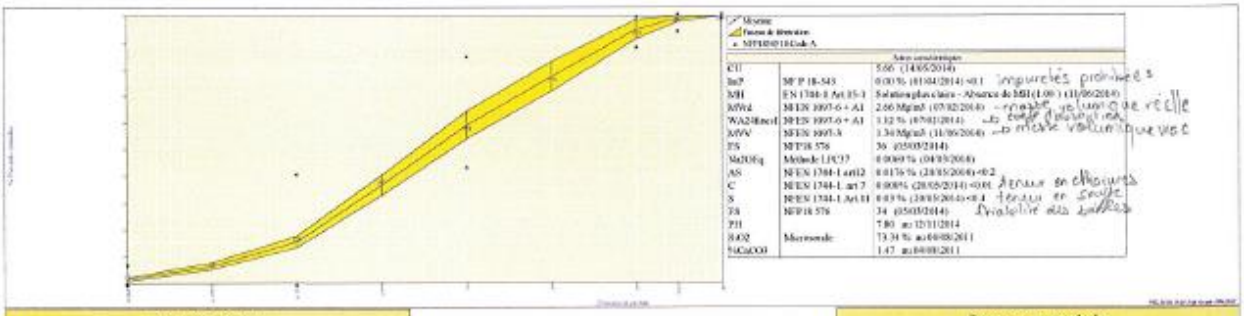

Le producteur :

Document remis à :

SABLIERES MALET - Site de PORTET

27 avenue de Palarin
31120 Portet sur Garonne
Tel:0561728080

Fiche Technique - NOV 2014 / 01

Engagement du 29/11/2014 au 28/05/2015

Gravillon 4/10R code 24 SMP

CE

Pétrographie : Alluvionnaire Siliceux de Garonne
Elaboration : Roulé Lavé
Site de production : PORTET SUR GARONNE

Les essais LA et MDE sont effectués sur la fraction 6.3/10.

Partie normative

Valeurs spécifiées sur lesquelles le producteur s'engage

Classe granulaire		Norme	Spécification
4	10	NFP18-545 Art 10 - EN12620/EN13139 - Granulats pour bétons hydrauliques,mortiers	Code A sauf D code D

		d/2	d		D	1.4D	2D	
	0.063	2	4	8	10	14	20	FI
Etendue e			15		15			
Incertitude U	0.3	1	5		5	1		4
V.S.S.+U	1.8	6	23		100	100		24.00
V.S.S.	1.5	5	18		100	100	100	20.00
V.S.I.	0.0	0	3		90	100	100	
V.S.I.-U	0.0	0	0		85	99		

Partie informative

Résultats de production

	du 23/06/14 au 24/11/14							
	0.063	2	4	8	10	14	20	FI
Maximum	0.9	3	17	91	100	100	100	16.23
Xf+1.25xEcart-types	0.7	3	13	89	100	100	100	15.68
Moyenne Xf	0.4	2	9	84	99	100	100	14.54
Xf-1.25xEcart-types	0.1	1	5	78	97	100	100	13.39
Minimum	0.0	0	3	74	92	100	100	13.76
Ecart-type	0.26	0.7	3.4	4.6	1.7	0.0	0.0	0.916
Nombre de résultats	22	22	22	22	22	22	22	6
Norme								NFEN 933-3
Dernier	24/11/2014	24/11/2014	24/11/2014	24/11/2014	24/11/2014	24/11/2014	24/11/2014	03/11/2014

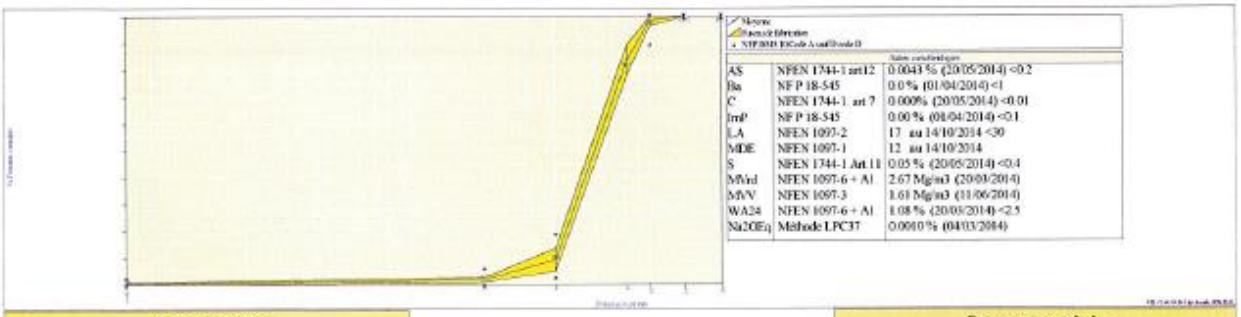

AS	NFEN 1744-1 art12	0.0043 % (20/05/2014) <0.2
Ba	NF P 18-545	0.0 % (01/04/2014) <1
C	NFEN 1744-1 art 7	0.000% (20/05/2014) <0.01
ImP	NF P 18-545	0.00 % (08/04/2014) <0.1
LA	NFEN 1097-2	17 au 14/10/2014 <30
MDE	NFEN 1097-1	12 au 14/10/2014
S	NFEN 1744-1 Art.11	0.05 % (20/05/2014) <0.4
MVrd	NFEN 1097-6 + Al	2.67 Mg/m3 (20/03/2014)
MVV	NFEN 1097-3	1.61 Mg/m3 (11/06/2014)
WA24	NFEN 1097-6 + Al	1.08 % (20/03/2014) <2.5
Na2OEq	Méthode LPC37	0.0010 % (04/03/2014)

Le producteur :	*Document remis à :*

This page is intentionally left blank

Appendix C

Predictive calculation of crack width and spacing According to Eurocode 2

In this section, the calculation of crack width and spacing using recent formulation in Eurocode 2 are presented.

This page is intentionally left blank

C. 1. Eurocode 2 Formulation for crack opening and spacing

The proposed formulations by Eurocode 2 (Eurocode 2, 2005) presented in Chapter 1 are used to calculate the design crack width and spacing. The criteria of crack opening maximal is describe as in table below (crack opening is expressed in millimetre).

Exposure Class	Reinforced members and prestressed members with unbonded tendons	Prestressed members with bonded tendons
	Quasi-permanent load combination	Frequent load combination
X0, XC1	0,4[1]	0,2
XC2, XC3, XC4	0,3	0,2[2]
XD1, XD2, XD3, XS1, XS2, XS3		Decompression
Note 1: For X0, XC1 exposure classes, crack width has no influence on durability and this limit is set to give generally acceptable appearance. In the absence of appearance conditions this limit may be relaxed. Note 2: For these exposure classes in addition decompression should be checked under the quasi-permanent combination of loads.		

In the comment case, the crack opening is limited at 300 μm.

C. 2. Crack Opening and Spacing for RC Prismatic Element (Tensile Test)

As expressed in Equation (1.3), the maximum crack spacing depends on the bond condition, the diameter of the bar, and the spacing of each bar as rewritten in the following expression. For the case of tensile stress, regarding the Figure 2.14 presented in Chapter 2, the parameters taken are as follow.

$$s_{r,\max} = k_3\, c + k_1\, k_2\, k_4 \,\phi / \rho_{p,eff} \qquad \text{(C. 1)}$$

Where:

- c = The cover concrete to the longitudinal reinforcement = 44 mm for $\phi = 12$ mm.
- k_1 = The coefficient which considers the bond properties. $k_1 = 0{,}8$ for ribbed bar
- k_2 = The distribution of strain coefficient. $k_2 = 1{,}0$ for pure tension
- k_3 = For cover concrete $c > 25$ mm, $k_3 = 3{,}4\left(25/c\right)^{2/3} = 2{,}33$
- k_4 = 0,425
- ϕ = The bar diameter

Hence, the maximum crack spacing $s_{r,\max} = 45{,}9$ cm. According to (Mosley et al., 2007), where the maximum crack spacing exceeds $5\left(c + \phi/2\right) = 25$ cm, the maximum spacing is

$s_{r,\max} = 1{,}3(h - x)$. So, we obtain 13 cm of spacing maximum. Then, according to Eurocode, the average deformation can be calculated as expressed below.

$$\varepsilon_{sm} - \varepsilon_{cm} = \frac{\sigma_s - k_t \dfrac{f_{ct,eff}}{\rho_{p,eff}}\left(1 + \alpha_e \ \rho_{p,eff}\right)}{E_s} \geq 0{,}6 \frac{\sigma_s}{E_s} \qquad \text{(C. 2)}$$

Where:

σ_s = The stress in the tension reinforcement calculated in the cracked concrete section

k_t = The factor dependent on the duration of the loading. $k_t = 0{,}6$ for a short-term loading

E_s = The design value of a modulus of elasticity of reinforcing steel = 200 GPa.

$f_{ct,eff}$ = The mean value of the tensile strength of the concrete effective at the time when the first cracks occur $\approx f_{ctm}$

$\rho_{p,eff}$ = The effective reinforcement ratio. For non-pre-stressed beam:

$\rho_{p,eff} = A_s / A_{c,eff}$

A_s = The area of reinforcing steel

$A_{c,eff}$ = The effective area of concrete in tension = 100 cm²

α_e = The ratio E_s / E_{cm}

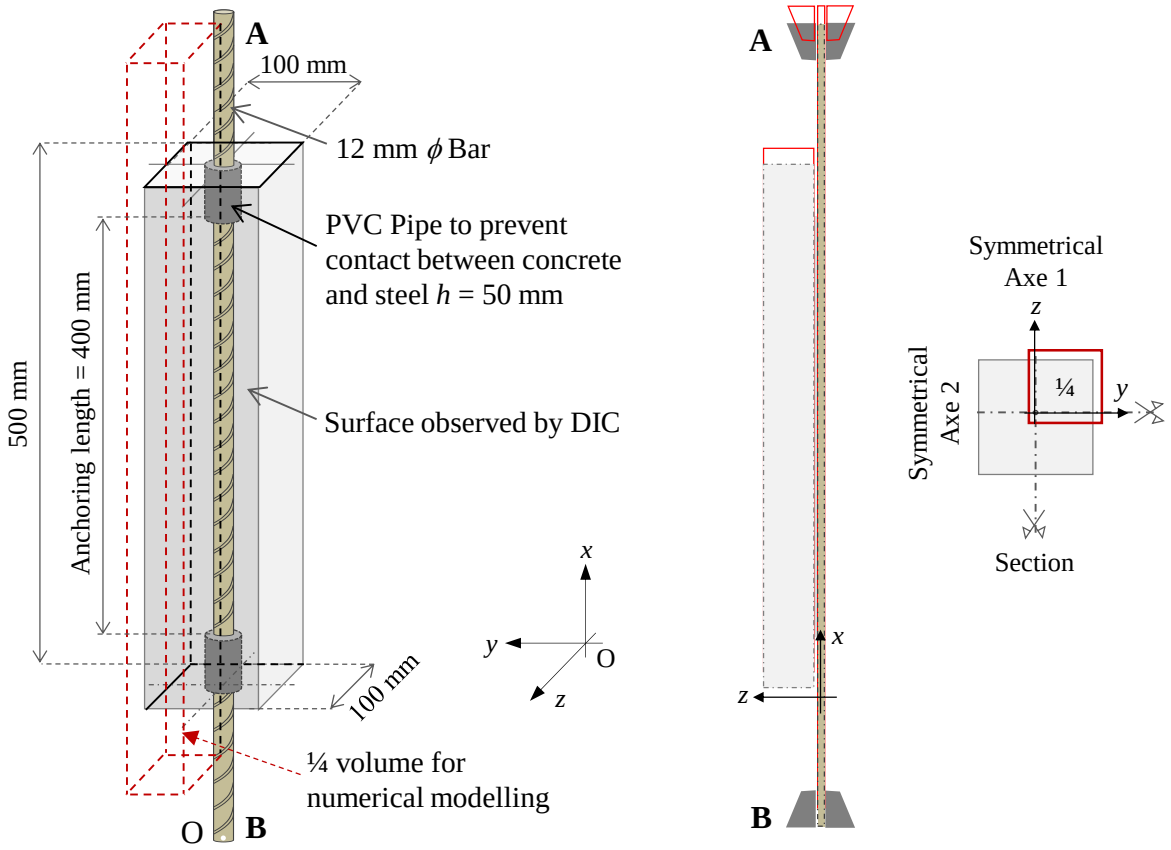

Figure C. 1. Detail of dimension for tensile test.

Using the obtained results, the evolution of crack opening is compared to the experimental

and modelling results of tensile test (colour black in Figure C.2). As we can see here, analytical formulation of Eurocode is underestimated the evolution of crack opening.

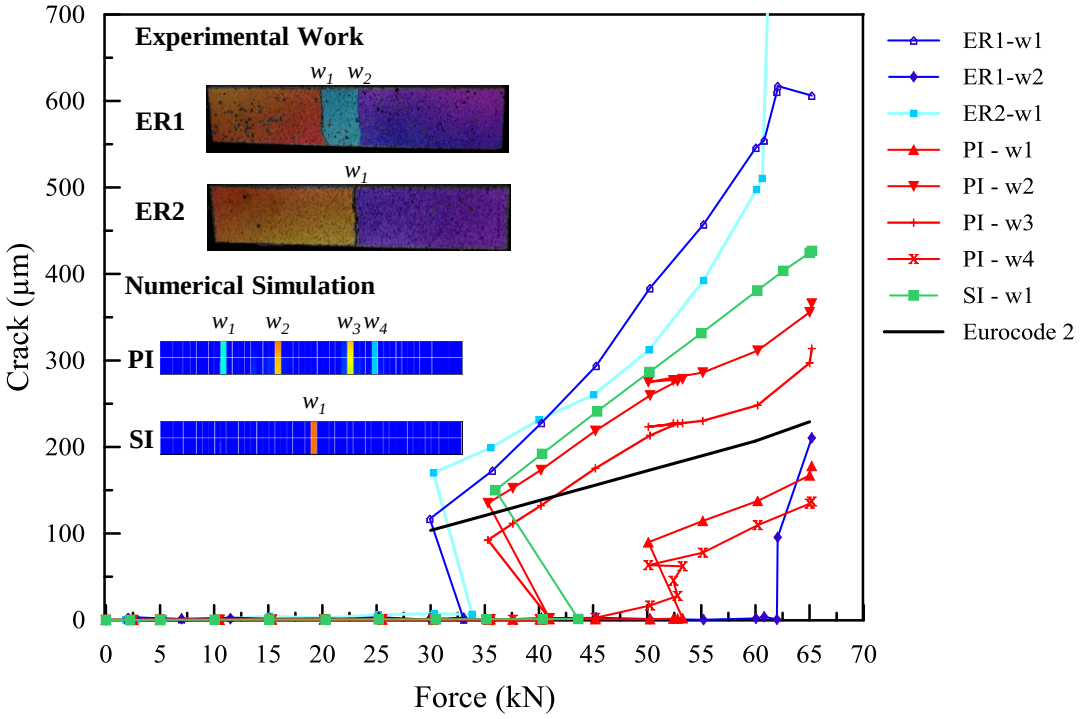

Figure C. 2. Evolution of the maximum crack width with $S_{r,max}$ = 13 cm.

C. 3. Crack Opening and Spacing for RC Beam with rectangular section (Bending Test)

For the case of RC beam with rectangular cross section, regarding the Figure 3.3 presented in Chapter 3 (represented in Figure C.3), using the same expression in Equation C.1, the parameters taken are as follow.

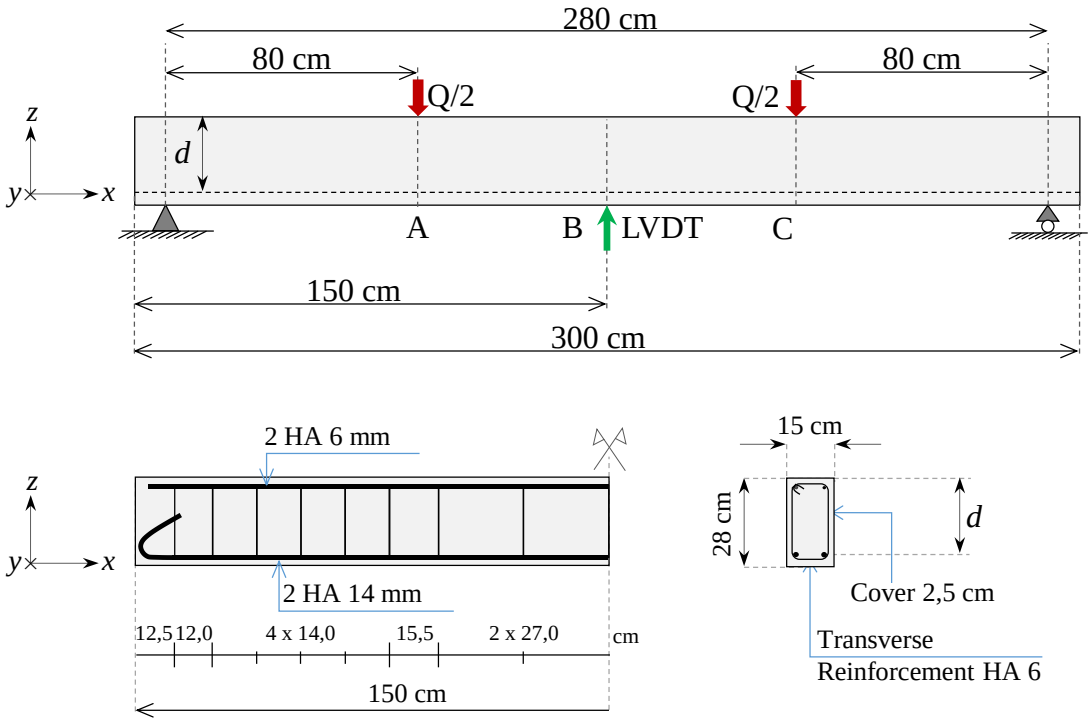

Figure C. 3. Detail dimensions of RC beam and its loading application.

Where:

c = The cover concrete to the longitudinal reinforcement = 25 mm.

k_1 = The coefficient which considers the bond properties. $k_1 = 0{,}8$ for ribbed bar.

k_2 = The distribution of strain coefficient. $k_2 = 0{,}5$ for bending.

k_3 = For cover concrete $c \leq 25$ mm, $k_3 = 3{,}4$

k_4 = 0,425

Hence, the maximum crack spacing $s_{r,\max} = 168{,}12$ mm. Then, according to Eurocode, the average deformation can be calculated using Equation (C.2) and the parameters are:

k_t = for a short-term loading $k_t = 0{,}6$

E_s = The design value of a modulus of elasticity of reinforcing steel = 200 GPa.

$f_{ct,eff}$ = The mean value of the tensile strength of the concrete effective at the time when the first cracks occur $\approx f_{ctm}$

$\rho_{p,eff}$ = The effective reinforcement ratio. For non-pre-stressed beam: $\rho_{p,eff} = A_s / A_{c,eff}$

A_s = The area of reinforcing steel

$A_{c,eff}$ = The effective area of concrete in tension surrounding the reinforcement with

$h_{c,eff} = \min\left(2{,}5(h-d);(h-x)/3;h/2\right)$

We obtained that using the analytical expression of crack width from Eurocode 2, the crack prediction is also underestimated.

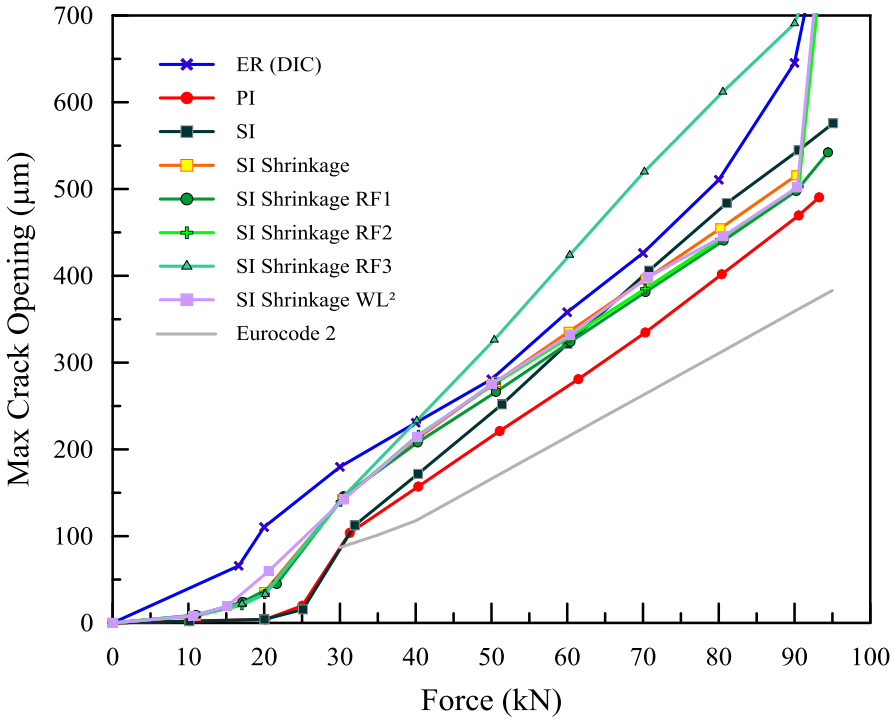

Figure C. 4. Detail dimensions of RC beam and its loading application.

This page is intentionally left blank